ISSN 2712-8172

MAGAZINE OF CIVIL ENGINEERING

Magazine of Civil Engineering

ISSN 2712-8172

Online peer-reviewed open-access scientific journal in the field of Civil and Construction Engineering

Founder and Publisher: Peter the Great St. Petersburg Polytechnic University

This journal is registered by the Federal Service for Supervision of Communications, Information Technology, and Mass Media (ROSKOMNADZOR) in 2020. Certificate El No. FS77-77906 issued February 19, 2020.

Periodicity: 8 issues per year

Publication in the journal is open and free for all authors and readers.

Indexing: Scopus, Web of Sceince (ESCI, RSCI), DOAJ, Compendex, Google Academia, Index Copernicus, ProQuest, Ulrich's Serials Analysis System, CNKI

Corresponding address: 29 Polytechnicheskaya st., Saint Petersburg, 195251, Russia

Chief science editor:
D.Sc., Galina L. Kozinetc

Deputy chief science editors:
D.Sc., Sergey V. Korniyenko

Executive editor: Ekaterina A. Linnik

Translator, editor: Irina Ye. Lebedeva

Proofreader: Philipp Chrysanthes S. Bastian

DT publishing specialist:
Anastasiya A. Kononova

Contacts:
E-mail: mce@spbstu.ru
Web: http://www.engstroy.spbstu.ru

Date of issue: 29.09.2025

Contents

Magazine of Civil Engineering

ISSN 2712-8172

journal homepage: http://engstroy.spbstu.ru/

Research article

UDC 624.97

DOI: 10.34910/MCE.138.1

Numerical analysis of Arctic wind turbines supporting structures

I.V. Rigel ✉ , ***V.V. Elistratov***

Peter the Great St. Petersburg Polytechnic University, St. Petersburg, Russian Federation

✉ *ivan.rigel@yandex.ru*

Keywords: Arctic wind turbine, environmental conditions, supporting structures, numerical modeling, stress-strain state, dynamic response, permafrost degradation, ground reaction forces

Abstract. The paper presents numerical modeling methods for the supporting structures of wind turbines operating under Arctic conditions on permafrost soils. The relevance of the research is determined by the strategic priorities for the development of the Russian Arctic zone and the need to consider the specific environmental and climatic conditions in the energy infrastructure design. An integrated methodology is developed for analyzing the structural behavior of Arctic wind turbines, including the stress–strain state and dynamic response of the supporting structures finite element modeling, accounting for wind and operational loads, nonlinear soil–structure interaction, thermal regime, and temperature-dependent soil properties. The methodology is tested through a case study of a 100 kW wind turbine with a 30 m tower and a 24 m rotor diameter, for the Yamal-Nenets Autonomous Okrug environmental conditions. The results show that the permafrost degradation leads to increased displacements and stresses in the structural system by up to 25 % and reduces the structure natural frequencies by up to 10 %, due to a local 70-fold decrease in reactive soil resistance. The identified factors should be considered in the Arctic wind turbines design to ensure accurate assessment of structural performance and resonance risks.

Funding: The research was supported by the Russian Science Foundation grant No. 25-29-00497, https://rscf.ru/project/25-29-00497/.

Citation: Rigel, I.V., Elistratov, V.V. Numerical analysis of Arctic wind turbines supporting structures. Magazine of Civil Engineering. 2025. 18(6). Article no. 13801. DOI: 10.34910/MCE.138.1

1. Introduction

Wind turbines are structures that convert wind energy into electricity and represent a promising solution for remote regions of the Arctic, where energy supply is predominantly provided by diesel power plants. This results in high energy costs due to the logistical challenges of fuel delivery and has a negative environmental impact. The potential of Arctic wind energy is supported by the presence of strong and stable winds in northern regions [1]. According to forecasts [2], wind energy potential in the Russian Arctic is expected to increase throughout the 21st century, while the frequency of wind speeds outside the operational range of wind turbines will decrease across much of Eastern Siberia, thereby improving the capacity factor. These trends create long-term prospects for the deployment of Arctic wind power systems; however, the extreme climatic conditions of the Russian Arctic present significant engineering challenges.

One of the key characteristics of the object under study is the installation of wind turbines on permafrost ground, i.e., soils that remain in a frozen state for three or more years and ensure the stability of the supporting structural system in its design position. The loads acting on the supporting structure of a wind turbine are balanced by reactive forces from the soil, which depend on its physical and mechanical properties. Studies have shown that climate warming, occurring faster in the Arctic than the global average [3], leads to permafrost thawing, posing a threat to the reliable operation of infrastructure, including wind turbines. Permafrost degradation manifests itself in the deepening of the seasonally thawed layer and the change of the physical and mechanical properties of permafrost soils due to temperature increase, which

can lead to excessive settlements, tilting, loss of stability of wind turbines and increased static and dynamic loads on structural elements [4, 5]. This phenomenon is recognized as one of the critical factors affecting the reliability and durability of building structures in permafrost zones, since the reduction of bearing capacity and stiffness of the ground compromises structural performance and may lead to emergency condition of structure [6]. The study of these aspects is essential for the development of adapted structural solutions that ensure the safe and stable operation of wind turbines under Arctic conditions.

Wind turbines are subjected to dynamic loads resulting from wind gusts and rotor rotation, which induce structural vibrations. Environmental factors such as icing, snow, seasonal and long-term changes in permafrost properties affect the natural frequencies of the wind turbine and its structural elements [5, 7, 8]. A reduction of the supporting structures fixation stiffness, increased mass and inertia of the rotor and nacelle assembly (RNA) due to icing and snow loads, leads to system natural frequencies decrease and an amplification of its dynamic response. If the structure natural frequencies approach the frequencies of external loads, resonance may occur, which can lead to an emergency condition of the wind turbine. As noted in [9], neglecting the ground–structure interaction leads to distorted estimations of internal forces in the superstructure and does not allow for an accurate assessment of displacements. Accounting the ground stiffness is particularly important when developing damping devices to mitigate wind and seismic loads acting on the structure [4, 10].

Modern research in wind turbine design focuses on aerodynamic blades modeling, wind-induced loads assessment, evaluation of the static stress–strain state (SSS) and analysis of the supporting structural systems dynamic response. To this end, numerical methods and specialized software are employed for aeroservoelastic modeling of wind turbines, including OpenFAST and QBlade, as well as finite element software packages for structural mechanics simulations, such as ANSYS Mechanical, Abaqus, SAP2000 and others [4, 11–22].

Nonlinear boundary conditions allow for a more realistic representation of soil response and enable more accurate prediction of the behavior of wind turbine support structures under loading, which is essential for developing reliable and durable designs in Arctic environments. The fixation stiffness in calculation schemes of wind turbines can be incorporated using various approaches. Most studies related to the modeling of fixation conditions refer to offshore wind turbines with monopile foundations [23–26]. In [24], the primary modern methods for modeling soil–structure interaction in wind turbine analysis are presented, including the apparent fixity method, coupled spring method, and distributed spring method. Reference [25] provides an extensive review of modeling techniques for offshore wind turbines on monopile foundations, considering foundation response under monotonic and cyclic loading. In [27], an overview is given of pile–soil interaction models under static and dynamic loading for various types of unfrozen soils.

The calculation approaches described are quite universal and can be applied to onshore wind turbines with various types of support structures. For example, in [28], coupled spring models are used for gravity-based foundations, while in [4], nonlinear distributed springs are employed as boundary conditions for simulating wind turbines on piles embedded in permafrost soils.

Grounds in Arctic regions are subject to seasonal changes and long-term degradation due to the permafrost thawing. At the same time, permafrost does not exist in all countries and is primarily found across large areas of Russia, the United States (Alaska), Canada, the Nordic countries, and the Chinese plateau [29]. As a result, only a limited number of studies incorporate the permafrost reaction into wind turbine models, which restricts the ability to assess dynamic loads and structural stability under realistic conditions. In [5], the results of field investigations of the dynamic response of a wind turbine on a pile foundation embedded in permafrost in Alaska are presented. It is noted that the ground stiffness varies due to seasonal and long-term temperature changes and permafrost degradation, which affects the overall stiffness and dynamic behavior of the structural system and can lead to resonance. In [4], numerical studies of the same wind turbine are presented, in which a foundation response model based on the average foundation temperature obtained from field measurements was used to describe the interaction between the foundation and the frozen ground.

However, studies on the supporting structures of Arctic wind turbines that account for foundation response derived from predictive thermophysical models are currently lacking.

Thus, the design of structures in Arctic regions requires the development of models for investigating thermophysical processes in permafrost foundations. Such processes are usually simulated using specialized tools for thermophysical modeling, such as Frost 3D, or universal finite element software packages like Midas GTS NX. These tools enable the simulation of soil temperature regimes, including heat and moisture transfer within the ground, while accounting for climatic factors, solar radiation, and the implementation of thermal stabilization systems. References [30, 31] provide examples of applying temperature regime modeling to assess temperature distribution within the ground.

The interaction between thermophysical and mechanical processes in the ground under structures with dynamic loads is partially discussed in [32–38]. Reference [32] notes that soils, like other materials, may experience heating under dynamic loading, which is likely one of the key mechanisms contributing to the degradation of permafrost properties under such conditions. At the same time, the pronounced creep behavior of frozen soils leads to a noticeable increase in their stiffness with higher loading rates. In [33], it is reported that frozen soils exhibit competing mechanisms: as the rate of dynamic loading increases, mechanical properties tend to decrease due to heating but simultaneously increase due to creep effects. Experimental studies focused specifically on temperature rise under dynamic loading are scarce in the literature; however, this effect is indirectly considered in studies of the dynamic elastic modulus of frozen soils. References [34, 35] provide an overview of experimental research on the behavior of frozen soils under dynamic loads. Empirical data show that the deformation modulus of frozen soils increases with decreasing temperature and increasing loading frequency, but decreases with increasing amplitude. Studies [36–38] present experimental data on the stiffness of pile foundations in frozen soils and propose mathematical models for calculating the parameters of nonlinear springs that simulate foundation response as a function of temperature.

However, studies that examine the conditions of fixation influence under potential permafrost degradation on the SSS and dynamic characteristics of Arctic wind turbines, including natural frequencies and resonance risk, are virtually absent.

The objective of this study is to develop an integrated methodology for analyzing the behavior of Arctic wind turbines under specific environmental and climatic conditions, based on the supporting structures SSS and dynamic response finite element modeling, considering wind and operational loads, nonlinear ground response and the thermophysical and mechanical properties of permafrost.

To achieve this objective, the following tasks were solved:

- a computational model of the wind turbine structural system was developed to simulate the SSS and natural vibrations of the supporting structures, considering nonlinear conditions of fixation;
- a model of nonlinear constraints for the wind turbine support structure was developed to calculate reactive forces in degrading permafrost under dynamic loading, incorporating soil properties and the thermal regime of the ground;
- a thermophysical model of the permafrost foundation was developed, considering the effects of air temperature, solar radiation, and thermal stabilization systems, to define nonlinear constraints parameters for the structural model of the wind turbine;
- an integrated methodology for modeling the supporting structures of Arctic wind turbines was formulated based on the developed models;
- the proposed methodology was tested through a case study of a 100 kW Arctic wind turbine with a 30 m tower and a 24 m rotor diameter, operating under the conditions of the Yamal-Nenets Autonomous Okrug.

2. Methods

Modeling the supporting structural system of a wind turbine using finite element software for analyzing the SSS of structural components and the dynamic response of the structure under Arctic environmental conditions require consideration of wind-induced and operational loads, nonlinear ground response, thermal regime, and temperature-dependent soil properties.

Fig. 1 presents the scheme of loads and environmental impacts acting on the supporting structural system of the Arctic wind turbine.

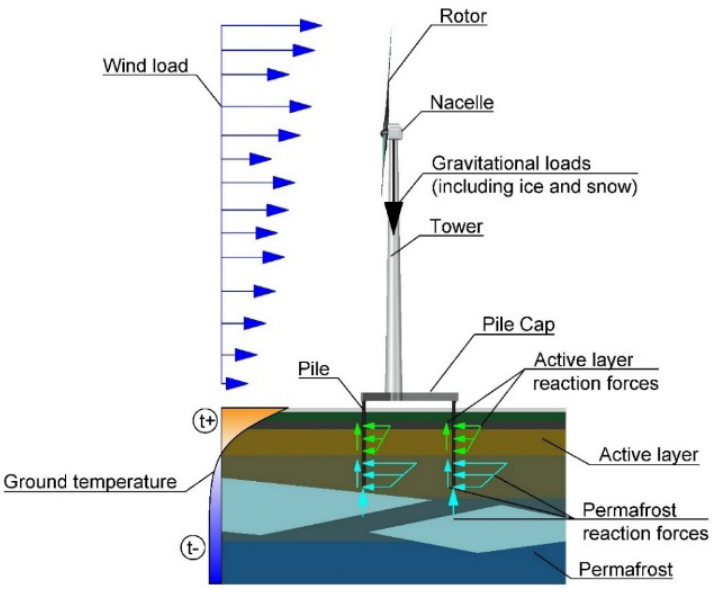

Figure 1. Scheme of loads and environmental impacts on the supporting structural system of the Arctic wind turbine.

A distinctive feature of the proposed methodology is its systemic approach, which includes thermophysical modeling of the "structure–ground" system, analysis of pile–soil interaction and detailed numerical modeling of the wind turbine supporting structures.

Fig. 2 presents the structure of the Arctic wind turbine supporting structures computational study.

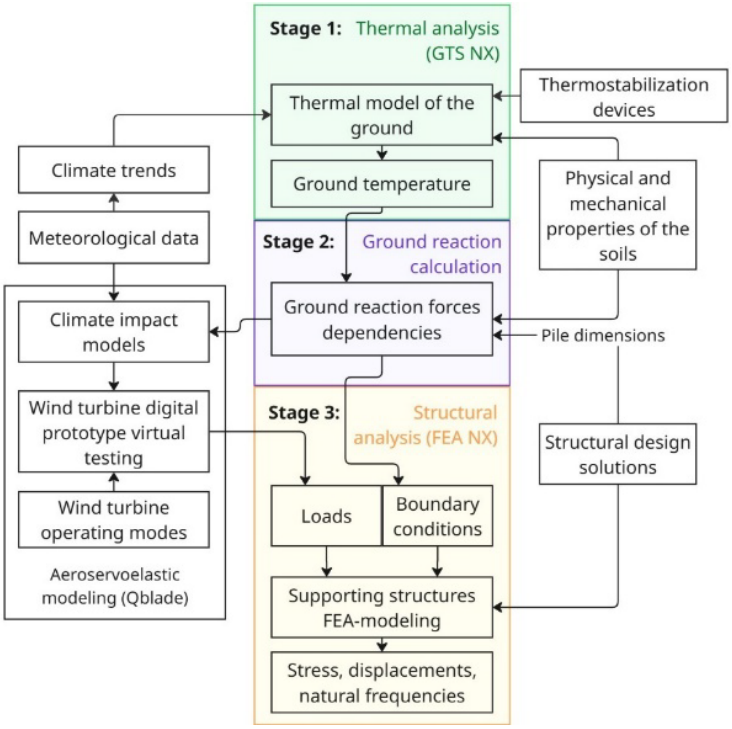

Figure 2. Structure of the Arctic wind turbine supporting structures computational study. The computational methodology consists of three main stages: Stage 1: Thermal analysis with thermophysical modeling of the ground; Stage 2: Calculation of the ground reactive force – displacement relationships considering temperature; Stage 3: Structural analysis, including the stress–strain state and determination of the natural frequencies and mode shapes of the wind turbine.

At Stage 1, thermophysical processes in the permafrost ground are simulated to assess the temperature distribution in the soil, considering variations in air temperature, solar radiation, and the thermal stabilization systems. The finite element method (FEM), implemented in the GTS NX software package [39], is employed for this purpose. This approach enables consideration of the complex geometry of the

foundation and soil layers, the heterogeneity of thermophysical soil properties, and allows for the numerical solution of nonlinear equations, including the effects of phase transitions.

The following calculation scenarios are considered:

1. the site under natural conditions without accounting for the thermostabilization and climatic trends.
2. the site considering the structure with thermostabilization.
3. the site under natural conditions accounting for climatic trends.
4. the site considering both climatic trends and the structure with thermostabilization.

The thermophysical properties of structural materials and foundation soils are determined based on survey results or reference data.

Heat exchange with the atmospheric air throughout the year is modeled using a convective thermal boundary condition in accordance with the following formula:

$$q_a = \alpha \Delta T = \alpha \left(T_a - T_{sur} \right), \tag{1}$$

where q_a – heat flux from atmospheric air through the ground surface; α – convective heat transfer coefficient, which depends on wind speed and the thermal conductivity of the snow cover; T_a – air temperature, which varies throughout the year; T_{sur} – ground surface temperature.

The heat flux received from solar radiation is described by the following formula:

$$q_s = G\left(1 - A\right), \tag{2}$$

where G – total solar radiation on a horizontal surface for the latitude in question, determined from reference data; A – surface albedo, taken as 0.9 when snow cover is present and 0.4 when it is absent.

To account for heat losses due to ground surface back radiation, evaporation, and to compensate for inaccuracies in the parameters of natural climatic conditions, a reduction coefficient k is proposed, determined through calibration of the thermophysical model. Thus, the total heat flux, considering solar radiation, can be represented by a temperature correction applied to the convective heat transfer boundary condition:

$$q = q_a + kq_s = \alpha \left(T_a - T_{sur} + k \frac{G\left(1 - A\right)}{\alpha} \right) = \alpha \left(T_a - T_{sur} + kT_{corr} \right) = \alpha \left(T_{a.c.} - T_{sur} \right), \tag{3}$$

where T_{corr} – temperature correction that takes into account solar radiation; $T_{a.c.}$ – corrected air temperature; k – calibration coefficient.

A numerical model of the ground in its natural state is created for parameter calibration, with parameters adjusted to ensure the condition of constant temperature in the permafrost soil at a depth of 15 m.

To simulate long-term degradation, corrections based on linear trends of climate change are introduced into the climatic parameters.

The result of the thermophysical modeling is the temperature distribution within the ground and its temporal variation, which enables the determination of the active layer thickness and the calculation of reactive forces exerted by the ground on the Arctic wind turbine supporting structural system.

At Stage 2, the calculation of foundation reactive forces resulting from the deformation of the supporting structures is performed. To model the foundation reactive forces considering the temperature distribution obtained at Stage 1, the distributed spring method is employed. The deformation of the springs is described using nonlinear force-displacement relationships in the corresponding directions. Three types of springs are used in the model:

- “p-y” springs – model the lateral resistance of the pile;
- “t-z” springs – model the axial resistance along the pile shaft;
- “Q-z” springs – model the axial resistance beneath the pile tip.

The parameters of the “p-y” springs are adopted according to Equation 4, which has been validated in [37] based on field tests of piles in frozen silty soils:

$$p = \frac{p_u}{2}\left(\frac{y}{y_m}\right)^{\frac{1}{3}}, \quad (4)$$

where p_u – ultimate lateral resistance of the pile; q_u – uniaxial compressive strength of the frozen soil; d – pile diameter; y – horizontal displacement of the pile; $y_m = \varepsilon_{50} \cdot d$, ε_{50} – relative strain at 50 % of the frozen soil strength.

The ultimate lateral resistance p_u is determined using Equation 5 [36]:

$$p_u = 3cd + \sigma_v d + Jzc, \quad (5)$$

where σ_v – vertical stress at depth z; c – soil cohesion; J – empirical coefficient, typically taken as 0.5; z – depth from the ground surface.

The "t-z" and "Q-z" springs parameters used to model the response of frozen soils are adopted according to the methodology described in [40], based on the values of the cohesion of frozen soil. Given the predominance of dynamic loads on the wind turbine supporting structures, the short-term value of the cohesion of frozen soil is used for extreme load cases and dynamic simulations.

The influence of temperature in the calculation of spring parameters is taken into account through the short-term cohesion of frozen soil, c_f, which is calculated using the formula provided in [41]:

$$c_f = c_t + \frac{\rho_w L_f}{T_f}\left(T_f - T\right)^{1-\alpha}\left(\frac{n - w_w}{n}\right)^{\beta}, \quad (6)$$

where c_t – cohesion of unfrozen soil; ρ_w – water density (1000 kg/m³); L_f – latent heat of phase transition (334 kJ/kg); T_f – soil freezing point temperature; T – temperature; n – soil porosity; w_w – unfrozen water content; α and β – model parameters.

The damping coefficients for the springs are determined using the formula provided in [26]:

$$c_m = 2k_s \frac{\beta_m}{\omega}, \quad (7)$$

where ω – wind turbine fundamental natural angular frequency; k_s – secant stiffness of the spring; β_m – hysteretic damping ratio, assumed to be 5 %.

The described mathematical model of ground response links thermal and mechanical processes through temperature-dependent material properties, enabling the assessment of foundation reactive forces under subzero temperatures for the design of structures on permafrost. This model can be applied in nonlinear static analysis of supporting structures as well as in aeroservoelastic simulations of wind turbines.

For modal analysis of the structural system and determination of the wind turbine natural frequencies, linearized springs are used, accounting for the expected deformation levels under dynamic loading during normal operation. To determine the expected deformation levels, the structural system of the wind power plant is analyzed with nonlinear springs under the maximum design load corresponding to normal power generation mode, after which the secant stiffnesses of the springs are evaluated.

The result of Stage 2 is the set of relationships between the foundation reactive forces and the deformations of the supporting structures.

At Stage 3, Arctic wind turbine supporting structural system finite element modeling is carried out using the FEA NX software package [42]. The calculation scheme of the wind turbine used for finite element analysis is shown in Fig. 3.

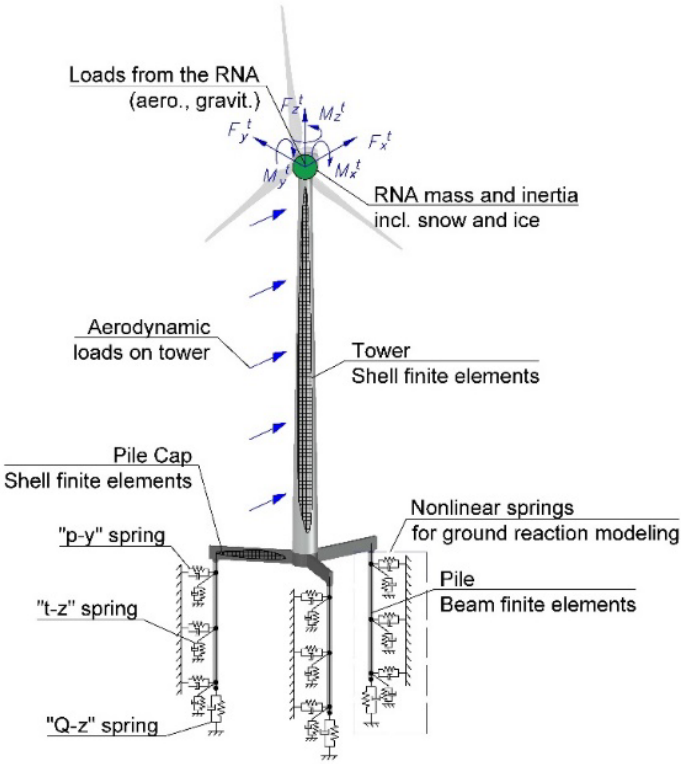

Figure 3. Arctic wind turbine supporting structural system calculation scheme with nonlinear constraints.

Since the subject of the study is the supporting structures, the RNA is modeled using an equivalent concentrated mass and inertia element. Loads from the RNA applied to the top point of the tower, taking into account natural climatic conditions and operational modes of the wind power plant, are determined based on aeroservoelastic simulations performed in the QBlade software package [13]. These loads are applied as a combination of forces and moments along six degrees of freedom (three forces $F_x^t,\ F_y^t,\ F_z^t$ and 3 moments $M_x^t,\ M_y^t,\ M_z^t$).

The stress and deformation analysis under extreme load combinations is conducted using a nonlinear static formulation. The governing equation of the problem can be expressed as:

$$\left[K\right]\left\{u\right\} = \left\{F_{ASEM}\right\}, \tag{8}$$

where $\left[K\right]$ – stiffness matrix of the structural system; $\left\{u\right\}$ – vector of absolute displacements of the structural system; $\left\{F_{ASEM}\right\}$ – load vector determined based on the results of aeroservoelastic modeling.

Freezing and thawing of the soil change the mechanical properties of the ground, affecting the structural fixation conditions and its dynamic behavior. In the finite element model of the structural system, compliant boundary conditions are employed, with ground reaction modeled using single-node nonlinear springs whose parameters are defined based on the calculations from Stage 2. The problem, incorporating nonlinear spring parameters and geometric nonlinearity, is solved iteratively using a modified Newton–Raphson method.

For stress analysis under complex stress states, equivalent von Mises stresses are considered, generally defined by the following formula:

$$\sigma_{eq} = \sqrt{\frac{\left(\sigma_1 - \sigma_2\right)^2 + \left(\sigma_2 - \sigma_3\right)^2 + \left(\sigma_3 - \sigma_1\right)^2}{2}}. \tag{9}$$

Modal analysis is performed to determine the natural frequencies of vibration, with the governing equation expressed as:

$$\left(\left[K\right]+\omega_i^2\left[M\right]\right)\left\{\varphi\right\}_i=\left\{0\right\},\tag{10}$$

where ω_i – natural frequency; $\left[M\right]$ – mass matrix of the wind turbine; $\left\{\varphi\right\}$ – eigenmode (mode shape) vector.

The supporting structural system above the ground surface is modeled using four-node shell finite elements. The interaction between the structure and the ground is modeled by representing piles with beam elements, which are connected to nonlinear springs simulating the soil reaction. In the model discretization, a mesh size of 0.01 m is used for the shell finite elements, while the pile beam elements are segmented with a step of 0.5 m.

Ice accretion on the blades and snow on the nacelle increase the mass of the wind turbine. To account for this in the modal frequency analysis of the supporting structures, two sets of equivalent mass and inertia parameters for the wind turbine are defined – one for normal conditions and one for conditions with snow and ice, according to the following formulas:

$$m_{RNA}=\sum m_i;\tag{11}$$

$$c_{RNAj}=\frac{\sum m_i c_{ji}}{\sum m_i};\tag{12}$$

$$I_{RNAj}=\sum m_i r_i^2,\tag{13}$$

where m_{RNA} – mass of the RNA; m_i – mass of the i-th component of the RNA, including the mass of snow and ice; c_{RNAj} – coordinate of the wind turbine's center of mass along axis j relative to the top of the tower; c_{ji} – coordinate of the center of mass of the i-th component, including snow and ice mass, along axis j; I_{RNAj} – moment of inertia of the RNA about axis j; r_i – distance to the center of mass of the i-th component, including the mass of snow and ice.

Thus, two sets of mass-inertia characteristics of the RNA are considered, along with three foundation support conditions:

- under projected foundation degradation;
- in a thermally stabilized ground;
- under complete soil freezing (modeled as a rigid support at ground level).

Based on the results of the finite element analysis conducted at Stage 3, the following parameters are determined for the considered load cases:

1. maximum equivalent structural elements stresses and displacements, enabling the assessment of structural strength, identification of stress concentration zones, and evaluation of deviations from the design geometry.
2. natural frequencies and mode shapes of the Arctic wind turbine structure, allowing to assess the resonance risk at rotor and blade-passing frequencies.

3. Results and Discussion

The methodology was tested on an Arctic-designed wind turbine with a rated power 100 kW, a tower height of 30 m, nacelle dimensions of 2 × 1.3 × 1.5 m, and a rotor with a diameter of 24 m with an optimized blade shape developed by SPbPU for operation in Arctic conditions [43].

The supporting structural system of the wind turbine is made of S355 steel and includes a conical tubular steel tower and a three-point supported pile cap for loads transfer to the piles and ground. The top diameter of the tower is 1 m, the base diameter is 2 m, and the wall thickness is 10 mm. The pile cap consists of a tower mounting flange with a diameter of 2 m and a wall thickness of 30 mm, as well as 7-meter-long box-section beams with cross-section dimensions of 1000×320 mm, composed of 40 mm thick horizontal plates and 30 mm thick vertical plates. The pile cap is elevated and designed for construction on permafrost soils according to the principle of keeping frozen state of ground. The cap beams rest on bored-in-place circular steel piles with a cross section of 426×8 mm and a length of 11.5 m.

The scheme of the wind turbine under investigation is shown in Fig. 4, and the operating mode parameters are presented in Table 1.

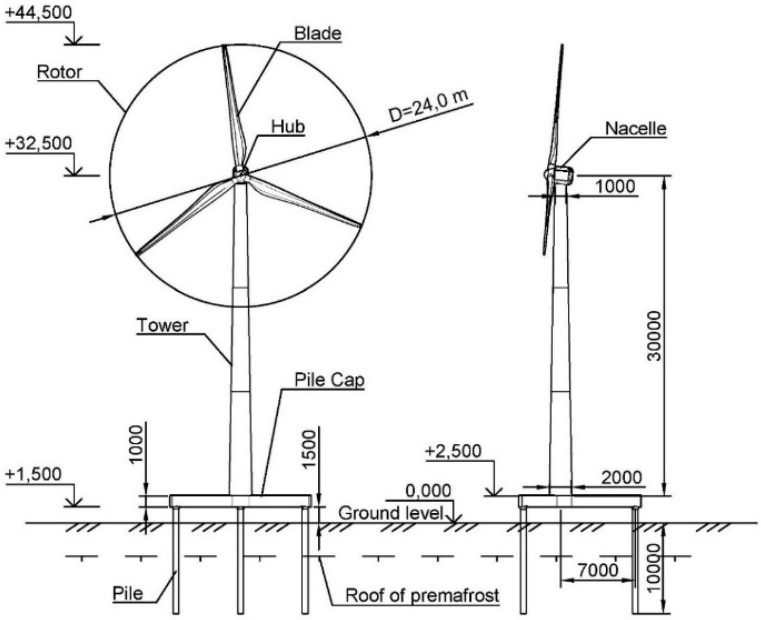

Figure 4. Scheme of the wind turbine under investigation.

Table 1. Wind turbine operation modes parameters.

Rated wind speed V_r	8 m/s
Rated tip speed ratio λ_r	8
Rotor rotational speed	variable from 0 to 75 rpm
Rated power of wind turbine P_r	100 kW
Operating wind speed range $V_{in} – V_{out}$	2–25 m/s
Orientation to the wind (yaw)	active, upwind
Power control	active, by rotating the blades (pitch control)
Control at extreme wind speeds	rotor stop, vane position of blades

The loads at the top of the tower were determined from aeroservoelastic modeling presented in [44] and are presented in Table 2.

Table 2. Loads from RNA on the tower top.

Load combination	F_x^t, kN	F_y^t, kN	F_z^t, kN	M_x^t, kNm	M_y^t, kNm	M_z^t, kNm	F_{xy}^t, kN	M_{xy}^t, kNm
Extreme mode	22.07	–12.25	–80.69	238.43	–10.72	–0.06	25.24	238.67
Normal operating mode	5.68	–0.88	–83.49	12.73	–9.25	3.96	5.75	15.74

To calculate the ground reactive forces, geological conditions obtained from engineering surveys for the construction of a wind-diesel power plant in the Yamalo-Nenets Autonomous Okrug (YaNAO) were used. The foundation consists of non-saline silty-sandy soils, classified into two layers, with their main characteristics summarized in Table 3. Thermal conductivity of the soils in frozen and unfrozen states, as well as the temperature-dependent unfrozen water content, were adopted in accordance with the regulatory guidelines of SP 25.13330.2020.

Table 3. Permafrost soils characteristics.

Layer number	1	2
Type of soil	Silty sand with silt inclusions	Silty sand with silt inclusions
Dry density ρ_d	1280 kg/m^3	1550 kg/m^3
Total moisture content W_{tot}	35 %	21 %
Freezing point temperature T_{bf}	–0 °C	–0 °C
Porosity coefficient e	0.99	0.72
Cohesion in unfrozen state c_t	5 kPa	10 kPa

According to the engineering survey data, the temperature of the permafrost (at the depth of zero annual temperature amplitude fluctuations, 15 m) was recorded as –0.5 °C, and the depth of the seasonally thawed layer was 2.2 m.

Air temperature and snow cover thickness were adopted based on data from the nearest meteorological station. Solar radiation was considered according to regulatory guidelines for the given latitude.

The annual variation of climatic parameters is presented in Fig. 5.

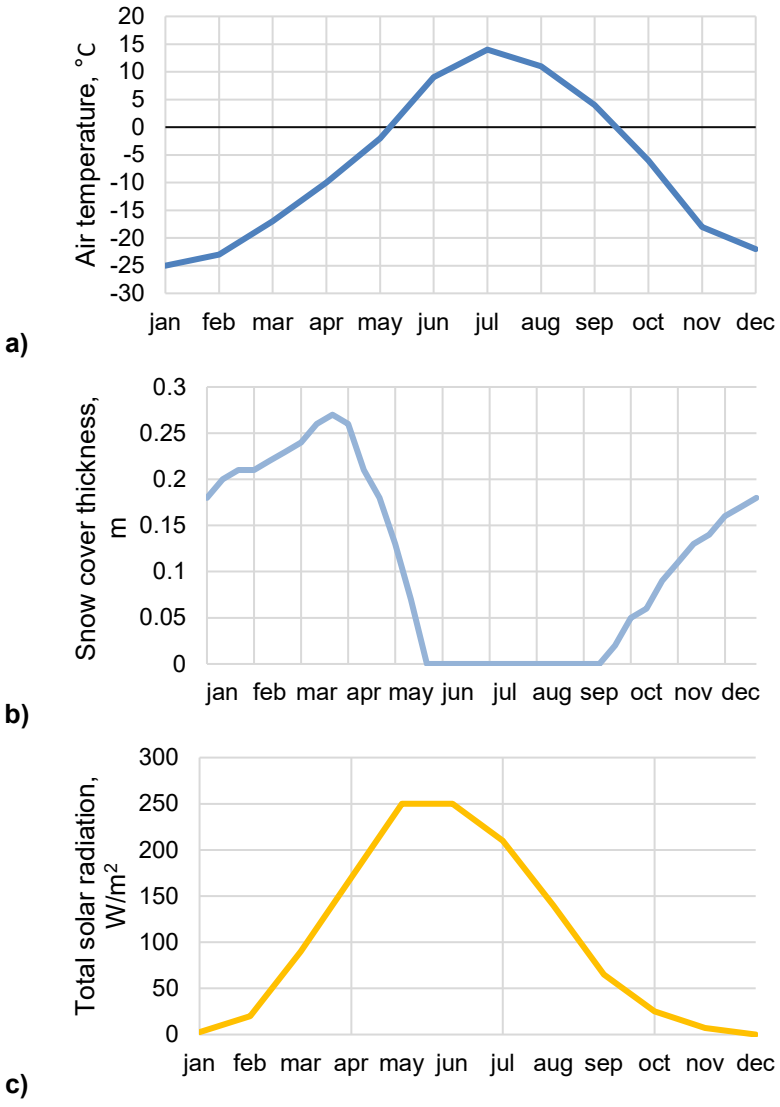

Figure 5. Annual variation of climatic parameters:
a) air temperature, b) snow cover thickness, c) total solar radiation.

As a passive thermal stabilization system, a ventilated space above the foundation surface protected by a shielding screen on the pile cap is considered. The thermal stabilization effect is achieved by shading the foundation from solar radiation and maintaining an exposed (snow-free) soil surface during winter. In the thermophysical model, this is accounted for by an increased heat transfer coefficient in winter and the absence of solar radiation heat flux on the shaded area.

To model the global climate change, an increase in the average air temperature of 0.71 °C per 10 years and a 15 % increase in snow cover depth over 30 years were adopted, based on meteorological data [3].

The results of the thermophysical modeling at Stage 1 yielded the temperature distribution within the ground under various conditions.

Fig. 6 shows the temperature distributions along the pile after 20 years of wind turbine operation for various design scenarios.

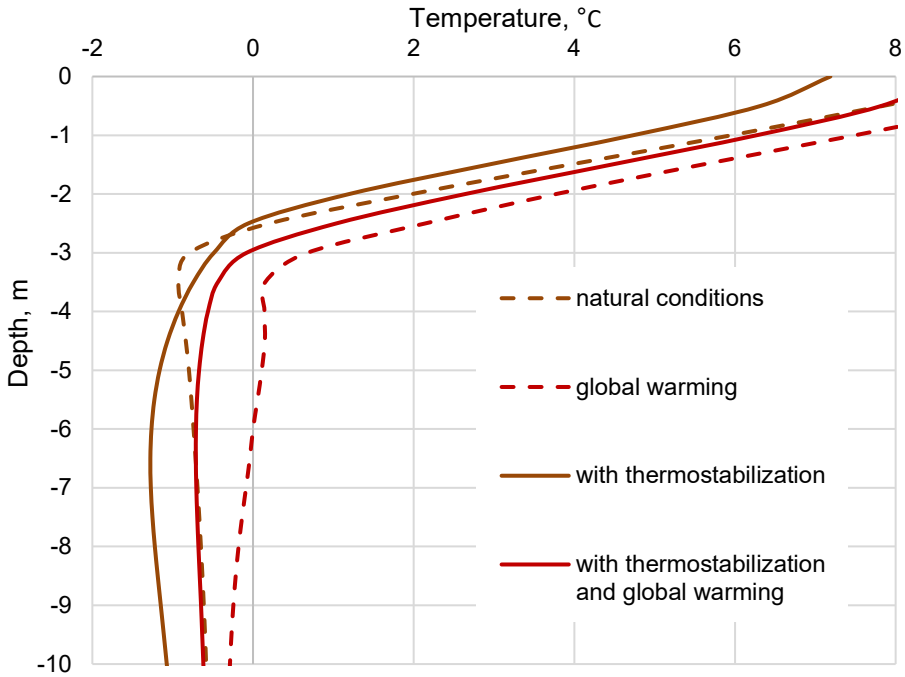

Figure 6. Temperature distributions along the pile after 20 years of wind turbine operation.

The modeling results show that the depth of seasonal thaw under natural conditions was 2.5 m, which closely corresponds to the engineering survey data. The presence of a pile cap with a shielding screen provided cooling of the foundation in August of the final year by 0.3–2.4 °C compared to the first year. This finding correlates with field studies of structures with ventilated spaces on permafrost [45], where a temperature reduction of 0.6–2.5 °C in the permafrost was observed for structures employing a similar thermal stabilization method.

When calculated with climatic trends considered, the thickness of active layer increased to 6 m by the end of the design service life of the wind turbine. The protective screen helped to offset the negative impact of warming and slowed permafrost degradation, ensuring stabilization of the annual average temperature with depth. At the same time, the thickness of the seasonally thawed layer at the pile location, considering the protective effect of the screen, was 3 m in the final year of operation.

The temperature distributions shown in Fig. 6 are used as input data at Step 2 for calculating the parameters of nonlinear springs modeling the reaction of the permafrost ground under loads from the structure. The primary calculation scenario assumes the temperature distribution considering both global warming and thermostabilization effects. Additional calculation scenarios include the temperature distribution with global warming but without thermostabilization, as well as rigid fixation of the piles at the ground surface to provide an upper bound estimate of the natural vibration frequencies in the case of increased foundation stiffness due to full freezing.

Fig. 7a presents a comparison of the calculated dependence of the soil cohesion on temperature with experimental data from [36]. Fig. 7b shows the temperature distribution along the pile length for the considered calculation scenarios.

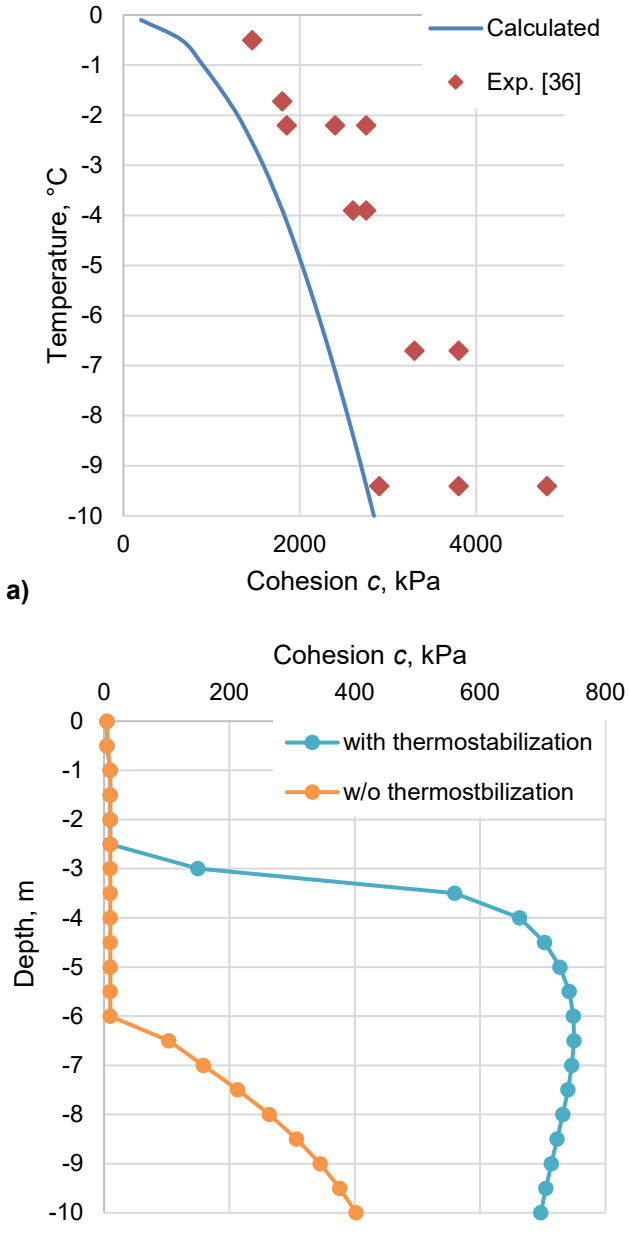

Figure 7. Variation of soil cohesion: a) comparison of the calculated dependence of soil cohesion on temperature with experimental data, b) temperature distribution along the pile length.

The analysis of the dependence of the frozen soil cohesion on temperature showed that the calculated estimates of cohesion do not exceed the values obtained experimentally. As the foundation temperature increases, the strength decreases exponentially, especially in the temperature range from –2 °C to 0 °C, where intense melting of ice in the soil pores occurs. Within this interval, even a slight increase in temperature leads to a sharp reduction in strength.

Such behavior is reflected in the stiffness of the spring elements modeling the ground response. When the soil transitions from a frozen state at a temperature of –0.5 °C to an unfrozen state, the reaction forces of the soil at the same displacement decrease by a factor of 70.

Fig. 8 shows the “p-y” spring relationships describing the lateral resistance of the foundation at depths of 3, 6, and 9 m. With long-term degradation of the permafrost (scenario of +0.7 °C increase over 10 years), there is a systematic decrease in the stiffness of the ground, which should be taken into account when assessing the operational reliability of the wind turbine.

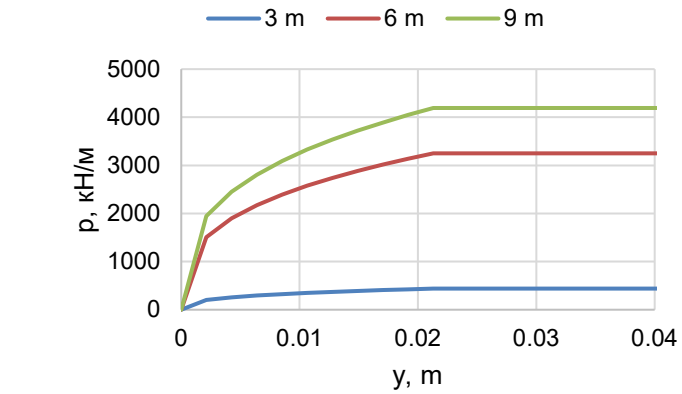

a)

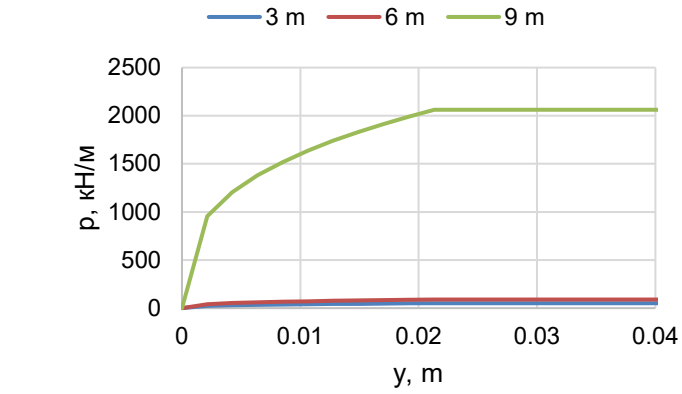

b)

Figure 8. Dependencies of foundation reaction *p* on horizontal displacement *y* along the pile: a) with thermostabilization, b) without thermostabilization.

In the long term, cyclic wind and operational loads may induce cumulative effects such as progressive soil stiffening degradation and permanent settlements, which warrants further investigation as a direction for future research

At Stage 3, a finite element analysis of the wind turbine supporting structural system was performed for the extreme load combination (Table 3) based on three calculation schemes:

1. rigid fixation of the supporting structures at ground level (complete freezing of the ground);
2. nonlinear fixation of the supporting structures considering warming and thermostabilization;
3. nonlinear fixation of the supporting structures under warming without thermostabilization.

The results of the FEM analysis are the stresses and displacements of the supporting structures.

Fig. 9 shows the calculated absolute horizontal displacements of the tower, as well as the horizontal displacements relative to the tower base.

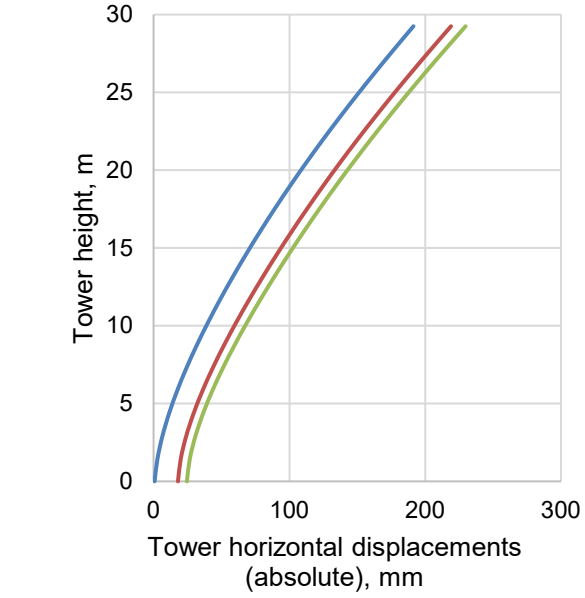

a)

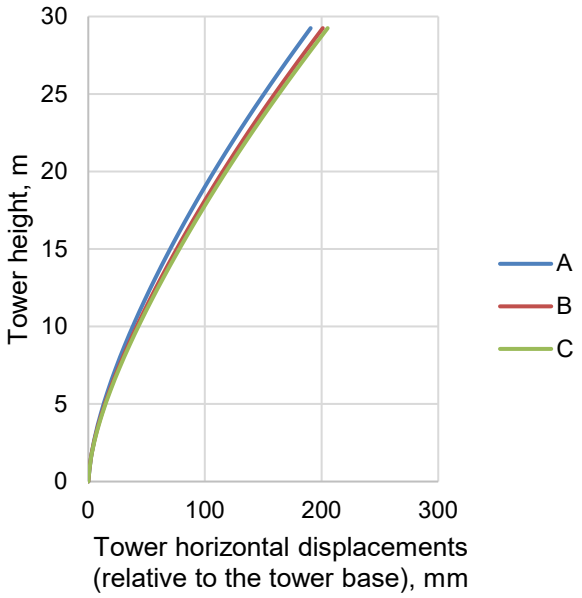

b)

Figure 9. Horizontal displacement of the tower in the calculation schemes A, B, and C: a) absolute, b) relative to the tower base.

Fig. 10a shows that thawing of the ground leads to increased tower displacements. The main difference is associated with the displacement of the tower base due to reduced stiffness of the foundation: the displacements at the tower top increased by 14–20 % compared to rigid fixing, while the displacements of tower base increased by 24–33 times. The increase in horizontal tower displacements without thermostabilization ranged from 5 % to 37 % compared to the thermostabilized ground. The tower displacements relative to the tower base increased by 6–8 % compared to rigid fixing.

The study showed that permafrost degradation over the service life will not lead to a significant increase in internal forces and stresses within the tower material. However, a noticeable increase in absolute displacements under extreme loading indicates the potential for excessive amplification of the wind turbine vibration amplitudes.

To analyze the deformation of the pile cap, displacements at characteristic points were considered. Fig. 10 shows the layout of control points: point 0 lies along the tower axis and corresponds to the tower mounting flange located at the center of the pile cap, while points 1, 2, and 3 are located at the ends of the pile cap beams. The displacements at these points obtained from the analyses of schemes A, B, and C are presented in Table 4.

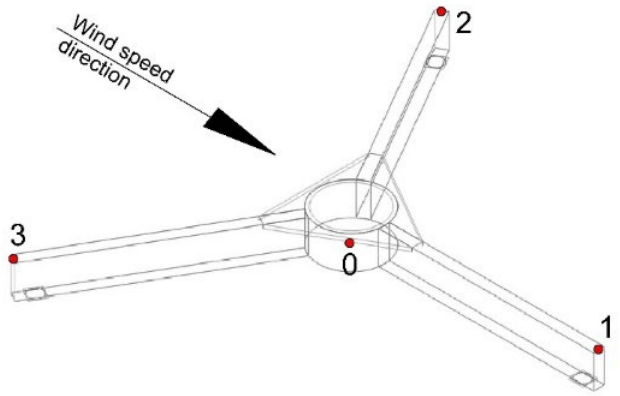

Figure 10. Scheme of control points for monitoring pile cap displacements.

Table 4. Pile cap structural elements displacements.

Structural element	Control point (Fig. 10)	Displacements in calculation scheme, mm		
		A	B	C
Tower mounting flange	0	0.17	17.5	24
Pile cap beam 1	1	0.79	17.06	23.6
Pile cap beam 2	2	1.74	14.44	20.05
Pile cap beam 3	3	2.5	12.7	17.89

From Table 4, it is evident that thawing of the ground leads to an increase in pile cap deformations. The displacements of the tower mounting flange increase by a factor of 10–14 when considering the compliance of the ground compared to the rigid fixation case. Overall, the pile cap displacements under the scenario without thermal stabilization (scheme C) are 40 % higher compared to the scenario with a thermally stabilized foundation (scheme B).

To assess the impact of ground thawing on the stresses in the supporting structures, the maximum equivalent stresses in structural elements were determined (Table 5).

Table 5. Maximum equivalent stress in the wind turbine supporting structures.

Structural element	Maximum stress $\sigma_{eq,\,max}$ in calculation scheme, MPa		
	A	B	C
Tower	167	167	167
Pile cap beam	144	174	180
Tower mounting flange	253	285	293
Piles	242	291	283

Based on Table 5, thawing of the foundation does not lead to a significant increase in stresses in the tower but it primarily affects the pile cap beams, the tower mounting flange and the piles. The maximum stresses at the supporting structure are 10–25 % higher when ground compliance is considered compared to the rigid fixation case. The greatest increase in stresses is observed in the pile cap beams. In all considered scenarios, the maximum stresses are localized at the tower mounting flange and at the points where the pile cap beams connected to the piles.

To analyze the dynamic response of the wind turbine, the inertial characteristics of the RNA were calculated both with and without the inclusion of additional masses of ice and snow (Table 6). These values were used to determine the natural frequencies of structural vibrations and assess the risk of resonance. The computed natural frequencies include bending modes along and across the wind direction (longitudinal and lateral), as well as the torsional mode, and are presented in Table 7.

Table 6. RNA inertial characteristics.

RNA inertial characteristic	1. Normal conditions	2. With ice and snow
RNA mass, kg	8500	9313
Coordinates *x, y, z* of the RNA center of mass relative to tower top, m	(–0.327; 0.000; 0.750)	(–0.343; 0.000; 0.840)
Moments of inertia of the RNA inertia about axes *x, y, z*, kg·m^2	(37858; 20867; 23600)	(38574; 21092; 23792)

Table 7. Wind turbine natural frequencies under various environmental conditions.

No.	Mode of vibration	Natural frequency, Hz					
		Normal conditions			With ice and snow		
		A1	B1	C1	A2	B2	C2
1	Bending lateral	0.93	0.89	0.88	0.88	0.85	0.83
2	Bending longitudinal	0.93	0.89	0.88	0.89	0.85	0.84
3	Torsional	7.39	6.91	6.77	7.36	6.88	6.74
4	Bending lateral	11.09	10.64	10.52	11.04	10.58	10.46
5	Bending longitudinal	12.53	11.59	11.37	12.02	11.1	10.88

For the considered wind turbine, the presence of blade icing and snow on the nacelle reduces the natural frequencies of the structure by up to 5 %. Seasonal variation of the natural vibration frequencies due to thawing of the seasonal active layer reaches 4–7 % with thermostabilization and 6–10 % without it. This result is in good agreement with the findings of field and computational studies of an Arctic wind turbine with a similar configuration conducted in Alaska [4, 5], where a seasonal variation in the natural frequency of the tower-foundation system of up to 9 % was observed. Despite some differences in the parameters of the supporting structures of the considered wind turbine compared to those in [4, 5], this agreement indirectly validates the adequacy of the integrated methodology in assessing the variability of the structure's natural frequencies under permafrost degradation.

Fig. 11 shows the ranges of resonance frequencies and the natural vibration frequencies in accordance with Table 7.

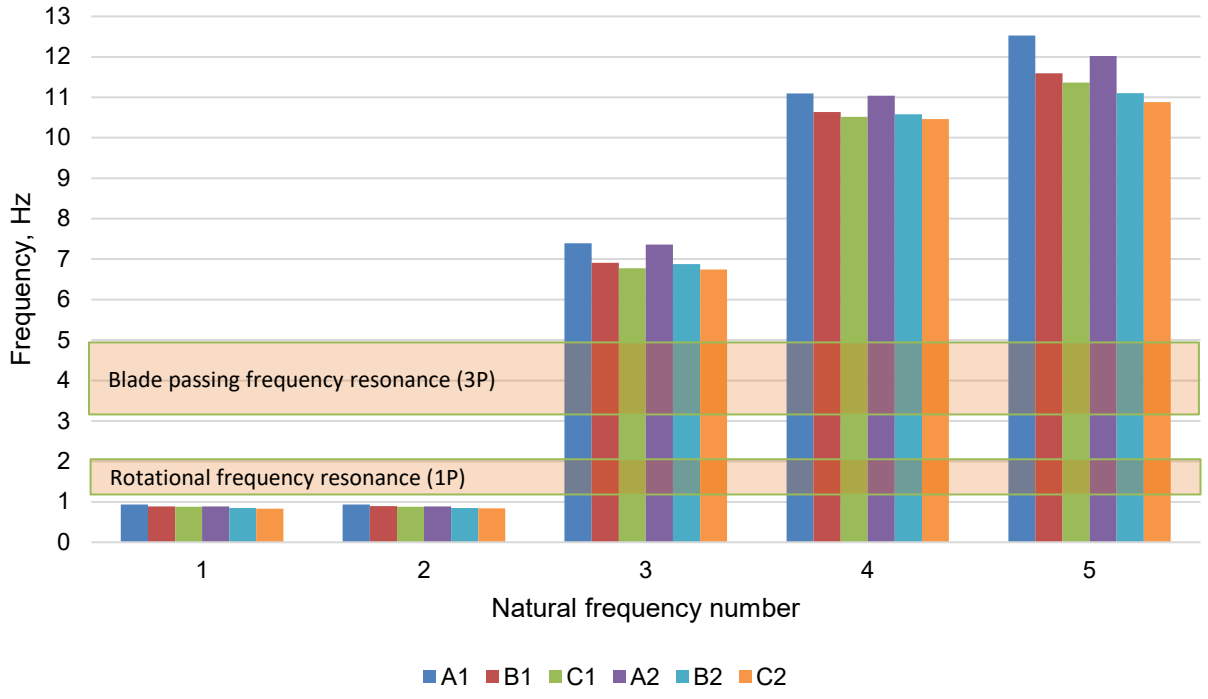

Figure 11. Ranges of resonance frequencies and the natural vibration frequencies.

It can be seen from Fig. 12 that the natural vibration frequencies of the considered wind turbine do not fall within the ranges of dangerous resonance frequencies. The closest to the resonance frequencies are the natural frequencies in case A1 – when the ground is fully frozen and there is no snow load or icing.

It should be noted that snow loads and icing have the greatest effect on vibration modes 1, 2, and 5 (4–5 %), while having almost no effect on modes 3 and 4 (0.5 %). Ground thawing has the greatest impact on torsional vibrations (7 %). The highest amplitudes of torsional vibrations in cases B and C (with ground thawing) are observed at the pile cap beams ends, whereas in case A (rigid support), the highest amplitudes are localized at the top of the tower.

Based on the calculation results under various conditions, it has been established that accounting for additional ice and snow masses, as well as the permafrost degradation, enables a more accurate assessment of the stress-strain state and dynamic response of the wind turbine. These factors are particularly important for evaluating the natural frequencies of the structure and the stresses and deformations in the foundation structural elements, while having a secondary influence on the stresses in the tower. A more precise assessment of the SSS allows for a more accurate evaluation of the structural safety margins and the development of efficient structural solutions.

Accounting for the influence of Arctic climatic factors is crucial in aeroservoelastic modeling and in the development of resonance avoiding strategies. For example, when avoiding resonance by ensuring that the natural frequency of the wind turbine is lower than the rotor's rotational frequency ("soft-soft" strategy), and by tuning the control system to bypass resonant rotor speeds, a wider range of natural frequencies should be considered.

4. Conclusion

1. An integrated methodology has been developed for Arctic wind turbine behavior analyzing under specific environmental condition, based on finite-element modeling of wind turbine supporting structures SSS and dynamic response considering wind and operational loads, nonlinear soil-structure interaction, thermal regime, and temperature-dependent soil properties.
2. Based on the case study of a 100 kW wind turbine:
    - it was established that without thermostabilization, seasonal thawing depth increases from 2.5 m to 6 m under climate trends, leading to a sharp reduction in soil strength within the thawed zone and a 70-fold decrease in ground reaction forces when transitioning from frozen to thawed conditions;
    - it was shown that permafrost degradation increases horizontal displacements of the tower by 14–20 %, and displacements of the tower mounting flange by 24–33 times; the degradation of the ground reduces the natural frequencies of wind turbine by up to 10 %;
    - it was found that blade icing and snow loads increase the mass and inertia of the wind turbine, reducing the supporting structures natural frequencies by up to 5 %;
    - it was demonstrated that the expected changes in natural frequencies during the wind turbine service life do not lead to resonance risks. The frequencies closest to potential resonance correspond to conditions of fully frozen foundation and absence of snow and ice loads;
    - it was revealed that the greatest increase in stresses in the structures due to ground thawing occurs in the foundation structures, particularly in the pile cap beams (up to 25 % compared to rigid foundation), while stresses in the tower remain practically unchanged.
3. It is demonstrated that accounting for additional masses and temperature-dependent ground stiffness is essential in aeroservoelastic modeling of wind turbines and in developing resonance avoidance strategies. The range of potential resonances should be expanded to account for variability in natural frequencies.
4. The derived relationships and results enable a more accurate assessment of the SSS and dynamic response of Arctic wind turbines, to develop rational structural solutions that ensure operational reliability in degrading permafrost conditions.

References

1. Minin, V.A., Tselishcheva, M.A. Wind resources of the Western sector of the Arctic zone of Russian Federation and possible areas of their use. Arctic: ecology and economy. 2023. 13(1). Pp. 72–84. DOI: 10.25283/2223-4594-2023-1-72-84
2. Akperov, M., Eliseev, A.V., Rinke, A., Mokhov, I.I., Semenov, V.A., Dembitskaya, M., Matthes, H., Adakudlu, M., Boberg, F., Christensen, J.H., Dethloff, K., Fettweis, X., Gutjahr, O., Heinemann, G., Koenigk, T., Sein, D., Laprise, R., Mottram, R., Nikiéma, O., Sobolowski, S., Winger, K., Zhang, W. Future projections of wind energy potentials in the arctic for the 21st century under the RCP8.5 scenario from regional climate models (Arctic-CORDEX). Anthropocene. 2023. 44. Article no. 100402. DOI: 10.1016/j.ancene.2023.100402
3. Kattsov, V.M., Akentyeva Ye.M., Anisimov, O.A., Bardin, M.Yu., etc. Tretiy otsenochnyy doklad ob izmeneniyakh klimata i ikh posledstviyakh na territorii Rossiyskoy Federatsii. Obshcheye rezyume [Third assessment report on climate change and its consequences in the Russian Federation. General Summary]. SPb.: Naukoyemkiye tekhnologii. 124 p.

4. Zheng, M., Yang, Z.(J.), Yang, S., Still, B. Modeling and mitigation of excessive dynamic responses of wind turbines founded in warm permafrost. Engineering Structures. 2017. 148. Pp. 36–46. DOI: 10.1016/j.engstruct.2017.06.037
5. Yang, Z.(J.), Still, B.A., Wait, I., Chen, G. Dynamic Responses of a Wind Turbine Founded in Warm Permafrost. Journal of Cold Regions Engineering. 2018. 32(4). Article no. 04018011. DOI: 10.1061/(ASCE)CR.1943-5495.0000169
6. Liew, M., Ji, X., Xiao, M., Farquharson, L., Nicolsky, D., Romanovsky, V., Bray, M., Zhang, X., McComb, C. Synthesis of physical processes of permafrost degradation and geophysical and geomechanical properties of permafrost. Cold Regions Science and Technology. 2022. 198. Article no. 103522. DOI: 10.1016/J.COLDREGIONS.2022.103522
7. Gantasala, S., Luneno, J.C., Aidanpää, J.O. Influence of Icing on the Modal Behavior of Wind Turbine Blades. Energies. 2016. 9(11). Article no. 862 DOI: 10.3390/en9110862
8. Li, F., Cui, H., Su, H., Iderchuluun, Ma, Z., Zhu, Y.X., Zhang, Y. Icing condition prediction of wind turbine blade by using artificial neural network based on modal frequency. Cold Regions Science and Technology. 2022. 194. Article no. 103467. DOI: 10.1016/J.COLDREGIONS.2021.103467
9. Sokolov, V.A., Strakhov, D.A., Sinyakov, L.N. Design of tower type structures to dynamic effects taking into account flexibility of the pile foundation and the base. Magazine of Civil Engineering. 2013. 4(39). Pp. 46–50.
10. Bondarev, D.E. Tuned mass damper for reduction seismic and wind loads. Magazine of Civil Engineering. 2024. 17(5). Article no. 12904. DOI: 10.34910/MCE.129.4
11. Wang, T., Zhong, W., Qian, Y., Zhu, C. Unsteady Blade Element Momentum Method. Wind Turbine Aerodynamic Performance Calculation. Springer. Singapore, 2023. 99–112. DOI: 10.1007/978-981-99-3509-3_6
12. Anderson, C.G. Wind Turbines: Theory and Practice. 2nd ed. Cambridge University Press. Cambridge, 2025, DOI: 10.1017/9781009499040
13. Marten, D. QBlade: A Modern Tool for the Aeroelastic Simulation of Wind Turbines. PhD Thesis. Berlin, 2020. 187 p. DOI: 10.14279/depositonce-10646
14. Jonkman, B., Platt, A., Mudafort, R., Branlard, E., Sprague, M., Ross, H. et al. OpenFAST/openfast: v3.5.3. Zenodo. 2024. DOI: 10.5281/zenodo.10962897
15. Brown, K., Bortolotti, P., Branlard, E., Chetan, M., Dana, S., de Velder, N., Doubrawa, P., Hamilton, N., Ivanov, H., Jonkman, J., Kelley, C., Zalkind, D. One-to-one aeroservoelastic validation of operational loads and performance of a 2.8 MW wind turbine model in OpenFAST. Wind Energy Science. 9 (8). Pp. 1791–1810, DOI: 10.5194/wes-9-1791-2024
16. Papi, F., Troise, G., Behrens de Luna, R., Saverin, J., Perez-Becker, S., Marten, D., Ducasse, M.-L., Bianchini, A. Quantifying the impact of modeling fidelity on different substructure concepts – Part 2: Code-to-code comparison in realistic environmental conditions, Wind Energy Science. 9 (4). Pp. 981–1004. DOI: 10.5194/wes-9-981-2024
17. Elistratov, V.V. Engineering Feasibility and Designing of Energy Systems Based on Renewable Energy Sources for Difficult Natural and Climatic Conditions. Elektrichestvo [Electricity]. 2023. 10. Pp. 4–21. DOI: 10.24160/0013-5380-2023-10-4-21
18. Elistratov, V.V., Panfilov, A.A., Petrov, S.G. The use of digital technologies in substantiating the energy and design parameters of the Arctic wind power plant. Plumbing, Heating, Air Conditioning. 2024. 6(270). Pp. 56–59.
19. Bolshev, A.S., Frolov, S.A., Kharseyev, A.Ye., Rozov, I.O. Raschet prochnosti osnovaniya arkticheskoy vetroenergeticheskoy ustanovki pri deystvii ekstremalnykh vneshnikh nagruzok [Arctic wind turbine foundation strength calculation under extreme external loads]. Polyarnaya mekhanika: Sbornik dokladov VI Vserossiyskoy nauchno-prakticheskoy konferentsii s mezhdunarodnym uchastiyem [Polar mechanics. Proceedings of the VI All-Russian Scientific and Practical Conference with International Participation]. Nizhniy Novgorod: NGTU im. R.Ye. Alekseyeva, 2023. Pp. 87–97. DOI: 10.46960/polmech_2023_87
20. Wu, X., Zhang, X., Bhattarai, H.B. et al. Structural Behavior Analysis of UHPC Hybrid Tower for 3-MW Super Tall Wind Turbine Under Rated Wind Load. International Journal of Concrete Structures and Materials. 2022. 16. Article no. 52. DOI: 10.1186/s40069-022-00542-8
21. Al-Sanad, S., Parol, J., Wang, L., Kolios, A. Design optimisation of wind turbine towers with reliability-based calibration of partial safety factors. Energy Reports. 2023. 9. Pp. 2548–2556. DOI: 10.1016/j.egyr.2023.01.090
22. Partovi-Mehr, N., Branlard, E., Song, M., Moaveni, B., Hines, E.M., Robertson, A. Sensitivity Analysis of Modal Parameters of a Jacket Offshore Wind Turbine to Operational Conditions. Journal of Marine Science and Engineering. 2023. 11(8). Article no. 1524. DOI: 10.3390/jmse11081524
23. Kim, D.J., You, Y.S., Sun, M.Y. Variable Natural Frequency Damper for Minimizing Response of Offshore Wind Turbine: Effect on Dynamic Response According to Inner Water Level. Journal of Marine Science and Engineering. 2024. 12(3). Article no. 491. DOI: 10.3390/jmse12030491
24. Bergua, R., Robertson, A., Jonkman, J., Platt, A. Specification Document for OC6 Phase II: Verification of an Advanced Soil-Structure Interaction Model for Offshore Wind Turbines. Report number: NREL/TP-5000-79938. National Renewable Energy Laboratory. Golden, CO, 2021. DOI: 10.2172/1811648
25. Jindal, S., Rahmanli, U., Aleem, M., Cui, L., Bhattacharya, S. Geotechnical challenges in monopile foundations and performance assessment of current design methodologies. Ocean Engineering. 2024. 310(1). Article no. 118469. DOI: 10.1016/J.OCEANENG.2024.118469
26. Xi, R., Xu, C., Du, X., El Naggar, M.H., Wang, P., Liu, L., Zhai, E. Framework for dynamic response analysis of monopile supported offshore wind turbine excited by combined wind-wave-earthquake loading. Ocean Engineering. 2022. 247. Article no. 110743. DOI: 10.1016/j.oceaneng.2022.110743
27. Wu, J., Pu, L., Zhai, C. A Review of Static and Dynamic *p-y* Curve Models for Pile Foundations. Buildings. 2024. 14(6). Article no. 1507. DOI: 10.3390/buildings14061507
28. Mawer, B.W., Kalumba, D. Stiffness considerations of local wind turbine gravity foundations. Proceedings of the 1st Southern African Geotechnical Conference. CRC Press. London, 2016. Pp. 31–36. DOI: 10.1201/b21335-8
29. Harris, S.A., Brouchkov, A.V., Guodong, C. Geokriologiya: kharakteristiki i ispolzovaniye vechnoy merzloty [Geocryology: Characterictics and Use of Permafrost]. Vol 1. Moscow, Berlin: Direkt-Media, 2020. 437 p.
30. Zhaysambaev, E.A., Maltseva, T.V., Kraev, A.N. Calculation of the temperature condition of a thermostabilizable base with a single pile. Construction and Geotechnics. 2023. 14(4). Pp. 5–18. DOI: 10.15593/2224-9826/2023.4.01
31. Nikiforova, N.S., Konnov, A.V. Forecast of the Soil Deformations and Decrease of the Bearing Capacity of Pile Foundations Operating in the Cryolithozone. International Journal for Computational Civil and Structural Engineering. 2022. 18(1). Pp. 141–150. DOI: 10.22337/2587-9618-2022-18-1-141-150

32. Voznesenskiy, Ye.A. Dinamicheskaya neustoychivost gruntov [Dynamic instability of soils]. Moscow: URSS, LELAND, 2019. 263 p.
33. Zhu, Z., Kang, G., Ma, Y., Xie, Q., Zhang, D., Ning, J. Temperature damage and constitutive model of frozen soil under dynamic loading. Mechanics of Materials. 2016. 102. Pp. 108–116. DOI: 10.1016/j.mechmat.2016.08.009
34. Mirnyy, A.Yu., Idrisov, I.H., Mosina, A.S. Dinamicheskiye svoystva merzlyh gruntov. Chast' 1. Ispytaniya v rezonansnoy kolonke [Dynamic properties of frozen soils. Part 1. Resonant column tests]. GeoInfo. 2024. 6(1/2). Pp. 28–35 DOI: 10.58339/2949-0677-2024-6-1/2-28-35
35. Mirnyy, A.Yu., Idrisov, I.H., Mosina, A.S. Dinamicheskiye svoystva merzlyh gruntov. Chast' 2. Ispytaniya metodom trehosnogo szhatiya [Dynamic properties of frozen soils. Part 2. Triaxial compression tests]. GeoInfo. 2024. 6(3). Pp. 24–32 DOI: 10.58339/2949-0677-2024-6-3-24-32
36. Crowther, G.S. Lateral Pile Analysis Frozen Soil Strength Criteria. Journal of Cold Regions Engineering. 2014. 29(2). Article no. 04014011. DOI: 10.1061/(asce)cr.1943-5495.0000078
37. Li, Q., Yang, Z.(J.). P–Y Approach for Laterally Loaded Piles in Frozen Silt. Journal of Geotechnical and Geoenvironmental Engineering. 2017. 143(5). Article no. 04017001. DOI: 10.1061/(asce)gt.1943-5606.0001556
38. Bekele, Y., Sinitsyn, A. O. Impact of Climate Change on Infrastructure in Longyearbyen. Case study of pile foundations on sloping terrains. SINTEF Academic Press. Oslo, 2020. 50 p. DOI: 10.13140/RG.2.2.33278.33601
39. MIDAS GTS NX. Integrated Solution for Ground Analysis. [Online]. URL: https://www.midasuser.com/en/product/gts-nx/ (reference date: 16.12.2025).
40. ANSI/API. Recommended practice 2 GEO/ISO 19901-4. Geotechnical and Foundation Design Considerations. 1st ed. API. Washington, D.C., 2011. 26 p.
41. Tsegaye, A.B., Nordal, S., Simple Models for Frozen Soil. Modelling the Strength of Saturated Frozen Soil. Report number: NTNU report. Norwegian University of Science and Technology, 2015. 42 p. DOI: 10.13140/RG.2.2.25386.06088
42. MIDAS FEA NX. Elevating Design Excellence with Advanced Simulation. [Online]. URL: https://www.midasuser.com/en/product/fea-nx/ (reference date: 16.12.2025).
43. Voinov, I.B., Elistratov, V.V., Keresten, I.A. et al. Profiling a Wind Wheel Blade Using Parametric Optimization and Computational Aerodynamics Methods. Thermal Engineering. 2024. 71. Pp. 513–522. DOI: 10.1134/S0040601524060053
44. Rigel, I.V., Elistratov, V.V. Support structure strength assessment based on aeroservoelastic modeling of an Arctic wind turbine, Vestnik MGSU [Proceedings of the Moscow State University of Civil Engineering]. 2025. 20(7). 1030–1050. DOI: 10.22227/1997-0935.2025.7.1030-1050
45. Hou, X., Chen, J., Sheng, Y., Rui, P.F., Liu, Y.Q., Zhang, S.H., Dong, T.C., Gao, J.W. Field observations of the thermal stability of permafrost under buildings with an underfloor open ventilation space and pile foundations in warm permafrost at high altitudes. Advances in Climate Change Research. 2023. 14(2). Pp. 267–275. DOI: 10.1016/j.accre.2023.03.004

Information about the authors:

Ivan Rigel,
ORCID: https://orcid.org/0009-0003-0940-372X
E-mail: ivan.rigel@yandex.ru

Viktor Elistratov, *Doctor of Technical Sciences*
ORCID: https://orcid.org/0000-0001-7051-6027
E-mail: elistratov@spbstu.ru

Received 05.06.2025. Approved after reviewing 24.09.2025. Accepted 24.09.2025.

Magazine of Civil Engineering

ISSN 2712-8172

journal homepage: http://engstroy.spbstu.ru/

Research article

UDC 624

DOI: 10.34910/MCE.138.2

Optimizing concrete mix design with a high percentage of microsilica: Enhancing strength, Sustainability

K. Fallah-Mehrjardi[1], ***A. Shariat***[2], ***M.R. Eftekhar***[3] ✉

[1] *Department of Civil Engineering, Sharif University of Technology, Tehran, Iran*

[2] *Department of Civil Engineering, Western University, London, Ontario, Canada*

[3] *Isfahan University of Technology, Isfahan University of Technology, Isfahan, Iran*

✉ *eft@iut.ac.ir*

Keywords: compressive strength, microsilica, light artificial aggregate, modulus of elasticity, water absorption

Abstract. Microsilica is a highly reactive pozzolanic material widely known for improving the strength and durability of concrete. In this study, we explored how replacing 10%, 20%, and 30% of cement with microsilica affects the performance of lightweight concrete over 7, 14, and 28 days. The concrete mixes were prepared using a blend of natural and artificial lightweight aggregates with cement content ranging from 350 to 550 kg/m^3. To ensure good workability, a 2% modified lignosulfonate-based superplasticizer was used, and water-to-cement ratios varied between 0.30 and 0.45. Along with compressive strength, we also measured the modulus of elasticity, specific weight, and water absorption under both dry and wet conditions. The results clearly showed that higher levels of microsilica led to notable gains in strength and elasticity, while also reducing the weight and water absorption of the concrete. The most effective mix combined 30% microsilica with a cement content above 500 kg/m^3, delivering excellent mechanical performance and durability. These findings highlight the potential of microsilica not only to enhance structural quality but also to reduce environmental impact by lowering cement usage. This study supports the thoughtful use of microsilica as a sustainable and performance-boosting material in modern concrete design.

Citation: Fallah-Mehrjardi, K., Shariat, A., Eftekhar, M.R. Optimizing concrete mix design with a high percentage of microsilica: Enhancing strength, Sustainability. Magazine of Civil Engineering. 2025. 18(6). Article no. 13802. DOI: 10.34910/MCE.138.2

1. Introduction

Reducing the dead load of structures using concrete with lower specific weight and higher compressive strength is a key focus for engineers, especially in seismic zones where earthquake forces are proportional to structural mass [1]. Lightweight concrete not only enhances seismic performance but also reduces construction costs, energy use, and noise pollution [2]. To improve its mechanical properties, various mineral additives have been explored, among which microsilica stands out as one of the most effective. Microsilica is a highly reactive pozzolanic material with particles 50–100 times smaller than cement. It fills voids between cement grains, enhances adhesion, and reacts with calcium hydroxide from cement hydration to form a dense, gel-like compound. This reaction significantly increases concrete strength and decreases its weight, making microsilica a valuable additive in the production of high-performance lightweight concrete [3].

Extensive research has been conducted on the effect of microsilica on the properties of concrete with different percentages of cement, and the results have been collected [4]. Studies show that replacing

5% and 10% of cement with microsilica increases 28 day compressive strength by 9.6% and 24.8% respectively [5]. Additionally, for producing concrete with high strength, replacing 10% of the weight of cement with microsilica is a suitable option [6]. Previous research has shown that the use of 20% microsilica and 30% fly ash results in an increase in the flexural and compressive strength of concrete [7]. Other studies have also demonstrated that the use of microsilica can reduce sudden drying shrinkage and the likelihood of concrete cracking [8]. Incorporating microsilica in concrete can improve resistance to chemical and physical attacks [9].

Although most studies limit microsilica replacement to ≤ 20%, preliminary trials in this study suggest that a 30% replacement level may still enhance strength, provided a higher cement grade and adequate dispersion are employed. Empirical data on such high microsilica mixtures remain virtually absent from the literature.

This study aims to develop an optimized concrete mix design that delivers exceptionally high compressive strength while lowering specific weight. The mix designs combine natural and artificial lightweight aggregates with microsilica used as a partial replacement for cement.

While most previous research limits microsilica replacement to 10–20%, this work investigates the effects of a higher replacement level (30%) to assess its potential for further enhancing mechanical and durability properties. This experiment evaluates a range of cement content, water-to-cement ratios, and aggregate types to identify the optimal combination that leads to increased strength, reduced density and water absorption, and improved overall structural performance. The outcomes are intended to offer actionable insights for structural engineers and material scientists seeking to design sustainable, lightweight, and high-performance concrete systems.

2. Method

2.1. Cement

The cement used in this research is ordinary Portland cement type 2. The mechanical, physical, and chemical characteristics of the used cement are listed in Tables 1 and 2 respectively {Horkoss, 2004 #1}.

Table 1. Mechanical and physical characteristics of the used cement

3-day compressive strength	> 17 MPa	10 MPa	Min
7-day compressive strength	> 27 MPa	17 MPa	Min
28-day compressive strength	> 37 MPa	31 MPa	Min
Initial capture time	95±5	45	Min
Final capture time	150±10	360	Max
Surface smoothness	3000±50 cm^2/gr	2800	Min

Table 2. Percentage of cement components

SiO_2	Al_2O_3	Fe_2O_3	CaO	MgO	SO_3	K_2O	Na_2O	Cl-	L.O.I	L.S.F	C3A
22.00± 0.4	5±0.3	3.82± 0.2	64.00± 0.5	1.9± 0.2	1.5± 0.2	0.49± 0.2	0.25± 0.15	0.019± 0.001	1.0± 0.2	91.00± 1.0	6.5± 1

2.2. Microsilica

Microsilica is a highly soft white powder consisting of crystals with a diameter of 0.1 to 0.2 μm. Following the hydration of cement, the released calcium hydroxide accounts for about 20% of the mortar volume (Relation 1). Also, this component can be dissolved in water, move out of concrete, and weaken the mechanical properties and durability of concrete. Alkaline reactions of aggregates are also intensified by the presence of calcium hydroxide in cement paste. In this way, calcium hydroxide is a weakening part of the concrete mixture. Moreover, due to its instability, it is considered a weakness for concrete. The addition of microsilica to the concrete mixture causes its active SiO_2 to combine with the free calcium hydroxide solution $Ca(OH)_2$ in the capillary pores of the concrete and produce insoluble calcium silicate crystals (Relation 2), which ultimately causes the compaction of the cement paste structure [11]. This compaction also decreases permeability and ultimately increases the mechanical resistance of concrete [12]. Preventing the penetration of chlorine ions, sulfates, and other harmful chemicals into the concrete and enhancing its durability are the result of reducing the permeability of concrete in this chemical process [13]. This research used microsilica produced by a Chemical Construction Company in Iran.

$$\begin{aligned} &\mathrm{OPC}\left(\text{ordinary Portland cement}\right)+\mathrm{H_2O}\rightarrow \\ &\rightarrow \mathrm{CSH}\left(\text{Calcium silicate hydrate}\right)+\mathrm{Ca}\left(\mathrm{OH}\right)_2; \end{aligned} \tag{1}$$

$$\mathrm{Ca}\left(\mathrm{OH}\right)_2+\mathrm{SiO_2}\rightarrow \mathrm{H_2O}+\mathrm{CSH}. \tag{2}$$

2.3. Superplasticizer

Due to the exceptional microsilica grains, special surfaces will have a visible enhancement. For this reason, the amount of water used for mixing will increase, causing a reduction in the strength of concrete. The use of superplasticizers in concrete containing microsilica can prevent water consumption [14]. The superplasticizer mix used (which is based on modified lignosulfonate) is manufactured by Shimi Company in Iran. In this investigation, about 2% by weight of cement was used. The technical and chemical specifications of the superplasticizer are presented in Table 3 [15].

Table 3. Mechanical and chemical characteristics of the used superplasticizer

Chloride (ppm)	Special Weight (kg/lit)	Physical state	Color	Lonic nature	Chemical mixture
max 500	1.19±0.02 at 20 °C	liquid	Brown	anionic	modified lignosulfonate

2.4. Natural aggregate

To make concrete with high compressive strength, it is inevitable to use grains with small dimensions. In this research, aggregates with dimensions less than 4.75 mm (0–4 sand) were used. In addition, grain consistency is one of the basic and obvious principles for the production of durable and high-strength concrete. In Fig. 1, the curve of aggregates and the permissible range of granularity according to the standard ASTM C404 [16] are shown.

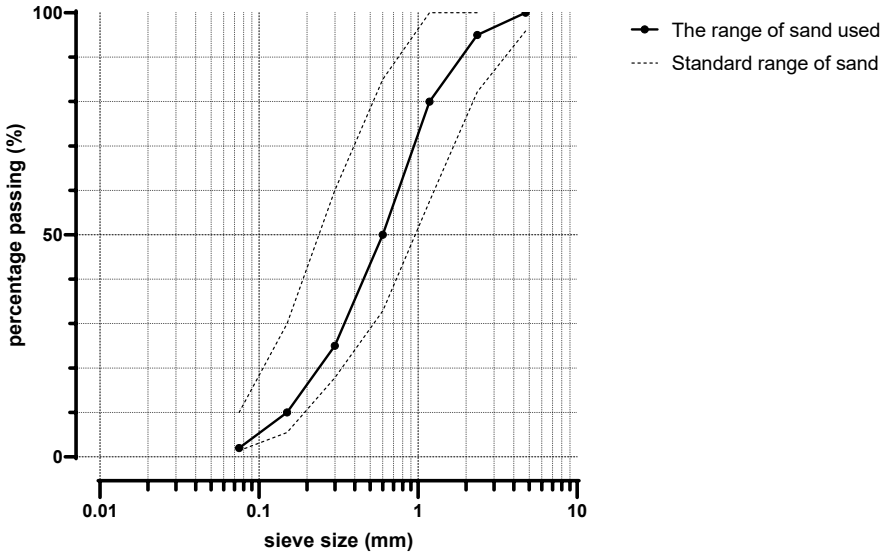

Figure 1. Granulation curve of the used sand.

2.5. Artificial aggregate

To make concrete with low specific weight, lightweight expanded clay aggregate (LECA), an artificial aggregate has been used in some concrete mix designs. Similar to the grading of natural aggregates, the dimensions of artificial aggregates are less than 4.75 mm. These grains are obtained from the expansion of clay in rotary furnaces with a temperature of about 1200 degrees Celsius. Microscopically, the outer surface of the seeds has small brown pores and the inner part of the seeds has black cell tissue [17]. A combination of desirable properties such as light weight, low thermal conductivity, effective noise attenuation, fire resistance, durability, and chemical stability has broadened the range of applications for these artificial aggregates across building construction, infrastructure projects, agriculture, environmental works, road construction, and more [18, 19].

2.6. Mix designs

To achieve the objectives of the project, 15 concrete mix designs containing natural aggregate and 7 concrete mix designs containing different artificial aggregates were examined according to ACI 211-77 [20], by Tables 4 and 5. In the aforementioned concrete mix designs, five different amounts of cement, 350, 400, 450, 500, and 550 kg/m^3 were used. Moreover, 10%, 20% and 30% microsilica (containing 2% superplasticizer based on modified lignosulfonate) were utilized as a replacement for cement. Additionally, the water-to-cement ratio was varied to 0.30, 0.35, 0.40, and 0.45. Compressive strength was evaluated on 50 mm cube specimens prepared in accordance with ASTM C109 [21]. The details of concrete mix designs can be seen in Tables 4 and 5. The letters A, B, C, D, and E indicate cement contents of 350, 400, 450, 500, and 550 kg/m^3, respectively.. Also, the letters L, M, and H indicate 10, 20, and 30% of microsilica consumption, respectively, and the numbers after them indicate the water-to-cement ratio used in the design.

Table 4. Details of concrete mix designs containing natural aggregate

Mix designs	Cement content (kg/m^3)	Microsilica (%)	Cement-Microsilica paste (gr)	Water (gr)	Aggregate (gr)
AL35	350	10	160.4	56.2	680.5
AL40	350	10	160.4	64	672.5
AL45	350	10	160.4	72.2	664.5
AH45	350	30	189.6	85.3	622.2
BH30	400	30	216.6	65	616.6
BH45	400	30	216.6	97.5	582.5
CL45	450	10	206.25	92.8	597.2
CM45	450	20	225	101.25	570
CH45	450	30	243.75	109.7	542.8
D045	500	0	208.3	93.75	598
DL35	500	10	229.1	80.2	588.5
DH45	500	30	270.8	121.8	503
EL45	550	10	252	113	530
EM45	550	20	275	123.75	496.9
EH45	550	30	298	134	463.5

Table 5. Details of concrete mix designs containing artificial aggregates

Mix plans	Cement content (kg/m^3)	Microsilica (%)	Cement-Microsilica paste (gr)	Water (gr)	Aggregate (gr)	Artificial aggregate (%)
BH30'	400	30	216.6	65	616.6	50% No. 16 50% No. 30
BH30'	400	30	216.6	65	616.6	50% No. 16 50% No. 30
DL35'	500	10	229.1	80.2	588.5	30% No. 30
DM30'	500	20	250	75	572.9	15% No. 8 15% No. 16
DM35'	500	20	250	87.5	560.4	15% No. 16 15% No. 30
DH35'	500	30	270.8	94.8	532.3	15% No. 16 15% No. 30
DH35'	500	30	270.8	94.8	508.6	100% No. 16 100% No. 30

2.7. Curing

In each concrete mix design, to measure the compressive strength of concrete at the ages of 7, 14, and 28 days, three cubic samples with dimensions of 50 mm (total of 9 concrete samples in each mix design) were molded and cured. After staying in the mold for one day, the samples were transferred to a water tank at a temperature of 23–25 °C for 6, 13, and 27 days. To prevent moisture loss, the concrete samples in the molds are covered by a plastic membrane immediately after concreting [22].

3. Results and Discussion

3.1. Compressive strength

The results of the compressive strength tests for various concrete mix designs are presented in Tables 6 and 7. The progression of compressive strength development at different ages is illustrated in Figs. 2 and 3. Initial analysis of the data suggests that the 28-day compressive strength of the concrete samples increases with higher percentages of microsilica and higher cement content. Mix designs incorporating 10% microsilica exhibit a steady and consistent increase in strength up to their ultimate value. However, this trend diverges in mixes containing 30% microsilica.

Table 6. Compressive strength of concrete containing natural aggregate

	Ccompressive strength (MPa) at		
Mix plans	**7 days**	**14 days**	**28 days**
AL35	24.2	34.8	39.5
AL40	23	28.3	38.9
AL45	21.3	27	35.7
AH45	34.4	29.6	43.2
BH30	37	48.5	53.6
BH45	36.8	45.1	42.5
CL45	34.4	47.6	54
CM45	39.4	51	49.6
CH45	40.8	50.4	45.4
D045	40.4	52.6	60.2
DL35	43.8	53	62.4
DH45	49.2	62.8	63.3
EL45	38.6	53.3	59.7
EM45	37.3	49.7	60.7
EH45	40.8	45.2	65.2

Table 7. Compressive strength of concrete containing artificial aggregates

	Ccompressive strength (MPa) at		
Mix plans	**7 days**	**14 days**	**28 days**
BH30'	36.5	47	44.2
BH30'	35.2	45.8	44
DL35'	40.2	49.5	60
DM30'	42.5	51	61.8
DM35'	40.8	51	62.1
DH35'	46	61.7	60.5
DH35'	42.6	55	56.6

In mix designs containing 30% microsilica and cement content of 350 kg/m^3, a decline in strength is observed at the 14-day mark. Similarly, a reduction in 28-day strength is evident in mixes with 30% microsilica and cement content of 400 and 450 kg/m^3. Nonetheless, this declining trend appears to be stabilized in the mix with 20% microsilica and cement content of 450, as well as in the mix with 30% microsilica and cement grade 500.

Interestingly, in the mix design containing 30% microsilica and cement content of 550 kg/m^3, strength development appears normal, and the upward trend resumes. This behavior may be attributed to the higher cement content , which compensates the effects of excessive microsilica, similar to the balanced performance observed in mixes with 20% microsilica and cement content of 450 kg/m^3, and 30% microsilica with cement content of 500 kg/m^3. Excessive microsilica can disrupt the uniform rate of cement hydration, and this delayed hydration may temporarily weaken the cement matrix due to the increased presence of microsilica powder.

Also, in artificial aggregate mix designs, adding 30% microsilica alters the process of gaining strength in the same manner as in mix designs with natural aggregates. Adding LECA lowers both sample weight and compressive strength due to LECA particles being porous. This can be observed when comparing identical mix designs without adding LECA.

An increase in the water-to-cement ratio leads to a decrease in the compressive strength of the samples. In mix designs containing 30% microsilica, the irregular strength development is compensated by increasing the cement content, which counteracts the effects of excessive microsilica.

Briefly, with 10% microsilica, 28-day compressive strength increased steadily with cement grade, peaking at ≈42 % above the plain-cement control when 550 kg/m^3 cement was used. Raising the dosage to 20% produced a further boost, yielding up to ≈58 % strength gain in the C-series mix (450 kg/m^3 cement). By contrast, 30% microsilica behaved in a threshold-dependent manner:

- With 350 kg/m^3 cement, strength fell ≈12 % at 14 days and remained ≈8 % lower than the 10 % mix at 28 days.
- When cement was raised to 500 kg/m^3, the 30 % mix recovered and matched the 20 % mix at 28 days.
- At 550 kg/m^3 it exceeded all other mixes, delivering ≈18 % higher strength than its 20 % counterpart, confirming that adequate $Ca(OH)_2$ is essential for pozzolanic utilisation of such a high microsilica content.

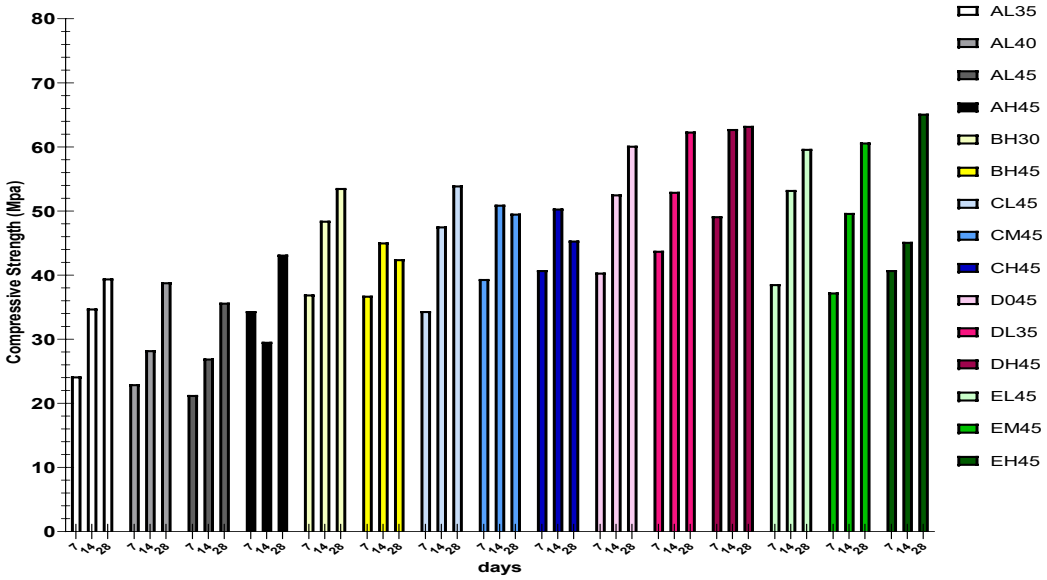

Figure 2. Strength acquisition curve of mixing designs containing natural aggregate.

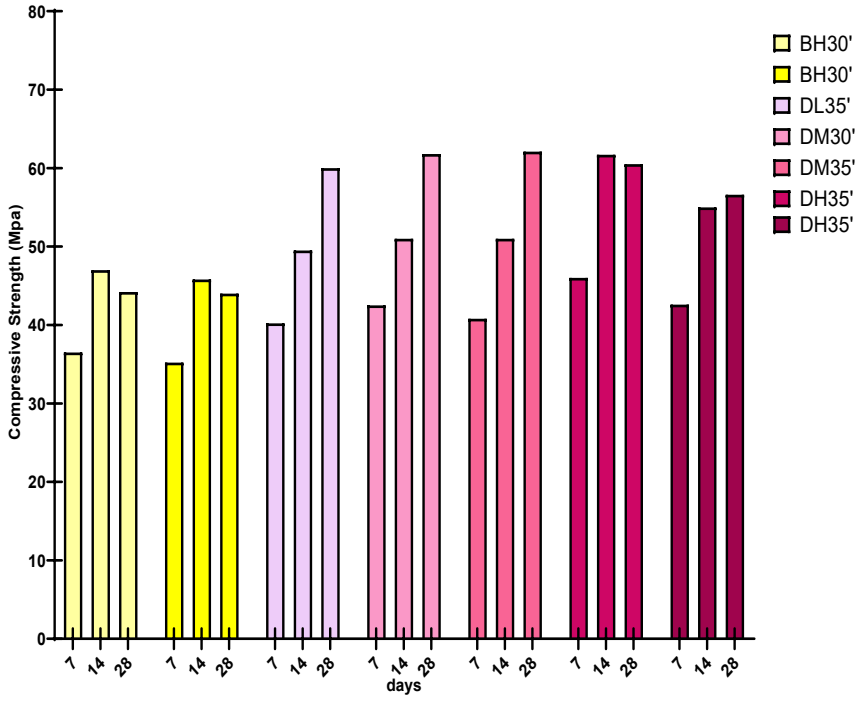

Figure 3. Strength acquisition curve of mixing designs containing artificial aggregate.

3.2. Specific weight

The progress in technology and the human need for various structures has led to extensive research on the properties and behavior of materials, which results in the creation of various types of structures and the use of various materials. Concrete can be divided into three categories in terms of specific weight: normal concrete, light concrete, and heavy concrete. However, this classification is not comprehensive and does not include the properties and applications of different types of concrete [23].

According to the definition of ordinary concrete, concrete is normally made with the ordinary type (I) to type (V) Portland cement. This concrete has a specific weight from to 2200 to 2500 kg/m^3 (usually 2400 kg/m^3). This difference is related to the type of grains and the density of the concrete. The findings indicate that the specimens have a density between 2100 and 2300 kg/m^3; despite their high compressive strength, they are still classified as lightweight structural concrete [24] (Figs. 4 and 5).

All natural-aggregate mixes fell between 2100–2300 kg/m^3, already 4–12% lighter than ordinary concrete. Substituting 50% LECA dropped density by a further ≈6 %, with only a 10–15 % reduction in strength at identical binder levels.

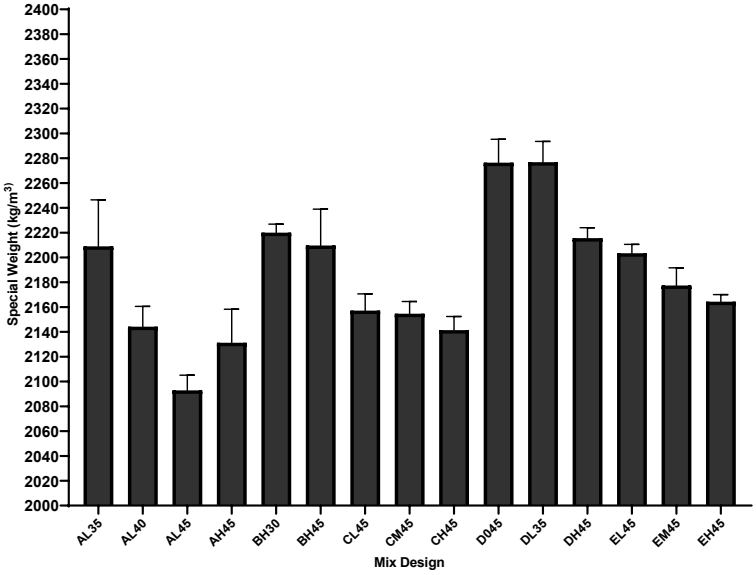

Figure 4. Specific weight of mixing designs containing natural aggregate (kg/m^3).

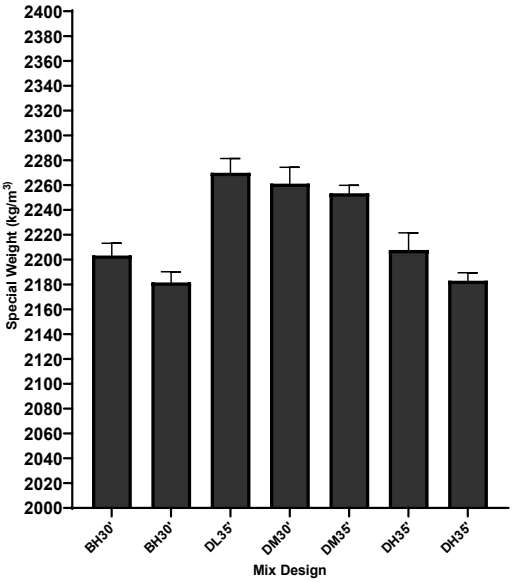

Figure 5. Specific weight of mixing designs containing artificial aggregates (kg/m^3).

3.3. Elastic modulus

One of the important parameters of concrete in the analysis and design of concrete structures is the modulus of elasticity. The modulus of elasticity is important to estimate the change in the shape of the

structure under the effect of the incoming loads. Additionally, it indicates the resistance of the material to the change in shape. The modulus of elasticity is directly related to the material's hardness. The factors that can influence the value of the modulus of elasticity of concrete are aggregates, loading rate, chemical additives, curing conditions of concrete, and water-cement ratio. Since concrete is brittle, the stress-strain ratio in the elastic region cannot be used to determine the modulus of elasticity, so there are other approaches to determining concrete's static and dynamic modulus [25].

In this research, the static modulus of elasticity of concrete has been investigated. During this path, the formulas of the American code ACI-318 [26], the Canadian code [27], the European concrete regulation (EC), the Indian regulation [28], and the CEB-FIP regulation [29] were analyzed (Figs. 6 and 7).

The static modulus correlated linearly with compressive strength (R^2 = 0.92 across all 10% and 20 % mixes). Samples with 30% microsilica deviated downward by ≈15 % from this trend, attributable to their lower bulk density and the delayed clinker hydration discussed above.

1. American Concrete Code ACI-318

$$E_c = 0.043 w^{1.5} \sqrt{f_c'}$$

2. Canadian concrete code (CSA-A23.3)

$$E_c = \left(3300\sqrt{f_c'} + 6900\right)\left(\gamma/2300\right)^{1.5}$$

3. European Concrete Regulation (EC)

$$E_c = 22\left[\left(f_c'/10\right)\right]^{0.3}$$

4. Indian regulation (IS-456)

$$E_c = 5000\sqrt{f_c'}$$

5. CEB-FIP regulation

$$E_c = 21500\alpha_E \left(f_{ck}/10\right)^{\frac{1}{3}}$$

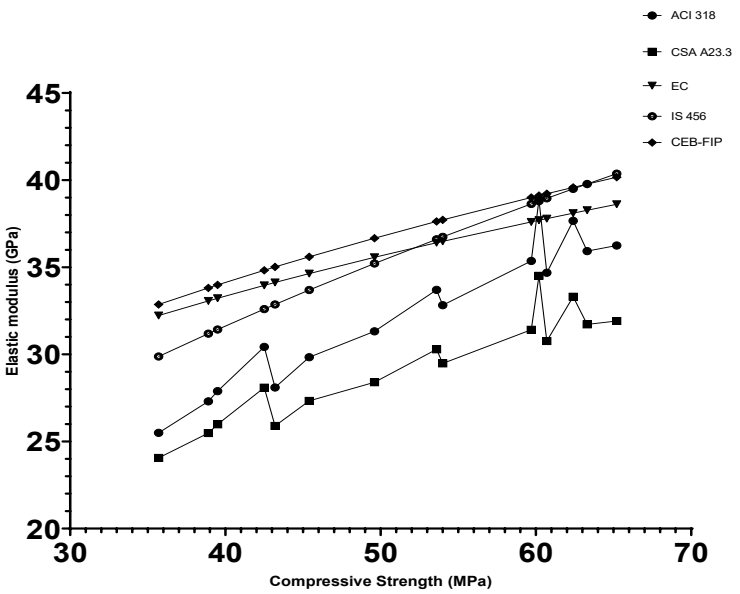

Figure 6. Comparison chart of modulus of elasticity and compressive strength of mixing designs containing natural aggregate.

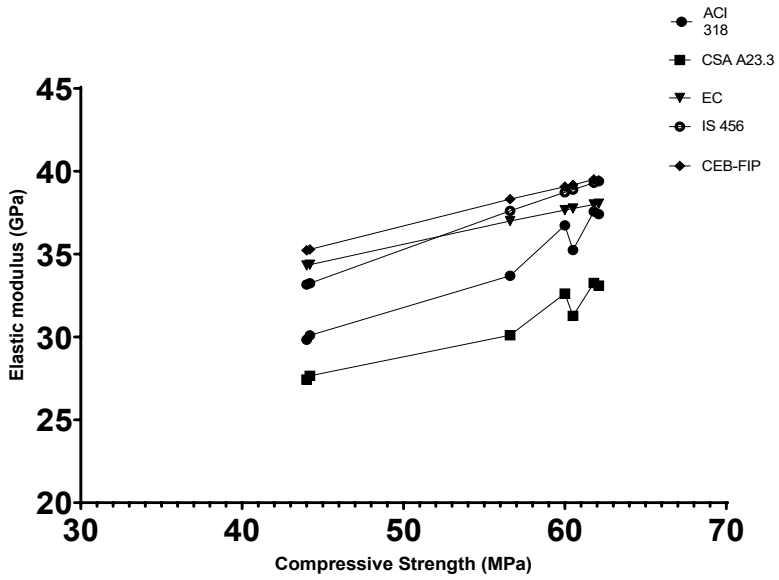

Figure 7. Comparison chart of modulus of elasticity and compressive strength of concrete mix designs containing artificial aggregate.

3.4. Water absorption

The resistance of concrete to aggressive chemical attacks is a critical factor that significantly impacts its durability. Water absorption serves as an indicator of concrete's porosity and provides insight into the volume of permeable pores and their interconnectivity. Moreover, water is a necessary component for the hydration reactions of cement. The increase in the weight of the samples depends on the effect of the water present in the pores. Depending on the environmental conditions and the thickness of the samples, gradually most of the evaporable water in the concrete is lost and the pores of the concrete become empty or unsaturated. In this research, concrete samples were placed inside the oven for 8 hours and then their dry weight was measured [30].

The results are shown in figures 8 and 9 for different mix designs. In general, with the increase in the water-to-cement ratio, the amount of water absorption of the samples also increases. The addition of microsilica strengthens the concrete’s pore structure, thereby reducing its water absorption. The difference in the amount of water absorption between the mixing design without microsilica and other mixing designs containing microsilica confirms the reason for the decrease in the amount of water absorption in the samples having microsilica.

Incorporating 10–20% microsilica reduced 24-hour water absorption by 25–40% compared to the control mix, indicating effective pore structure refinement. However, combining 30% microsilica with ≥ 500 kg/m^3 cement reversed the trend, producing an ≈18% rise in absorption. This suggests that an initial moisture deficit and agglomerated silica powder can offset the expected densification unless dispersion is improved. LECA lowered absorption by ≈10% compared with corresponding natural-aggregate mixes because of its intrinsic pore suction and internal curing effect.

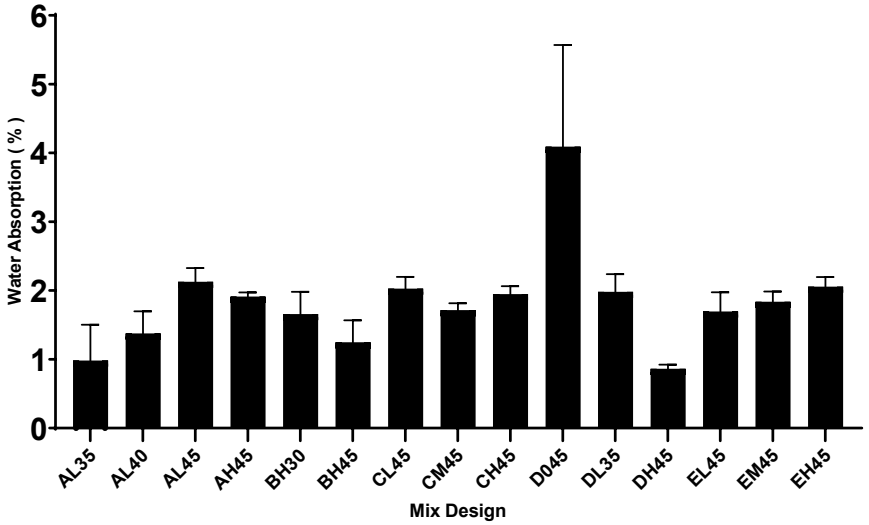

Figure 8. Water absorption percentage of mixing plans containing natural aggregate.

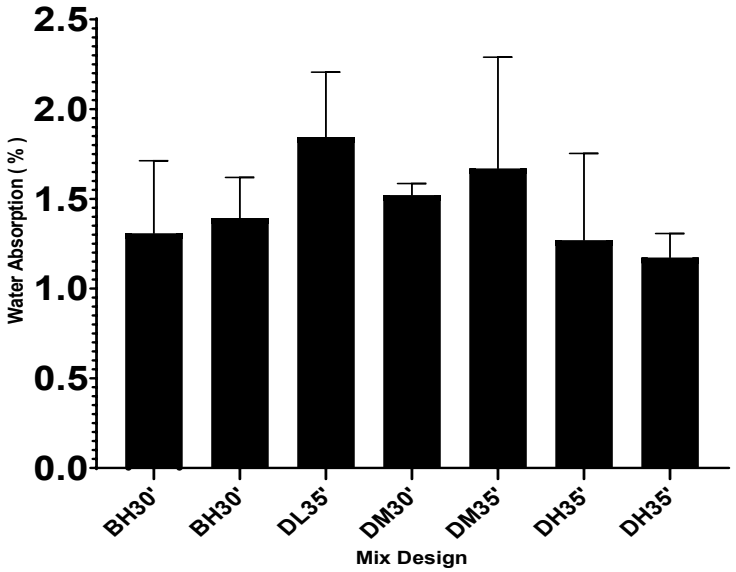

Figure 9. Water absorption percentage of mixing designs containing artificial aggregate.

4. Conclusion

Primarily, incorporating microsilica as a substitute for cement in concrete mixtures offers a dual advantage of enhancing compressive strength while also lowering the concrete's density. However, the choice of aggregate plays a critical role. Replacing natural aggregates with artificial ones (LECA) reduces compressive strength by approximately 10–15%, while simultaneously lowering water absorption.

This research demonstrates that high-microsilica lightweight concrete can attain compressive strengths exceeding 70 MPa while maintaining a specific weight below 2300 kg/m^3 when 30% microsilica is paired with ≥ 500 kg/m^3 cement and properly dispersed. An initial decline in 7–14 day strength is evident at this high microsilica percentage because agglomerated microsilica particles and a shortfall of early $Ca(OH)_2$ hamper hydration; however, higher cement content supply the needed calcium hydroxide, allowing the 28-day strength to recover and ultimately surpass that of 10% and 20% mixes.

The same dosage-and-binder balance governs other properties. The static modulus of elasticity – normally proportional to strength drops in low-density mixes that pair microsilica with LECA. Water absorption, on the other hand, improves by up to 40% when typical microsilica contents of 10–20% are used. However, it rises when 30% microsilica and high cement content are employed without extra water reducers.

Practically, achieving > 70 MPa at reduced density offers 10% mass reduction that lowers seismic demand and enables lighter lateral systems; substituting one-third of the cement with this industrial by-product trims clinker consumption and embodied carbon; and the pore-refinement induced by 10–20% microsilica enhances durability in chloride and sulfate environments. The investigation is limited to 50 mm cubes, a single lignosulfonate superplasticizer, and short-term tests, leaving long-term durability, creep–shrinkage interaction, and life-cycle cost unaddressed; as a result, future work should examine full-scale elements under field curing, trial higher range water reducers to counter high microsilica absorption, and employ response-surface methods to evaluate hybrid supplementary cementitious blends (e.g., microsilica–fly ash) that could further refine rheology, sustainability, and robustness.

References

1. Yasar, E., Atiş, C.D., Kiliç, A. High Strength Lightweight Concrete Made with Ternary Mixtures of Cement-Fly Ash-Silica Fume and Scoria as Aggregate. Turkish Journal of Engineering and Environmental Sciences. 2004. 28(2). Pp. 95–100.
2. Aïtcin, P.-C. High Performance Concrete. CRC Press. London, 1998. 624 p. DOI: 10.4324/9780203475034
3. Ajay, V., Rajeev, C., Yadav, R. Effect of micro silica on the strength of concrete with ordinary Portland cement. Research Journal of Engineering Sciences. 2012. 1–3. Pp. 1–4.
4. Rahman, M.A., Zawad, M.F., Priyom, S.N. Potential use of microsilica in concrete: a critical review. 5th International Conference on Advances in Civil Engineering (ICACE 2020). Chattogram, 2020. Pp. SE-173–SE-180.
5. Zhang, J., Zhao, Y., Li, H. Experimental Investigation and Prediction of Compressive Strength of Ultra-High Performance Concrete Containing Supplementary Cementitious Materials. Advances in Materials Science and Engineering. 2017. Pp. 1–8. DOI: 10.1155/2017/4563164
6. Alexander, M.G., Magee, B.J. Durability performance of concrete containing condensed silica fume. Cement and Concrete Research. 1999. 29(6). Pp. 917–922. DOI: 10.1016/S0008-8846(99)00064-2
7. Zhang, J., Zhao, Y., Li, H. Experimental Investigation and Prediction of Compressive Strength of Ultra-High Performance Concrete Containing Supplementary Cementitious Materials. Advances in Materials Science and Engineering. 2017. 2017. Article no. 4563164. DOI: 10.1155/2017/4563164
8. Mazloom, M., Ramezanianpour, A.A., Brooks, J.J. Effect of silica fume on mechanical properties of high-strength concrete. Cement and Concrete Composites. 2004. 26(4). Pp. 347–357. DOI: 10.1016/S0958-9465(03)00017-9
9. Ayan, T.I., Nawar, N., Chowdhury, I.A., Chowdhury, S.R. A study of micro-silica as a substitution of cement for sustainable concrete. International Journal Of Engineering Research And Development. 2024. 20(4). Pp. 82–92.
10. S. Horkoss, "Middle East Standards and Specifications for Cements," 2004, pp. 1241-1254..
11. Kim, T., Seo, K.-Y., Kang, C., Lee, T.-K. Development of Eco-Friendly Cement Using a Calcium Sulfoaluminate Expansive Agent Blended with Slag and Silica Fume. Applied Sciences. 2021. 11(1). Article no. 394. DOI: 10.3390/app11010394
12. Sharma, H.J., Garg, E.R., Sharma, E.D., Beg, M.U., Sharma, R. Investigation on Mechanical Properties of Concrete Using Microsilica and Optimised dose of Nanosilica as a Partial Replacement of Cement. International Journal of Recent Advancement in Engineering & Research. 2016. 3(4). Pp. 23–29.
13. Rao, G.A. Influence of silica fume replacement of cement on expansion and drying shrinkage. Cement and Concrete Research. 1998. 28(10). Pp. 1505–1509. 1998. DOI: 10.1016/S0008-8846(98)00127-6
14. Huang, C., Ma, J., Zhang, W., Huang, G., Yong, Q. Preparation of Lignosulfonates from Biorefinery Lignins by Sulfomethylation and Their Application as a Water Reducer for Concrete. Polymers. 2018. 10(8). Article no. 841. DOI: 10.3390/polym10080841
15. Mailvaganam, N.P., Rixom, M.R., Manson, D.P., Gonzales, C. Chemical Admixtures for Concrete. CRC Press, 1999.
16. ASTM C404-18. Standard Specification for Aggregates for Masonry Grout. ASTM International. West Conshohocken, PA, 2018.
17. Kohno, K., Okamoto, T., Isikawa, Y., Sibata, T., Mori, H. Effects of artificial lightweight aggregate on autogenous shrinkage of concrete. Cement and Concrete Research. 1999. 29(4). Pp. 611–614. DOI: 10.1016/S0008-8846(98)00202-6
18. Mamatha, K.H., Mothilal, M. Experimental Study Light Weight Concrete Using LECA, Silica Fumes, and Limestone as Aggregates. International Journal for Research in Applied Science & Engineering Technology (IJRASET). 2022. 10(12). Pp. 1103–1110. DOI: 10.22214/IJRASET.2022.47916
19. Youssf, O., Hassanli, R., Mills, J.E., Abd Elrahman, M. An experimental investigation of the mechanical performance and structural application of LECA-Rubcrete. Construction and Building Materials. 2018. 175. Pp. 239–253. DOI: 10.1016/j.conbuildmat.2018.04.184
20. ACI Committee. Recommended Practice for Selecting Proportions for Normal and Heavyweight Concrete (ACI 211.1-77). The Institute Detroit. Detroit, 1977.
21. ASTM C109 / C109M-16a. Standard Test Method for Compressive Strength of Hydraulic Cement Mortars (Using 2-in. or [50-mm] Cube Specimens). West Conshohocken, PA, 2016. 10 p.
22. Tam, C.M., Tam, V.W.Y., Ng, K.M. Assessing drying shrinkage and water permeability of reactive powder concrete produced in Hong Kong. Construction and Building Materials. 2012. 26(1). Pp. 79–89. DOI: 10.1016/j.conbuildmat.2011.05.006
23. A. M. Rashad, "Lightweight expanded clay aggregate as a building material – An overview," *Construction and Building Materials,* vol. 170, pp. 757-775, 2018/05/10/ 2018, doi: https://doi.org/10.1016/j.conbuildmat.2018.03.009.
24. Thienel, C., Haller, T., Beuntner, N. Lightweight Concrete – From Basics to Innovations. Materials. 2020. 13(5). Article no. 1120. DOI: 10.3390/ma13051120
25. Mermerdaş, K., İpek, S., Algın, Z., Ekmen, S., Güneş, İ. Combined effects of microsilica, steel fibre, and artificial lightweight aggregate on the shrinkage and mechanical performance of high strength cementitious composite. Construction and Building Materials. 2020. 262. Article no. 120048. DOI: 10.1016/j.conbuildmat.2020.120048
26. American Concrete Institute. ACI 318-14. Building Code Requirements for Structural Concrete and Commentary (Metric). American Concrete Institute, 2014.

27. C.S. and S.C.o. Canada. A23.3-94 Design of Concrete Structures: Structures (design). The Associatio, 1994.
28. Indian Standard. IS 456: Plain and Reinforced Concrete – Code of Practice. Bureau of Indian Standards. New Delhi, 2000. 107 p.
29. Comité Euro-International du Béton. Concrete Structures – First complete draft, Laussane (CEB-FIP MODEL CODE 1990). 2010.
30. Şanal, İ. Performance of Macrosynthetic and Steel Fiber–Reinforced Concretes Emphasizing Mineral Admixture Addition. Journal of Materials in Civil Engineering. 2018. 30(6). Article no. 04018101. DOI: 10.1061/(ASCE)MT.1943-5533.0002292

Information about the authors:

Kiavash Fallah-Mehrjardi,
E-mail: kiavashfallah@gmail.com

Afagh Shariat,
E-mail: sshari56@uwo.ca

Mohammad Eftekhar, *PhD*
E-mail: eft@iut.ac.ir

Received 14.10.2023. Approved after reviewing 24.08.2025. Accepted 24.08.2025.

Magazine of Civil Engineering

ISSN 2712-8172

journal homepage: http://engstroy.spbstu.ru/

Research article

UDC 691.43

DOI: 10.34910/MCE.138.3

Phase formation, structure and properties of ceramic materials based on binary mixtures “refractory clay – steel slag”

T.V. Vakalova ✉ , ***N.P. Sergeev*** , ***D.T. Tolegenov*** , ***I.B. Revva***

National Research Tomsk Polytechnic University, Tomsk, Russian Federation

✉ *tvv@tpu.ru*

Keywords: refractory clay, steel slag, sintering, mechanical strength, gehlenite, anorthite, building ceramics

Abstract. The work is devoted to the current problem of creating high-strength ceramic materials using techno-genic waste. This problem is solved by using refractory clay as the main raw material component with the addition of high-iron calcium silicate steel slag in various proportions. The processes of phase formation that occur during heating of steel slag are considered. It has been established that the use of steel slag to produce ceramic materials is possible only if the destructive effect of dicalcium silicate formed in the slag at firing temperatures above 1000 °C is neutralized. This is possible due to the chemical transformation of dicalcium silicate into other calcium-containing minerals that are safe from the point of view of molded sample destruction, such as anorthite, wollastonite, gehlenite, and others that do not have polymorphism. Compositions of ceramic masses have been developed that ensure the production of high-strength anorthite ceramics (with water absorption from 2.8 to 13.4 % and compressive strength of up to 200 MPa) for a wide range of purposes – structural (wall) building ceramics, clinker building ceramics, ceramic proppants, etc.

Citation: Vakalova, T.V., Sergeev N.P., Tolegenov, D.T., Revva, I.B. Phase formation, structure and properties of ceramic materials based on binary mixtures “refractory clay – steel slag”. Magazine of Civil Engineering. 2025. 18(6). Article no. 138703. DOI: 10.34910/MCE.138.3

1. Introduction

Among building ceramic materials, clinker ceramics have been gaining popularity in the last decade, which is divided into construction (finishing, facade), road (pavement), and technical ceramics. Ceramics are classified as clinker if the value of its water absorption is no more than 6 %, the compressive strength is not less than 30.0 MPa. However, according to some data [1], the compressive strength of building clinker with a water absorption of 2–2.5 % can exceed 200–250 MPa, and with a water absorption of 2–4 %, as a rule, it is higher than 80–100 MPa. In addition to improved quality characteristics, clinker brick has distinctive aesthetic characteristics – color transitions due to a higher firing temperature [2]. The production of products with such properties largely depends on the quality of the clay raw materials used, which must be low-temperature sintered and, preferably, with a wide sintering range (at least 100 °C), which is typical for refractory and ball clays, the deposits of which are quite scarce, and the reserves limited [3]. Replacing at least part of such in short supply clay raw materials in ceramic masses with other, preferably more abundant and cheaper natural or man-made raw materials, would allow for significant savings in high-quality raw materials, which, together with the use of waste, would reduce production costs and improve the environment [4]. Thus, in the context of decreasing reserves of explored natural raw materials, as well as increasing anthropogenic load on the environment, the problem of expanding the areas and volumes of use of industrial waste from the mining, metallurgical, fuel, and energy complexes is of particular importance.

Among man-made waste, a special place is occupied by sludge and slag from metallurgical production. Steel slag is a by-product of processing iron into steel in a converter furnace, or melting scrap to produce steel in an electric arc furnace [5, 6]. Steel slag dumps occupy large areas of land and lead to many serious environmental problems. In this regard, the search for a new, effective way to increase the volume of steel slag recycling is of serious concern. The chemical composition and cooling conditions of molten steel slag have a great influence on its physical and chemical properties in the solidified state. The main chemical compositions of steel slag include CaO, SiO_2, Al_2O_3, Fe_2O_3, MgO, and FeO [7–9]. The common minerals in steel slag are olivine, merwinite, dicalcium silicate (C_2S), tricalcium silicate (C_3S), tetracalcium aluminoferrite (C_4AF), dicalcium ferrite (C_2F), RO phase (CaO–FeO–MnO–MgO solid solution), and free CaO [6, 10, 11]. It is well known that belite C_2S and alite C_3S have binding properties, therefore, steel slag is widely used as an additive to cement and concrete [12–16]. In addition, steel slag is recommended for the production of glass ceramics [17–20], special-purpose ceramics [21–23], and especially for the production of building ceramics [24–26]. The involvement of waste in silicate technologies necessitates the search for new scientific approaches to the selection of raw materials, the development of criteria for assessing the possibility of using such raw materials to obtain high-quality building materials. Solving these problems requires theoretical and exploratory research to find ways and methods for obtaining ceramic and composite structures that ensure the achievement of high mechanical characteristics and other performance properties. The purpose of this work is to study the processes of formation of the phase composition, structure, and physical and mechanical properties of ceramics based on refractory (kaolinite) clay using steel slag in various proportions.

To achieve this objective, it is necessary to solve the following tasks:

- to establish the chemical composition, mineralogical (phase) composition, structural features of the initial steel slag;
- to study structural and phase changes during heating of steel slag;
- to carry out theoretical and exploratory research on the development of compositions and technological parameters for the obtaining of high-strength ceramic materials based on composition of refractory clay and steel slag.

2. Methods

2.1. Characteristics of Initial Raw Materials Used

Refractory clay from the Latnenskoye deposit was used as a clay raw material. According to the chemical composition, it belongs to the main clayey raw material with an average content of coloring oxides (>1.5 % Fe_2O_3 and >1.5 % TiO_2) in the calcined state (Table 1), according to the mineralogical composition – kaolinite-hydromica clay with an admixture of quartz in the coarse part (Fig. 1), in terms of sinterability – high-temperature sintering clay with a sintering temperature above 1200 °C (Fig. 2).

Table 1. Chemical composition of the investigated raw materials.

Raw materials	Content of oxides, wt. %									
	SiO_2	**Al_2O_3**	**Fe_2O_3**	**Fe_2O_3**	**MnO**	**CaO**	**MgO**	**K_2O**	**Na_2O**	**LOI**
refractory clay										
Absolutely dry state	49.87	30.55	1.70	1.46	–	1.29	0.67	0.38	0.17	13.91
Calcined state*	57.95	35.50	1.98	1.68	–	1.48	0.77	0.44	0.20	–
steel slag										
Absolutely dry state	7.62	7.80	0.68	21.45	4.72	35.33	8.07	0.09	0.51	3.46
Calcined state*	8.28	8.08	0.70	22.22	4.89	36.60	8.36	0.09	0.52	–

* – after calcination at 950 °C

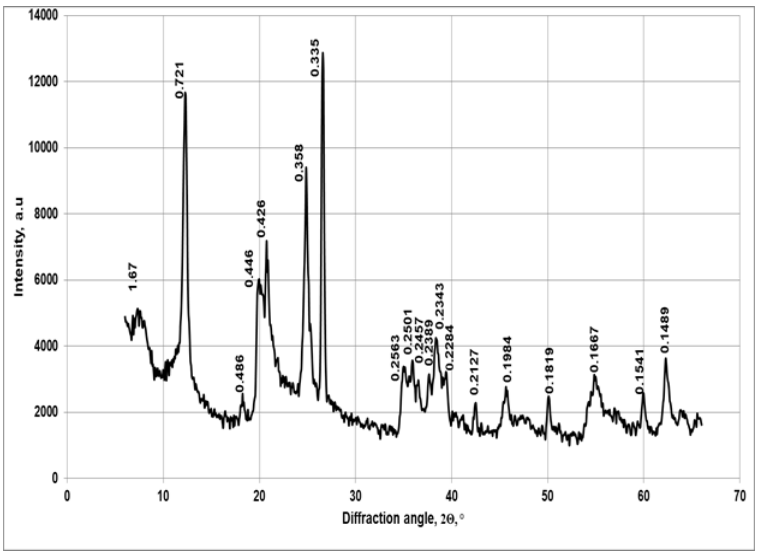

Figure 1. X-ray diffraction pattern of refractory clay used.

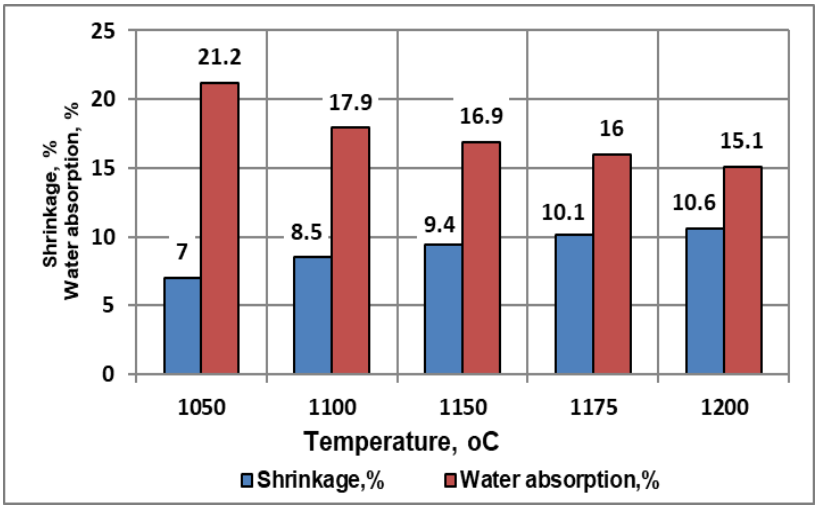

Figure 2. Histogram of changes in the physical and mechanical properties of semi-dry pressing samples from studied clay, fired at 1050–1200 °C.

Steel slag, a waste product from steel production, was tested as a technogenic raw material at the KSP Steel, Republic of Kazakhstan. According to the chemical composition (Table 1), the slag under study is represented mainly by oxides of calcium (35.33 %), iron (21.45 %), silicon (17.62 %), and aluminum (7.80 %), the sum of which is more than 80 %.

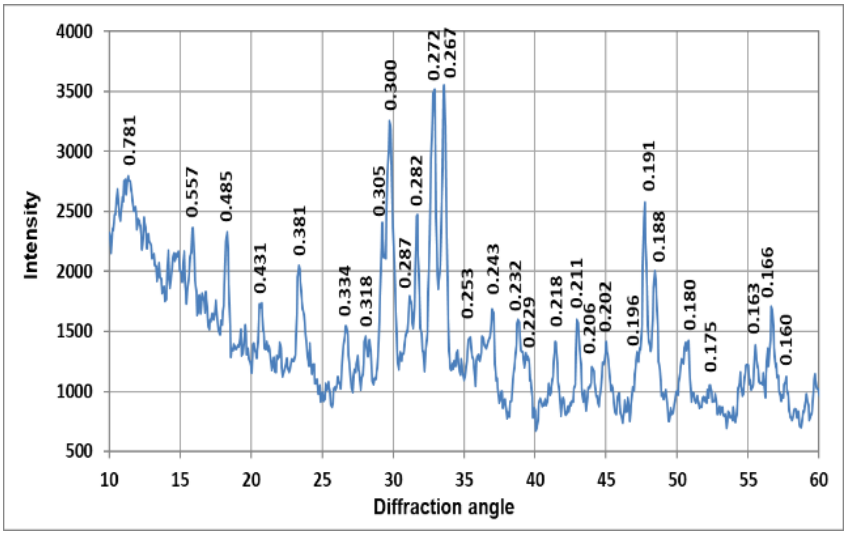

Figure 3. X-ray diffraction pattern of the original steel slag.

A comparative analysis of the chemical composition (Table 1) and X-ray analysis data (Fig. 3) indicates that the calcium component in steel slag is represented by hydrated calcium oxide – portlandite $Ca(OH)_2$, as evidenced by reflections with d/n – 0.492, 0.316, 0.263, 0.193, 0.179 nm, as well as silicates and hydrated calcium silicates – okermanite $2CaO•MgO•2SiO_2$ (0.429, 0.379, 0.306, 0.287, 0.243, 0.232, etc.), tobermorite $5CaO•6SiO_2•5H_2O$ (0.56, 0.306, 0.297 0.282 nm, etc.), and dicalcium hydrosilicate $2CaO•SiO_2•H_2O$ (0.429, 0.379, 0.306, 0.282, 0.273, 0.247 nm, etc.). Aluminate, magnesium, and ferrous components are represented by monocalcium aluminate $CaO•Al_2O_3$ (0.56, 0.46, 0.298, 0.254, 0.243 nm), enstatite $MgO•SiO_2$ (0.316, 0.288, 0.252, 0.245, 0.205 nm), and monocalcium ferrite $CaO•Fe_2O_3$ (0.282, 0.273, 0.268, 0.254, 0.210, 0.181 nm).

2.2. Procedures and Methods

All analyzed clay-slag compositions were grouped into two types: the first group of compositions were mixtures, in which clay was the base, and steel slag was an additive in an amount from 10 to 50 %, the second group of compositions were mixtures, in which the base was steel slag, and clay was added in an amount of 10 to 40 %.

Clay dried to an air-dry state was crushed to a size of less than 0.5 mm, steel slag – to a size of less than 0.063 mm. Prepared clay and steel slag were dosed in a ratio from 90:10 to 10:90 with an interval of 10 %.

The study of the behavior of upon heating refractory clay and steel slag as well as samples from their mixtures was carried out on semi-dry pressing samples in the form of tablets with a diameter of 20 mm and cylinders 20×20 mm. The required degree of compaction of the press powder and the pressure required for this were selected empirically. The optimum pressing pressure was 20 MPa (based on the maximum bulk density of the compacts). The samples were dried to an air-dry state, after which clay samples were fired in the range of 1050–1200 °C, steel slag samples – in the range of 950–1300 °C, and their mixtures – in the range of 1050–1200 °C with an interval of 50 °C and time-exposure at the final temperature for 2 h. The calcined samples were cooled together with a furnace in a free mode.

2.3. Experimental Method

The physicochemical and processing properties of the initial refractory clay and steel slag upon heating, the studied mixtures of refractory clay with steel slag and finished products were investigated using physical and chemical methods. These methods include traditional chemical and elemental analyses by an Oxford XSupreme 8000 X-ray fluorescence analyzer. The phase compositions of the specimens were analyzed via an X-ray diffractometer (Shimadzu XRD-7000S) with $CuK\alpha$ radiation ($\lambda K\alpha$ = 0.154186 nm) at 40 kV and 25 mA. The specimens were tested in the angle range of 10–60° (2θ). Moreover, the crystalline phases were identified on the basis of the experimental patterns using the Powder Diffraction File Database of the International Center for Diffraction Data. The microstructures were observed using a scanning electron microscope (Hitachi S-570 and JEOL JSM-840).

Air and fire shrinkage was determined on the tablet samples. Drying shrinkage of samples were measured by controlling of sample length, width, and height before and after drying process. The measurements of water absorption were performed via the Archimedes method. The compressive strength of the fired samples was measured by using cylindrical samples. The reported compressive strength (MPa) is the average of five measurements.

3. Results and Discussion

3.1. Characteristic of Phase Changes during Heating of the Steel Slag Used

The use of steel slag as raw materials for the production of ceramics makes it necessary to study their behavior when heated.

It was revealed that semi-dry pressing samples from steel slag, fired to 1000 °C, are characterized by high porosity, low strength but still retain their integrity. When heated to 1100 °C, the samples are covered with a network of cracks, and, starting from 1150 °C, they completely crumble after cooling into a fine powder (Fig. 4).

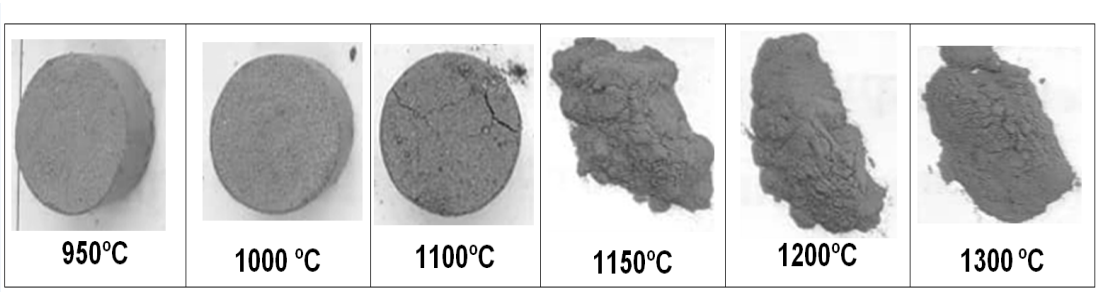

Figure 4. Appearance of molded samples from steel slag, fired at temperatures of 950–1300 °C.

To explain this behavior of the slag when heated, a study was carried out of the phase changes that occur when the slag is heated.

The nature of the ongoing physicochemical processes was considered in two temperature ranges – with low-temperature heating (from 650 to 1000 °C), at which the integrity of the fired samples was maintained (Fig. 5A), and high-temperature heating (from 1100 to 1300 °C), at which the samples completely crumbled (Fig. 5B).

A comparative analysis of X-ray diffraction patterns corresponding to low-temperature heating (Fig. 5A) indicates that heat treatment of metallurgical slag at temperatures up to 1000 °C is accompanied by the following physical and chemical processes leading to a change in the diffraction pattern:

1. Complete dehydration of portlandite, which is manifested in the disappearance in the diffraction pattern of the main reflections of portlandite $Ca(OH)_2$ with interplanar distances d/n – 0.492, 0.316, 0.193, 0.179 nm.
2. The disappearance of reflections at 0.559, 0.297, 0.280 nm at a temperature of 900 °C and the appearance of reflections at 0.255, 0.247, 0.218 nm is due to the process of decomposition of tobermorite $5CaO{\bullet}6SiO_2{\bullet}5H_2O$ with the formation of wollastonite $CaO{\bullet}SiO_2$ and silica [27]:

$$5CaO \cdot 6SiO_2 \cdot 5H_2O \rightarrow 5\left(CaO \cdot SiO_2\right) + SiO_2 + 5H_2O. \quad (1)$$

3. The appearance of X-ray reflections of dicalcium silicate in form γ-$2CaO{\bullet}SiO_2$ (0.289, 0.279, 0.261, 0.244 nm, etc.) occurs due to the partial dehydration of dicalcium hydrosilicate:

$$2CaO \cdot SiO_2 \cdot H_2O \rightarrow 2CaO \cdot SiO_2 + H_2O. \quad (2)$$

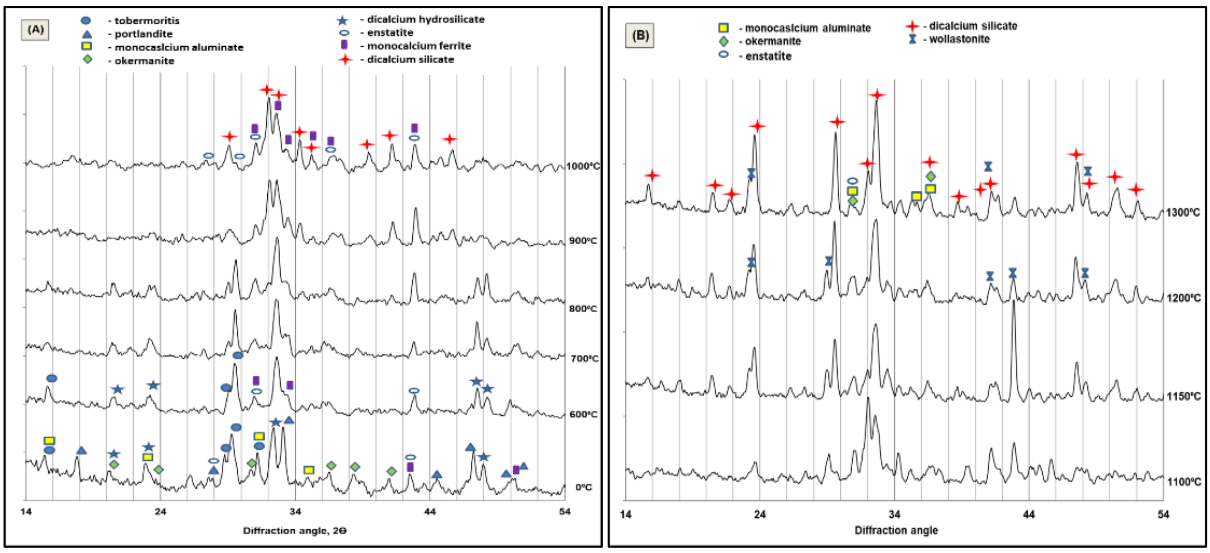

Figure 5. X-ray diffraction patterns of metallurgical slag fired at 600–1000 °C (A) and at 1100–1300 °C (B).

When the firing temperature of pressed samples from the steel slag increases above 1000 °C (Fig. 5B), the diffraction pattern is characterized by:

1. Disappearance of reflections of monocalcium ferrite $CaO{\bullet}Fe_2O_3$ (0.282, 0.267, 0.254 nm, etc.) at temperature of 1200 °C. This is most likely due to the process of its melting:

$$CaO \cdot Fe_2O_3 \rightarrow melt. \quad (3)$$

2. A sharp increase in the intensity of dicalcium silicate reflections is caused by the completion of the dehydration process of dicalcium hydrosilicate:

$$2CaO \cdot SiO_2 \cdot H_2O \rightarrow 2CaO \cdot SiO_2 + H_2O. \quad (4)$$

3. The disappearance of reflections of wollastonite CaO•SiO₂ at a temperature of 1200 °C and a sharp increase in reflections of dicalcium silicate γ–2CaO•SiO₂ is caused by synthesis of dicalcium silicate due to the reaction:

$$CaO \cdot SiO_2 + CaO \rightarrow 2CaO \cdot SiO_2. \quad (5)$$

Changes in the phase composition of the studied slag during low-temperature (up to 1000 °C) and high-temperature heating (from 1000 to 1300 °C) are given in Table 2.

Table 2. Phase composition of the studied slag before firing and fired up to 1000 °C and above 1000 °C.

Phase	Formula	Presence*		
		in the initial steel slag	after firing up to 1000 °C	after firing above 1000 °C
portlandite	$Ca(OH)_2$	+	– $Ca(OH)_2 \rightarrow CaO + H_2O$	–
tobermoritis	$5CaO•6SiO_2•5H_2O$	+	– $5CaO•6SiO_2•5H_2O \rightarrow 5(CaO•SiO_2) + SiO_2 + 5H_2O$	–
dicalcium hydrosilicate	$2CaO•SiO_2•H_2O$	+	– $2CaO•SiO_2•H_2O \rightarrow$ γ-$2CaO•SiO_2 + H_2O$	–
okermanite	$2CaO•MgO•2SiO_2$	+	+	+
monocalcium ferrite	$CaO•Fe_2O_3$	+	+	– $CaO•Fe_2O_3 \rightarrow$ melt
monocalcium aluminate	$CaO•Al_2O_3$	+	+	+
enstatite	$MgO•SiO_2$	+	+	+
wollastonite	$CaO•SiO_2$	–	+	+
dicalcium silicate	γ–$2CaO•SiO_2$	–	+ $2CaO•SiO_2•H_2O \rightarrow$ γ-$2CaO•SiO_2 + H_2O$	+ $CaO•SiO_2 + CaO \rightarrow$ γ-$2CaO•SiO_2$

Thus, after firing at 1300 °C, the crystalline phase of the steel slag is represented by a mixture of okermanite $2CaO•MgO•2SiO_2$, monocalcium aluminate $CaO•Al_2O_3$, enstatite $MgO•SiO_2$, wollastonite $CaO•SiO_2$, and dicalcium silicate γ–$2CaO•SiO_2$, the polymorphism of which, when the molded samples are cooled, causes their complete disintegration (Fig. 4) [28]. Therefore, the use of steel slag to produce ceramic materials is possible only if the destructive effect of dicalcium silicate formed in the steel slag at firing temperatures above 1000 °C is neutralized. This is possible due to the chemical transformation of dicalcium silicate into other calcium-containing minerals that are safe from the point of view of molded sample destruction, such as anorthite, wollastonite, gehlenite, and others that do not have polymorphism.

3.2. Theoretical Substantiation of the Choice of the Studied Compositions "Refractory Clay – Steel Slag"

At the first stage, to predict the processes occurring when heating the studied compositions of metallurgical slag with refractory clay, a theoretical analysis of the behavior of the studied compositions in the $CaO-Al_2O_3-SiO_2$ system was carried out. For this purpose, the chemical compositions of ceramic masses were initially calculated (Table 3).

Table 3. Chemical composition of the investigated mixtures of refractory clay with steel slag.

Mixture code	Content of oxides, %								
	SiO_2	Al_2O_3	Fe_2O_3	TiO_2	MnO	CaO	MgO	K_2O	Na_2O
refractory clay – base, steel slag – additive									
$C_{100}S_0$	57.95	35.50	1.68	1.98	–	1.48	0.77	0.44	0.20
$C_{90}S_{10}$	53.99	32.76	3.74	1.85	0.49	5.00	1.53	0.41	0.23
$C_{80}S_{20}$	50.03	30.02	5.80	1.72	0.98	8.52	2.29	0.37	0.26
$C_{70}S_{30}$	46.06	27.28	7.86	1.60	1.47	12.05	3.05	0.34	0.30
$C_{60}S_{40}$	42.10	24.54	9.92	1.47	1.96	15.57	3.81	0.30	0.33
$C_{50}S_{50}$	38.14	21.80	11.98	1.34	2.45	19.09	4.58	0.27	0.36
steel slag – base, refractory clay – additive									
$S_{100}C_0$	18.33	8.10	22.28	0.70	4.90	36.70	8.38	0.09	0.52
$S_{90}C_{10}$	22.29	10.84	20.22	0.83	4.41	33.18	7.62	0.13	0.49
$S_{80}C_{20}$	26.25	13.58	18.16	0.96	3.92	29.66	6.86	0.16	0.46
$S_{70}C_{30}$	30.22	16.32	16.10	1.08	3.43	26.13	6.10	0.20	0.42
$S_{60}C_{40}$	34.18	19.06	14.04	1.21	2.94	22.61	5.34	0.23	0.39

• here and below, symbol in mixture code corresponds to the type of raw material (C – clay, S – steel slag), number in mixture code – to the content of clay and steel slag, wt.%.

The calculated chemical compositions of the studied compositions indicate that in clay-based compositions with the addition of steel slag, an increase in the steel slag content from 10 to 50 % causes an almost 3–4 times increase in the content CaO (from 5 to 19 %) and Fe_2O_3 (from 3.7 to 12 %) while simultaneously reducing the content of aluminum oxide and silica. In the case of compositions in which steel slag serves as the base and clay as an additive, when the clay content increases from 10 to 40 %, the content of aluminum Al_2O_3 almost doubles (from 10.8 to 21.8 %) and the content of calcium and iron oxides decreases by 2 times (CaO from 33 to 22.6 % and Fe_2O_3 from 20 to 14 %).

Then the multicomponent chemical compositions of the studied mixtures (Table 3) were recalculated to the three-component composition $CaO–Al_2O_3–SiO_2$.

The representative points of the calculated three-component chemical compositions of the studied mixtures were plotted on $CaO–Al_2O_3–SiO_2$ state diagram (Fig. 6)and melting profiles were determined (Fig. 7).

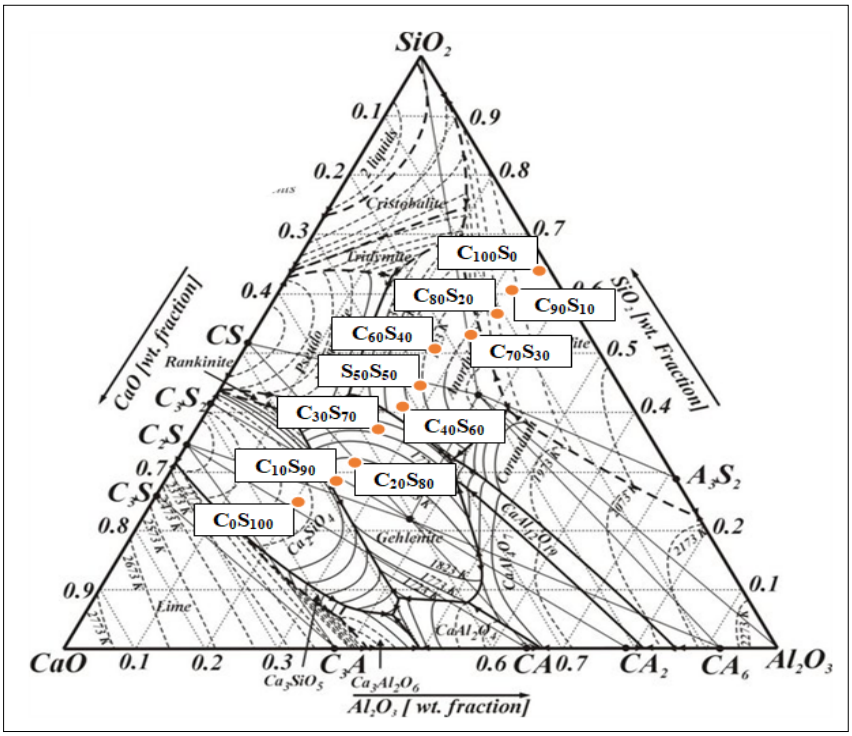

Figure 6. Location of studied compositions of refractory clay with steel slag in $CaO–Al_2O_3–SiO_2$ system.

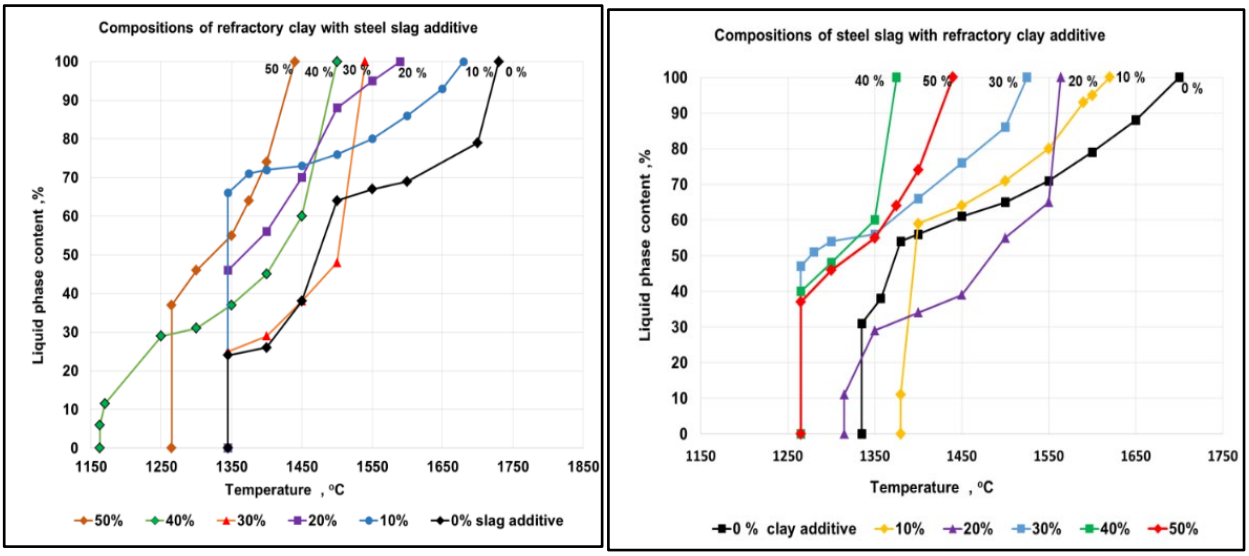

Figure 7. Melting curves of refractory clay with steel slag in $CaO–Al_2O_3–SiO_2$ system.

Table 4. Characteristics of study mixtures in $CaO–Al_2O_3–SiO_2$ system.

Mixture code	Addition %	Oxide content, wt. %			Characteristics of the eutectic phase				Complete melting temperature, °C
		CaO	Al_2O_3	SiO_2	Temperature, °C	Eutectic melt content, %	Crystalline phase content, %		
							content, %	dominant phase	
refractory clay – base, steel slag – addition									
$C_{100}S_0$	0	3.03	36.94	60.03	1345	24	76		1730
$C_{90}S_{10}$	10	8.10	35.68	56.22	1345	66	34	mullite	1680
$C_{80}S_{20}$	20	13.22	34.22	52.37	1345	46	54		1590
$C_{70}S_{30}$	30	18.41	33.12	48.47	1345	25	75		1540
$C_{60}S_{40}$	40	23.63	31.82	44.55	1163	6	94	anorthite	1500
$C_{50}S_{50}$	50	29.14	30.42	40.44	1265	37	63		1440
steel slag – base, refractory clay – addition									
$S_{100}C_0$	0	56.22	23.70	20.08	1335	31	69	calcium disilicate	1700
$S_{90}C_{10}$	10	50.64	25.11	24.25	1380	11	89		1620
$S_{80}C_{20}$	20	45.13	26.48	28.39	1315	11	89	gehlenite	1564
$S_{70}C_{30}$	30	39.66	27.84	32.50	1265	47	53		1525
$S_{60}C_{40}$	40	34.27	29.18	36.55	1265	40	60	anorthite	1375

The characteristics of the resulting melts (Table 4) show that, theoretically, the heating behavior of both steel slag and refractory clay in the initial state is very similar. In particular, the temperature, at which the eutectic melt appears, in the slag when heated is 1335 °C in an amount of 31 %, and in clay – 1345 °C in an amount of 24 %. The steel slag will completely melt at 1700 °C, and the refractory clay at 1730 °C. Thus, it has been theoretically revealed that in all mixtures of "refractory clay – steel slag", in which clay is the main component, additions of steel slag in the amount of 10–50 % (mixtures $C_{90}S_{10}$ – $C_{60}S_{50}$) will activate the sintering process of refractory clay due to sintering the general effect of iron oxide introduced with steel slag (Table 5), with the formation of ceramic materials of predominantly mullite (with 10–30 % slag) and anorthite (40–50 % slag) composition. In "steel slag – refractory clay" compositions, in which steel slag is the basis, the use of refractory clay additives in an amount of 10–40 % (mixtures $S_{90}C_{10}$ – $S_{60}C_{40}$) will reduce not only the temperature of appearance of eutectic melts from 1335 °C (without additives) to 1265 °C (with the addition of clay 30–50 %) but also the temperature of complete melting of these mixtures from 1700 to 1375 °C, transferring them into the category of infusible (with 10–30 % refractory clay) and low-melting (with 40 % refractory clay) ceramic materials gehlenite-anorthite composition.

3.3. Phase Formation, Structure, and Properties of Ceramics Based on "Refractory Clay – Steel slag" Mixtures

It has been established that an increase in the firing temperature from 1050 to 1200 °C of semi-dry pressing samples from refractory clay without additives of the studied slag is accompanied by their sintering with a decrease in the value of water absorption from 21 to 15 % (Fig. 8) and providing compressive strength of up to 55 MPa at 1200 °C.

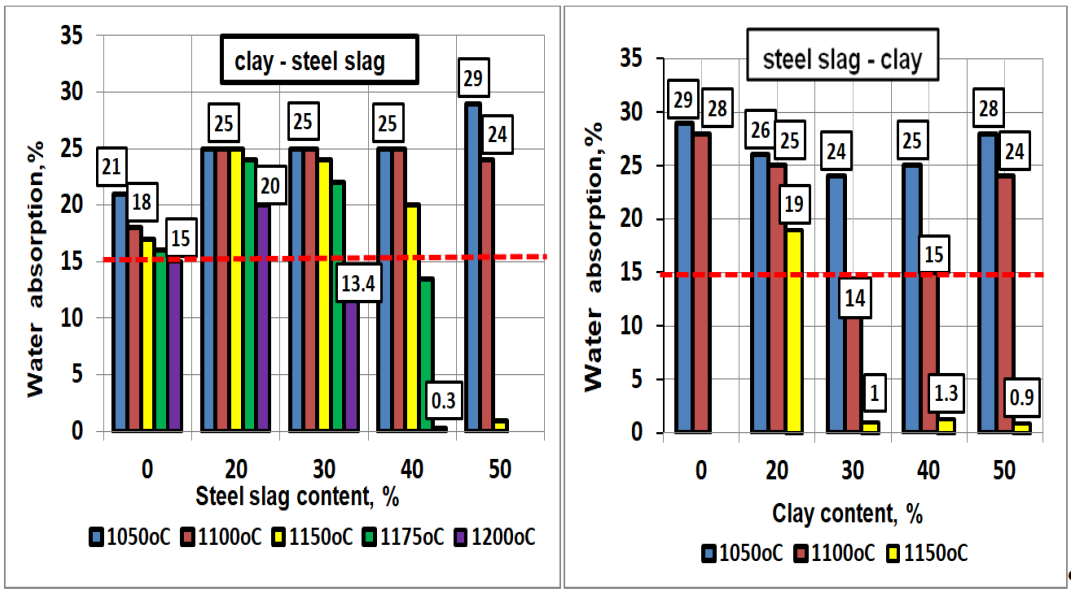

Figure 8. Histogram of changes in water absorption of semi-dry pressing samples from "refractory clay – steel slag" compositions, fired at 1050–1200 °C.

Adding 20 % steel slag to refractory clay leads to a sharp increase in water absorption (up to 25 %) over the entire temperature range. Increasing the content of steel slag additive to 30 % ensures sintering of samples at a temperature of 1200 °C with a density (in terms of water absorption) comparable to the density of clay samples without additive (13.4 and 15 %, respectively) but with almost 2 times greater compressive strength (97 MPa and 55 MPa respectively). A further increase in the amount of steel slag addition from 30 to 40–50 % leads to a sharp activation of the sintering process of the samples, providing a densely sintered state (with water absorption less than 1 %) at 1150 °C (with the addition of 50 % steel slag) – 1200 °C (with the addition of 40 % steel slag). In the case of steel slag compositions with refractory clay additives, as predicted theoretically, clay additives in the entire range of used contents (from 20 to 40 %) and used firing temperatures (1050–1150 °C) not only eliminate the phenomenon of self-disintegration of samples from the original steel slag (for due to synthesis during firing of dicalcium silicate) but also have a sintering-hardening effect, ensuring the formation of densely sintered structures with water absorption of less than 1 % (Fig. 8) and compressive strength from 26 to 56 MPa already at 1150 °C. However, with relatively good strength, all these samples from steel slag compositions with clay additives are deformed at 1150 °C in form of sample center failure from the side of the base in contact with the substrate during firing.

An explanation for these changes should be sought in the study of the physicochemical processes that occur during the firing of these compositions.

The X-ray method made it possible to evaluate changes in the main minerals of the studied refractory clay with the addition of steel slag (Fig. 9) and steel slag with the addition of refractory clay (Fig. 10) in the heating temperature range of 1050–1150 °C.

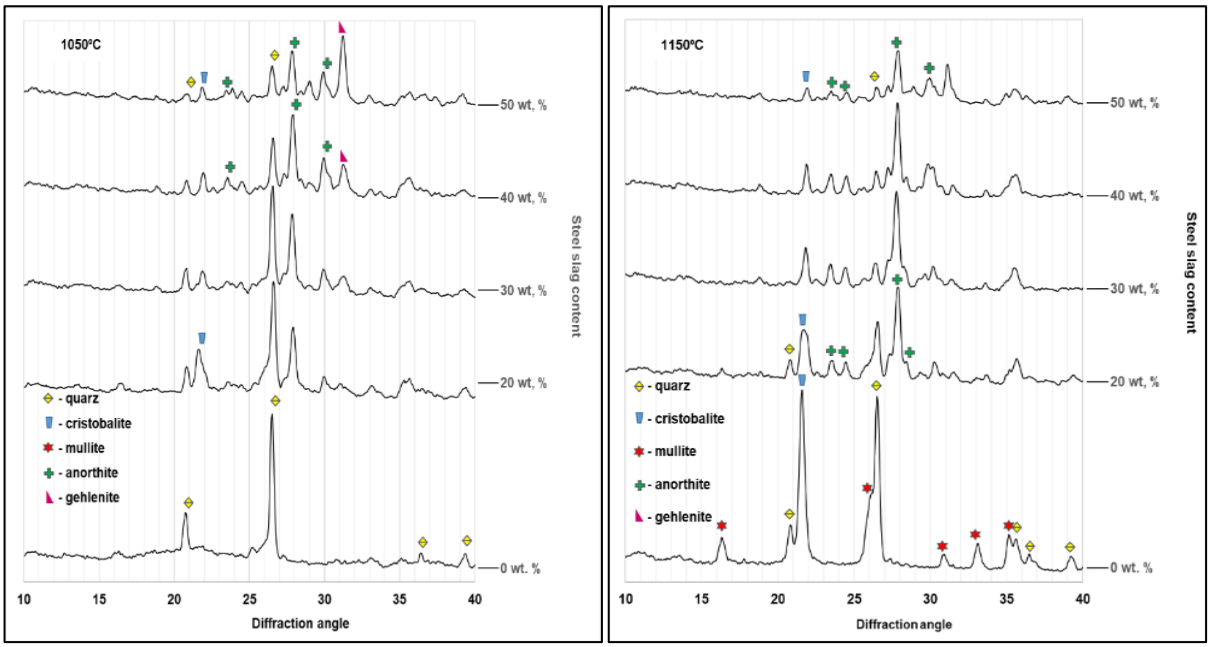

Figure 9. X-ray diffraction patterns of fireclay compositions with steel slag additives at temperatures of 1050 and 1150 °C.

In the case of compositions, in which the base is refractory clay, and steel slag is used as an additive, it was found that even at the minimum of the steel slag contents used (20 wt. %), starting from 1050 °C, in addition to quartz reflections (impurities in clay), cristobalite, and mullite (formed during the thermal dissociation of kaolinite), the presence of anorthite reflections is also recorded.

The preservation of molded samples integrity from all studied mixtures of refractory clay with steel slag additives, as well as the absence of dicalcium silicate reflections in the X-ray diffraction patterns indicates that the formation of anorthite occurs due to the reaction between kaolinite and dicalcium silicate:

$$5\left(Al_2O_3 \cdot 2SiO_2 \cdot 2H_2O\right) + 2CaO \cdot SiO_2 \rightarrow$$
$$\rightarrow \underset{\text{mullite}}{3Al_2O_3 \cdot 2SiO_2} + \underset{\text{anorthite}}{2\left(CaO \cdot Al_2O_3 \cdot 2SiO_2\right)} + \underset{\text{cristobalite}}{5SiO_2} + 10H_2O. \quad (6)$$

An increase in the steel slag content to 30 % at a temperature of 1050 °C is accompanied by a decrease in the intensity of reflections of quartz, cristobalite (due to the presence of clay as a base in the mixture), an increase in the reflections of anorthite, and the appearance of gehlenite reflections:

$$4\left(Al_2O_3 \cdot 2SiO_2 \cdot 2H_2O\right) + 2CaO \cdot SiO_2 \rightarrow$$
$$\rightarrow \underset{\text{mullite}}{3Al_2O_3 \cdot 2SiO_2} + \underset{\text{gehlenite}}{2CaO \cdot Al_2O_3 \cdot 2SiO_2} + \underset{\text{cristobalite}}{5SiO_2} + 8H_2O. \quad (7)$$

With a further increase in the content of the introduced steel slag to the refractory clay to 40–50 %, mullite reflexes disappear, the intensity of gehlenite reflexes increases, which leads to the ratio of the intensity of the anorthite and gehlenite reflections changes in favor of gehlenite:

$$Al_2O_3 \cdot 2SiO_2 \cdot 2H_2O + 2CaO \cdot SiO_2 \rightarrow \underset{\text{gehlenite}}{2CaO \cdot Al_2O_3 \cdot 2SiO_2} + \underset{\text{cristobalite}}{5SiO_2} + 8H_2O. \quad (8)$$

Increasing the firing temperature of samples to 1100 and 1150 °C practically does not change the sequence of phase formation processes in the “refractory clay – steel slag” compositions. And only at a temperature of 1175–1200 °C, when the mixture contains steel slag in an amount of 30–40 % in a mixture with refractory clay, ceramics of an almost anorthite composition is formed.

In the compositions “steel slag – refractory clay” at all applied heating temperatures (from 1050 to 1150 °C) with steel slag (Fig. 10) additive in an amount of 20–30 %, the first synthesized phase is gehlenite formed by reaction (8), and intensity the reflexes of which increase with increasing temperature to 1150 °C.

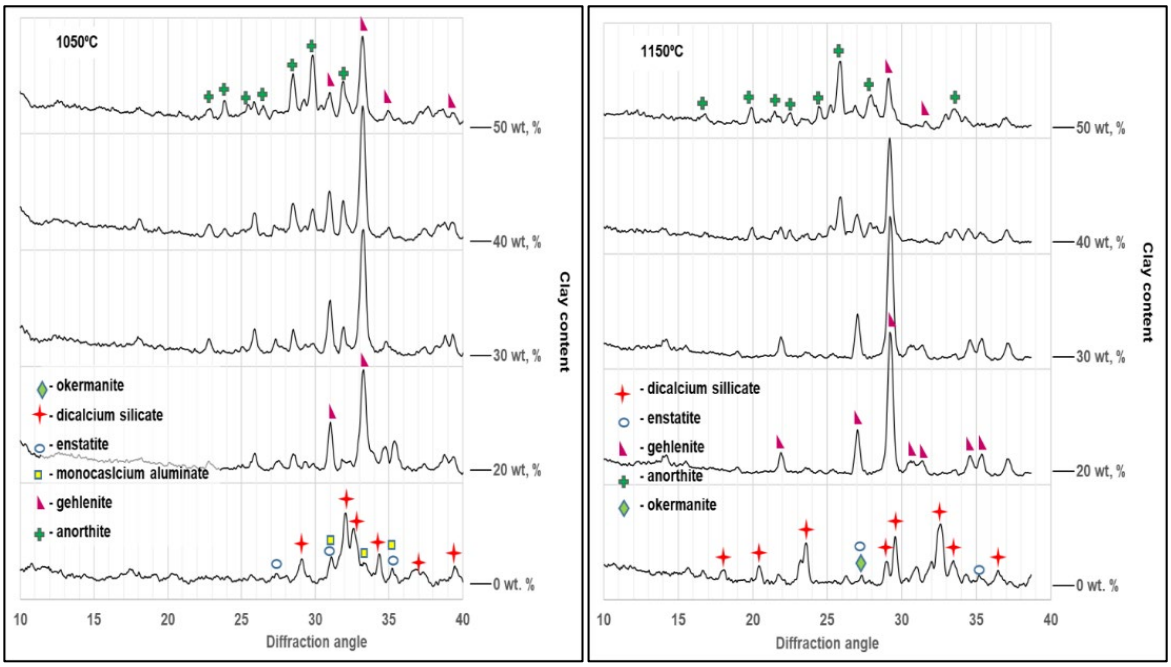

Figure 10. X-ray diffraction patterns of a mixture of steel slag with the refractory clay addition, fired at temperatures of 1050 and 1150 °C.

An increase in the clay additive content from 30 to 40 % causes the synthesis of the second crystalline phase – anorthite throughout the entire range of firing temperatures used. With the addition of 50 % refractory clay, anorthite reflexes increase and the intensity of gehlenite reflexes decreases, especially at 1150 °C. Thus, when adding of refractory clay to the steel slag in an amount of 20–30 % at temperatures of 1050–1150 °C, gehlenite ceramics are formed, when adding of clay in the amount of 40–50 %, ceramics of anorthite-gehlenite composition are formed. The studies carried out make it possible to determine the optimal compositions and technological regimes for obtaining of ceramics based on the studied raw materials (Table 5).

Table 5. Optimum compositions, technological parameters and properties of ceramics based on refractory clay with steel slag.

Composition code	Component composition, %		Firing temperature, °C	Ceramic properties			Type of ceramics
	clay	slag		shrinkage %	water absorption, %	compressive strength, MPa	
clay without steel slag							
$C_{100}S_0$	100	0	1200	10.6	14.2	55.8	mullite-siliceous
clay with steel slag							
$C_{70}S_{30}$	70	30	1200	8.9	13.4	97.2	anorthite
$C_{60}S_{40}$	60	40	1175	8.0	6.3	205.9	anorthite
			1200	13.0	2.8	215.5	

It has been established that the mechanical strength of samples with anorthite crystalline phase (with the addition of 30 % steel slag) is 1.7 times greater than with a mullite crystalline phase (without additive) with almost the same degree of sintering. The strengthening effect of the anorthite crystalline phase on the mechanical properties of building ceramics was previously noted in [29, 30].

Thus, compositions of refractory clay with additions of steel slag from 30 to 40 % at a firing temperature of 1175–1200 °C form ceramic structures with anorthite crystalline phase and compressive strength 1.7–2.8 times higher than the strength of samples from the studied clay without additives (97–215 MPa and 56 MPa, respectively).

Electron microscopy made it possible to evaluate the structure of the fired samples. In particular, electron microscopic images of cleavage of semi-dry pressing samples from the studied clay without the addition of steel slag, fired at 1200 °C (Fig. 11A), as well as samples from a mixture of the studied steel slag with the addition of 40 % refractory clay $S_{60}C_{40}$, fired at 1150 °C (Fig. 11B) show that the samples in

both cases at the fracture represent a loosely sintered material, the microstructure of which is represented by individual fine-porous aggregates, separated from each other by deep tortuous pores.

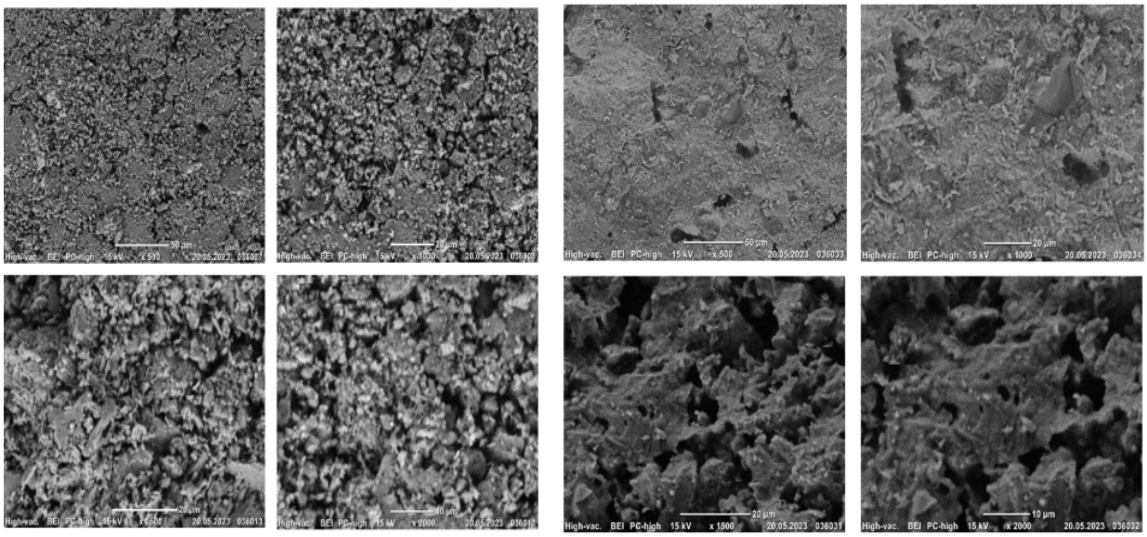

A B

Figure 11. Electron micrographs of cleavage of semi-dry pressed samples made of clay without steel slag (A), fired at 1200 °C, and from a mixture of steel slag with 40 % clay (B), fired at 1150 °C.

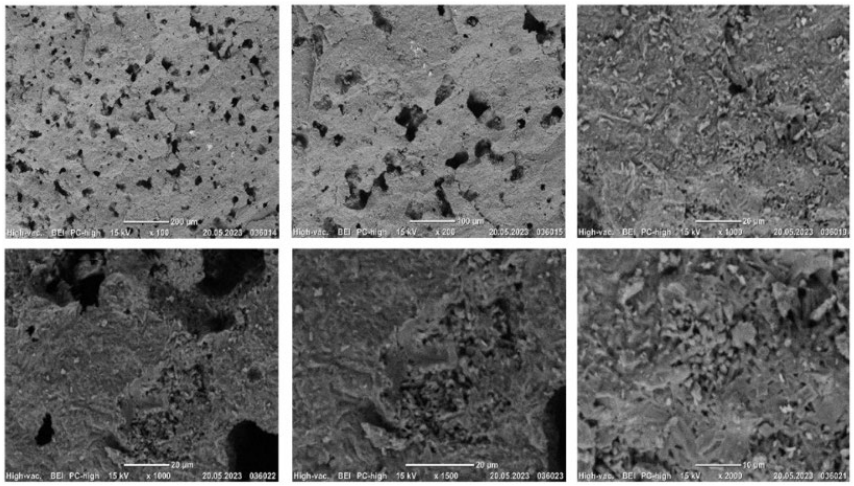

Figure 12. Electron micrographs of cleavage of semi-dry pressing samples from a mixture of refractory clay with the addition of 40 % steel slag ($C_{60}S_{40}$), fired at 1200 °C.

The introduction of a 40 % steel slag additive into the composition of the refractory clay used (composition $C_{60}S_{40}$) activates the process of liquid-phase sintering of the samples, which leads to the formation of a monolithic structure with separated internal pores, in shape approaching spherical, with a diameter of up to 20–25 microns (Fig. 12).

4. Conclusions

1. Steel slag in terms of chemical composition is represented mainly by oxides of calcium (35.33 %), iron (21.45 %), silicon (17.62 %), and aluminum (7.80 %), the sum of which is more than 80 %. In terms of mineralogical composition, it is composed of portlandite $Ca(OH)_2$, silicates, and hydrated silicates of calcium and magnesium (enstatite $MgO•SiO_2$, okermanite $2CaO•MgO•2SiO_2$, tobermorite $5CaO•6SiO_2•5H_2O$ and dicalcium hydrosilicate $2CaO•SiO_2•H_2O$), aluminates and calcium ferrites (monocalcium aluminate $CaO•Al_2O_3$, monocalcium ferrite $CaO•Fe_2O_3$).
2. The crystalline component of steel slag after heating in the temperature range of 1100–1300 °C is represented by a mixture of okermanite $2CaO•MgO•2SiO_2$, monocalcium aluminate $CaO•Al_2O_3$, enstatite $MgO•SiO_2$, and dicalcium silicate γ–$2CaO•SiO_2$ polymorphism, which causes complete destruction of the molded samples after cooling.

3. The use of steel slag to produce ceramic materials is possible only by neutralizing the destructive effect of dicalcium silicate formed in steel slag at firing temperatures above 1000 °C, converting it into other calcium-containing minerals without destroying molded products.

4. Compositions of refractory clay with additions of steel slag from 30 to 40 % at a firing temperature of 1175–1200 °C form ceramic structures with water absorption from 2.8 to 13.4 %, with a compressive strength of 1.7–2.8 times the strength samples from the studied clay without additives (97–215 MPa and 56 MPa, respectively), which determines their prospects for producing high-strength anorthite ceramics for a wide range of purposes.

References

1. Ezerskiy, B.A. Clinker. Technology and properties. Stroitel'nye Materialy [Construction Materials]. 2011. Pp. 79–81.
2. Ezerskiy, V.A. Quantitative assessment of the color of ceramic face products. Stroitel'nye materialy [Construction Materials]. 2015. 8. Pp. 76–80. DOI: 10.31659/0585-430X-2015-728-8-76-80
3. Crespo-López, L., Cultrone, G. Improvement in the petrophysical properties of solid bricks by adding household glass waste. Journal of Building Engineering. 2022. 8. Article no. 105039. DOI: 10.1016/j.jobe.2022.105039
4. Vakalova, T.V., Revva, I.B. Highly porous building ceramics based on «clay-ash microspheres» and «zeolite-ash microspheres» mixtures. Construction and Building Materials. 2022. 317. Article no. 125922. DOI: 10.1016/j.conbuildmat.2021.125922
5. Shi, C. Steel slag – its production, processing, characteristics, and cementitious properties. Journal of Materials in Civil Engineering. 2004. 16(3). 230–236. DOI: 10.1061/(ASCE)0899-1561(2004)16:3(230)
6. Sun, P., Guo, Z. Preparation of steel slag porous sound-absorbing material using coal powder as pore former. Journal of Environmental Sciences. 2015. 36. Pp. 67–75. DOI: 10.1016/j.jes.2015.04.010
7. Wang Q., Yan, P., Feng, J. A discussion on improving hydration activity of steel slag by altering its mineral compositions. Journal of Hazardous Materials. 2011. 186(2–3). Pp. 1070–1075. DOI: 10.1016/j.jhazmat.2010.11.109
8. Shi, C., Qian, J. High performance cementing materials from industrial stags – a review. Re-sources, Conservation and Recycling. 2000. 29(3). Pp. 195–207. DOI: 10.1016/S0921-3449(99)00060-9
9. Tüfekçi, M., Demirbaş, E.A., Genç, H. Evaluation of steel furnace slags as cement additives. Cement and Concrete Research. 1997. 27(11). Pp. 1713–1717. DOI: 10.1016/S0008-8846(97)00158-0
10. Kourounis, S., Tsivilis, S., Tsakiridis, P.E., Papadimitriou, G.D., Tsibouki, Z. Properties and hydration of blended cements with steelmaking slag. Cement and Concrete Research. 2007. 37(6). Pp. 815–822. DOI: 10.1016/j.cemconres.2007.03.008
11. Beshr, H., Almusallam, A.A., Maslehuddin, M. Effect of coarse aggregate quality on the mechanical properties of high strength concrete. Construction and Building Materials. 2003. 17(2). Pp. 97–102. DOI: 10.1016/S0950-0618(02)00097-1
12. Wu, Z., Feng, Z., Pu, S., Zeng, C., Zhao, Y., Chen, C., Song. H., Feng, X. Mechanical properties and environmental characteristics of the synergistic preparation of cementitious materials using electrolytic manganese residue, steel slag, and blast furnace slag. Construction and Building Materials. 2024. 411. Article no. 134480 DOI: 10.1016/j.conbuildmat.2023.134480
13. Gu, X., Wang, H., Liu, J., Zhu, Z., Wang, S., Xu, X. Synergistic effects of steel slag and metakaolin in cementitious systems: Packing properties, strength, and microstructure. Construction and Building Materials. 2024. 411. Article no. 134395. DOI: 10.1016/j.conbuildmat.2023.134395
14. Chen, G., Wang, S. Research on macro-microscopic mechanical evolution mechanism of cement-stabilized steel slag. Journal of Building Engineering. 2023. 75. Article no. 107047. DOI: 10.1016/j.jobe.2023.107047
15. Aliyah, F., Kambali, I., Setiawan, A.F., Radzi, Y.M., Rahman, A.A. Utilization of steel slag from industrial waste for ionizing radiation shielding concrete: A systematic review. Construction and Building Materials. 2023. 382. Article no. 131360. DOI: 10.1016/j.conbuildmat.2023.131360
16. Luo, T., Wang, X., Zhuang, S. Value-added utilization of steel slag as a hydration heat con-trolling material to prepare sustainable and green mass concrete. Case Studies in Construction Materials. 2023. 19. Article no. e02619. DOI: 10.1016/j.cscm.2023.e02619
17. Liu, L., Liu, J., Liu, T., Zhang, Y., Liang, H., Ning, T., Lin, X., Bai, Z., Lu, A. Preparation, crystallization kinetics and stabilization behavior of the heavy metal ions of all-solid waste-based glass-ceramics from steel slag and coal gangue. Journal of Non-Crystalline Solids. 2022. 592. Article no. 121750. DOI: 10.1016/j.jnoncrysol.2022.121750
18. Deng, L., Yun, F., Jia, R., Li, H., Jia, X., Shi, Y., Zhang, X. Effect of SiO_2/MgO ratio on the crystallization behavior, structure, and properties of wollastonite-augite glass-ceramics derived from stain-less steel slag. Materials Chemistry and Physics. 2020. 239. Article no. 122039. DOI: 10.1016/j.matchemphys.2019.122039
19. Luo, Z., He, F., Zhang, W., Xiao, Y., Xie, J., Sun, R., Xie, M. Effects of fluoride content on structure and properties of steel slag glass-ceramics. Materials Chemistry and Physics. 2020. 242. Article no. 122531. DOI: 10.1016/j.matchemphys.2019.122531
20. 20. Pioro, L.S., Pioro, I.L. Reprocessing of metallurgical slag into materials for the building industry. Waste Management. 2004. 24(4). Pp.371–379. DOI: 10.1016/S0956-053X(03)00071-0
21. Zong, Y., Chen, W., Fan, Y., Yang, T., Liu, Z., Cang, D. Complementation in the composition of steel slag and red mud for preparation of novel ceramics. International Journal of Minerals, Metallurgy and Materials. 2018. 25(9). Pp. 1010–1017. DOI: 10.1007/s12613-018-1651-2
22. Bantsis, G., Sikalidis, C., Betsiou, M., Yioultsis, T., Bourliva, A. Ceramic building materials for electromagnetic interference shielding using metallurgical slags. Advances in Applied Ceramics. 2011. 110(4). Pp. 233–237. DOI: 10.1179/1743676111Y.0000000009
23. El-Mahllawy, M.S. Characteristics of acid resisting bricks made from quarry residues and waste steel slag. Construction and Building Materials. 2008. 22(8). Pp. 1887–1896. DOI: 10.1016/j.conbuildmat.2007.04.007
24. Rahou, H., Rezqi, M., Ouahabi, N., Fagel. Characterization of Moroccan steel slag waste: The potential green resource for ceramic production. Construction and Building Materials. 2022. 314(B). Article no. 125663. DOI: 10.1016/j.conbuildmat.2021.125663

25. Karayannis, V.G., Moutsatsou, A.K., Baklavaridis, A.N., Katsika, E.L., Domopoulou, A.E. Synergistic Sintering of Lignite Fly Ash and Steelmaking Residues towards Sustainable Compacted Ceramics. Advances in Materials Science and Engineering. 2017. Article no. 1735268. DOI: 10.1155/2017/1735268
26. Teo, P.T., Anasyida, A.S., Kho, C.M., Nurulakmal, M.S. Recycling of Malaysia's EAF steel slag waste as novel fluxing agent in green ceramic tile production: Sintering mechanism and leaching assessment. Journal of Cleaner Production. 2019. 241. Article no. 118144 DOI: 10.1016/j.jclepro.2019.118144
27. Cao, P., Xing, L., Luo, J., Jiang, H., Zhang, X., Li, G. Preparation of calcium silicate board from to-bermorite-rich residue for energy conservation in buildings. Construction and Building Materials. 2023. 407. Article no. 133547. DOI: 10.1016/j.conbuildmat.2023.133547
28. Wesselsky, A., Jensen, O.M. Synthesis of pure Portland cement phases Cement and Concrete Re-search. 2009. 39(11). Pp. 973–980. DOI: 10.1016/j.cemconres.2009.07.013
29. Vakalova, T.V., Sergeev, N.P., Tolegenov, D.T., Tolegenova, D.Zh. High-strength building ceramics based on fly ash – red mud mixtures. Magazine of Civil Engineering. 2023. 121(5). Article no. 12104. DOI: 10.34910/MCE.121.4
30. Shakhov, S.A. Structural and phase features of ceramics from loam and incinerated sewage sludge ash. Magazine of Civil Engineering. 2023. 121(5). Article no. 12110. DOI: 10.34910/MCE.121.10

Information about the authors:

***Tatiana Vakalova**, Doctor of Technical Sciences*
ORCID: https://orcid.org/0000-0002-1756-3526
E-mail: tvv@tpu.ru

***Nikolay Sergeev**,*
ORCID: https://orcid.org/0000-0002-7656-5628
E-mail: axioma-13@yandex.ru

***Dias Tolegenov**,*
ORCID: https://orcid.org/0000-0001-8242-0655
E-mail: www.dika-92@mail.ru

***Inna Revva**, PhD in Technical Sciences*
ORCID: https://orcid.org/0000-0003-4184-1554
E-mail: revva@tpu.ru

Received 17.02.2024. Approved after reviewing 06.09.2025. Accepted 07.09.2025.

Magazine of Civil Engineering

ISSN 2712-8172

journal homepage: http://engstroy.spbstu.ru/

Research article

UDC 624

DOI: 10.34910/MCE.138.4

Mechanical and durability properties of stabilized river drudged sediments

H.M. Mohammed ✉ **, *N.S. Mahmood***

University of Anbar, Ramadi, Al Anbar, Iraq

✉ *hus22e1009@uoanbar.edu.iq*

Keywords: dredged sediments, cement stabilization, polypropylene fiber, soil durability

Abstract. Large volumes of sediments are being drudged from the Euphrates River to maintain the stream of the river. These sediments are classified as loose sand with poor engineering properties such as poor grain size distribution, poor compaction, high permeability, and low shear strength. Therefore, these sediments need to be stabilized in order to be utilized as an available and cost-effective engineered fill. In this research, cement by 4, 6, and 8 % was used to improve the strength and durability properties of loose sand sediments dredged from the Euphrates River. Additionally, polypropylene fibers were added by 0.5 % to the cement-treated specimens. A series of laboratory tests were performed to evaluate the unconfined compressive strength and wetting-drying properties of the prepared specimens that were cured to 7 and 28 days. The results showed that adding cement led to improve the compaction process of the cement-treated soil. Furthermore, adding cement by 8 % produced an unconfined compressive strength value as high as 2000 kN/m^2. Furthermore, when the polypropylene fibers were added, the strength was further increased by 52 %. The results also showed that treatment with cement caused a significant improvement in the resistance to wetting and drying cycles, as the treated specimens passed the test with loss in weight ranging from 16 to 39 % compared to the untreated specimens that collapsed in the first cycle of the test. As discussed herein, the improved sand may provide a valuable source of engineered fill that can be used for many projects such as dams, levees, and road ways.

Citation: Mohammed, H.M., Mahmood, N.S. Mechanical and durability properties of stabilized river drudged sediments. Magazine of Civil Engineering. 2025. 18(6). Article no. 13804. DOI: 10.34910/MCE.138.4

1. Introduction

Sediment materials carried by rivers are a crucial part of the erosion and removal of the Earth land surface due to river processes. The movement of material from land to water bodies also has a significant impact on global geochemical cycling [1, 2]. Human activity has significantly affected these natural processes, leading to faster erosion due to changes in land utilization and disruption of the transport of sediment from land to water because of storing vast amounts of material behind dams [3–6]. The movement of sediments from river basins and its transportation by river streams may cause numerous challenges including the reduction of soil resources and the accumulation of sediment in waterways for humanity [7]. The rapid global expansion of international trade and business, as well as the need for deeper navigation channels to accommodate the increasing size of contemporary ships [8]. To preserve or improve their economic competitiveness, ports, harbors, and rivers have to expand the depth of their fairways. Dredging is the process of excavating and extracting silt and rocks from the bed of channels, lagoons, rivers, and other bodies of water with the purpose of increasing the depth and width of these navigation routes. Dredging may also be utilized for the purpose of rehabilitating environmentally affected areas. Dredging is a long-standing method for handling vast amounts of sediments, whereas the quality management of these sediments is a relatively recent concern [9]. The management and control of sediments are now recognized

as crucial environmental concerns for the sustainable use of the available resources [10, 11]. In recent years, the necessity of managing dredging operations and evaluating their economic, social, and environmental impacts caused by polluted sediments has grown significantly in both developing and industrialized nations [12].

According to the directorate of water resources of Al-Anbar Governorate, an estimated volume of 1.5 million cubic meters is being drudged annually from the Euphrates River within the Governorate that costs more than 1.3 billion Iraqi Dinar [13]. As for the engineering aspect, loose sand sediments are usually not suitable for civil engineering constructions because of the poor grain size distribution that cause poor compaction and strength characteristics [12]. Therefore, these sediments need to be stabilized for the purpose of improving the engineering properties by many methods such as adding cement to reduce the high permeability and compressibility and increase cohesion and shear strength for the sediments [14, 15].

Soil stabilization is a controlled technique that improves the soil by incorporating chemicals, allowing it to be used as a foundation or sub-base for roads to withstand the anticipated traffic and pavement stresses [16]. Various techniques are frequently utilized to stabilize soils. There are two approaches to enhance the characteristics of sandy soils [17, 18]. The first technique is mechanical stabilization, which involves mixing the natural soil with a stabilizing material to create a uniform mixture [19]. The second technique is to introduce a stabilizing material into undisturbed soils, allowing it to permeate through the empty spaces in the soil and interact with it [20, 21]. Chemical stabilization involves modifying the qualities of locally accessible soil to enhance its strength and durability. The two most often utilized chemical stabilization procedures are lime and cement stabilization [22]. Portland cement is widely recognized as a material binder for soil stabilization. It is used because it is widely available, easy to use, cheap in price, and has a high bonding ability and various uses. Soil-cement is a mixture of soil, cement, and water that is thoroughly compacted. It is widely used to enhance the soil foundation for dams, dykes, parking areas, and roads on a significant scale. On the other hand, cement-stabilized soils could exhibit notable brittleness property. This can lead to the occurrence of brittle fractures and cracks in subgrade or pavement layers once they are exposed to high lateral earth pressure, seismic loads, or substantial horizontal displacements [23]. When cement is added to the soil, it enters the voids and reduces them, when water is added to mixture, a chemical reaction occurs that causes harden cement, this increasing the density of mixture and reducing permeability.

Soil strengthening involves using natural or synthetic fibers to enhance the mechanical properties, such as strength and load-bearing capacity, of soil. Occasionally, the enhancement of mechanical properties is accomplished by strategically positioning the fibers in key areas within the soil mass [24, 25]. The presence of randomly dispersed fibers in the clay soil leads to enhancements in the flexural toughness, strain in a split test, ductility, and peak compressive strength. The presence of fibers greatly alters the failure process by inhibiting the development of tension fractures. Since the 1970s, researchers have examined the mechanical properties of this type of soil reinforcement by performing relevant studies [26]. Polypropylene fiber (PPF) was a type of synthetic fiber derived from the polymerization of propylene, a linear polymer. There are several benefits to consider, including its lightweight nature, compressive strength, exceptional toughness, and resistance to corrosion [27]. The PPF is commonly utilized with concrete, which is known for its drawbacks such as limited crack resistance, vulnerability to deformation, and relatively low tensile strength [28]. Using of both chemical stabilization and reinforcement with fibers may provide dual advantages by enhancing the mechanical characteristics of soil, such as increased strength and improved ductility. The work of [29] investigated the feasibility of incorporating fibers into cement to enhance the mechanical characteristics of collapsible soil and thereby enhance the behavior of cement-treated soil. A study conducted by [30] used a blend of steel fiber (SF) and cement to improve drudged sediments. The findings demonstrated that augmenting the amount of cement or reducing the amount of water had a substantial positive impact on the compressive strength and exacerbated the fragility of the treated soil.

Improving the engineering properties of sediments will provide a valuable source of engineered fill that can be used for many projects such as dams, levees and road ways. Many previous studies have used cement to stabilize various types of weak and problematic soils. Cement has been proven to be a good stabilizing material. In this research, cement and PPFs were used to improve the strength and durability properties of loose sand sediments dredged from the Euphrates River. Specifically, the unconfined compressive strength and wetting-drying characteristics were evaluated thorough a laboratory testing program.

2. Materials and Methods

2.1. Materials

The sediment materials were collected from Euphrates River bank in the center of Al-Ramadi city, west of Iraq. This location was considered as significant amount of sediments materials are being drudged on the daily base. The particle size distribution and soil properties are shown in Fig. 1 and Table 1. The chemical tests were conducted according to the British Standards (BS 1990-part3) [31].The soil is classified as poorly graded sand (SP) according to the Unified Soil Classification System (USCS) per the ASTM D2487-17 [32]. The soil is not suitable as engineered fill, according to the Iraqi Standard Specifications for Roads and Bridges (SORB/R6) [33].

Table1. Soil properties.

Property	Value
Maximum dry density (MDD), g/cm^3	1.58
Optimum moisture content (OMC), %	10.52
SO_3	0.013
Total dissolved salts, %	0.029
Total soluble salts, %	0.613
Specific Gravity (G_S)	2.67
Soil type	SP

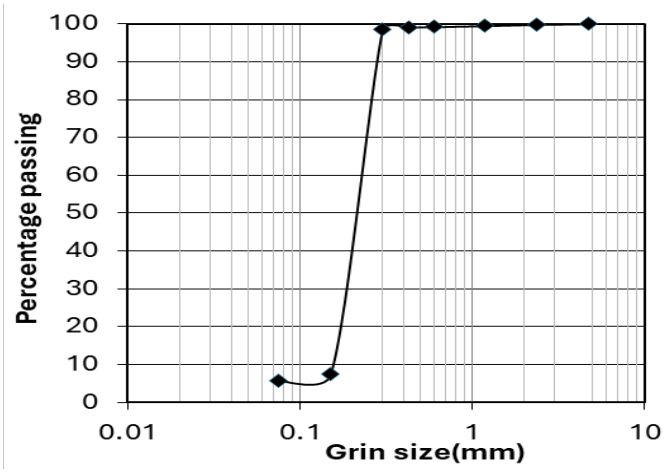

Figure 1. Grain size distribution curve for sediments.

Ordinary Portland Cement (OPC) was used for improvement in this study. The chemical and mechanical tests on the cement were conducted by the Construction Materials Laboratory at the University of Anbar. The physical and chemical properties of the used cement are listed in Tables 2 and 3, respectively. These properties were compared to the requirements of the Iraqi specifications for OPC (IQ. S No.5/1984) [34].

Table 2. Physical and mechanical properties of the OPC.

Property		Test results	IQ. S No. 5/1984
Initial setting time, min		190	≥ 45 min
Final setting time, min		315	≤ 600 min
Fineness, m^2/kg		303	≥ 250 m^2/kg
Compressive strength, MPa	3 days	23	≥ 15 MPa
	7 days	29	≥ 23 MPa

Table 3. Chemical composition of the OPC.

SiO_2	CaO	Al_2O_3	Fe_2O_3	SO_3	MgO	L.O.I	I.R
19.43	61.34	4.62	5.35	2.28	4.36	3.21	0.96

PPF material, as shown in Fig. 2, used in this study to decrease deformation by increasing the tension resistance. The PPF is Sika fiber PPM-12 with the properties as listed in Table 4.

Table 4. The PPF properties.

Property	Description
Composition	100 % polypropylene
Appearance / Color	Transparent fibers
Density	~0,91 g/cm^3
Diameter	32 μm
Length	12 mm
Melting point	~160 °C
Specific tensile strength	~30 cN/tex

Figure 2. Photograph of polypropylene discrete fiber (12 mm).

2.2. Compaction Test

The purpose of this laboratory examination is to establish the relationship between the amount of moisture and the soil dry density under a particular compaction energy. The term "compaction energy" refers to the quantity of mechanical energy, which is exerted on a given soil mass. The standard Proctor test was used to compact the specimens. The ASTM D689 [35]outlines the standard testing procedures for determining the laboratory compaction properties of soil by employing a standard effort.

2.3. Unconfined Compression Strength (UCS)

For cohesive soils, the UCS test measures shear strength. The test performed without applying confining pressure, making it a simple and fast testing method. The experiment was carried on 12 selected specimens prepared from the soil before and after treatment. The UCS values for the prepared samples were obtained using the standard approach outlined in ASTMD2166 [36].

2.4. Specimen Preparation and Curing

The specimens used for the UCS tests were compacted under the predetermined MDD and OMC. The first set of specimens was produced by adding cement in three percentages of (4, 6, and 8 by weight of dry soil). These specimens were tested after 7 and 28 days of curing. Other set of specimens was treated by adding 0.5 % of PPF in addition to the specified cement proportions. The UCS specimen had to be two to three and a half times its diameter to meet the requirements of the test. Samples were compacted using the split compaction mold and a hammer. The mold had a diameter of 63 mm and a height of 128 mm. The soil in this mold was placed in three layers, with each layer receiving 11 blows for compaction. The number of layers and blows were calculated to accomplish the same standard compaction effort (600 kN.m/m^3) as the conventional Proctor test, as presented in Equation 1.

$$\text{Energy } E = \left(\begin{matrix}\text{number of blow} \\ \text{per layer}\end{matrix}\right)\times\left(\text{number of layer}\right)\times\left(\text{weight of hammer}\right)\times\left(\text{height of drop}\right) = \frac{}{\text{volume of mold}}. \quad (1)$$

Soil specimens that had been treated were sealed with a nylon tape and stored at plastic bags for keep them wet until testing, whereas those that had not undergone treatment were tested immediately upon compaction. At a temperature of 25±2 °C, the specimens were left to cure for 7 and 28 days, respectively.

2.5. Durability Test

A durability test aim to observation a performance of the sediment materials with different cement ratios. The test was carried out, as per ASTM D599 [36], on both untreated soil and treated soil with different cement ratios of 4, 6, and 8 %. Two specimens were prepared using the same mold as for the UCS test. One specimen was used to determine the weight loss and the other to determine the volume change. The specimens were initially cured at room temperature 25±2 °C for 7 and 28 days. Weight loss and volume change were recorded after each wet-dry cycle that the treated specimens underwent. The first step of the cycle was to soak the samples in water for five hours. After that, they were taken out of the water and their mass and dimensions were measured. The next step is to bake the specimens in an oven set at 105±3 °C for 42 hours. Once a specimen is taken out of the oven, it is given two coats of brushstrokes on each surface to remove the adhered materials, as shown in Fig. 3. The other specimen was used (without brush strokes) to monitor the volume change by measuring the dimensions after each cycle. The technique was done 12 times and each cycle lasted 48 hours. Once the 12 cycles were completed, the specimens were baked at 105 °C until they attained a consistent mass. Using Equation 2, we were able to determine the specimen's weight decrease.

$$\text{Weight loss } \% = \frac{\text{initial weight} - \text{final dry weight}}{\text{initial weight}} \times 100. \quad (2)$$

To evaluate the possibility of specimen failure (collapse), its status was monitored during the wetting-drying cycles. Upon finishing the test and noting the volume change and weight reduction.

Figure 3. Photographs of the durability test specimens.

3. Results and Discussion

3.1. Compaction Test Results

To determine the MDD and optimal water content, a curve is plotted correlating the water content and dry density. The results of the compaction tests are presented in Fig. 4. The MDD value increased from 1.59 to 1.76 gm/cm^3 when increasing the cement ratio from 0 to 8 %. The OMC value decreased from 10.33 to 9.2 % when increasing the cement ratio from 0 to 8 %. This trend may be attributed to the increase in physical properties of cement that has finer particle size with higher G_s which tends to fill the voids of the specimens.

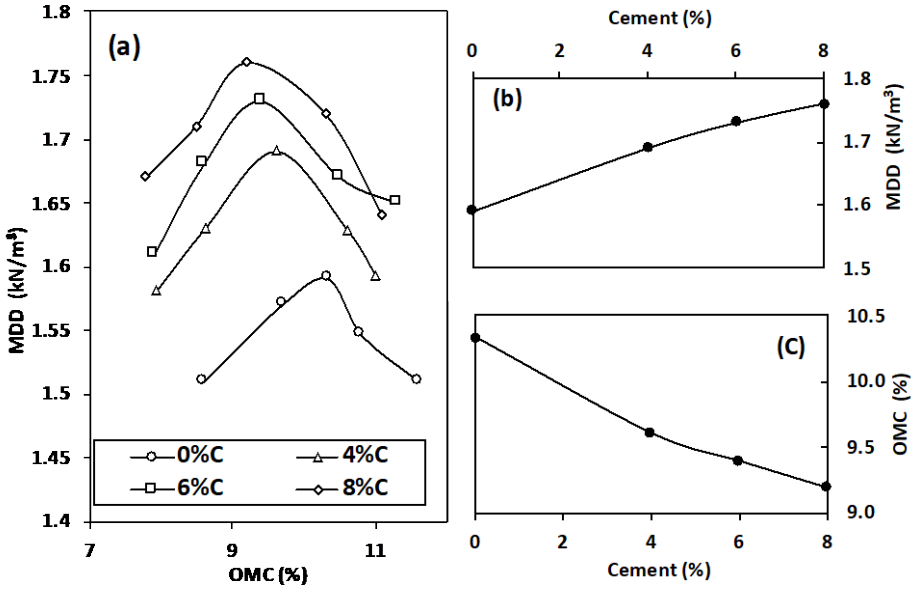

Figure 4. The compaction test results: (a) compaction curves; (b) cement-MDD relationships; (c) cement-OMC relationships.

3.2. The UCS Test Results

The USC test is convenient and cost-effective test to evaluate the shear strength in the laboratory to select the most suitable material for different geotechnical structures. The values of the UCS for specimens treated with cement (c) and cement-PPF (c-PPF) are shown in Fig. 5 and 6, respectively. Because the untreated soil is very loose poorly graded sand, the UCS could not be conducted on this soil. For the cement-treated specimens, the UCS values increased gradually with increasing cement ratio from 4 to 8 % for both curing durations because the increase in cement lad to reduce the void ratio and increase the hardness of the specimens. Increasing cement ratio from 0 to 8 % led to increase the UCS values from 0 to greater than 2000 kN/m^2. Moreover, using the PPF led to increase the UCS value for all curing periods, this is because PPF acted as reinforcement to the sediment particles. For optimum value, further experiments can be carried out with greater percentages of PPF, and compatible the results. A comparison between the two methods of treatment is presented in Fig. 7. For the curing period of 7 days, the UCS values increased from 29 to 46 % when PPF was added. Likewise, the UCS values increased from 9 to 52 % when the PPF was added for the curing period of 28 days. The figures also show that the as the curing period increased from 7 to 28 days, the UCS values increased from 13 to 38 %. These results indicate the importance of providing sufficient curing time to develop the strength of cement-PPF treated soil.

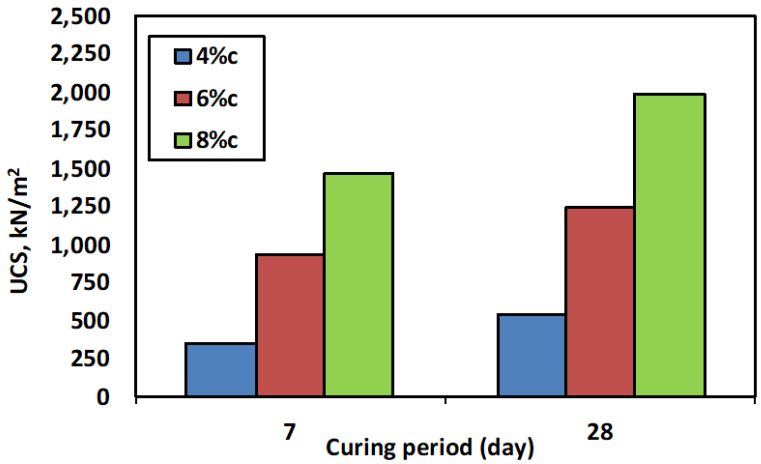

Figure 5. The UCS values for the specimens treated by cement.

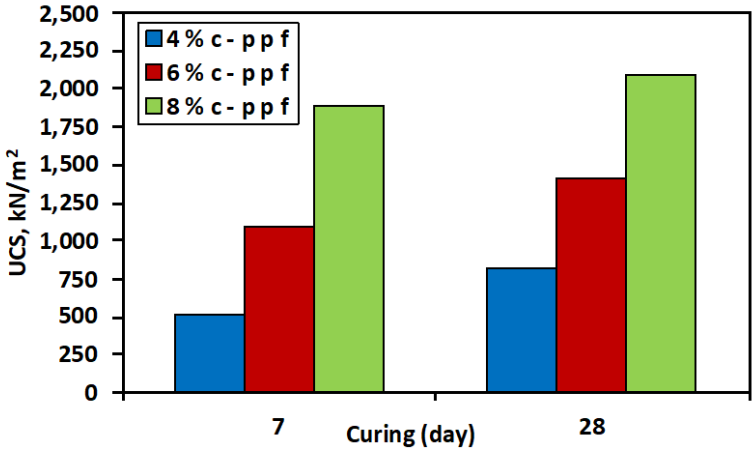

Figure 6. The UCS values for the specimens treated by cement and PPF.

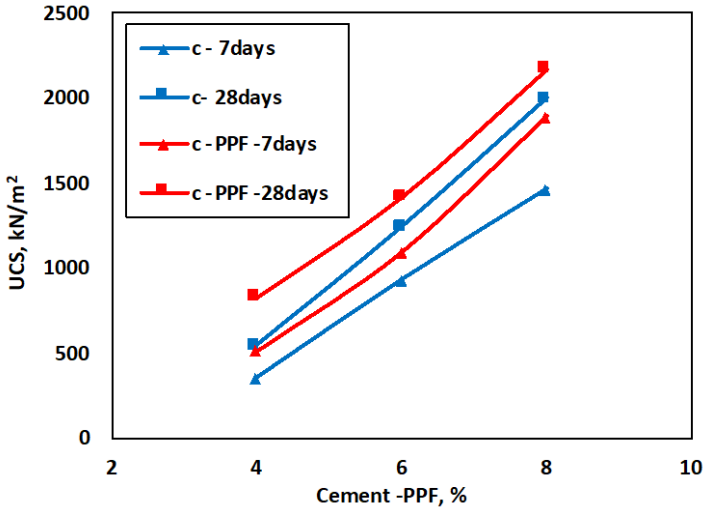

Figure 7. The effect of treatment methods on the UCS values.

3.3. Durability Test Results

The primary focus in the chemical stabilization of soils is ensuring long-term performance under different conditions. The composition of soil particles is affected by water, causing leaching of chemical components. This leads to inadequate soil stability, which is further impacted by seasonal variations and climatic circumstances. The durability test examines the volumetric stability and strength loss in the UCS using two approaches. The samples chosen for testing in wet and dry circumstances were produced using the optimal mixes determined from the UCS test. The weight loss, volume alteration, and durability of the samples were assessed after undergoing 12 cycles of soaking and drying, as shown in Table 5. The results showed the significant improvement in resistance for wetting and drying. The untreated specimens collapsed in the first cycle while the treated specimens successfully passed the cycles with loss in weight ranging from 16 to 39 %. These results indicate the feasibility of using these materials for earth structures that are exposed to sever change in climatic conditions such as earth dams and levees.

Table 5. The results of the durability tests.

Cement, %	Age, day	Weight loss, %	Volume change
0	–	Collapsed in the first cycle	–
4	7	39	No volume change
	28	34	
6	7	30	No volume change
	28	26	
8	7	22	No volume change
	28	16	

4. Conclusions

The objective of this research is to assess the effectiveness of employing OPC with PPF to stabilize dredged sediments for geotechnical engineering purposes. This study focused on investigating the mechanical, physical, and durability properties of sediments drudged from the Euphrates River. The findings of this research suggest that:

1. The sediment materials that were studied are classified as loose poorly graded sand that is not suitable as engineered fill.
2. Increasing the cement ratio from 4 to 8 % led to increase the MDD and reduce the OMC of the cement-treated compacted specimens.
3. Adding cement to the sand significantly increased the UCS, as the 8 % cement produced a UCS value as high as 2000 kN/m^2.
4. Applying PPF to cement-treated specimens led to an improvement in the UCS values that reached 52 %.
5. As the curing period increased from 7 to 28 days, the UCS values increased from 13 to 38 %.
6. The cement-treated specimens successfully passed the durability test with loss in weight ranging from 16 to 39 % compared to the untreated specimens that collapsed in the first cycle of wetting-drying.
7. The aforenoted results demonstrated that cement and PPF can be used as affective additives to improve the mechanical properties of loose sand sediments.

References

1. Syvitski, J, Ángel, J.R., Saito, Y., Overeem, I., Vörösmarty, C.J., Wang, H., Olago, D. Earth's sediment cycle during the Anthropocene. Nature Reviews Earth & Environment. 2022. 3(3). Pp. 179–196. DOI: 10.1038/s43017-021-00253-w
2. Mahmood, N.S., Alboresha, R., Sulaiman, S.O., Al Ansari, N. Seepage Problem Through the Foundation of a Spillway with Selected Treatment Methods. Mathematical Modelling in Civil Engineering. 2022. 9(3). Pp. 819–824. DOI: 10.18280/mmep.090331
3. Owens, P.N. Soil erosion and sediment dynamics in the Anthropocene: a review of human impacts during a period of rapid global environmental change. Journal of Soils and Sediments. 2020. 20. Pp. 4115–4143. DOI: 10.1007/s11368-020-02815-9
4. Zeini, H.A., Al-Jeznawi, D., Imran, H., Bernardo, L.F.A., Al-Khafaji, Z., Ostrowski, K.A. Random Forest Algorithm for the Strength Prediction of Geopolymer Stabilized Clayey Soil. Sustainability. 2023. 15(2). Article no. 1408. DOI: 10.3390/su15021408
5. Mahmood, N.S., Aude, S.A., Abdullah, H.H., Sulaiman, S.O., Al-Ansari, N. Analysis of Slope Stability and Soil Liquefaction of Zoned Earth Dams Using Numerical Modeling. International Journal of Design & Nature and Ecodynamics. 2022. 17(4). Pp. 557–562. DOI: 10.18280/ijdne.170409
6. Mohammed, O.A. Geoinformatics-based approach for aquifer recharge zone identification in the western desert of Iraq. International Journal of GEOMATE. 2023. 25(110). Pp. 220–234. DOI: 10.21660/2023.110.3448
7. Al-Husseinawi, F.N., Atherton, W., Al-Khafaji, Z., Sadique, M., Yaseen, Z.M. The Impact of Molar Proportion of Sodium Hydroxide and Water Amount on the Compressive Strength of Slag/Metakaolin (Waste Materials) Geopolymer Mortar. Advances in Civil Engineering. 2022. 2022. Article no. 5910701. DOI: 10.1155/2022/5910701
8. Song, D.W., Panayides, P. Maritime logistics: Maritime Logistics: A Guide to Contemporary Shipping and Port Management. Kogan Page Publishers. London. Philadelphia. New Delhi, 2015. 480 p.
9. Mossa, J., Chen, Y.H., Walls, S.P., Kondolf, G.M., Wu, C.Y. Anthropogenic landforms and sediments from dredging and disposing sand along the Apalachicola River and its floodplain. Geomorphology. 2017. 294. Pp. 119–134. DOI: 10.1016/j.geomorph.2017.03.010
10. Hauer, C., Wagner, B., Aigner, J., Holzapfel, P., et al. State of the art, shortcomings and future challenges for a sustainable sediment management in hydropower: A review. Renewable and Sustainable Energy Reviews. 2018. 98. Pp. 40-55. DOI: 10.1016/j.rser.2018.08.031
11. Ali A, bin Waheed U, Ashiq M, AL ASTA MS, Khorram M. Machine Learning Model for Estimation of Local Scour Depth around Cylindrical Bridge Piers. Iraqi Journal of Civil Engineering. 2022. 16(2). Pp. 1–13. DOI: 10.37650/ijce.2022.160201
12. Crocetti, P., González-Camejo, J., Li, K., Foglia, A., Eusebi, A.L., Fatone, F. An overview of operations and processes for circular management of dredged sediments. Waste Manag. 2022. 146. Pp. 20–35. DOI: 10.1016/j.wasman.2022.04.040
13. The Directorate of Water Resources of Al-Anbar Governorate. Annual Drudged Sediments from the Euphrates River in Al-Anbar. Ramadi, 2024.
14. Ameen, S.K., Abdulkareem, A.H., Mahmood, N.S. The durability of an organic soil treated with fly ash and alkaline activators. AIP Conference Proceedings. 2024. 3009(1). Article no. 030122. DOI: 10.1063/5.0190501
15. Ameen, S.K., Abdulkareem, A.H., Mahmood, N.S. Shear strength behavior of organic soils treated with fly ash and fly ash-based geopolymer. Journal of the Mechanical Behavior of Materials. 2023. 32(1). Article no. 20220264. DOI: 10.1515/jmbm-2022-0264
16. Al-Khafaji, Z.S., Jafer, H., Dulaimi, A., Atherton, W., Al Masoodi, Z. The Soft Soil Stabilisation Using Binary Blending of Ordinary Portland Cement and High Alumina Silica Waste Material. The 3rd BUiD Doctoral Research Conference. The British University in Dubai, 2017. DOI: 10.13140/RG.2.2.22248.16641
17. Le Bissonnais, Y. Soil Characteristics and Aggregate Stability. Soil Erosion, Conservation, and Rehabilitation. CRC Press, 2023. Pp. 41–60.

18. Kamil, K.S., Abdulkareem, A.H., Mahmood, N.S. Using a Laboratory Model Test to Evaluate Collapsibility of Gypseous Soils Improved by Sludge. E3S Web of Conferences. 2023. 427. Article no. 01004. DOI: 10.1051/e3sconf/202342701004
19. Ameen, S., Abdulkareem, A., Mahmood, N. Compressibility Characteristics of an Organic Soil Treated with Fly Ash and Fly Ash-Based Geopolymer. Iraqi Journal of Civil Engineering. 2022. 16(2). Pp. 23–29. DOI: 10.37650/ijce.2022.160203
20. Otoko, G.R. A review of the stabilization of problematic soils. International Journal of Engineering and Technology Research. 2014. 2(5). 1–6.
21. Mahmood, N.S., Salazar, S.E., Coffman, R.A. Small-Strain Characteristics of Reconstituted Soils: The Effect of Slurry Water Content and Fabric Anisotropy. Journal of Testing and Evaluation. 2023. 51(2). Pp. 1010–1020. DOI: 10.1520/JTE20220143
22. Amhadi, T.S., Assaf, G.J. Overview of soil stabilization methods in road construction. In Sustainable Solutions for Railways and Transportation Engineering: Proceedings of the 2nd GeoMEast International Congress and Exhibition on Sustainable Civil Infrastructures, Egypt 2018–The Official International Congress of the Soil-Structure Interaction Group in Egypt (SSIGE) 2019 (pp. 21–33).
23. Roshan, M.J., Rashid, A.S.B.A. Geotechnical characteristics of cement stabilized soils from various aspects: A comprehensive review. Arabian Journal of Geosciences. 2024. 17(1). Article no. 1. DOI: 10.1007/s12517-023-11796-1
24. Yeldeen, M., Azzam, W., Arab, M.G. The Use of Fiber to Improve the Characteristics of Collapsible Soil Stabilized with Cement. Geotechnical and Geological Engineering. 2022. 40. Pp. 1873–1885. DOI: 10.1007/s10706-021-01997-4
25. Ali, A.M., Falah, M.W., Hafedh, A.A., Al-Khafaji, Z.S., Radhi, S. Evaluation the influence of steel-fiber on the concrete characteristics. Periodicals of Engineering and Natural Sciences (PEN). 2022. 10(3). Pp. 368–379. DOI: 10.21533/pen.v10i3.3111
26. Haeri, S.M., Noorzad, R., Oskoorouchi, A.M. Effect of geotextile reinforcement on the mechanical behavior of sand. Geotext Geomembranes. 2000. 18(6). Pp. 385–402. DOI: 10.1016/S0266-1144(00)00005-4
27. Liu, Y., Wang, L., Cao, K., Sun, L. Review on the Durability of Polypropylene Fibre-Reinforced Concrete. Advances in Civil Engineering. 2021. Article no. 6652077. DOI: 10.1155/2021/6652077
28. Blazy, J., Blazy, R. Polypropylene fiber reinforced concrete and its application in creating architectural forms of public spaces. Case Studies in Construction Materials. 14. Article no. e00549. DOI: 10.1016/j.cscm.2021.e00549
29. Ayeldeen, M., Azzam, W. & Arab, M.G. The Use of Fiber to Improve the Characteristics of Collapsible Soil Stabilized with Cement. Geotechnical and Geological Engineering. 2022. 40(4). Pp 1873–1885. DOI: 10.1007/s10706-021-01997-4
30. Li, J.S., Chen, X., Lang, L., He, X.-X., Xue, Q. Evaluation of natural and artificial fiber reinforcements on the mechanical properties of cement-stabilized dredged sediment. Soils and Foundations. 2023. 63(3). Article no. 101319. DOI: 10.1016/j.sandf.2023.101319
31. BSI BS 1377-3-1990. Methods of test for soils for civil engineering purposes – Part 3: Classification tests. London, 1990.
32. ASTM D2487. Standard Practice for Classification of Soils for Engineering Purposes (Unified Soil Classification System). West Conshohocken, PA, 2017.
33. The State Corporation for Roads and Bridges. Standard Specifications for Roads and Bridges- SORB/R6. Baghdad, 2003.
34. Central Organization for Standardization & Quality Control (COSQC). Iraqi Specification No.5 'Portland cement'. Baghdad, 1984.
35. ASTM D689. Standard Test Methods for Laboratory Compaction Characteristics of Soil Using Standard Effort (12,400 ft-lbf/ft3 (600 kN-m/m^3)). West Conshohocken, PA, 2012.
36. ASTM D2166. Standard Test Method for Unconfined Compressive Strength of Cohesive Soil. West Conshohocken, PA, 2016.
37. ASTM D0559. Standard Test Methods for Wetting and Drying Compacted Soil-Cement Mixtures. West Conshohocken, PA, 2015.

Information about the authors:

***Hussam Mohammed**,*
E-mail: hus22e1009@uoanbar.edu.iq

***Nabeel Mahmood**, PhD*
ORCID: https://orcid.org/0000-0002-4886-2529
E-mail: nabeelshm@uoambar.edu.iq

Received 07.06.2024. Approved after reviewing 05.09.2025. Accepted 10.09.2025.

Magazine of Civil Engineering

ISSN 2712-8172

journal homepage: http://engstroy.spbstu.ru/

Research article

UDC 624

DOI: 10.34910/MCE.138.5

Finite element analysis of fatigue damaged reinforced concrete one-way slabs repaired with CFRP sheets

M.O. Hameed [1] ✉ , ***R.A. Daud*** [2]

[1] *College of Engineering, Al-Nahrain University, Baghdad, Iraq*

[2] *Al-Nahrain University, Baghdad, Iraq*

✉ *st.mohammed.a.h.f@nahrainuniv.edu.iq*

Keywords: ABAQUS, fatigue damage, EBR, CFRP sheet, one-way slab

Abstract. In twenty-eight samples in this study, the structural behavior of fatigue-damaged one-way slabs was produced using a nonlinear finite element model that was created using ABAQUS. The effect of carbon fiber-reinforced polymer (CFRP) parameters and fatigue-damaged percentages is examined to obtain a better reaction. The full model accounts for the elastic and plastic behavior of the materials and uses three-dimensional parts (solid, shell, and truss). To investigate the accuracy of the model, the authors' experimental data (monotonic and fatigue damage) is used to validate the numerical outputs. For the four verified slabs, the average and coefficient of variations for ultimate load of finite element analysis to ultimate load of experimental work were 0.997 and 5.35 %, respectively; for the deflection of finite element analysis to deflection of experimental work, they were 1.197 and 15.99 %, and for energy absorption, they were 1.134 and 12.2 %, respectively. Twenty-four samples parametric studies using the impacts of CFRP sheet thickness, CFRP sheet modulus of elasticity, CFRP sheet length, the concrete compressive strength value, and the fatigue damage percentage. Examining these metrics was intended to provide insight into the efficacy and structural performance of the employed fortification technology. The numerical findings demonstrated that the technique of externally bonding CFRP sheets to strengthen damaged slabs may be regarded as a successful, and cost-effective method.

Citation: Hameed, M.O., Daud, R.A. Finite element analysis of fatigue damaged reinforced concrete one-way slabs repaired with CFRP sheets. Magazine of Civil Engineering. 2025. 18(6). Article no. 13805. DOI: 10.34910/MCE.138.5

1. Introduction

The majority of the bridges constructed during the past 40 years are made of reinforced concrete. The fatigue damage to the bridges grew as a result of increased traffic volume and load, reducing the spans' service life. Over a bridge's service life, fatigue loading is characterized by a large number of load cycles, which can surpass 100 million. Fatigue loading is induced by moving wheels. Frequent and prolonged load action caused the bridge's rigidity to decrease and demonstrated cumulative deterioration [1]. Concerns regarding the fatigue life and performance of reinforced concrete buildings were growing among academics [2–6]. Because of the increased traffic load and deformed structural parts, there is a noticeable need for improvements to the current transportation infrastructure. Most reinforced concrete slabs and beams will have cracks at some point. Restoring the damaged parts' structural capability requires strengthening and retrofitting [7, 8]. The rehabilitation community has given great attention to the utilization of carbon fiber-reinforced polymer (CFRP) composites among other strengthening solutions because of its durable performance [9]. The inevitable cracking of any structural part is a fact of life. Restoring their flexural capabilities requires strengthening or repairing the injured parts [10–12]. CFRP can be firmly positioned using a bonding agent by inserting it into the tiny groove that has been precut along the cover of a reinforced or prestressed concrete beam or by applying adhesive bonding to the tensile soffit of a structural element.

These CFRP applications are commonly referred to as numerical simulation model (NSM) or employed fortification (EB) strengthening techniques, respectively. Similar to traditional EB CFRP strengthening, NSM CFRP has seen a notable increase in popularity recently in terms of field testing and laboratory study [13]. Improved bond, durability, fatigue performance, quick installation, corrosion resistance, and labor savings are just a few of the numerous noteworthy advantages of NSM CFRP [14–16]. Despite having great tensile strength (more than ten times the yield strength of structural steel, for example) [17], CFRP materials can only be used in a restricted strength range in real-world applications. The rationale is that concrete crushing or CFRP-debonding, as opposed to CFRP-rupture, is often what controls the failure of a CFRP-strengthened concrete part. To get over this constraint and increase the serviceability of a reinforced member even more, NSM CFRP may be post-tensioned. There are several methods for post-tensioning NSM CFRP strips or rods: external jacking apparatus [18, 19], side brackets [20], and embedded anchors [21].

Daud et al. [22] examined how a layer of CFRP adhesive covering one-way reinforced concrete slabs behaved nonlinearly. By forecasting the stiffness deterioration in the concrete for both compression and tension impacts, the finite element (FE) model includes the nonlinearity of the concrete under cyclic loading. A three-dimensional FE model has been presented to more effectively reflect composite sheets' interface and slip profile with the concrete slab under different cyclic loading phases [22]. The authors' experimental data (monotonic and fatigue damage) is used to validate the numerical outputs [23]. This paper's objectives are: (1) to determine interest in expanding our understanding of concrete slab fatigue behavior; (2) to capture the mode of failure and mimic the behavior of damaged one-way slabs, maximum deflection, and ultimate load using an intricate numerical model. (3) A parametric analysis was carried out to determine the impact of adding CFRP thickness, the elastic modulus of CFRP sheet, length of CFRP, and concrete compressive strength and the effect of fatigue-damaged one-way slabs.

2. Methods

2.1. Numerical Simulation Model

With the help of the universal numerical software suite ABAQUS, the actual model was displayed. Concrete was represented by the isoperimetric eight-node brick element (C3D8R). Every node may move along the *x*, *y*, and *z* axes in three dimensions. The three-dimensional four-node with reduced integration and hourglass control (S4R5) served as a representation of the CFRP sheet. Conversely, the three-dimensional two-node bar element with three-dimensional movements, or truss element (T3D2), represented the reinforced steel rebars. Two-line loads were uniformly applied at the top of each slab in the same location for the experimental test. To represent the end supports of the model properly and in a way that was similar to the tested slabs, displacement boundary conditions were used. Wherever the specimens are supported during experimental testing [23], these boundary requirements must be implemented. Considering that the specimens were only held up by the two shorter edges, as shown in Fig. 1. One supporting line had all of its nodes fixed translated in the *y* and *z* directions, whereas the other supported line had all of its nodes fixed translated in the *x*, *y*, and *z* directions.

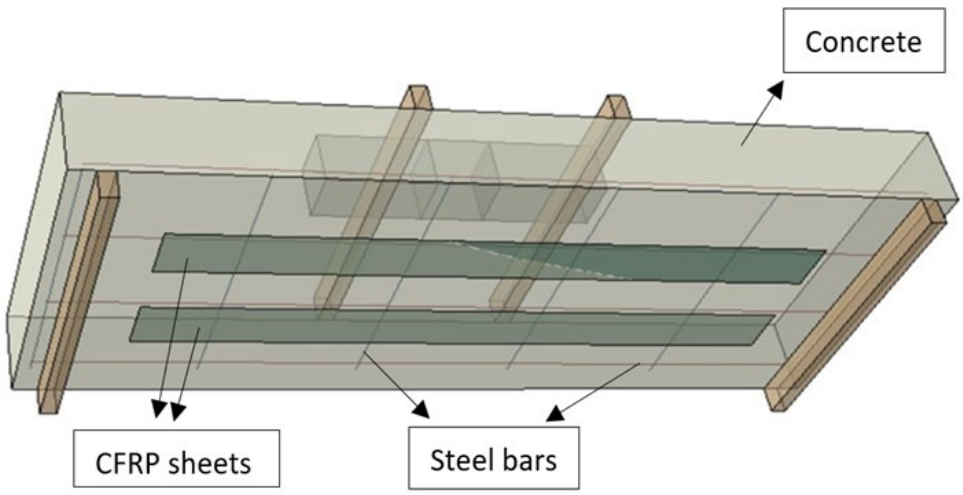

Figure 1. Boundary condition and applied load isometric view for ends supports.

2.2. Material Models

2.2.1. Concrete

Using the yield function from [24], the concrete damaged plasticity model (CDP) was created. This model includes two types of failure processes: tensile cracking and compression fractures. One popular model used to explain concrete's behavior is the CDP. For the nonlinear calculation of concrete members, it is also utilized as it provides an accurate depiction of the material's behavior [25]. The input values for concrete damage plasticity parameters are displayed in Table 1 [26].

Table 1. Data input for the plasticity parameters of concrete damage [26].

The modulus of Young	32286.69412
Poisson's ratio	0.15
Angle of dilation	36
Eccentricity	0.1
$\epsilon_{bo}/\epsilon_{co}$	1.16
k_c	0.667
The parameter of viscosity	0

2.2.1.1. Behavior of concrete compressive strength

The compressive strength of concrete is great; the elastic linear route accounts for around 40 % of the overall compressive strength; cracks result in non-linear behavior. According to inelastic concrete stress and strain, respectively, ABAQUS specifies the strain ascending range and descending range. In the present FE study, The Concrete Structure Design Model for Euro Code Two [27] was employed. Table 2 displays data on the compressive strength of concrete [26].

Table 2. Concrete compressive strength [26].

Yield stress (MPa)	Inelastic strain
7.044263303	0
13.27540985	2.88E–05
18.71156607	8.03E–05
23.37032356	0.000156018
27.26875871	0.000255237
30.42345141	0.000377493
32.85050297	0.000522285
34.56555325	0.000689129
35.58379709	0.000877555
35.92	0.001087106
35.7849029	0.001231536
35.38202351	0.001384259
34.71493152	0.001545166
33.7871334	0.001714148
32.6020739	0.001891098
31.16313731	0.00207591
29.47364884	0.002268484

2.2.1.2. Concrete tensile behavior

Three parameters may be used in ABAQUS/standard to define the post-cracking tension softening curve: fracture energy, displacement, and strain. The concrete's tensile stress-strain curve utilized in this study was provided by [28] in ABAQUS and had a linear rising line whose gradient matched the concrete's elastic modulus, as well as an exponential slide. Table 3 presents specific facts regarding stress [26].

Table 3. Specific tension measurements [26].

Yield stress (MPa)	Strain
3.6	0
0.386731643	0.031101255

2.2.2. Steel reinforcement

A bilinear elastic-plastic curve was used in ABAQUS to model the behavior of the steel reinforcement. The plastic curve was constructed using experimental data derived from the stress-strain curve, and the elastic modulus and Poisson's ratio were used to evaluate the behavior's linear elastic zone. Table 4 displays the attributes of steel reinforcement [26].

Table 4. Steel reinforcement's characteristics [23].

fy	619 (MPa)
fu	732 (MPa)
Poisson's ratio	0.3
Es	200 (GPa)
elongation	15%

2.2.3. Carbon fiber reinforced polymer

An orthotropic material was used to mimic the CFRP composite sheet. The behavior is linear until the point of failure. According to the manufacturer's data, the longitudinal elastic main modulus was calculated, and the other two transverse elastic moduli were taken to be around 10 % of the longitudinal elastic main modulus. Additional attributes were presumed based on those delineated by [29]. The elastic characteristics of CFRP sheets are shown in Table 5 [26, 30]. There are other types of carbon fiber, such as plate [31].

Table 5. Characteristics of CFRP sheet [26].

Material	Description	CFRP sheet
CFRP sheet	Longitudinal modulus (E1), GPa	230
	Transverse in-plane modulus(E2), GPa	23
	Transverse out-plane modulus(E3), GPa	23
	In-plane shear modulus (G12), GPa	6.894
	Out-of-plane shear modulus (G23), GPa	4.136
	Out-of-plane shear modulus(G13), GPa	6.894
	Major in-plane Poisson's ratio, v12	0.3
	Out-of-plane Poisson's ratio, v23	0.25
	Out-of-plane Poisson's ratio, v13	0.25

2.3. Predefined Field

The fatigue damage stage of damaged slabs may be defined using the ABAQUS/Standard technique. The initial state field presents this strategy. When importing ABAQUS/CAE model data for analysis, at specific points and increments of the research, it is possible to identify the task name linked to the analysis, for which the initial state variable is imported. Any component instance in an ABAQUS/CAE model can be linked to data imported from an earlier ABAQUS/Standard model result. More crucially, before evaluating the data in ABAQUS/Standard, to establish more model definitions, the outcomes and model data could be transferred to new research. This feature permits the application of 50 and 70 % of the ultimate load on specimens with CFRP sheets in this investigation and allows the material condition's distorted model to be utilized as the starting state.

2.4. Finite Element Simulation Model Validation

Comparisons with the experimental results are shown in this section. Among these are the load-deflection relationship in the end stage, when monotonic loads and fatigue damage are applied, and the connection between load and deflection when a pressure load is applied following slab repairs. Fig. 2 [23] shows the experimental and numerical results for the monotonic load test in terms of load against deflection relation after the damaged slabs have been fixed. It can be demonstrated that numerical models were, on average, stiffer than experimental data for both the linear and non-linear behavior domains.

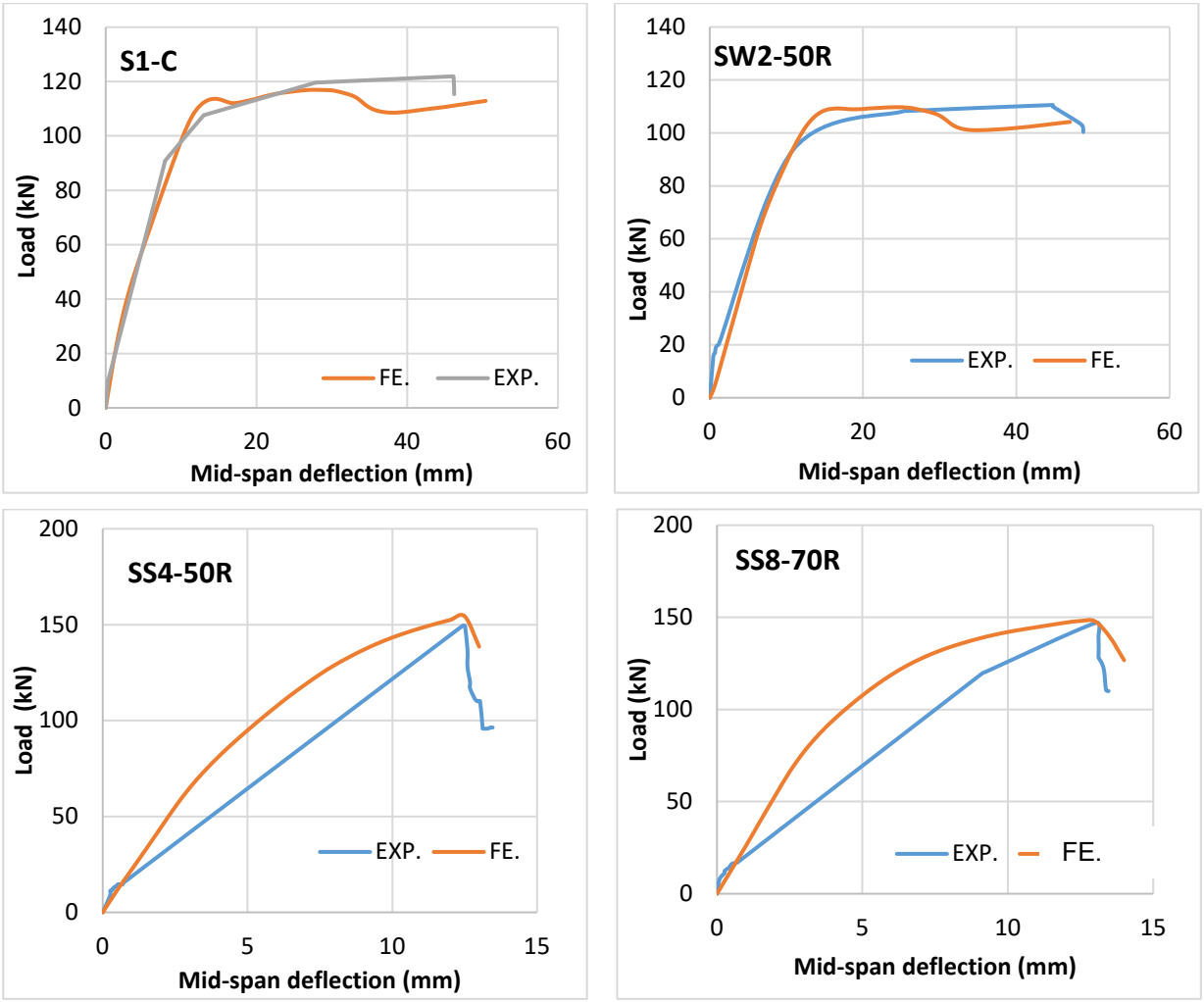

Figure 2. Numerical and experimental load-deflection curves for selected four slabs [23].

Table 6 [23] presents a comparison between the failure load and center deflection generated by the FE model and the experimental test conducted at the failure stage (near the failure load) for four slabs under a monotonic test (after fatigue damage). A fair amount of agreement was reached between the deflections and ultimate loads of the FE numerical models, and that was discovered experimentally. For the ultimate loads, the values of the mean and C.V for $(Pu)_{FE}/(Pu)_{Exp}$ were 0.997 and 5.35 %, respectively, and for the deflection of δ_{FE}/δ_{Exp}, they were 1.197 and 15.99 %, and for energy absorption, they were 1.134 and 12.2 %, respectively.

Table 6. Failure load and mid-span deflection at failure load, both numerical and experimental [23].

Slab's labeling	Failure Load (kN)		$(Pu)_{FE}/(Pu)_{Exp}$	Mid-span deflection (mm)		δ_{FE}/δ_{Exp}	Energy Absorption (EA)		EA_{FE}/EA_{Exp}
	$(Pu)_{Exp}$	$(Pu)_{FE}$		δ_{Exp}	δ_{FE}		EA_{Exp}	EA_{FE}	
S1-C	122	117	0.959	46	60	1.304	4797.8	5105.3	1.064
SW2-50R	110.5	109.7	0.992	45	47	1.044	4575.9	4353.8	0.951
SS4-50R	149.3	154.35	1.033	12.51	15.5	1.239	1089.6	1318.2	1.209
SS8-70R	147	148	1.006	13.03	15.7	1.204	1159.1	1525.3	1.315
–	Mean		0.997	Mean		1.197	Mean		1.134
–	C.V		5.35%	C.V		15.99%	C.V		12.2%

The load-deflection relationship under applied load, as determined by FE analysis, indicates that the models have more stiffness than the test specimens. There are various possible explanations for the higher stiffness shown in the findings of the FE investigation. The experiment shows how the drying process left the concrete with microcracks, shrinking, and curing. As a result, the specimen's true stiffness would

decrease. The FE models do not consider these microcracks. The FE study deems the link between the steel reinforcement and the concrete to be flawless. This assumption will not hold for the actual specimen. The composite work that exists between the concrete and the steel reinforcement is lost as a result of a bond sliding. The specimen's overall stiffness may thus be lower than that of the FE study.

3. Results and Discussion

Using the FE model, based on the experimental data used in this investigation's earlier FE verification. A thorough parametric analysis was carried out. The effects of CFRP sheet thickness are one of the study's variables, CFRP sheet modulus of elasticity, CFRP sheet length, and the concrete compressive strength value.

3.1. Effect of Added CFRP Thickness on the Structural Performance of One-Way Slabs

Examined were the effects of the additional CFRP's thickness on the slabs' load-deflection relationship and ultimate load capacity. Based on the CFRP strip's 1000 mm length, three thickness values (one layer, two layers, and four layers) were selected for each thickness with three slabs. Fig. 3 shows the effect of increasing CFRP thickness on the load-mid span deflection relation of slabs. Thicker CFRP sheets increased the rigidity of the slabs, hence raising the maximum load capacity.

According to Table 7, for slab S50-0.34 and S50-0.68, in relation to slab S50-0.17 for group of CFRP fatigue damage equal to 50 %, the percentage of a rise in load capacity is 9.09 and 18.18 %, respectively, and for slab S70-0.34 and S70-0.68, in relation to slab S70-0.17 for group of CFRP fatigue damage equal to 70 %, the percentage of a rise in load capacity is 12.16 and 22.97 %, respectively. The impact of increased CFRP thickness and fatigue damage (50 and 70 %) on ultimate load capacity is depicted in Fig. 4. The debonding CFRP sheet and the concrete surface for each slab were the cause of the failure.

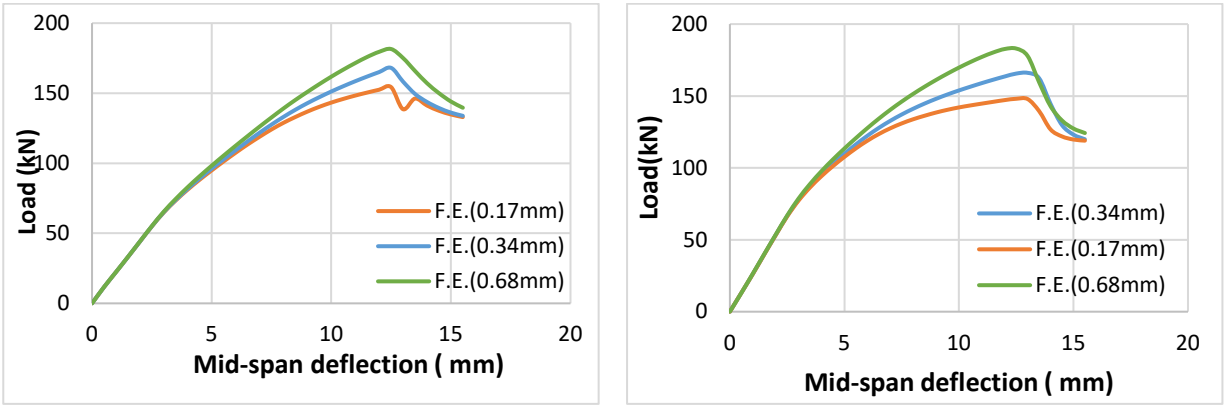

Fatigue damage 50% **Fatigue damage 70%**

Figure 3. Impact of thickness of CFRP sheet on load-mid span deflection curve of slabs.

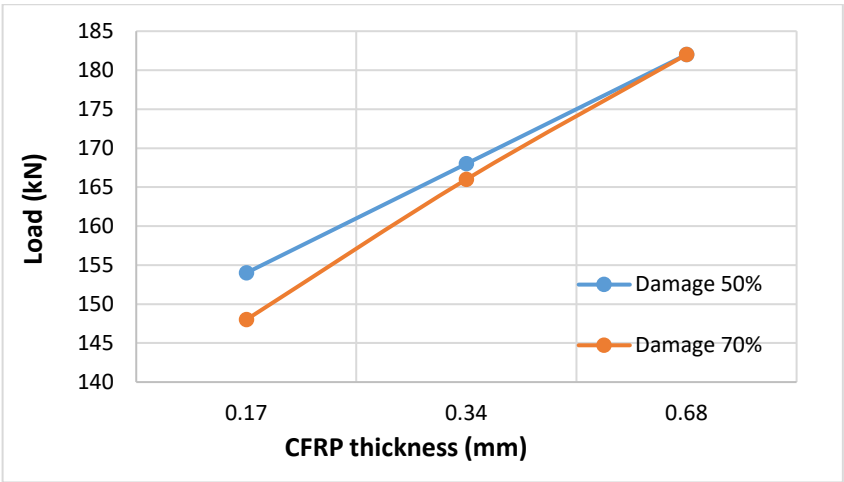

Figure 4. Impact of CFRP thickness and fatigue damage (50 and 70%) on load capacity.

Table 7. The effect of increased CFRP thickness on the load capacity.

Slab ID	Length of CFRP sheet (mm)	Thickness of CFRP sheets (mm)	$Pu=P_{ult.}$ (kN)	Increase in Pu percentage relative to Pu of 0.17 mm in each group (%)	Failure mode
S50-0.17	1000	0.17	154	Ref.	de-bonding
S50-0.34	1000	0.34	168	9.09	de-bonding
S50-0.68	1000	0.68	182	18.18	de-bonding
S70-0.17	1000	0.17	148	Ref.	de-bonding
S70-0.34	1000	0.34	166	12.16	de-bonding
S70-0.68	1000	0.68	182	22.97	de-bonding

3.2. Effect of Added CFRP Modulus of Elasticity on Structural Performance of One-Way Slabs

For slabs, the impact of the increased CFRP's modulus of elasticity on the load-deflection relationship and ultimate load capacity was investigated. Three values for the modulus of elasticity 160, 230, and 640 GPa were selected. The effect of the additional CFRP strips' modulus of elasticity and fatigue damage (50 and 70 %) on the load-mid span deflection relation of slabs is depicted in Fig. 5. It is evident that adding more CFRP strips with a higher modulus of elasticity made the slabs stiffer, which raised the ultimate load capacity. The impact of CFRP modulus of elasticity and fatigue damage (50 and 70 %) on ultimate load capacity is depicted in Fig. 6.

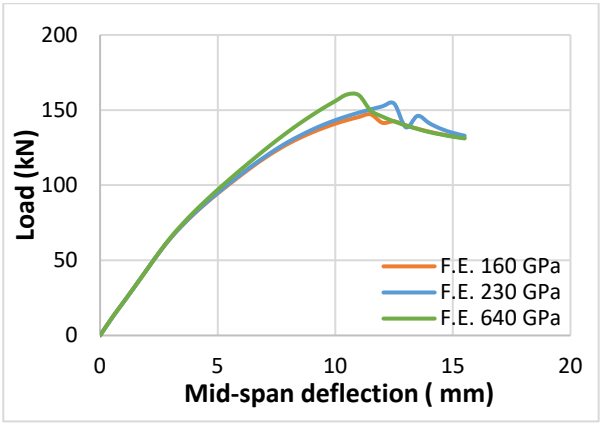

Fatigue damage 50%

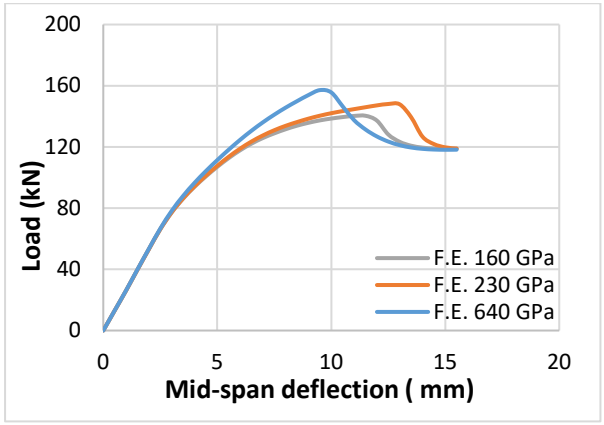

Fatigue damage 70%

Figure 5. Impact of modulus of elasticity of CFRP on load of slabs.

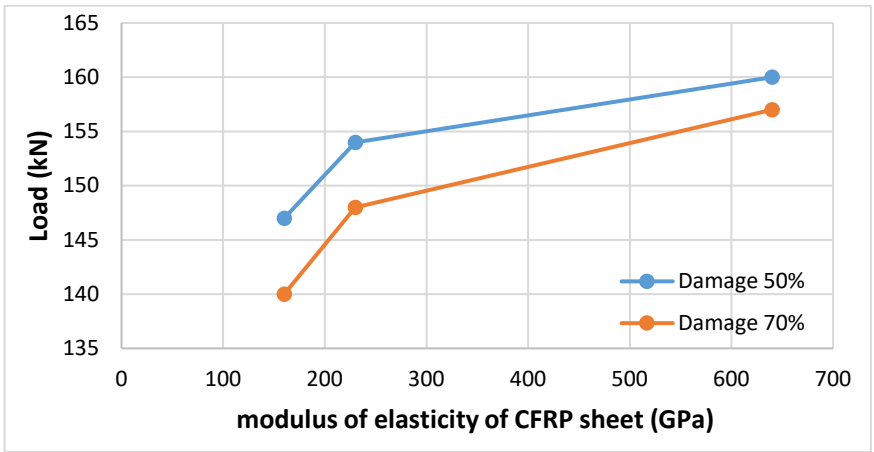

Figure 6. Impact of modulus of elasticity of CFRP on load relation of slabs.

According to Table 8, for slab S50-230 and S50-640, compared with slab S50-160 for group of CFRP fatigue damage equal to 50 %, the percentage of an improvement in load capacity is 8.84 and 4.76 %, respectively, while for slab S70-230 and S70-640, compared with slab S70-160 for group of CFRP fatigue damage equal to 70 %, the percentage of the improve in load capacity is 12.14 and 5.71 %, respectively. Debonding the CFRP sheet and the concrete surface for each slab was the cause of the failure.

Table 8. Impact of modulus of elasticity of CFRP sheet on ultimate load capacity.

Slab ID	Length of CFRP sheet (mm)	CFRP sheet modulus of elasticity (GPa)	$Pu=P_{ult.}$ (kN)	Increase in Pu percentage relative to Pu of 160 GPa in each group (%)	Failure mode
S50-160	1000	160	147	Ref.	de-bonding
S50-230	1000	230	154	4.76	de-bonding
S50-640	1000	640	160	8.84	de-bonding
S70-160	1000	160	140	Ref.	de-bonding
S70-240	1000	230	148	5.71	de-bonding
S70-640	1000	640	157	12.14	de-bonding

3.3. Effect of CFRP Length on One-Way Slabs Structural Performance

Using verified FE modeling (ABAQUS), parametric research was conducted on the application of bonded CFRP sheet in the flexural strengthening of reinforced concrete one-way slabs. This part sought to shed light on the effects of CFRP length by breaking the slab down into two groups: three slabs measuring 600, 800, and 1000 mm each, with 50 % fatigue damage, and three slabs measuring 600, 800, and 1000 mm each, with 70 % fatigue damage. The load-deflection curves of the CFRP length effect are displayed in Fig. 7.

According to Table 9, for slab S50-800 and S50-1000, compared with slab S50-600 for the group of fatigue damage 50 %, the percentage of a rise in ultimate load capacity is 2.19 and 12.4 %, respectively. Similarly, for slab S70-800 and S70-1000, compared with slab S70-600 for the group of fatigue damage 70 %, the percentage of the improve in load capacity is 0.74 and 9.63 %, respectively. Figure 8 illustrates how the ultimate load capacity is affected by the length of CFRP sheets. Debonding between the sheet of CFRP and the surface of concrete for each slab was the cause of the failure.

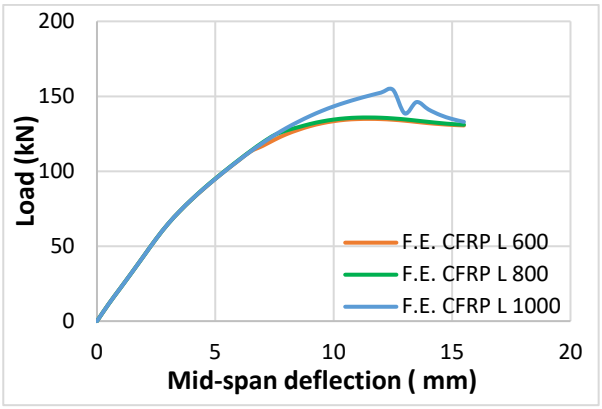

Fatigue damage 50%

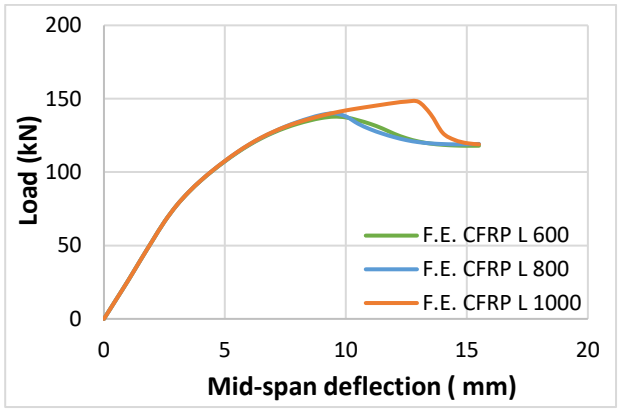

Fatigue damage 70%

Figure 7. Impact of CFRP sheet length on load-mid span deflection relation of slabs.

Table 9. Impact CFRP sheet length on ultimate load capacity.

Slab ID	No. of CFRP strips *width (mm)	Length of CFRP sheet (mm)	Thickness of CFRP sheets (mm)	$Pu=P_{ult.}$ (kN)	Increase in Pu percentage relative to Pu of length 600mm in each group (%)	Failure mode
S50-600	2*100	600	0.17	137	Ref.	de-bonding
S50-800	2*100	800	0.17	140	2.19	de-bonding
S50-1000	2*100	1000	0.17	154	12.4	de-bonding
S70-600	2*100	600	0.17	135	Ref.	de-bonding
S70-800	2*100	800	0.17	136	0.74	de-bonding
S70-1000	2*100	1000	0.17	148	9.63	de-bonding

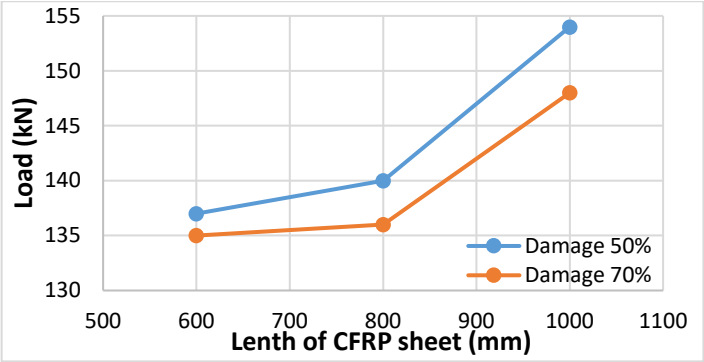

Figure 8. Effect of length of CFRP sheets on ultimate load.

3.4. Effect of Concrete Compressive Strength Value on Structural Performance of One-Way Slabs

Three values of the compressive strength of concrete's 25, 35, and 45 MPa, were selected in order to examine the impact of compressive strength of concrete on the ultimate load capacity. The effect of concrete compressive strength on ultimate load capacity is depicted in Fig. 8, and it is evident that as the compressive strength of concrete grows, so will the ultimate load capacity.

According to Table 10, for slab S50-35 and S50-45, in relation to slab S50-25 for the group of CFRP fatigue damage 50 %, the percentage of increased ultimate load capacity is 20.31 and 35.93 %, respectively. Similarly, for the slab S70-35 and S70-45, in relation to the slab S70-25 for the group of CFRP fatigue damage 70 %, the percentage of increased ultimate load capacity is 34.54 and 40.9 %, respectively. Figure 9 illustrates how compressive strength affects ultimate load capacity. The failure was caused by the CFRP sheets and each slab's concrete surface debonding.

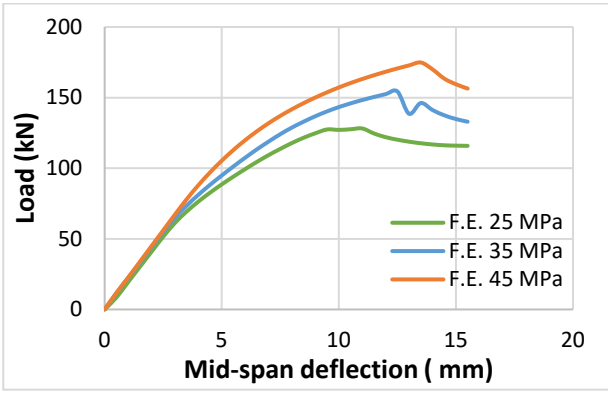

Fatigue damage 50%

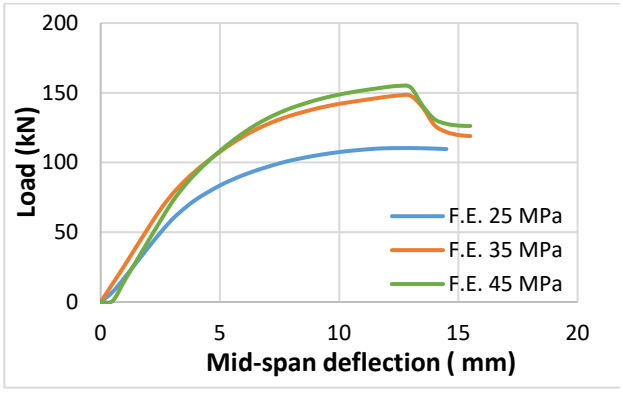

Fatigue damage 70%

Figure 8. Impact of concrete compressive strength on the ultimate load capacity.

Table 10. Impact of compressive strength on ultimate load capacity.

Slab ID	Compressive strength (MPa)	Length of CFRP sheet (mm)	Thickness of CFRP sheets (mm)	Pu=$P_{ult.}$ (kN)	Increase in Pu percentage relative to Pu of length 600mm in each group (%)	Failure mode
S50-25	25	1000	0.17	128	Ref.	de-bonding
S50-35	35	1000	0.17	154	20.31	de-bonding
S50-45	45	1000	0.17	174	35.93	de-bonding
S70-25	25	1000	0.17	110	Ref.	de-bonding
S70-35	35	1000	0.17	148	34.54	de-bonding
S70-45	45	1000	0.17	155	40.9	de-bonding

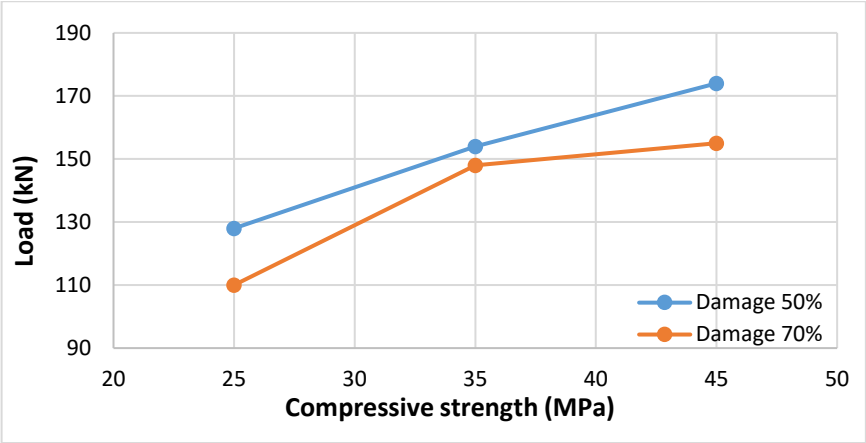

Figure 9. Impact of compressive strength on load capacity.

4. Conclusions

1. A reasonable degree of agreement was reached between the deflections, ultimate loads, and energy absorption of FE models obtained through numerical methods and those discovered through experimentation. For example, the values of the mean and C.V for ultimate loads for $(Pu)_{FE}/(Pu)_{Exp}$ were 0.997 and 5.35 %, respectively, while for deflection of δ_{FE}/δ_{Exp}, values of mean and C.V were 1.197 and 15.99 %, respectively, and for energy absorption, the values of the mean and C.V were 1.134 and 12.2 %, respectively.
2. A numerical analysis was conducted to examine the impact of CFRP thickness on ultimate load capacity. For slab S50-0.34 and S50-0.68, in relation to slab S50-0.17 for group of CFRP fatigue damage equal to 50 %, the percentage of the rose in load capacity is 9.09 and 18.18 %, respectively, and for slab S70-0.34 and S70-0.68, in relation to slab S70-0.17 for group of CFRP fatigue damage equal to 70 %, the percentage of the rose in load capacity is 12.16 and 22.97 %, respectively.
3. A numerical analysis was conducted to determine how the CFRP modulus of elasticity affected the ultimate load capacity. For slab S50-230 and S50-640, in relation to slab S50-160 for a group of CFRP fatigue damage equal to 50 %, the percentage of increased ultimate load capacity is 8.84 and 4.76 %, respectively, and for slab S70-230 and S70-640, in relation to slab S70-160 for a group of CFRP fatigue damage equal to 70 %, the percentage of increased ultimate load capacity is 12.14 and 5.71 %, respectively.
4. A numerical analysis was conducted to examine the impact of CFRP sheet length on ultimate load capacity. The results showed that the percentage increases in load capacity for slab S50-800 and S50-1000, in relation to slab S50-600 for the CFRP fatigue damage 50 % group, were 2.19 and 12.4 %, respectively, and for the slab S70-800 and S70-1000, in relation to the slab S70-600 for the CFRP fatigue damage 70 % group, were 0.74 and 9.63 %, respectively.
5. A numerical study was used to examine how the compressive strength of concrete affected the structural performance of slabs. Findings indicated that the ultimate load capacity rose by a percentage for slab S50-35 and S50-45, related to slab S50-25 for the group of CFRP fatigue damage 50 %, was 20.31 and 35.93 %, respectively, while for slab S70-35 and S70-45 related to slab S70-25 for the group of CFRP fatigue damage 70 %, the percentage increase in load capacity was 34.54 and 40.9 %, respectively.

References

1. Zhang, J., Li, P., Mao, Y., Dong, Zh. The Mechanical Properties of Reinforced Concrete Plate-Girders when Placed Under Repeated Simulated Vehicle Loads. Materials. 2019. 12(11). Article no. 1831. DOI: 10.3390/ma12111831
2. Do, M.-T., Chaallal, O., Aïtcin, P.-C. Fatigue Behavior of High-Performance Concrete. Journal of Materials in Civil Engineering. 1993. 5(1). Pp. 96–111. DOI: 10.1061/(ASCE)0899-1561(1993)5:1(96)
3. Holmen, J.O. Fatigue of Concrete by Constant and Variable Amplitude Loading. ACI Special Publication. 1982. 75. 71–110.
4. Chen Hao-jun, Peng Yi-bin, Zhang Qi-sen. Research on Fatigue Behavior of Concrete Beams Reinforced by Cold-Rolled Deformed Steel Bar. China Journal of Highway and Transport. 2006. 19(1). Pp. 23–27.
5. Schläfli, M., Brühwiler, E. Fatigue of existing reinforced concrete bridge deck slabs. Engineering Structures. 1998. 20(11). Pp. 991–998. DOI: 10.1016/S0141-0296(97)00194-6
6. Wang Chun-sheng, Zhou Jiang, Wu Quan-you, Wang Yu-jiao, Dong Xiao-hong. Fatigue Life and Service Safety Assessment for Existing Concrete Bridges. China Journal of Highway and Transport. 2012. 25(6). Pp. 101–107.

7. Daud, S.A., Daud, R.A., Al-Azzawi, A.A. Behavior of reinforced concrete solid and hollow beams that have additional reinforcement in the constant moment zone. Ain Shams Engineering Journal. 2021. 12(1). Pp. 31–36. DOI: 10.1016/j.asej.2020.07.017
8. Najm, I.N., Daud, R.A., Al-Azzawi, A.A. Behavior of reinforced concrete segmental hollow core slabs under monotonic and repeated loadings. Structural Monitoring and Maintenance. 2019. 6(4). Pp. 269–289. DOI: 10.12989/smm.2019.6.4.269
9. Bakis, Ch.E., Bank, L.C., Brown, V.L., Cosenza, E., Davalos, J.F., Lesko, J.J., Machida, A., Rizkalla, S.H., Triantafillou, Th. Fiber-Reinforced Polymer Composites for Construction – State-of-the-Art Review. 2002. 6(2). Pp. 73–87. DOI: 10.1061/(ASCE)1090-0268(2002)6:2(73)
10. Lateef, H.E., Al-Allaf, M.H., Daud, R.A. Experimental study on bond-slip behavior of NSM-CFRP plate and recycled aggregates concrete substrate. Innovative Infrastructure Solutions. 2024. 9(10). Article no. 368. DOI: 10.1007/s41062-024-01699-9
11. Daud, R.A., Daud, S.A., Al-Azzawi, A.A. Tension stiffening evaluation of steel fibre concrete beams with smooth and deformed reinforcement. Journal of King Saud University – Engineering Sciences. 2021. 33(3). Pp. 147–152.
12. Al-Allaf, M.H., Daud, RA, Daud, SA. Nonlinear Finite Element analysis of concrete corbels with hybrid reinforcements. Mechanics of Advanced Materials and Structures. 2024. 32(21). Pp. 5245–5255. DOI: 10.1080/15376494.2024.2420910
13. Jasim, N.R., Daud, R.A. Behavior of hollow core slabs strengthened by NSM CFRP plates subjected to repeated loading. AIP Conference Proceedings. 2024. 3009(1). Article no. 030086. DOI: 10.1063/5.0193577
14. Fernandes, P.M.G., Silva, P.M., Sena-Cruz, J. Bond and flexural behavior of concrete elements strengthened with NSM CFRP laminate strips under fatigue loading. Engineering Structures. 2015. 84. Pp. 350–361. DOI: 10.1016/j.engstruct.2014.11.039
15. Dalfré, G.M., Barros, J.A.O. NSM technique to increase the load carrying capacity of continuous RC slabs. Engineering Structures. 2013. 56. Pp. 137–153. DOI: 10.1016/j.engstruct.2013.04.021
16. Peng, H., Zhang, J., Cai, C.S., Liu, Y. An experimental study on reinforced concrete beams strengthened with prestressed near surface mounted CFRP strips. Engineering Structures. 2014. 79. Pp. 222–233. DOI: 10.1016/j.engstruct.2014.08.007
17. ACI Committee 440. ACI 440R-07. Report on fiber reinforced polymer (FRP) reinforcement for concrete structures. American Concrete Institute. Farmington Hills, MI, 2007.
18. Wu, Zh., Iwashita, K., Sun, X. Structural Performance of RC Beams Strengthened with Prestressed Near-Surface-Mounted CFRP Tendons. Case Histories and Use of FRP for Prestressing Applications. American Concrete Institute. Farmington Hills, MI, 2007. Pp. 165–178.
19. Choi, H.T., West, J.S., Soudki, Kh.A. Effect of Partial Unbonding on Prestressed Near-Surface-Mounted CFRP-Strengthened Concrete T-Beams. Journal of Composites for Construction. 2011. 15(1). Pp. 93–102. DOI: 10.1061/(Asce)Cc.1943-5614.0000149
20. El-Hacha, R, Gaafar, M. Flexural strengthening of reinforced concrete beams using prestressed, near-surfacemounted CFRP bars. PCI Journal. 2011. 56(4). Pp. 134–151. DOI: 10.15554/pcij.09012011.134.151
21. De Lorenzis, L., Micelli F, La Tegola A. Passive and active near surface mounted FRP rods for flexural strengthening of RC beams. Proceedings of the Third International Conference on Composites in Infrastructure. CD-ROM version. Paper no. 83. San-Francisco, CA, 2002.
22. Daud, R., Cunningham, L., Wang, Y. Non-linear FE Modelling of CFRP-strengthened RC slabs under cyclic loading. Athens Journal of Technology and Engineering. 2015. 2(3). Pp. 161–180.
23. Hameed, M.O., Daud, R.A. Behavior of Fatigue Damaged Reinforced Concrete One-Way Slabs Repaired with CFRP Sheets. Civil And Environmental Engineering. 2024. 20(1). Pp. 364–376. DOI: 10.2478/cee-2024-0028
24. Lubliner, J., Oliver, J., Oller, S., Oñate, E. A plastic-damage model for concrete. International Journal of Solids and Structures. 1989. 25(3). Pp. 299–326. DOI: 10.1016/0020-7683(89)90050-4
25. Tyau, J.S. Finite element modeling of reinforced concrete using 3-dimensional solid elements with discrete rebar. Ph.D. thesis. Brigham Young University, 2009.
26. BS EN 1992-1-1. Eurocode 2: Design of concrete structures: Part 1–1: General rules and rules for buildings. British Standards Institution, 2004.
27. Wang, T., Hsu, Th.T.C. Nonlinear finite element analysis of concrete structures using new constitutive models. Computers & Structures. 2001. 79(32). Pp. 2781–2791. DOI: 10.1016/S0045-7949(01)00157-2
28. Reddy, J.N. Mechanics of Laminated Composite Plates and Shells: Theory and Analysis. CRC Press. Boca Raton, 2003. 858 p. DOI: 10.1201/b12409
29. Hibbitt, K., Karlsson, B.I., Sorenson, E.P. Virtual work. ABAQUS/Standard theory manual. Sorenson Inc, 2016. Pp. 421–422.
30. Abbood K.A., Daud R.A. Preloaded behavior of thick one-way slabs strengthened with NSM–CFRP plates. NeuroQuantology. 2022. 20(6). Pp. 8665–8679. DOI: 10.14704/nq.2022.20.6.NQ22858
31. Abbood K.A., Daud R.A. Experiment Investigation of Behavior of Preloaded Thick One-Way Slabs Repaired by NSM CFRP Plate. Mathematical Statistician and Engineering Applications. 2022. 71(4). Pp. 3695–3708. DOI: 10.17762/msea.v71i4.931

Information about the authors:

Mohammed Hameed,
E-mail: st.mohammed.a.h.f@nahrainuniv.edu.iq

Raid Daud,
E-mail: raid.a.daud@nahrainuniv.edu.iq

Received 08.06.2024. Approved after reviewing 23.12.2024. Accepted 14.01.2025.

Magazine of Civil Engineering

ISSN 2712-8172

journal homepage: http://engstroy.spbstu.ru/

Research article

UDC 69

DOI: 10.34910/MCE.138.6

Neural network modeling for real-time water quality assessment

A.A. Naumova[1] ✉ , ***V.V. Ilinich***[2] , ***M.A. Shiryaeva***[3]

[1] *Russian State Agrarian University – Moskow Timiryazev Agricultural Academy, Moscow, Russian Federation*
[2] *A.N. Kostyakov Federal Scientific Center for Hydraulic Engineering and Land Reclamation, Moscow, Russian Federation*
[3] *Federal Budgetary Institution of Science Federal Scientific Center of Hygiene named after F.F. Erisman of the Federal Service for Supervision of Consumer Rights Protection and Human Well-Being, Mytishchi, Moscow Region, Russian Federation*

✉ *koshevaya81@mail.ru*

Keywords: neural network, Tensorflows Keras 2.2.0, watershed, water, water flow, negative impact, water quality, water resources, optimization's algorithm.

Abstract. In recent decades, water quality problems have become even more pressing due to population growth, industrial expansion, and climate change. A number of studies by foreign researchers have shown the results of applying neural networks. There are studies confirming the reliability of water quality prediction results generated by neural networks. During the work, OpenAI Earth Pro, Microsoft Excel, a water flow sensor based on the Arduino UNO board with author's modifications (tail feathers and a built-in plugin for calculating flow velocity), Python, Tensorflows Keras 2.2.0, Scikit-learn, Pandas libraries for machine learning and developing the neural network architecture were used. Two neural network models were combined to build a hybrid neural network model for predicting water quality parameters in the research. Neural network models provide unique opportunities to improve water resource management at various levels, from local to global. One of the key advantages of such models is the ability to adapt to specific conditions and requirements, providing more accurate predictions and timely decision-making in the face of uncertainty. The relevance of the work is due to the application of neural networks for predicting water quality can contribute to improving the early warning system for pollution, optimizing operational processes at water treatment plants, and developing effective strategies for water resource management. During the research, an innovative hybrid neural network model for predicting water quality parameters was developed, based on the integration of a deep convolutional neural network and a bidirectional recurrent neural network, which consists of three functional parts.

Citation: Naumova, A.A., Ilinich, V.V., Shiryaeva, M.A. Neural network modeling for real-time water quality assessment. Magazine of Civil Engineering. 2025. 18(6). Article no. 13806. DOI: 10.34910/MCE.138.6

1. Introduction

Water resources assessment is critical in contemporary society, especially against progressive anthropogenic pressure on aquatic ecosystems and climate change manifestations. Rivers, lakes, and reservoirs are the main centralized sources of drinking water supply to the population, the key irrigation object for agriculture, the main provider of water resources for the industry, as well as an essential part of the recreation and leisure infrastructure for the population [1].

Due to the increasing human impact and pollution, there has been a significant degradation in the global watersheds' water quality in recent decades. This circumstance necessitates the development and implementation of innovative approaches to monitoring and forecasting the state of the hydrological

environment that exceed conventional methods in terms of accuracy, reliability and efficiency in obtaining results [2, 3].

One of the most prominent trends in this regard is the use of machine learning and neural networks for modelling and predicting factors determining the water quality dynamics [4–6]. Similar models are able to take into account the complex non-linear interrelationships of numerous factors and are self-learning, making them a highly effective tool for solving the assigned tasks.

Surface water quality represents a fundamental determinant of aquatic ecosystem health and the sustainability of water supply systems. Contamination by nutrients (e.g., ammonium, nitrates, phosphorus), organic pollutants, and pathogens can lead to eutrophication, hypoxia, and significant disruption of biogeochemical cycles, adversely affecting biodiversity and ecosystem services [7].

Recent assessments indicate a progressive decline in the chemical, microbiological, and physicochemical status of surface waters in regions with high anthropogenic pressure, including industrial, agricultural, and urban activities [8]. Agricultural runoff, in particular, contributes to elevated concentrations of nitrogenous compounds and pesticides, which exacerbate nutrient loading and pose challenges to conventional water treatment processes [9].

Effective management of water resources under changing climatic conditions requires accurate, timely, and predictive assessments of water quality. Traditional mechanistic models (e.g., QUAL2K, SWAT) often demand extensive input data and computational resources, limiting their adaptability to real-time monitoring and forecasting [10–13]. Machine learning approaches, particularly hybrid neural network models, offer an alternative framework capable of capturing nonlinear interactions among hydrological, chemical, and environmental variables, thereby enhancing predictive accuracy [3–5, 14].

Consequently, there is a demonstrable need for research integrating long-term monitoring data with advanced analytical methods to develop robust predictive models for surface water quality. Such studies are critical for informed decision-making in water resource management, pollution control, and ecological conservation.

The objective of the research was to develop and apply an innovative neural network-based algorithm for predicting key water quality parameters. To evaluate the effectiveness of the proposed approach, its performance was compared with existing statistical and neural network models: autoregressive integrated moving average (ARIMA), recurrent neural, long short-term memory (LSTM) networks.

Object of the study: A section of the Oka River channel within the Ryazan urban agglomeration. This section was selected as representative of the interactions between a major watercourse and surrounding anthropogenic influences.

Subject of the study: Temporal and spatial variations of key water quality parameters (ammonium, total nitrogen, chemical oxygen demand (COD), biochemical oxygen demand (BOD_5), total coliform bacteria (TBA)) and their prediction using machine learning models.

A review of existing approaches to water quality prediction was conducted to identify their methodological limitations and potential for improvement. On this basis, a neural network model was developed. The model structure, input parameters, and training dataset were defined using historical water chemistry data from the Oka River. Calibration of the algorithm was performed to optimize prediction accuracy.

The performance of the developed neural model was evaluated through comparative tests. Predicted values were compared with observed measurements as well as with the results of reference models (ARIMA, recurrent, and LSTM networks). This procedure allowed assessment of the relative advantages of the proposed approach and identification of conditions, under which its application is most effective.

The final stage was the comparison between the new approach and classical methods, through which the advantages and disadvantages of the proposed model were revealed. Finally, recommendations on the algorithm's practical application were formulated, and the prospects for subsequent improvement of the development were identified. The study is a significant contribution to the solution of the strategic problem of water resources quality forecasting.

2. Methods

The study employed a combination of observational, statistical, and computational methods:

1. **Data Collection:** water samples were collected at three intake stations (Sokolovskiy, Okskiy, Borkovskiy) of the Oka River from 2014 to 2022. Measured parameters included ammonium, total nitrogen, COD, BOD_5, and TBA, along with organoleptic and microbiological indicators.

2. **Statistical Analysis:** long-term averages, standard deviations, and exceedances relative to regulatory thresholds were calculated. Differences between intake stations were evaluated using appropriate statistical tests (e.g., t-test, ANOVA, $p < 0.05$).
3. **Neural Network Modeling:** a hybrid model combining convolutional neural networks (CNNs) and bidirectional recurrent neural networks (Bi-RNNs) was developed. Input data included historical water quality parameters and temporal hydrological features. The model was trained and validated using TensorFlow Keras, with hyperparameters optimized to minimize prediction error: root mean square error (RMSE), mean absolute error (MAE), the coefficient of determination (R-squared). Predictions were compared with benchmark models (ARIMA, LSTM, reverse recurrent networks) to assess relative performance.
4. **Data Visualization:** Spatial analysis and visualization were performed using Google Earth Pro. Temporal trends and model predictions were visualized using spreadsheet programs and standard plotting software.

2.1. The Research Object and Hydrological Monitoring

Research into the ecological status and dynamics of water quality parameters was carried out on a section of the Oka River channel located within the Ryazan urban agglomeration [6, 16]. This section serves as a representative model for the interaction of a major watercourse with an urbanized environment.

Effective prediction of the Oka River water quality, enabling timely detection of negative trends and the implementation of measures to prevent sanitary-epidemiological and environmental crises, requires comprehensive and systematic monitoring [17, 18].

A key factor in enhancing the efficiency and representativeness of the monitoring system is the optimal placement of data collection control points. This requires consideration of both the characteristics of the river's hydrological regime and the spatial distribution of potential pollution sources [19].

The presented figure (Fig. 1) proposes an approximate layout for modular weather stations integrated with automatic water sampling systems. Red circles indicate the measuring instruments, the green sector represents the observation area (400 km^2), and the blue sector indicates the zone where observations from two adjacent stations overlap. This overlap ensures the necessary data redundancy, which increases the reliability of the results.

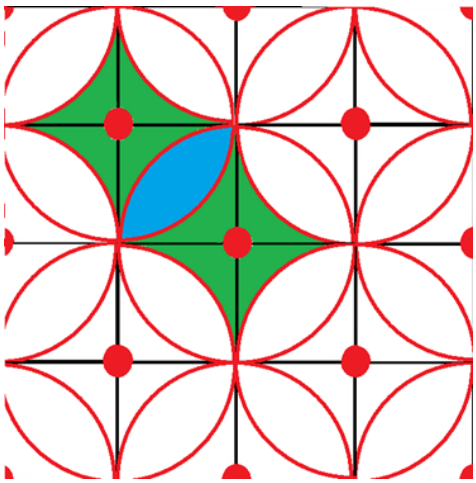

Figure 1. Location scheme of module meteorological stations (created by authors).

The proposed layout for the monitoring stations was designed to optimize economic considerations while maintaining the highest possible level of efficiency for the systematic monitoring system. This is particularly crucial given the stringent budgetary constraints often imposed on environmental protection programs [4, 20–22]. Employing mathematical modeling and optimization methods, considering the hydrological specifics of the water body, characteristics of anthropogenic impact distribution, and economic limitations, allows for a highly accurate determination of the necessary and sufficient number of measuring installations to effectively cover the entire watershed area of the investigated section of the Oka River.

This ensures systematic monitoring and prediction of its ecological status, taking into account the multi-factor dynamics of external influences.

The distances between the modular stations will be:

$$l_1 = 21.6\sqrt{2} = 30.5 \text{ km}; \quad l_2 = 21.6 \cdot 2 = 43.2 \text{ km}.$$

The overlapping area of the observations of the two stations can be determined:

$$F = 2 \cdot \left(\frac{21.6^2 \cdot P}{4} - \frac{21.6^2}{2} \right) = \frac{21.6^2 \cdot P}{2} - \frac{2 \cdot 21.6^2}{2} = \frac{21.6^2 \left(P - 2 \right)}{2} \approx 266 \text{ km}^2.$$

Every two neighbouring stations have one point of overlap of their measuring zones, three stations have two points of overlap and so on in accordance with the established pattern.

Using this trend, it is possible to predict the required number of observation stations for complete coverage of control measurements over the whole area of the considered catchment. To quantify the required value, we propose to build a mathematical model by setting the equation, in which the initial parameter $\left(n \right)$ will be the number of stations providing coverage of the territory of 400 km^2.

Then, the number of intersection points between stations in a 266 km^2 area can be written as $\left(n - 1 \right)$. Having solved this equation, it is possible to determine the minimum necessary number of hydrometric stations to form a regular observation grid and ensure quality hydrometeorological monitoring over the entire catchment area, as well as to design the optimal configuration of the observation network.

Therefore, the following equation is obtained:

$$400n + 266\left(n - 1 \right) = 245000 \text{ km}^2, \quad n \approx 368 \text{ units.}$$

2.2. Water Sampling

During the research and primary data collection, the following software and tools were used: Google Earth Pro for spatial analysis and data visualization, a spreadsheet program for statistical processing and preliminary analysis of the obtained results, and other standard software for data management and visualization.

To improve the measurement accuracy and expand the functional capabilities of the water flow sensor developed on the basis of the Arduino UNO board, a specialized software plug-in was created, which was based on a mathematically derived formula for converting data on water flow rate into flow velocity indicators, taking into account the geometrical parameters of the sensor, in particular, the diameter of the inlet and outlet holes, which was 11.9 mm, which provided an optimal ratio between the sensitivity of the device and its resistance to clogging by suspended particles.

Consequently, to determine the flow velocity (m/s) from the water flow rate (l/s), the following formulas were written into the data conversion plugin:

$$V = \frac{4W}{\pi \cdot D^2 \cdot 1000}, \quad V = \frac{4W}{\pi \cdot 0.0119^2 \cdot 1000}. \tag{1}$$

where π = 3.14, W – initial data of the water flow sensor in (l/s), D – cross-sectional diameters of sensor input and output port.

Fig. 2 shows the design of a high-precision water flow measurement sensor designed to provide continuous remote monitoring of the dynamics of the velocity characteristics of the flow at different depths of the watercourse by cyclic longitudinal scanning of its channel part. The sensor is equipped with a stability system in the guided steering wheel, allowing to automatically correct its attitude depending on the current vector parameters of water mass transport both in the stream thickness and directly on its surface.

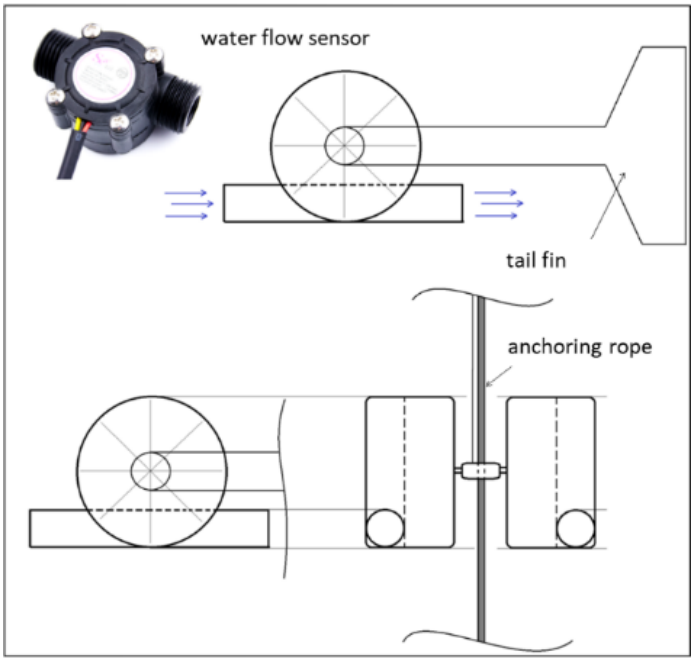

Figure 2. Device of the water flow sensor.

It is assumed that to ensure a stable drift position of the sensor at a given depth and within the required sector of the channel, it will be attached directly to the anchor cable of the unmanned hydrological probe using a flexible ring or hoop mount that provides compensation for its movements. This assembly scheme will make it possible to arrange permanent cyclic real-time hydraulic parameter tracking with high spatial and temporal resolution (Fig. 2).

This sensor sample had a tail fin made of polyvinyl chloride, an environmentally safe and durable thermoplastic material. The material ensured the reliability of the structure in watercourse conditions and minimized the impact on the hydro-ecosystem.

During laboratory approval of the device, it was revealed that at flow velocities over 5.5 m/s, there are limitations in qualitative transmission of measured parameters due to increased impact on the rotating elements of the sensor. Thus, at the rotational speeds of the blades, which ensure the collection of data on velocity, the microprocessor system of the measuring unit becomes overloaded, which complicates the processing of information.

Taking into account this factor, the limit of applicability of the tested model was determined at the level of 5.5 m/s. Further improvement of accuracy and operating range is possible by installing more advanced and expensive components that meet the stringent requirements of high-speed hydrometrics. However, implementation of such measures will require additional financial expenditures for design optimization.

2.3. Machine Learning and Neural Network

The developed machine learning model demonstrated high accuracy in forecasting key water quality parameters of surface water, which is a critical source for water supply. Comparative evaluation against benchmark models (ARIMA, recurrent, and LSTM networks) confirmed its improved predictive performance, indicating that the model can be effectively used for operational monitoring and management of water resources.

Data on the chemical composition of water were obtained in the course of laboratory studies.

The algorithm for integrated water quality prediction proposed in this study includes the following sequential steps:

Step 1: Data cleaning. Before direct water quality prediction, the isolation forest (iForest) method is applied to identify anomalous values in the water quality data set $X_{n\times m}$ (where n denotes the number of water quality parameters and m denotes the number of data groups; in the context of this paper, n and m are constant values: n = 9, m = 1360), and the identified anomalous values are replaced with empty values. Subsequently, the Lagrangian interpolation method is used to fill in the empty values to ensure data integrity and continuity.

Step 2: Data expansion. In the first step, the predicted target is removed from the $X_{n\times m}$ array, resulting in a new array $X_{n\times(m-1)}$. Considering that the water quality data are collected at 4-hour intervals, a sliding window averaging technique with a window size of 6 is applied to form a set of moving averages $Z_{n\times(m-1)}$, which minimises the influence of random factors of variation in water quality data and traces the trend of daily variation of water quality parameters more accurately. In the second step, principal component analysis (PCA) technique is used to reduce the dimensionality of $X_n\times_{(m-1)}$ and retain two principal components $P_{2\times m}$. In order to prevent model overtraining, $Z_{n\times(m-1)}$, $P_{2\times m}$, and $X_{n\times(m-1)}$ water quality data without target parameters are simultaneously fed to the model input, while the target prediction is generated at the model output.

Step 3: Training the model. The available water quality data set is divided into training and test sets in the ratio of 8:2. For this study, the training set included 1100 datasets covering the period from 25 June 2021 to 16 February 2022, while the test set contained 272 datasets collected between 17 February 2022 and 1 April 2022. Considering the long-term dependence of water quality data on temporal factors, a sliding window method [19, 20] is applied to divide the training set into fixed training windows with step length *i* in the time sequence, after which the data from the first *j* training windows are used to predict the (*j*+1)-th training window. At each new training cycle, the oldest window is discarded and the next new window is included in the analysis, and this process continues until the last training window is reached. This approach of discarding outdated data favors training the model with future trends. In the final step, according to each station's test set, the trained model is applied to predict key water quality parameters including total nitrogen, total phosphorus and permanganate oxidizability.

As part of the comprehensive study, a detailed evaluation of the effectiveness of the proposed hybrid neural network model for predicting water quality parameters was carried out, including a benchmarking analysis with reference methods used in the field. In order to obtain a quantitative characterization of forecasting accuracy, the researchers used a number of metrics generally accepted in the scientific community, including: MAE, reflecting the average deviation of predicted values from actual values; MAPE, which allows estimating the relative magnitude of the forecast error; RMSE, which takes into account the square of deviations and gives greater weight to large errors; and R-squared, characterizing the proportion of variance over the forecasted values.

In the initial phase of the study, outliers in the raw water quality data at the study stations were identified and quantified at approximately 1.1, 1.7, and 3.2 % of the total data, respectively, using the iForest method, which is an efficient algorithm for detecting anomalies in multivariate data. After careful removal of identified outliers that could significantly affect the accuracy of the model, the remaining missing values for stations 1–3 were approximately 3.9, 4.5, and 5 %, respectively, which necessitated the application of data reconstruction techniques, in particular, Lagrange interpolation was used to recover a continuous function from a discrete set of points.

3. Results and Discussion

3.1. Chemical Analysis

Long-term monitoring data (2014–2022) were analyzed for three intake stations of the Oka River: Sokolovskiy, Okskiy, and Borkovskiy. The dataset included 52 parameters, among them organoleptic, microbiological, and chemical indicators.

The analysis showed that average ammonium concentrations at the Sokolovskiy intake were 0.48 mg/L, significantly lower than those recorded at the Okskiy and Borkovskiy intakes by 1.6 and 2.1 times, respectively ($p < 0.05$). Exceedances of the maximum permissible concentration (MPC) for ammonium were detected in nearly 20 % of samples at Borkovskiy, compared with 7.5 % at the Oka intake, while no exceedances were found at Sokolovskiy.

For COD and BOD_5, long-term averages did not differ significantly among the three sites. However, 22.7–32.5 % of samples exceeded regulatory limits for COD and 61.8–75.0 % for BOD_5, reflecting persistent oxygen regime disturbances. The mean content of TBA at the Okskiy and Borkovskiy intakes (813.3 and 818.9 CFU/100 ml, respectively) exceeded the values at Sokolovskiy by 1.5 times ($p < 0.05$).

Some results are summarized in Fig. 3, which presents mean, maximum, and minimum values for selected indicators across the three intake points.

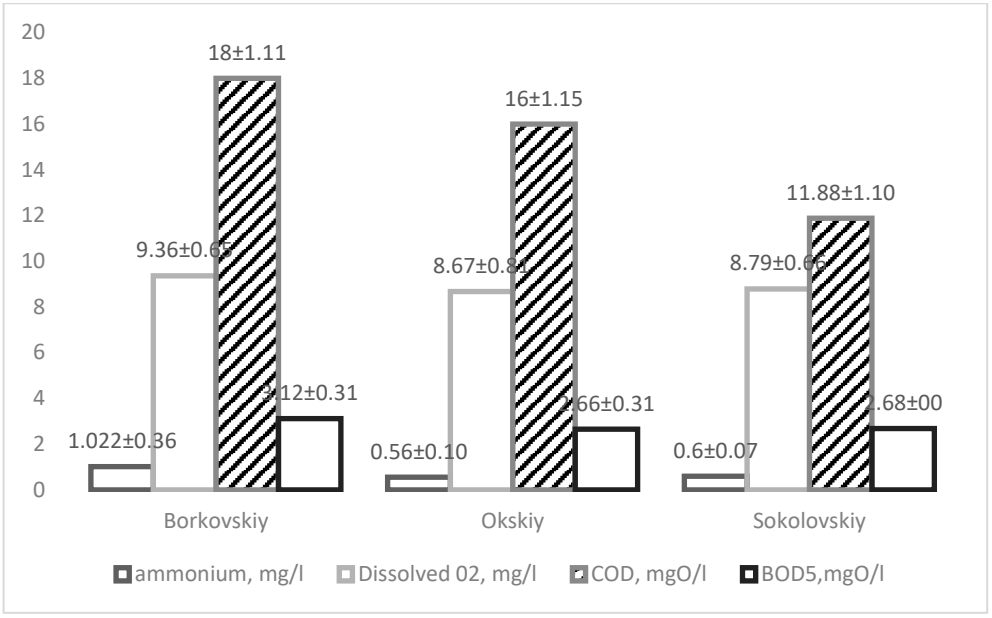

a

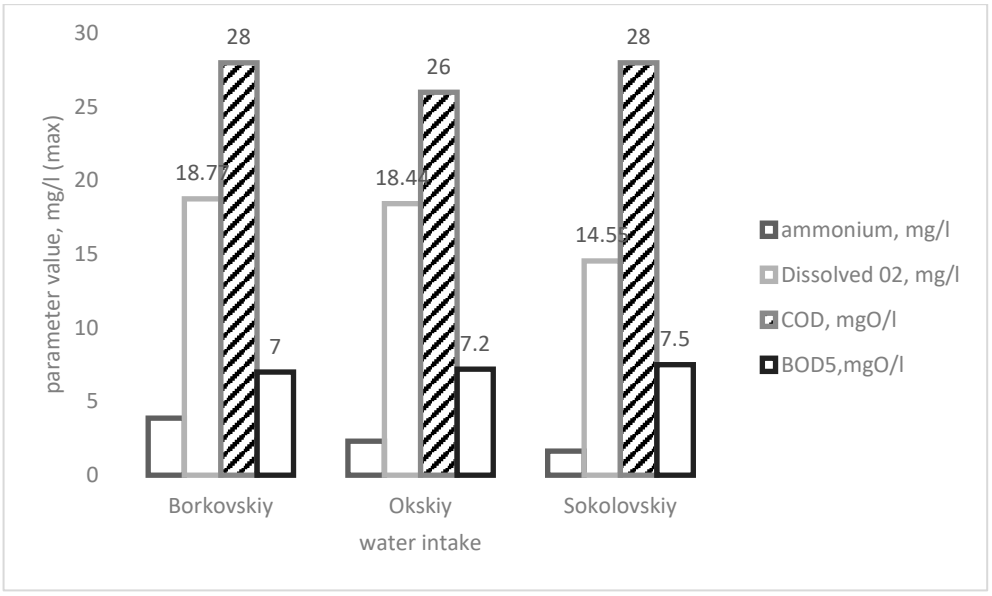

b

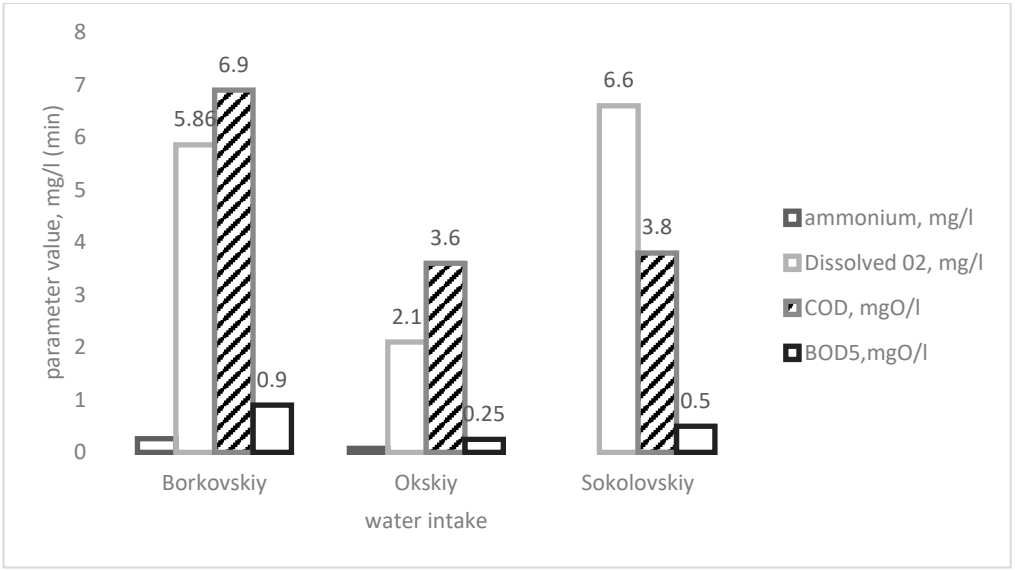

c

Figure 3. Some water quality indicators of the Oka River of three researched water intakes for the period 2014–2022, where: a – the mean values, b – the maximum values, c – the minimum values.

Overall, the data demonstrate spatial heterogeneity in water quality across intake sites and frequent exceedances of regulatory standards, particularly for oxygen-demanding substances and microbial contamination. These findings highlight the need for continuous monitoring and reliable prediction tools to support timely water quality management.

3.2. The Neural Network Development

Within the current research work, an innovative hybrid neural network model for predicting water quality parameters based on the deep CNN integration and Bi-RNN has been developed, which consists of three functional parts. At the initial stage, the model is applied to identify and extract potential non-linear relationships between the Oka River water quality time series data in order to generate effective low-dimensional features. Then, based on the extracted features, a vector of water quality features is constructed and used as input to a deep CNN. During the training process, the network continuously adjusts the weights and biases by considering the dependency of short-term, long-term, and contextual attributes of the time series data to further optimize the water quality information for more accurate feature expression. In the final step, a full connection layer is connected at the top of the model to act as an output layer for generating predicted values of water quality parameters.

The software implementation of the developed hybrid neural network prediction model was carried out using the high-performance deep learning library Tensorflows Keras version 2.2.0, which provides a wide range of tools for building and training neural networks. The model training process was carried out over 50 epochs using 120-time intervals to achieve an optimal balance between prediction accuracy and computational cost. The Adam method, which combines the advantages of adaptive gradient descent and method of moments methods, was applied as an optimization algorithm to adjust the weights and biases of the model. Once the convergence of the model was achieved, which indicated that the loss function was minimized, the final weights were obtained and subsequently used to predict water quality at the studied intake stations (Sokolovskiy, Okskiy, and Borkovskiy). The model architecture and parameters were carefully selected and set as follows: the number of hidden layers was two, which allowed the model to effectively capture complex non-linear dependencies in the data; the conjugate gradient method, known for its ability to quickly converge to an optimal solution, was chosen as the optimization algorithm; the minimum relative change in the learning error rate was set at 0.001, which provided a balance between model accuracy and the prevention of overtraining.

This makes it possible to use the presented neural network model to fill data gaps by calculating missing concentration values of certain compounds. Some results of the neural network modelling covering a 25-year observation interval (n = 25) are demonstrated as an example in Graph 3 for the ammonium indicator of the Oka water intake. The obtained regularities can be used for forecasting the dynamics of the studied indicators in the future.

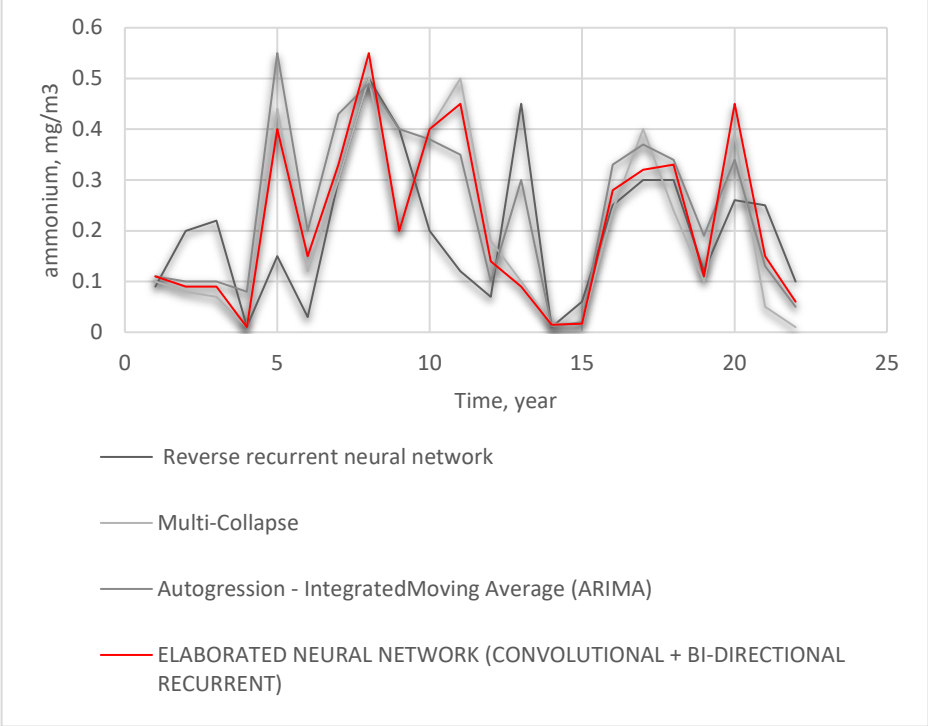

Figure 4. Predictive results of the Okskiy water intake based on neural network on the content of ammonium in comparison with existing neural network models.

This study proposes an alternative approach to water quality prediction based on the application of neural networks to analyze large historical data sets, which is a fundamentally different method from the traditional mechanistic models widely used in the field. Mechanistic models of water quality, which include such well-known systems as QUAL, WASP, MIKE, SWAT, BASINS and a number of others, are based on a detailed description of the structure of the water system under study and taking into account numerous constraints associated with the complex of physical, biological, and chemical processes occurring in the aquatic environment, which causes their high complexity and requires a significant amount of input information for the creation and subsequent solution of a system of equations describing the dynamics of changes in water quality in time and space [23, 24].

Despite their widespread use and acceptance in the scientific community, mechanistic models are characterized by a high degree of complexity and require a significant amount of input data, including numerous modelling parameters, conditions of pollutant sources and effluents, as well as other specific characteristics of the water system, which makes the process of building such models extremely time-consuming and the determination of optimal parameters difficult, significantly limiting their applicability to a wide range of watersheds.

The considered neural model, built on the basis of modern deep architectures, has shown high efficiency in solving this problem. Nonlinear multilayer data processing mechanisms underlying the model make it possible to identify complex interdependencies between water quality indicators and external factors, while forming statistically significant predictions. The conducted studies have confirmed a high degree of reliability of predictions, which is due to the model's ability to effectively analyze and predict non-linear processes under conditions of uncertainty.

Furthermore, the model is strongly multi-purpose, permitting its application to different watershed types, including rivers, lakes, and reservoirs. This significantly expands the potential use of the model for water quality monitoring and water resources management. There is an undeniable advantage of the proposed neural model over traditional numerical algorithms due to its higher prediction accuracy and computational efficiency. This model opens new perspectives for the development of promising approaches in the field of water resources monitoring and management.

3.3. Neural Network's Benefit for Crop Yields

Combining CNN with Bi-RNN offers a powerful approach to analyzing river parameters, which can significantly benefit agriculture in various ways. Here's how the integration of these neural network architectures can support agricultural practices in the context of monitoring water quality and river health:

1. **Data Fusion and Multi-Scale Feature Extraction**

- **Convolutional Layers**: CNNs are excellent at capturing spatial features from high-dimensional data, such as images of rivers, satellite imagery, or time-series data related to river conditions. They can analyze patterns in the data, such as water color changes, sediment transport, or algal blooms.
- **Bi-RNNs**: Once the CNN has extracted spatial features, the Bi-RNN can analyze sequential data by processing it in both forward and backward directions. This dual processing helps capture temporal dependencies and patterns over time, such as changes in water quality or flow rates that occur seasonally or due to specific weather events.

2. **Enhanced Prediction of Water Quality**

- **Water Quality Metrics**: By processing data related to water quality parameters (e.g., pH, turbidity, temperature, and chemical pollutants), the combined model can predict how these factors may evolve over time. This predictive capability is crucial for early detection of issues, such as contamination or harmful algal blooms, which can directly affect agricultural practices.
- **Impact on Crop Health**: Understanding the temporal trends and spatial distribution of river parameters allows farmers to make informed decisions about irrigation practices, such as when to water crops or when to take remedial actions (e.g., treating water or altering planting schedules) to mitigate adverse effects.

3. **Forecasting Hydrological Patterns**

- **Flow and Flood Predictions**: The model was applied to forecast river flow patterns and potential flooding events using historical and current hydrological data. These forecasts provide quantitative information on flow dynamics and water level variations, which can support operational water management and early warning systems for flood risk mitigation.
- **Irrigation Management**: Understanding river flow patterns and water availability assists in optimizing irrigation practices, thereby conserving water and improving crop yields. Accurate

predictions can help determine the best times to irrigate, reducing waste and ensuring adequate moisture for crops.

4. **Integration of Remote Sensing Data**

- **Satellite Imagery Analysis**: CNNs processes satellite images to monitor changes in land use, vegetation, and water bodies. When combined with Bi-RNNs for time-series analysis, the model can reveal temporal patterns and dependencies between key water quality parameters, providing insights into the dynamics and interactions of the river ecosystem.
- **Environmental Monitoring**: By continuously integrating and analyzing real-time data from various sources (e.g., weather stations, sensor networks), this combined model can help monitor the ecological health of river systems and the surrounding agricultural lands.

5. **Adaptive Management Strategies**

- **Decision Support Systems**: The insights derived from this model can feed into decision support systems for farmers, offering recommendations based on predictive analytics. For example, farmers can receive alerts about potential water quality issues or optimal irrigation timings based on predicted river conditions.
- **Sustainability Practices**: By understanding how agricultural practices impact river health and vice versa, stakeholders can implement more sustainable practices that balance agricultural productivity with environmental conservation.

3.4. Statistical Parameters

To evaluate the advantages and disadvantages of the proposed prediction model and other benchmark neural networks, such as ARIMA, LSTM, and reverse recurrent, the MAE, reflecting the average deviation of predicted values from actual values; MAPE, RMSE, accounting for the square of deviations; and R-squared were compared (Table 1). The developed model showed the strongest performance in comparison with the ARIMA reference neural network model and the reversible recurrent model. The strongest competitor was the multi-convergent model, which gave an average RMSE of 0.0557, while the developed model showed an error 0.0248 lower (i.e., average RMSE=0.0309).

Table 1. Table captions should be placed above the tables.

Water quality	Statistical processing model parameters	Neural network type			
		ARIMA	Reverse recurrent	LSTM	Elaborated (CNN + Bi-RNN)
COD, mgO2/l	R-squared	0.9408	0.9920	0.9996	0.9996
	RMSE	1.2030	0.5360	0.0566	0.0299
Total nitrogen, mg/l	R-squared	0.8760	0.9933	0.9999	0.9996
	RMSE	1.0000	0.5400	0.0542	0.0315
ammonium	R-squared	0.9400	0.9945	0.9999	0.9999
	RMSE	0.9850	0.5466	0.0520	0.0310
O2, mg/l	R-squared	0.9308	0.9900	0.9996	0.9999
	RMSE	1.0000	0.5280	0.0600	0.0312

4. Conclusion

Laboratory results indicated that water from the Sokolovskiy water intake had a significantly lower long-term average concentration of total ammonia equal to 0.48 mg/l. This value was significantly lower than similar values at the Okskiy and Borkovskiy water intakes, which were 1.6 and 2.1 times higher, respectively ($p < 0.05$). This value was significantly lower than similar values at the Okskiy and Borkovskiy water intakes, which were 1.6 and 2.1 times higher, respectively ($p < 0.05$). No significant differences were found in the long-term average values of COD and BOD_5 in the waters of the investigated water intakes. At the same time, the percentage of single samples, in which these parameters did not meet the established hygienic standards, ranged from 22.7 to 32.5 % for COD and from 61.8 to 75.0 % for BOD_5, respectively.

The developed neural network model was applied for the prediction of key water quality parameters (COD, total nitrogen, ammonium, and dissolved oxygen) at monitoring sites of the Oka River. Input variables included hydrological and meteorological data, as well as historical records of water chemistry. The model was trained and tested on time series from 2014–2022.

The evaluation demonstrated that the neural network provides reliable short-term forecasts of water quality. In particular, the combined CNN–Bi-RNN architecture achieved higher accuracy than ARIMA, simple recurrent, and LSTM models (Table 1). For example, RMSE values for ammonium prediction were reduced to 0.0310, while R-squared values approached 0.9999.

These results indicate that the proposed model can effectively capture nonlinear dependencies in hydrological and chemical datasets. The approach enables early detection of deviations from regulatory thresholds and can be integrated into monitoring systems for operational water quality control.

In order to ensure high reliability of the initial information base, advanced approaches to data processing, including the iForest algorithm and Lagrangian interpolation methods, were used at the preliminary stage of the study to not only effectively improve the integrity of the information set but also minimize the potential impact of errors and anomalies on the subsequent modelling process. In addition to pre-processing of the input data, the moving average method and PCA method were used to optimize water quality parameters and prevent the phenomenon of model overfitting, which is a critical factor for ensuring high accuracy of forecast calculations in the long term. Thus, we developed an innovative hybrid neural network model for predicting water quality parameters based on the integration of a deep CNN and a Bi-RNN, which consists of three functional parts.

The combination of CNNs and Bi-RNNs provides a robust framework for analyzing temporal and spatial patterns of key river water quality parameters. By leveraging spatial and temporal data, this integrated CNN–Bi-RNN approach improves the accuracy of water quality predictions and enables more comprehensive analysis of river dynamics, supporting effective monitoring and water management.

References

1. Liao, Z., Wang, X., Zhang, Yu., Qing, H., Li, Ch., Liu, Q., Cai, J., Wei, Ch. An integrated simulation framework for NDVI pattern variations with dual society-nature drives: A case study in Baiyangdian Wetland, North China. Ecological Indicators. 2024. 158. Article no. 111584. DOI: 10.1016/j.ecolind.2024.111584
2. Talal, M., Alamoodi, A.H., Albahri, O.S., Albahri, A.S., Pamucar, D. Evaluation of remote sensing techniques-based water quality monitoring for sustainable hydrological applications: an integrated FWZIC-VIKOR modelling approach. Environment, Development and Sustainability. 2024. 26(8). Pp. 19685–19729. DOI: 10.1007/s10668-023-03432-5
3. Shivam, K., Tzou, J.-Ch., Wu, Sh.-Ch. Multi-step short-term wind speed prediction using a residual dilated causal convolutional network with nonlinear attention. Energies. 2020. 13(7). Article no. 1772. DOI: 10.3390/en13071772
4. Wu, G.D., Lo, S.L. Predicting real-time coagulant dosage in water treatment by artificial neural networks and adaptive network-based fuzzy inference system. Engineering Applications of Artificial Intelligence. 2008. 21(8). Pp. 1189–1195. DOI: 10.1016/j.engappai.2008.03.015
5. Ho, J.Yu., Afan, H.A., El-Shafie, A.H., Koting, S.B., Mohd, N.S., Jaafar, W.Z.B., Hin, L.S., Malek, M.A., Ahmed, A.N., Mohtar, W.H.M.W., Elshorbagy, A., El-Shafie, A. Towards a time and cost-effective approach to water quality index class prediction. Journal of Hydrology. 2019. 575. Pp. 148–165. DOI: 10.1016/j.jhydrol.2019.05.016
6. Juwana, I., Muttil, N., Perera, B.J.C. Uncertainty and sensitivity analysis of West Java Water Sustainability Index – A case study on Citarum catchment in Indonesia. Ecological Indicators. 2016. 61(2). Pp. 170–178. DOI: 10.1016/j.ecolind.2015.08.034
7. Shamsutdinova, T.M. Application of Neural Network Modeling in Problems of Predicting the Level of River Floods. Vestnik NSU. Series: Information technologies. 2023. 21(2). Pp. 39–50. DOI: 10.25205/1818-7900-2023-21-2-39-50
8. Shitikov, V.K., Zinchenko, T.D., Golovatyuk, L.V. Neural network methods of surface water quality assessment by hydrobiological indicators. Izvestia Samara Scientific Centre of the Russian Academy of Sciences. 2002. 4(2). Pp. 280–289.
9. Noor, S.S.M., Saad, N.A., Akhir, M.F.M., Rahimet, M.S.A. QUAL2K water quality model: A comprehensive review of its applications and limitations. Environmental Modelling & Software. 2024. 184. Article no. 106284. DOI: 10.1016/j.envsoft.2024.106284
10. Vorobyev, S.N., Pokrovsky, O.S., Korets, M., Shirokova, L.S. A snap-shot assessment of carbon emission and export in a pristine river draining permafrost peatlands (Taz River, Western Siberia). Frontiers in Environmental Science. 2022. 10. Article no. 987596. DOI: 10.3389/fenvs.2022.987596
11. Kaal, J., González-Pérez, J.A., San Emeterio, L.M. Fingerprinting macrophyte Blue Carbon by pyrolysis-GC-compound specific isotope analysis (Py-CSIA). Science of the Total Environment. 2025. 836. Article no. 155598. DOI: 10.1016/j.scitotenv.2022.155598
12. Rosenthal, O.M., Fedotov, V.Kh., Identification of water polluting enterprises based on neural network analysis. Prirodoobustrojstvo. 2023. 1. Pp. 62–68. DOI: 10.26897/1997-6011-2023-1-62-68
13. Shamsutdinova, T.M. Application of Neural Network Modeling in Problems of Predicting the Level of River Floods. Vestnik NSU. Series: Information Technologies. 2023. 21(2), Pp. 39–50. DOI: 10.25205/1818-7900- 2023-21-2-39-50
14. Shitikov, V.K., Zinchenko, T.D., Golovatiyk, L.V. Methods of Neural Networks for Estimation of Superficial Waterís Quality by Usage of Hydrobiological Exponents. Institute of Ecology of the Volga River Basin of Russian Academy of Sciences. 2002. 4(2). Pp. 280– 289.
15. Zholdakova Z.I., Sinitsyna O.O., Turbinsky V.V. About adjustment of requirements to zones of sanitary protection of sources of the centralized economic and drinking water supply of the population. Hygiene and Sanitation. 2021. 100(11). Pp. 1192–1197. DOI: 10.47470/0016-9900-2021-100-11-1192-1197
16. Jiang, Y., Li, Ch., Sun, L., Guo, D., Zhang, Yi., Wanget, W. A deep learning algorithm for multi-source data fusion to predict water quality of urban sewer networks. Journal of Cleaner Production. 2021. 318. Article no. 128533. DOI: 10.1016/j.jclepro.2021.128533

17. Kim, J., Seo, D., Jang, M., Kim, J. Augmentation of limited input data using an artificial neural network method to improve the accuracy of water quality modeling in a large lake. Journal of Hydrology. 2021. 602. Article no. 126817. DOI: 10.1016/j.jhydrol.2021.126817
18. Liu, H., Zhang, F., Tan, Y., Huang, L., Li, Y., Huang, G., Luo, Sh., Zeng, A. Multi-scale quaternion CNN and BiGRU with cross self-attention feature fusion for fault diagnosis of bearing. Measurement Science and Technology. 2024. 35(8). Article no. 086138. DOI: 10.1088/1361-6501/ad4c8e
19. Lu, X., Dong, Yu, Liu, Q., Zhu, H., Xu, X., Liu, J., Wang, Yi. Simulation on TN and TP Distribution of Sediment in Liaohe Estuary National Wetland Park Using MIKE21-Coupling Model. 2023. Water. 15(15). Article no. 2727. DOI: 10.3390/w15152727
20. Tiyasha, Tung, T.M., Yaseen, Z.M. Deep Learning for Prediction of Water Quality Index Classification: Tropical Catchment Environmental Assessment. Natural Resources Research. 2021. 30(6). Pp. 4235–4254. DOI: 10.1007/s11053-021-09922-5
21. Wongburi, P., Park, J.K., 2023. Prediction of Wastewater Treatment Plant Effluent Water Quality Using Recurrent Neural Network (RNN) Models. Water. 15(19). Article no. 3325. DOI: 10.3390/w15193325
22. Zhu, M., Wang, J., Yang, X., Zhang, Y., Zhang, L., Ren, H., Wu, B., Ye, L. A review of the application of machine learning in water quality evaluation. Eco-Environment & Health. 2022. 1(2). Pp. 107–116. DOI: 10.1016/j.eehl.2022.06.001
23. Gao, L., Biderman, S., Black, S., Golding, L., Hoppe, T., Foster, C., Phang, J., He, H., Thite, A., Nabeshima, N., Presser, Sh., Leahy, C. The Pile: An 800GB Dataset of Diverse Text for Language Modeling. arXiv. 2020. arXiv:2101.00027v1. DOI: 10.48550/arXiv.2101.00027
24. Da Silva, A.C., das Graças Braga da Silva, F., de Mello Valério, V.E., Silva, A.T.Y.L., Marques, S.M., dos Reis, J.A.T. Application of data prediction models in a real water supply network: comparison between arima and artificial neural networks. Revista Brasileira de Recursos Hídricos. 2024. 29. Article no. e12. DOI: 10.1093/nar/gks1219

Information about the authors:

Anna Naumova,
ORCID: https://orcid.org/0000-0002-0373-8655
E-mail: koshevaya81@mail.ru

Vitaliy Ilinich, *PhD in Technical Sciences*
ORCID: https://orcid.org/0000-0003-2094-2882
E-mail: vilinitch@gmail.com

Margarita Shiryaeva,
ORCID: https://orcid.org/0000-0001-8019-1203
E-mail: margaretshiryaeva@gmail.com

Received 19.11.2024. Approved after reviewing 10.09.2025. Accepted 10.09.2025.

Magazine of Civil Engineering

ISSN 2712-8172

journal homepage: http://engstroy.spbstu.ru/

Research article

UDC 628.16.06

DOI: 10.34910/MCE.138.7

Physical and mathematical model of a settling tank with thin-layer modules

A.Ya. Gilmanov ✉ , ***B.V. Grigoriev*** , ***A.P. Shevelev*** , ***D.A. Vazhenin***

Tyumen State University, Tyumen, Russian Federation

✉ *a.y.gilmanov@utmn.ru*

Keywords: settling tank, thin-layer modules, hydraulics, mathematical model, experimental installation, plate tilt angle, substance concentration, coagulant, salinity, validation

Abstract. The presence of fine impurities in industrial water complicates the operation of fine water purification systems. To solve this problem, thin-layer settling tanks have become widespread in industry due to their high consumption characteristics. Depending on the application and the consumer, the maximum permissible concentrations of dispersed particles can vary in wide ranges. Optimizing the operation of a thin-layer tank requires conducting field experiments in laboratory and industrial installations. Mathematical modeling allows to reduce the number of experiments. The aim of the work is to develop a mathematical proxy model of a settling tank with thin-layer modules, which for the first time considers the influence of the concentration of coagulant and alkali on the particle size distribution, as well as salinity on the particle deposition rate. This model is based on simplified laws of conservation of mass and momentum in the hydraulic approximation. To study the effect of the parameters of the settling tank and reagents on the concentration of dispersed particles at the outlet, experiments were planned and conducted on a laboratory installation in a wide range of changes in these parameters. The values of the concentration of dispersed particles at the outlet at different angles of inclination of the plates, their quantity and concentrations of coagulant, alkali, and salt were obtained. The simulation results are compared with experiments, and their satisfactory agreement with each other is shown with an average error of 3 %. Based on the sensitivity analysis, ranges of parameters of the settling tank and chemical reagents were determined, for which the mathematical model gives representative results. It was found that with an increase in the concentration of chemical reagents, the proportion of particles with sizes less than 100 μm in the stream decreases, which leads to an increase in the degree of water purification.

Funding: The article was prepared within the framework of a Research Contract: "Creation of a laboratory sample of a coalescer settling tank" for JSC "HMS Neftemash".

Citation: Gilmanov, A.Ya., Grigoriev, B.V., Shevelev, A.P., Vazhenin, D.A. Physical and mathematical model of a settling tank with thin-layer modules. Magazine of Civil Engineering. 2025. 18(6). Article no. 13807. DOI: 10.34910/MCE.138.7

1. Introduction

Currently, various types of settling tanks are used to effectively purify water from oil treatment facilities. These devices should be carefully selected for the composition of the incoming water, the types and concentration of pollutants – oil, suspended mineral particles and their fractional composition. The requirements of subsurface users for the degree of water purification for the reservoir pressure maintenance system are quite high, and the key parameter here is the permeability of the reservoir near the well, through which hundreds of cubic meters of water are injected. The concentration of suspended particles leads to gradual colmatation of the rock and directly affects the dynamics of reducing its permeability, which in turn increases the load on pumping and compressor equipment and, in extreme cases, can completely shut

down the well. In this regard, the maximum concentration of suspended particles is regulated and should not exceed 50 mg/l[1], but in fact it should be even lower.

The mode of water injection into the pressure maintenance system, rock permeability, mineralization and density of water, and other parameters of the "above-ground equipment – fluid – reservoir" system are individual in each case, and the water treatment mode for pressure maintenance system also requires an individual approach: from a static tank for a low-flow well to a dynamic tank with a capacity of several hundred cubic meters per day. A similar approach is required by the design of settling tanks, the dimensions of which are limited by their transportability, primarily by rail transport, the requirements for ease of maintenance and a high degree of water purification with high productivity. The substantiation of the basic design of the settling tank and the effectiveness of its operation begins with the production of a laboratory sample that preserves the basic parameters of an industrial installation, and then testing its effectiveness on fluid models equivalent in composition and properties to the fluid in the field. Laboratory research is a mandatory and important component of research and development work [1], because it allows to avoid a lot of mistakes when designing a large-scale installation, save a lot of money and materials, test hypotheses and assumptions on a laboratory facility, which, unlike a full-scale installation, is easy to make changes, vary the initial and boundary parameters, easy to repair, etc. But probably the most important thing is that building a laboratory facility and testing it is relatively cheap.

Settling tanks with coalescent (thin-layer) modules are of particular interest for production and industrial implementation in field oil collection and treatment systems [2]. Such equipment is designed to purify water from mechanical impurities or oil products and has long proven itself for effective wastewater treatment. However, in order to adapt the technology for the oil industry, it is necessary, while maintaining the principle of operation, to review a number of features and materials used in the design, considering the requirements for the mode of operation of reservoir water treatment facilities and the quality of water treatment.

Thus, there is a need for a scientifically based description of the technology of separation of multiphase media using coalescer settling tanks, which includes both the creation of a laboratory installation for testing hypotheses, and a physical and mathematical model with a predictive function beyond laboratory tests, for example, in the case of scaling the installation to an industrial design, critically small or large flow rates, high concentration of suspended particles, and so on. Modeling becomes particularly relevant in the case of a significant number of influencing parameters and long-term experiments.

The existing models for calculating parameters in settling tanks with thin-layer modules are either based on a simplified hydraulic approach [3] using empirical relations [2, 4–8], or assume a detailed calculation of the multiphase flow in the settling tank using numerical methods [9–11] or commercial software [12–16]. The second approach allows to consider in more detail the nature of the flow in the device [12, 15] but requires significant time and financial costs, as well as long-term adjustment of the model to real data. The use of neural network modeling also requires a long learning process and a large sample of input information [17]. Therefore, the use of simplified modeling approaches is more justified [2]. Unfortunately, the existing models [2, 4–8] do not consider some of the effects observed in real experiments. In particular, simplified models do not consider the effect of the type and concentrations of reagents often used to increase the efficiency of the process [18, 19] on the particle size distribution, as well as mineralization of reservoir water on the particle deposition rate [20, 21].

The preparation of clean water is essential in various industries. Thus, water is used for heating rooms, cooling power plants, soil irrigation, and in many other cases [22, 23]. Since the oil and gas complex occupies a significant share in the Russian economy, the use of water for its purposes as a displacing agent in oil production should be considered [24]. As a rule, in this case, water previously extracted from the reservoir is used. Such water usually contains a large amount of various additional particles [25]. Injection of water with impurities into the reservoir can lead to contamination of the bottom-hole zone of wells and an increase in bottom-hole pressure to maintain the previous injection rates. Subsequently, this can lead to the formation of fractures in the formation [26]. Therefore, the relevant task is to clean water from impurities.

Therefore, the aim of the work is to create a physical and mathematical proxy-model of a settling tank with thin-layer modules, which for the first time considers the influence of the concentration of coagulant and alkali on the particle size distribution, as well as salinity on the particle deposition rate. Such

[1] OST 39-225-88. Voda dlya zavodneniya neftyanyh plastov. Trebovaniya k kachestvu [Water for flooding oil reservoirs. Quality requirements]. Industry standard: Approved by Order of the Ministry of Petroleum and Industry No. 147 dated 03/28/88: introduced for the first time, date of introduction 07/01/90. Developed by Giprovostokneft of the Ministry of Oil and Gas Industry, BashNIPIneft, VNIISPTNEFT, TatNIPIneft, All-Union Oil and Gas Research Institute. Moscow: Minnefteprom, 1990. 10 p.

a model will be based on a simplified hydraulic approach using empirical relationships. To achieve this aim, the following tasks were formulated and solved: development of a physical and mathematical proxy-model for the operation of a thin-layer tank; design of experiments to determine the effect of the parameters of the tank and reagents on the concentration of dispersed particles at the outlet; assembly of a laboratory installation and experiments; validation of the developed proxy-model for the operation of a thin-layer tank; sensitivity analysis of the model.

2. Methods

2.1. Experimental Installation

The experimental installation should, on the one hand, recreate a model of reservoir water with a given mineralization and suspended mineral particles, and, on the other hand, purify this water from mineral impurities. Therefore, the first part of the installation should include a container designed for long-term experiments, an agitator to maintain the homogenization of the mixture, a pump for injection the mixture, a system for measuring and controlling flow, a system for maintaining water temperature, and so on. The second part of the installation is a "coalescer tank", which in laboratory design should allow visual observation of the processes of separation and purification of water but should repeat the basic design solutions of industrial settling tanks.

As a result of the design and preparation of design documentation, considering the limitations and requirements imposed on the laboratory sample, the laboratory installation scheme shown in Fig. 1 was developed and approved. The installation consists of the following main elements: a T500l tank, a propeller agitator for a T500 tank, a TSM.50M resistance thermometer, a two-channel TRM202 regulator meter, a Vortex FN-250A pump, a flow meter and a flow meter controller, a 0.8 kW fuel tank, an ESQ-A500 frequency converter, pipelines, shut-off valves, etc. The coalescer tank is made of 12 mm thick plexiglass sheet, its geometric parameters are: length – 1050 mm; width – 152 mm; height – 450 mm. The block of thin-layer modules includes plates and brackets for fixing the plates, which allow to vary the angle of inclination of the plates and their number within the range of 45° and 60°; number of plates: for 45° angle, the maximum number is 26 pcs., for 60° angle, the maximum number is 42 pcs. The material of the plates and brackets is St3 steel. Plate sizes for 45° angle are 495×151×2 mm, for an angle of 60° are 404×151×2 mm. The schematic diagram is shown in Fig. 1.

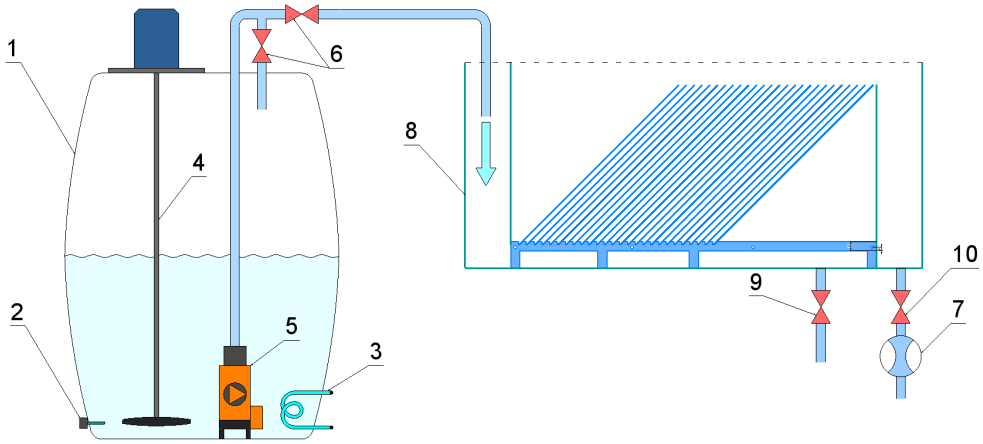

Figure 1. Schematic diagram of the laboratory installation: 1 – source water tank (500 l), 2 – temperature sensor, 3 – water heater, 4 – agitator, 5 – liquid pump, 6 – pressure control valves, 7 – flow meter, 8 – coalescer tank, 9 – sediment drain tap, 10 – tap for draining pure water.

The principle of operation of the installation is as follows. Process water is poured into the source water tank 1. The set temperature value is set on the controller of the temperature control system, the water is heated by the spiral heater 3, and the temperature is monitored using the temperature sensor 2. For uniform heating of the liquid, the top-mounted agitator 4 is switched on. If the experiment is carried out on mineralized water, the required amount of salt (NaCl) is poured into the water during the heating process to the value of the declared mineralization. To achieve concentrations of suspended solids, a combination of sand and clay of large and small fractions is poured into the container during mixing in a given mass ratio. If the experiment involved the use of chemical reagents to intensify purification, then aqueous solutions of these reagents were prepared in advance, and the solutions were added to the container based on the calculated concentration per volume of water in the container.

In parallel with the water preparation, the coalescer 8 was filled with the same 54 l of process water (the volume of the flow quenching zone and the zone of thin-layer modules), the water temperature was

adjusted to the water temperature in the source water tank. Next, the liquid injection pump 5 is started and the required flow rate is set using the control valves 6. The flow rate is monitored both by means of a 7-meter flow meter and visually on a measuring scale in the clean water area. To measure the flow rate using a scale, it is necessary to periodically turn off the tap 10 and measure the filling volume of the pure water zone for a fixed time.

First, water with mechanical impurities enters the flow damping zone in the tank. There, the flow rate decreases and some of the mechanical impurities fall out, after which the liquid enters through the passage window into the zone of thin-layer modules and rises up. A block of thin-layer modules made of plates at a certain angle is installed in the flow path. With the correct selection of the operating mode, suspended particles, moving in the space between adjacent plates, should settle on the lower shelf, concentrate and slide down, accumulating in the lower part of the zone of thin-layer modules, and purified water overflows into the zone of clean water (see Fig. 2).

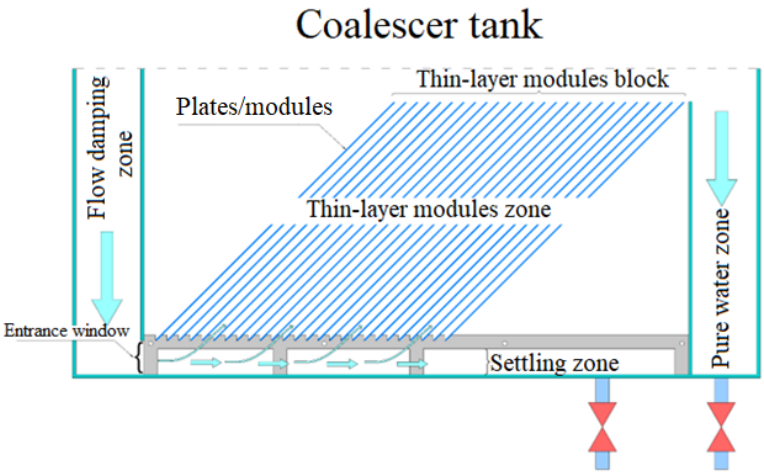

Figure 2. Scheme of the coalescer tank.

After injection of 100–130 l, it is assumed that the operation of the tank has reached a stationary mode, the water from the tank 1 has displaced all the original process water from the tank and enters the pure water zone. The last stage of the experiment involves sampling purified water from a pure water area. This stage is usually preceded by a control measurement of the flow rate on a measuring scale, after which the pump is turned off and 2 l of liquid are taken from the volume of liquid collected in the pure water zone to determine the degree of purification. The degree of water purification is assessed by filtering the selected samples through a blue-ribbon paper filter placed in a Buchner funnel mounted on a Bunsen flask connected to a vacuum pump. Based on the results of the difference in the mass of the filter before and after filtration, the efficiency of the coalescer sump was evaluated. The general view of the installation is shown in Fig. 3, the coalescer sump is shown in Fig. 4.

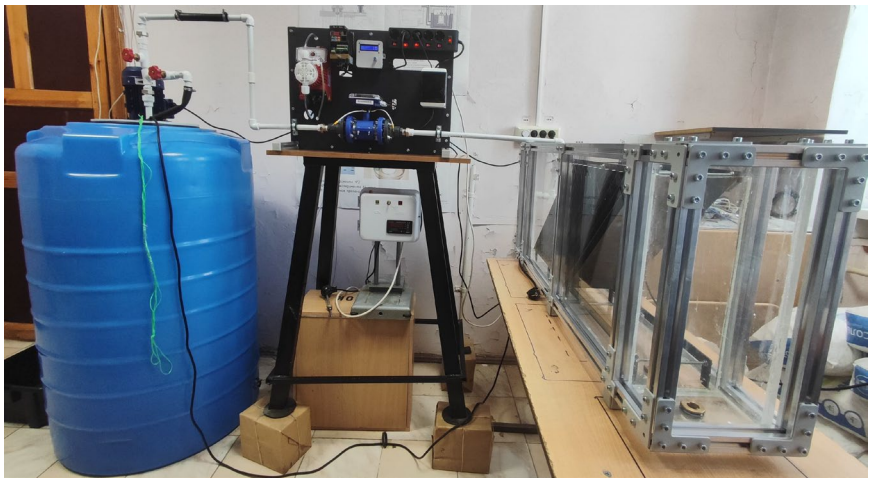

Figure 3. Assembled installation.

Figure 4. The final version of the coalescer tank.

2.2. Test Procedure

For testing, 200 l of process water is poured into the source water tank, and the temperature value is set on the temperature controller. The agitator turns on. To give the water the declared mineralization (200 g/l), NaCl salt is added to the water. A mixture of sand and clay in a 50/50 ratio and a total weight of 100 g is poured into the container. In the case of an experiment with chemical reagents, 0.9 l of NaOH alkali solution (100 g/l), 0.9 l of coagulant solution (100 g/l), and 0.2 l of flocculant solution (1 g/l) were added to 200 l of water. This sequence of addition of alkali and coagulant makes it possible to maintain the pH of the water in the range of 7.5–8.5. All reagents are pre-prepared in 1 l glass cups on a paddle mixer until they are completely dissolved in distilled water.

Depending on the experimental program, the shelves were placed at an angle of 45° in the amount of 13 or 26 pcs., or at an angle of 60° in the amount of 21 pcs.

2.3. Mathematical Model

The developed model is designed to calculate the concentration of substances at the outlet according to the known geometry of a settling tank with thin-layer modules and is based on a hydraulic approach using empirical ratios. The initial parameters of the model include: volumetric water flow Q_w, m³/h; the concentration of impurities at the tank inlet c_{in} mg/l; the proportion n_p of particles in the mixture with a radius of less than 100 μm, %; the length of the plate L_s, m; plate width B_s, m; plate inclination angle α, °; the distance between the plates in the perpendicular direction l_s, m; the height of the neutral layer under the module block h_n, m; the width of the hole at the inlet B_h, m; and its height L_h, m; the height of the settling zone H_1, m; water temperature, T, °C; water salinity n_s, ‰; device material, number of modules N, pcs.

Water inlet flow rate v_{win}, mm/s, is calculated considering the cross-sectional area of the hole at the inlet to the tank as:

$$v_{win} = \frac{1000 Q_w}{3600 B_h L_h}, \quad (1)$$

where the 3600 multiplier in the denominator considers the conversion of flow from m³/h to m³/s, the 1000 multiplier in the numerator considers the conversion of velocity from m/s to mm/s.

A uniform distribution of particles with sizes up to 100 μm is used for size values from 10 μm to 100 μm in increments of 10 μm, considering the proportion of n_p particles in the mixture with a radius of less than 100 μm. The particle size distribution over 100 μm is considered known, the total proportion of particles of all sizes is 100 %. For each range of radii with the particle index i, the arithmetic mean of the radius r_a, μm, is found. For particles over 1000 μm, it is found as 1500 μm. The particle fraction numbers are given in Table 1.

Table 1. Particle fractions index.

i	Size of particle, μm	*i*	Size of particle, μm
1	10	9	90
2	20	10	100
3	30	11	100–160
4	40	12	160–250
5	50	13	250–500
6	60	14	500–1000
7	70	15	Over 1000
8	80		

Based on the known values of the particle radius, the average mass value of the mass of one particle m_{ai}, mg, is calculated, considering the spherical shape of the particles:

$$m_{ai} = \frac{4}{3 \cdot 10^{12}} \pi r_{ai}^3 \rho_s, \tag{2}$$

where ρ_s is the particle density, which is equal to 2700 kg/m^3.

Inlet particle concentration with radius less than 100 μm c_{ins}, mg/l, is recalculated considering their share in the mixture according to the formula:

$$c_{ins} = \frac{n_p}{100} c_{in}. \tag{3}$$

Particle concentrations at the tank inlet in sizes from 10 μm to 100 μm with a step change in size of 10 μm are distributed uniformly, considering the value obtained from (3). For large particles, a uniform fraction distribution is also set, the proportion of the i-th fraction in the mixture n_{pi}, %, is calculated as:

$$n_{pi} = \frac{100\% - n_p}{5}, \quad i = 11, 12, \ldots, 15, \tag{4}$$

where the fraction of particles with sizes less than 100 μm n_p is substituted in %, index i is given in Table 1, number 5 is the number of isolated large fractions.

The particle concentrations at the tank inlet for the remaining fractions are calculated similarly to (3):

$$c_{ini} = \frac{n_{pi}}{100} c_{in}, \quad i = 11, 12, \ldots, 15, \tag{5}$$

where n_{pi}, %, is the fraction of particles of the i-th fraction in the mixture at the tank inlet.

In the pure water zone, the particle concentration of each fraction is assumed to be 0 if the angle between the direction of movement of the particle of the i-th fraction (i = 1, 2, ..., 10) and the direction of the diagonal between the plates β_i is positive, when the angle between the direction of movement of the particle and the direction of water flow α_{pwi} is greater than the angle between the direction of water flow and the direction of the diagonal between the plates γ, then the particle will sediment (see Fig. 5, where x is the horizontal coordinate axis). Otherwise, the particle will slip through the plates and get to the outlet of thin-layer modules zone, so the concentration of particles of such a fraction at the outlet will not change and will be equal to the concentration of particles of this fraction at the inlet. The resulting impurity concentration in the pure water zone c_{out} is found as the sum of the particle concentrations of all fractions in this zone.

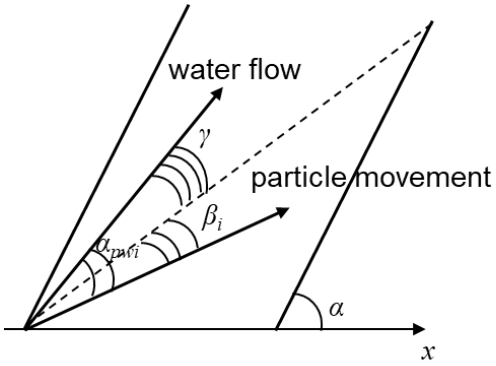

Figure 5. The case of a positive angle β_i when the particles will sediment.

For different particle radii of less than 100 μm, described in Table 1, as well as for particles with a radius of r_0 = 1 μm, the deposition time t_i, s, and the sedimentation rate u_{si}, mm/s, are calculated. To do this, the radius is converted from mkm to m, the acceleration of gravity g = 9.81 m/s² is set, the density of water is ρ_1, kg/m³, depending on the temperature T and salinity n_s, the density of sand is ρ_2, kg/m³, the dynamic viscosity of water is μ, mPa·s, depending on the water temperature T. After that, the volume of the spherical particle V_i, m³, is calculated:

$$V_i = \frac{4}{3}\pi r_{ai}^3, \tag{6}$$

where the particle radius is substituted in m.

The sedimentation rate, mm/s, is calculated based on Stokes' law:

$$u_{si} = 1000 \cdot \frac{2g(\rho_2 - \rho_1)r_{ai}^2}{9\mu_w}, \tag{7}$$

where the multiplier 1000 considers the conversion from m/s to mm/s, in formula (7) all values are substituted in SI.

To fulfill Stokes' law, laminar flow must be observed, so the Reynolds number must be less than 500. The Reynolds number itself for the i-th fraction is calculated as:

$$\mathrm{Re}_i = \frac{2\rho_1 u_{si} r_{ai}}{\mu_w}, \tag{8}$$

where all values are substituted in SI.

Sedimentation time is calculated as:

$$t_i = \frac{h_p}{u_{si}}, \tag{9}$$

where h_p is the height of particle sedimentation.

According to the known water flow velocity at the inlet v_{win}, mm/s, the plate inclination angle α, which is converted from degrees to radians, the real water flow velocity v_{tr}, mm/s, is calculated for movement in the module zone:

$$v_{tr} = \frac{v_{win}}{\cos\alpha}. \tag{10}$$

The angle between the direction of the water flow and the direction of the diagonal between the plater γ, °, is determined by the formula:

$$\gamma = \alpha - \varphi, \tag{11}$$

where φ, °, is the angle of the diagonal between the plates.

The angle between the direction of movement of the particle of the i-th fraction and the direction of the diagonal between the plates β_i (see Fig. 5), °, is calculated from geometric considerations:

$$\beta_i = \alpha_{pwi} - \gamma, \quad i = 1, 2, \ldots, 10, \tag{12}$$

where α_{pwi}, °, is the angle between the direction of movement of the particle of the i-th fraction (i = 1, 2, ..., 10) and the direction of the water flow.

If the angle (12) is positive, then the particle of the i-th fraction will sediment, if the angle is negative, then the particle will get to the outlet.

To verify the laminarity of the flow, the Reynolds number for the i-th fraction is calculated:

$$\mathrm{Re}_i = \frac{v_{resi} l_s}{1000 \nu_{cw}} \cdot 10^6, \tag{13}$$

where v_{resi} is the resulting velocity of a certain fraction particle, mm/s; v_{cw} is the kinematic viscosity of water, mm²/s; the distance between plates in the perpendicular direction l_s is substituted in m; the multiplier 1000 in the denominator (13) considers the translation of v_{resi} from mm/s to m/s; the multiplier 10^6 in the numerator considers the conversion of v_{cw} from mm²/s to m²/s. If the Re_i < 500, then the particle flow of the i-th fraction is laminar, otherwise, it is turbulent.

Next, the water flow velocity at the outlet of the plate cross-sectional area v_s, mm/s, is calculated:

$$v_s = \frac{1000 Q_w}{3600 l_s B_s \left(N - 1\right)}, \tag{14}$$

where the 3600 multiplier in the denominator considers the conversion of flow from m³/h to m³/s, the 1000 multiplier in the numerator is related to the conversion of velocity from m/s to mm/s.

Since the particle deposition velocity is perpendicular to the horizontal, and the true water flow velocity is directed along the plates inclined at an angle of α, °, the angle between u_{si} and v_{tr} is equal for any fraction (Fig. 6):

$$\alpha_v = 90^\circ + \alpha. \tag{15}$$

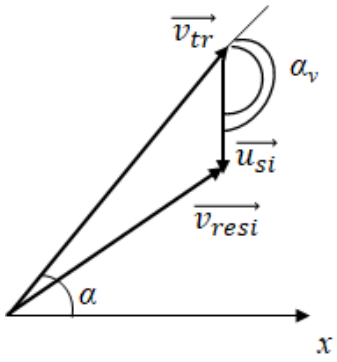

Figure 6. Calculation scheme of the resulting velocity vector.

This angle (15) can also be converted to radians. The direction of the resulting velocity is determined by adding vectors according to the rule of a triangle (Fig. 6) or a parallelogram, the modulus of the resulting velocity for the i-th fraction v_{resi} is calculated using the cosine theorem, considering that the angle between u_{si} and v_{tr} is adjacent to α_v:

$$v_{resi} = \sqrt{u_{si}^2 + v_{tr}^2 - 2u_{si}v_{tr}\cos\left(180^\circ - \alpha_v\right)}. \quad (16)$$

The angle of inclination of the resulting velocity to the horizontal axis $x\gamma_{resi}$, °, is calculated from geometric considerations:

$$\gamma_{resi} = \arccos\frac{v_{tr}\cos\alpha}{v_{resi}} = \arccos\frac{v_{tr}\sin\alpha_v}{v_{resi}}. \quad (17)$$

The resulting force is directed along the resulting velocity, so the angle δ_i, °, between this force and the sedimentation velocity is

$$\delta_i = 90^\circ + \gamma_{resi}, \quad (18)$$

where γ_{resi} is substituted in degrees.

Then the angle between the direction of motion of the particle of the i-th fraction (i = 1, 2, ..., 10) and the direction of the water flow α_{pwi}, °, is defined as:

$$\alpha_{pwi} = \alpha_v - \delta_i. \quad (19)$$

In addition, the coordinates of the vectors of the true water flow velocity, the particle deposition velocity, and the resulting velocity are determined. Horizontal axis is x, vertical axis is y. The origin of the vectors is placed at the origin. The end of the vector v_{tr} on the x axis corresponds to v_{win}, and on the y axis is defined as (in mm/s):

$$v_{try} = v_{tr}\sin\alpha = v_{tr}\sin\left(\alpha_v - 90^\circ\right). \quad (20)$$

The angle (in degrees) between the direction of v_{tr} vector and the *y* axis can be found as:

$$\delta_{try} = 90^\circ - \alpha. \quad (21)$$

The coordinate of the end of the u_{si} vector on the x axis is zero (the vector is perpendicular to this axis), and on the y axis it is equal to the u_{si} modulus taken with a minus sign. Accordingly, adding the coordinates of these vectors separately gives the coordinates of the end of the v_{resi} vector along these axes.

Finally, the angle between v_{resi} and the y-axis can be defined as:

$$\delta_{ryi} = \arccos\frac{v_{resiy}}{v_{resi}}, \quad (22)$$

where v_{resiy}, mm/s, is the coordinate of the v_{resi} vector end on the y-axis.

The overflow cross-sectional area between the flow damping zone and the thin-layer modules zone S_b, m², is defined as:

$$S_b = B_{sz}\left(H_1 + h_n\right), \quad (23)$$

where the width of the settling zone B_{sz}, m, is equal to the width of the modules B_s, m, increased by 0.2 m for the margin, all dimensions are substituted in m.

The area of one intermodular space S_1, m², is calculated as:

$$S_1 = B_s l_s. \quad (24)$$

Flow rate between two modules Q_{mod}, m³/h, is determined as:

$$Q_{\text{mod}} = \frac{3600 v_{tr} S_1}{1000}, \tag{25}$$

where the 3600 multiplier considers the conversion of flow rate from m³/s to m³/h, the 1000 multiplier in the denominator is associated with the conversion of velocity v_{tr}, mm/s, from mm/s to m/s.

Then, the total number of modules can be found using the formula:

$$N = \frac{Q_w}{Q_{\text{mod}}} + 1, \tag{26}$$

where the result is rounded up to the nearest integer.

The thickness of one module d_m, m, is known, as is the material density of the module ρ_m, kg/m³. From the geometry of the problem (Fig. 7), the horizontal distance between the plates b, m, is

$$b = \frac{l_s}{\sin\alpha}, \tag{27}$$

where l_s is substituted in m.

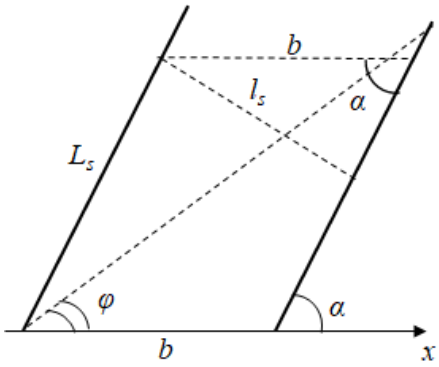

Figure 7. Calculation scheme of module dimensions.

Obviously, then the height of the particle sedimentation, h_p, mm, is

$$h_p = \frac{1000 l_s}{\cos\alpha}, \tag{28}$$

where l_s is substituted in m, the 1000 multiplier considers the conversion from m to mm.

By the cosine theorem, the diagonal distance between the plates is d, m, is

$$d = \sqrt{b^2 + L_s^2 + 2bL_s\cos\alpha}, \tag{29}$$

where all sizes are substituted in m.

The angle of inclination of the diagonal between the plates to the horizontal, φ, °, is also determined by the cosine theorem:

$$\varphi = \arccos\frac{b^2 + d^2 - L_s^2}{2bd}, \tag{30}$$

where all sizes are substituted in m.

As a result of applying the mathematical model, the concentration of impurities at the outlet of the tank is calculated, for which auxiliary parameters are determined using formulas (1)–(30).

3. Results and Discussion

To validate the correctness of the developed model, it was compared with 26 validation experiments. The installation parameters common to all experiments are shown in the Table 2. The sand density was ρ_2 = 1400 kg/m³, the concentration of impurities at the tank inlet c_{in} = 500 mg/l.

Table 2. Installation parameters common to all experiments.

Parameter	Value	Parameter	Value
B_s, m	0.151	h_n, m	0.05
B_h, m	0.152	L_h, m	0.05
H_1, m	0.05		

The first series of five experiments was carried out at low flow rate on an installation with N = 13 plates located at an angle of α = 45° to the horizontal. The proportion of particles with sizes less than 100 μm n_p in the mixture is 100 %. The parameters of such an installation are: L_s = 0.495 m, l_s = 0.022 m, the initial experimental data and the results of calculating the concentration at the outlet of the installation in comparison with the experimental values are shown in Table 3, where c_{out} is the calculated concentration of particles at the outlet of the installation, c_{oute} is the concentration of particles at the outlet of the installation based on the experimental results, ε is an error.

Table 3. Experimental data for the first series and the results of determining the particle concentration at the outlet of the installation.

No. / Parameter	1	2	3	4	5
Q_w, l/min	0.305	0.124	0.303	0.561	0.300
n_s, ‰	0	0	200	100	0
T, °C	26	26	26	26	26
c_{out}, % from initial	20	10	3	10	7
c_{oute}, % from initial	17	12	10	7	6
ε, %	3	2	7	3	1

According to the results of the first series of experiments, it was possible to establish that the salinity of water affects the sedimentation rate. Excluding this fact, the error in determining the concentration of particles at the outlet exceeds 15 %. The approximation of the calculated parameters to compare them with the experimental results gave a refined dependence for the sedimentation rate at flow rates Q_w less than 0.09 m³/h and salinity ns more than 1 %, when the sedimentation rate u_{si}, mm/s, is calculated from Stokes' law (7), considering the empirical correction for salinity:

$$u_{si} = 1000 \cdot \frac{2g\left(\rho_2 - \rho_1\right) r_{ai}^2}{9\mu_w} \sqrt{\frac{n_s}{10}}, \tag{31}$$

where the multiplier 1000 considers the conversion from m/s to mm/s, in formula (31), all values are substituted in SI, except for the salinity n_s, which is substituted in ‰, the multiplier 10 in the denominator converts the salinity from ‰ to %. In the absence of salinity of the water or at high Q_w flow rates of more than 0.09 m³/h, the formula (7) remains valid for the sedimentation rate.

The effect of reagents in the first series of experiments was not researched. In most experiments, the error in determining the concentration of particles at the outlet was not more than 3 %. The disagreement in the results in the third experiment is due to the changing flow rate during its implementation.

The second series of four experiments (Nos. 6–9). It was carried out with higher flow rates on the same installation, although in the ninth experiment, the flow rate for verification was set lower, in addition, the effect of concentration of coagulants and flocculants was investigated. The initial experimental data and the results of calculating the concentration at the outlet of the installation in comparison with the experimental values are shown in Table 4, where V_c is the volume of coagulant solution (100 g/l), V_n is the volume of alkali solution (100 g/l), and V_f is the volume of flocculant solution (1 g/l). All volumes are given for 200 l of water. The proportion of particles with sizes less than 100 μm n_p in the mixture in the absence of coagulant is 100 %.

Table 4. Experimental data for the second series and the results of determining the particle concentration at the outlet of the installation.

No. / Parameter	6	7	8	9
Q_w, l/min	4.300	4.430	4.560	0.561
n_s, ‰	0	200	200	0
V_c, l	0	0	0.9	0.5
V_n, l	0	0	0.9	0.5
V_f, l	0	0	0.2	0.2
T, °C	26	26	26	26
c_{out}, % from initial	20	20	7	8
c_{oute}, % from initial	24	21	57	8
ε, %	4	1	50	0

According to the results of the second series of experiments, it was found that at high flow rates, salinity does not affect the sedimentation rate due to the rapid flow through the installation. To account for the effect of the concentration of coagulants and flocculants on the fraction of particles with a size of less than 100 μm in the flow, this fraction was manually adjusted so that the calculated value of the impurity concentration at the outlet corresponded to the experimental one. After the third series of experiments, these values were adjusted so that for all identical volumes of chemical reagents, the error in determining the calculated impurity concentration at the outlet compared to the actual one was minimal. The data in Table 4 are already given considering this adjustment. In most experiments, the error in determining the concentration of particles at the outlet was not more than 4 %. The discrepancy in the results in the eighth experiment is due to the clumping of particles and their removal by the flow.

The third series of experiments consisted of varying various parameters of the settling tank (the angle of inclination of the plates and their number, flow rate and salinity of water) to refine the parameters of the model. It consisted of the following 17 experiments: Nos. 10–26. For an installation with a different number of plates or angle of inclination than in the first two series of experiments, the parameters are shown in Table 5, the initial experimental data are shown in Table 6, and the results of calculating the concentration at the outlet of the installation in comparison with the experimental values are shown in Table 7.

Table 5. Installation parameters with a different number of plates or angle of inclination.

Parameter	Value for 26 plates	Value for 21 plates
α, °	45	60
L_s, m	0.495	0.404
l_s, m	0.01	0.0223

Table 6. Experimental data for the third series.

No.	Q_w, l/min	n_s, ‰	V_c, l	V_n, l	V_f, l	N, pcs.	α, °	T, °C
10	3.730	0	0	0	0	26	45	26
11	1.660	0	0	0	0	26	45	26
12	3.500	200	0	0	0	26	45	26
13	2.500	200	0	0	0	26	45	29
14	1.650	0	0	0	0	26	45	29
15	3.730	200	0	0	0	26	45	26
16	2.210	200	0.9	0.9	0.2	26	45	26
17	3.460	200	0.9	0.9	0.2	26	45	25
18	4.430	200	0.9	0.9	0.2	13	45	23
19	4.390	200	0.45	0.45	0.2	13	45	23
20	4.290	200	0.6	0.6	0.2	13	45	30
21	1.540	200	0.45	0.45	0.2	21	60	28
22	3.870	200	0.6	0.6	0.2	26	45	28
23	3.970	0	0.9	0.9	0.2	26	45	26
24	1.870	0	0	0	0	21	60	26
25	1.940	0	0.9	0.9	0.2	21	60	26
26	1.540	200	0.45	0.45	0.2	21	60	26

Table 7. The results of determining the particle concentration at the outlet of the installation for the third series of experiments.

№	c_{out}, % from initial	c_{oute}, % from initial	ε, %
10	10	17	7
11	10	15	5
12	20	19	1
13	20	24	4
14	10	15	5
15	20	21	1
16	6	8	2
17	7	30	23
18	14	34	20
19	16	29	13
20	13	10	3
21	16	14	2
22	6	8	2
23	3	2	1
24	20	19	1
25	6	3	3
26	16	14	2

From the experiments in this series, the effect of coagulant and alkali concentrations on the proportion of particles with sizes less than 100 μm in the mixture n_p, %, was established. To do this, set the volume of coagulant (equal to the volume of alkali) in l per 200 l of water V_c, then, the proportion of particles with sizes less than 100 μm in the mixture n_p, %, is determined from the empirical correlation:

$$n_p = 103.7V_c^2 - 162.2V_c + 92.0. \quad (32)$$

In the absence of the addition of coagulant, the proportion of particles with sizes less than 100 μm n_p in the mixture is 100 %.

The correlation coefficient for dependence (32) exceeds 0.99.

In most experiments, the error in determining the concentration of particles at the outlet was not more than 5 %. The disagreement in the results in the tenth experiment is due to a probable change in water flow during the experiment, in the seventeenth, eighteenth, and nineteenth experiments is due to the flushing of clumped particles by a stream.

The average error in determining the concentration of particles at the outlet, with the exception of the eighth, seventeenth, eighteenth, and nineteenth experiments, in which clumped particles are removed by a flow, according to the modified model is 3 %.

Verification of the developed proxy-model was carried out by comparing the calculated drop in the concentration of dispersed particles at the outlet of the tank 1 hour after the start of its operation with the data from the work of Kovalev et al. [1]. As a result of this comparison, according to the data of the article [1], the concentration drops by 1.62 times, according to the developed model by 1.67 times, which is an error of 3 %.

4. Conclusions

A laboratory installation of a coalescer settling tank has been developed. Experimental data were obtained on the degree of purification in a design with a number of plates of 26 and 13 pcs. for an angle of inclination of 45° and with a number of plates of 21 pcs. for an angle of inclination and 60°.

It is shown that the lower the flow rate in the coalescer tank, the better the water purification. The effect of water mineralization and the addition of auxiliary chemical reagents for the precipitation of suspended particles on the degree of purification has been established.

A modified mathematical model of a thin-layer settling tank is proposed, which for the first time considers the effect of the concentration of coagulant and alkali on the particle size distribution, as well as salinity on the particle sedimentation rate.

It was found that with an increase in the concentration of chemical reagents, the proportion of particles with sizes less than 100 μm in the flow decreases, which leads to an increase in water purification.

It is shown that the modified model reproduces laboratory results with an average error of 3 % with a change in flow rate from 0.124 l/min to 4.560 l/min, water temperature from 23 °C to 30 °C, number of plates from 13 to 26, plate inclination angles of 45° and 60°, volume of coagulant and alkali from 0.45 l to 0.9 l of each reagent per 200 l of water and the volume of flocculant of 0.2 l per 200 of water, salinities from 0 ‰ to 200 ‰ and are recommended for use in calculating the impurity concentration at the outlet for these parameter ranges, therefore, the model is validated.

A certificate of registration of a computer program was obtained for the developed model[2].

References

1. Kovalev, R.A., Korneeva, N.N., Salnikov, B.F., Lifanov, D.O. Thin-layer Settling in Modern Water Treatment Technologies. News of the Tula state university. Sciences of Earth. 2020. 2. Pp. 114–124.
2. Gaballah, M.S., Abdelwahab, O., Barakat, K.M., Stefanakis, A.I. A pilot system integrating a settling technique and a horizontal subsurface flow constructed wetland for the treatment of polluted lake water. Chemosphere. 2022. 295. Article no. 133844. DOI: 10.1016/j.chemosphere.2022.133844
3. Tsarevsky, Ya.A., Tsyplenkov, D.S., Shiryaev, V.N., Taras'yants, S.A. Hydraulic Computation for Sludge Disposal Installation of Primary Sedimentation Tanks of Sewage Treatment Plants. Bulletin of the Kurgan State Agricultural Academy. 2019. 4. Pp. 77–80.
4. Hajjar, A., Scholtès, L., Oltéan, C., Buès, M.A. Transport and deposition of weakly inertial particles in closed channel flows at low Reynolds number. European Journal of Mechanics – B/Fluids. 2017. 65. Pp. 299–311. DOI: 10.1016/j.euromechflu.2017.05.004
5. Dushkin, S.S., Galkina, O.P. Thin-Layer Sedimentation Tanks in Water Clarification at Coke Plants. Coke and Chemistry. 2021. 64. Pp. 380–385. DOI: 10.3103/S1068364X21080020
6. Shamyan, V., Minasyan, A. Some Constructive Methods for Improving the Operation of Horizontal Settling Tanks. Journal of Architectural and Engineering Research. 2022. 3. Pp. 85–92. DOI: 10.54338/27382656-2022.3-010
7. Akramov, A., Juraev, Sh., Xoshimov, S., Axatov, D., Pathidinova, U. Optimum placement of thin-layer elements in a horizontal sedimentation tank purification of drinking water. IOP Conference Series: Earth and Environmental Science. 2022. 1112. Article no. 012139. DOI: 10.1088/1755-1315/1112/1/012139
8. Soleimani, M., Mohammadi, M. Feasibility of increasing the efficiency of primary settling tanks by using thin layer plates. Journal of American Science. 2012. 8(11). Pp. 39–48.

2 Gilmanov A.Ya., Shevelev A.P., Vurdova N.G. Certificate of state registration of the computer program 2025614405 Russian Federation. Programma dlya rascheta kolichestva plastin i geometricheskih razmerov tonkosloynogo otstoynika [A program for calculating the number of plates and geometric dimensions of a thin-layer tank]. Applicant and copyright holder JCS "HMS Neftemash". Application dated 02/12/2025, published on 02/21/2025. 1 p.

9. Lin, Z.Y., Dai, J.S., Oh, J.-M. Optimal discharge protocol for urban stormwater settling tank across different scenarios under limited data aided with Monte-Carlo simulation incorporated mathematical model. Journal of Water Process Engineering. 2023. 52. Article no. 103538. DOI: 10.1016/j.jwpe.2023.103538
10. Shah, M.T., Parmar, H.B., Rhyne, L.D., Kalli, C., Utikar, R.P., Pareek, V.K. A novel settling tank for produced water treatment: CFD simulations and PIV experiments. Journal of Petroleum Science and Engineering. 2019. 182. Article no. 106352. DOI: 10.1016/j.petrol.2019.106352
11. Baek, S., Park, Y.S., Seo, I.W. Settling velocity of weakly inertial particles in vertical flow. European Journal of Mechanics – B/Fluids. 2025. 109. Pp. 92–99. DOI: 10.1016/j.euromechflu.2024.09.001
12. Bartolome, P.S., Van Gerven, T. A comparative study on Aspen Hysys interconnection methodologies. Computers & Chemical Engineering. 2022. 162. Article no. 107785. DOI: 10.1016/j.compchemeng.2022.107785
13. Akhtar, S., Memon, S.A., Siddiqa, S., Park, C.W. Numerical Investigation of Solid–Liquid Dissolution for Nutrient Mixing Improvement in a Thin-Layer Cascade System. Waste and Biomass Valorization. 2024. 15. Pp. 771–785. DOI: 10.1007/s12649-023-02180-x
14. Grobbelaar, J.U., Soeder, C.J., Stengel, E. Modeling algal productivity in large outdoor cultures and waste treatment systems. Biomass. 1990. 21(4). Pp. 297–314. DOI: 10.1016/0144-4565(90)90079-Y
15. Yu, J., Chen, Q., Zhang, J., Zhong, J., Fan, C., Hu, L., Shi, W., Yu, W., Zhang, Y. *In situ* simulation of thin-layer dredging effects on sediment metal release across the sediment-water interface. Science of The Total Environment. 2019. 658. Pp. 501–509. DOI: 10.1016/j.scitotenv.2018.12.226
16. Zhang, H., Liang, Y., Yan, X., Wang, B., Wang, N. Simulation on water and sand separation from crude oil in settling tanks based on the particle model. Journal of Petroleum Science and Engineering. 2017. 156. Pp. 366–372. DOI: 10.1016/j.petrol.2017.06.012
17. Liu, H., Chen, Y., Pan, X., Zhang, J., Huang, J., Lichtfouse, E., Zhou, G., Ge, H. Image recognition enhances efficient monitoring of the coagulation-settling in drinking water treatment plants. Journal of Cleaner Production. 2024. 482. Article no. 144251. DOI: 10.1016/j.jclepro.2024.144251
18. Kuzin, E.N. Krutchinina, N.E. Purification of circulating and waste water in metallurgical industry using complex coagulants. CIS Iron Steel Review. 2019. 18(2). Pp. 72–75. DOI: 10.17580/cisisr.2019.02.15
19. Galkina, O. Blahodarna, H. The Use of Effective Coagulants and Flocculants to Intensify the Process of Water Purification at Coke Plants. Slovak Journal of Civil Engineering. 2019. 27(2). Pp. 21–28. DOI: 10.2478/sjce-2019-0012
20. Ulrich, E.B., Barkova, A.S. Use of flocculants for wastewater treatment. Ecosystem Transformation. 2023. 6(1). Pp. 168–187. DOI: 10.23859/estr-220525
21. Ye, L., Chen, Y., Wu, Y., Zhang, J., Chen, Y., Seo, J.Y., Wu, J. New insight of biophysical aggregates' geometric distributions from side and bottom views during their flocculation and settling in saline water. Water Research. 2025. 272. Article no. 122916. DOI: 10.1016/j.watres.2024.122916
22. Myradova, G., Komekov, K. The Main Directions of the Use of Water by the Population and the Use Of Water In Production. In Situ. 2022. 11. Pp. 163–165.
23. Davydov, E.I., Lyamaev, B.F. Research and calculation of the vertical sediment tank with spiral-wound nozzle. Magazine of Civil Engineering. 2011. 23(5). Pp. 10–15. DOI: 10.5862/MCE.23.4
24. Fakhretdinov, R.N., Fatkullin, A.A., Pasanayev, E.A., Volgin, I.R., Orazmetov, D.F. New prospects in the development of chemical technologies for regulating the coverage of reservoirs by flooding. Oil Industry. 2022. 8. Pp. 65–69. DOI: 10.24887/0028-2448-2022-8-65-69
25. Bedrikovetsky, P., Zeinijahromi, A., Siqueira, F.D., Furtado, C.A., de Souza, A.L.S. Particle Detachment Under Velocity Alternation During Suspension Transport in Porous Media. Transport in Porous Media. 2012. 91. Pp. 173–197. DOI: 10.1007/s11242-011-9839-1
26. Gil'manov, A.Ya., Fedorov, K.M., Shevelev, A.P. Problem of Blocking a Technogenic Fracture in the Reservoir Using a Suspension Mixture. Fluid Dynamics. 2022. 57(6). Pp. 720–728. DOI: 10.1134/S0015462822600936

Information about the authors:

***Aleksandr Gilmanov**, PhD in Physics and Mathematics*
ORCID: https://orcid.org/0000-0002-7115-1629
E-mail: a.y.gilmanov@utmn.ru

***Boris Grigoriev**, PhD in Technical Sciences*
ORCID: https://orcid.org/0000-0002-2757-1386
E-mail: b.v.grigoriev@utmn.ru

***Aleksandr Shevelev**, PhD in Physics and Mathematics*
ORCID: https://orcid.org/0000-0003-0017-4871
E-mail: a.p.shevelev@utmn.ru

***Denis Vazhenin**,*
E-mail: d.a.vazhenin@utmn.ru

Received 20.03.2025. Approved after reviewing 17.09.2025. Accepted 17.09.2025.

Magazine of Civil Engineering

ISSN 2712-8172

journal homepage: http://engstroy.spbstu.ru/

Research article

UDC 539.3

DOI: 10.34910/MCE.138.8

Parameter identification of the concrete damaged plasticity model

I.R. Murtazin[1] ✉ , ***R.V. Fedorenko***[1] , ***A.V. Lukin***[1] , ***V.S. Modestov***[1] , ***A.S. Malinkin***[2], ***M.A. Fedotov***[2], ***S.N. Panarin***[2]

[1] *Peter the Great St. Petersburg Polytechnic University, St. Petersburg, Russian Federation*

[2] *TEKHNOARM+, St. Petersburg, Russian Federation*

✉ *murtazin_ir@spbstu.ru*

Keywords: parameter identification, stress-strain curve, cyclic loading, concrete damage, analytical approximation, ABAQUS

Abstract. The article is devoted to the development of methods for identification and validation of the parameters of the "Concrete Damage Plasticity" material model based on experimental studies. During the experiments, prismatic samples were tested for sign-constant cyclic load after preliminary heat treatment at various temperatures. According to the test results, the temperature dependences of the mechanical properties were established: the conditional proportionality limit, the ultimate strength, Young's modulus, and the scalar damage variable. Piecewise analytical envelopes were used to plot the stress-strain curves, which describe linear, inelastic, and descending parts. Accumulated concrete scalar damage variable during compression is determined based on the elastic modulus degradation analysis at each loading cycle. Parameters of analytical approximations are determined directly through experimental data or using numerical identification method based on an iterative process of searching for the minimum functional. The structure of the minimized functional contains auxiliary subfunctions due to well-known statistical indicators: the standard deviation of the compared values, the linear correlation coefficient, and the area under the compared dependencies. The search for the minimum of the desired value is carried out using the gradient descent method according to the criterion of the minimum contribution of the sum of three subfunctions. At the last step of the study, the obtained model is validated based on the calculation for uniaxial and cyclic loading of a single-element prismatic sample in the ABAQUS FEA. The developed calculation method makes it possible to complete the loading cycle at any axial force value, including zero, as well as to continue the next loading cycle from the current stress state. The considered method for validating the inelastic deformation model for concrete is characterized by its consistency and versatility. The results demonstrate sufficient accuracy in approximating uniaxial and cyclic stress-strain curves, and the proposed approximation relationships are free from ambiguity when converting the inelastic part of strain to plastic one.

Funding: World-class Research Center program: Advanced Digital Technologies, No. 075-15-2022-311 dated 20.04.2022

Citation: Murtazin, I.R., Fedorenko, R.V., Lukin, A.V., Modestov, V.S., Malinkin, A.S., Fedotov, M.A., Panarin, S.N. Parameter identification of the concrete damaged plasticity model. Magazine of Civil Engineering. 2025. 18(6). Article no. 13808. DOI: 10.34910/MCE.138.8

1. Introduction

Today, mechanical design methods are characterized by increased requirements for safety and wear resistance, especially during operation in high-temperature conditions. Along with this, the issue of correctly

assessing the viability of critical elements of structures is becoming acute. It is impossible to imagine solving such problems without carrying out full-scale tests and numerical modeling procedures using modern computational environments.

One of the main structural materials is concrete. A distinctive feature of concrete is its fundamentally different behavior during compression and tension, as well as the phenomenon of cracks and damage formation and propagation [1–3]. Tests for cyclic sign-constant loading without transition to the tensile region make it possible to determine the main mechanical characteristics of the material – the initial Young modulus, the conditional proportionality limit, the compressive strength of concrete, as well as to identify the material stiffness degradation by determining the dependence of the scalar variable of accumulated damage on the magnitude of inelastic deformations [4–7]. It is often important to understand how the key characteristics of a structure change under thermal conditions. In this case, it is about a family of experiments for different temperature values [8]. The numerical modeling of inelastic deformation processes is based on mathematical models. One of the most wide-spread models for concrete is the "Concrete Damaged Plasticity" (CDP) model [9–13], implemented in the ABAQUS FEA [14]. The model is widely used and finds its application in many tasks related to the deformation and fracture of concrete and concrete-like (with a granular structure) materials [15–21].

This model considers inelastic behavior in both compression and tension and takes into account not only material damage [22–24] but also partial recovery of properties during reverse-sign loading [25]. The CDP model is purposed for calculating structures under the influence of monotonous, cyclic, and dynamic loads.

Analytical approximations are often used to describe compression diagrams and scalar damage variables [25–27]. A distinctive feature of such approaches is the unambiguous relationship between plastic and inelastic strain. In contrast to the case of an arbitrarily defined envelope of the diagram, such a relationship eliminates the disadvantages associated with the decrease, including to negative values, of plastic strain when they are recalculated from inelastic ones. In addition to the basic constants of the material, the parameters included in the approximation dependences are also subject to identification.

As already mentioned, some model parameters are explicitly defined based on existing dependencies. However, a more sophisticated approach is required to determine the proportion of plastic strain contained in the inelastic part. In this case, the algorithm proposed in [28] was used as the basis for the identification procedure. In the current work, a modified criterion is used, presented as the sum of the simplest ones.

Using the interpolation method, the obtained parameters make it possible to form universal analytical dependencies for arbitrary temperature values. The corresponding curves are supposed to be used for the verification task in the ABAQUS FEA. The kinematic loading of a single-element prismatic sample for uniaxial and cyclic action is assumed. The criterion for the model's operability in this case will be the coincidence of the sample response in terms of stress and strain, as well as the nature of the Young modulus (stiffness) degradation with the initially set properties.

2. Methods

2.1. Processing of Experimental Data

During the experiments, prismatic concrete samples of 70×70×280 mm were tested for cyclic sign-constant compression until failure under normal conditions (20 °C), as well as after heat treatment at temperatures of 100, 400, and 600 °C in a cooled state. The tests were carried out on samples of heat-resistant concrete from a self-sealing mixture.

The amount of deformation of the samples during their loading/unloading was measured using digital electronic indicators mounted on each side of the prismatic sample according to a scheme similar to that used to determine the Young modulus of concrete. The load value was determined by a compression dynamometer. The readings were recorded at a sampling rate of 140 ms using a hardware and software package developed separately for this task.

Figs. 1 and 2 show the condition of the samples after the first and last loading cycle for temperatures of 20 and 600 °C.

Figure 1. The state of the sample after the first (left) and last (right) loading cycle at a temperature of 20 °C.

Figure 2. The state of the sample after the first (left) and last (right) loading cycle at a temperature of 600 °C.

Primary processing of cyclic loading diagrams involves finding the ultimate strength, the conditional proportionality limit, and analyzing the Young modulus (stiffness) degradation. The conditional proportionality limit here is a value equal to 0.4 of the ultimate strength.

Fig. 3 shows the cyclic loading diagrams for the given temperatures, as well as the initial modulus of normal elasticity and its degradation, the conditional limit of proportionality and the ultimate strength.

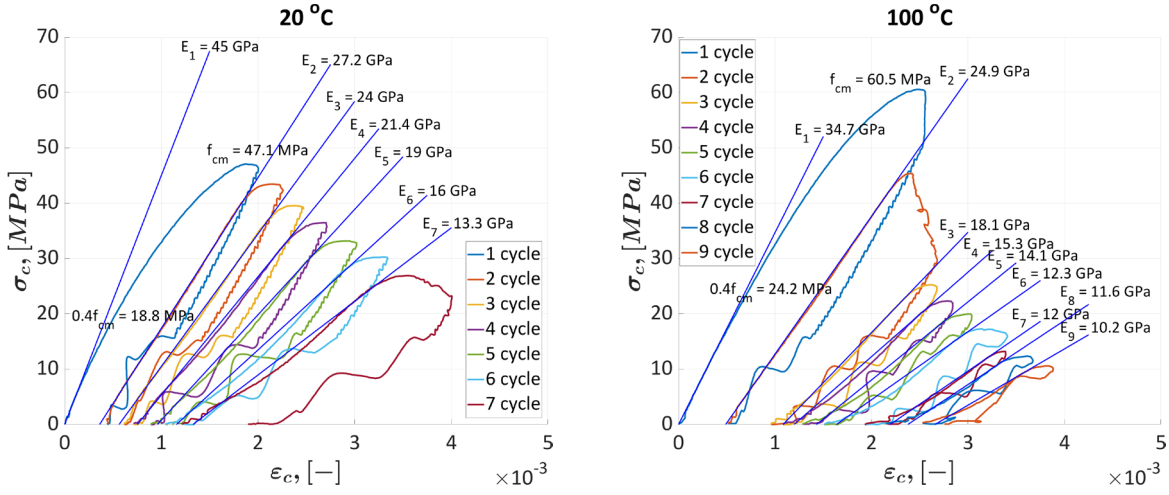

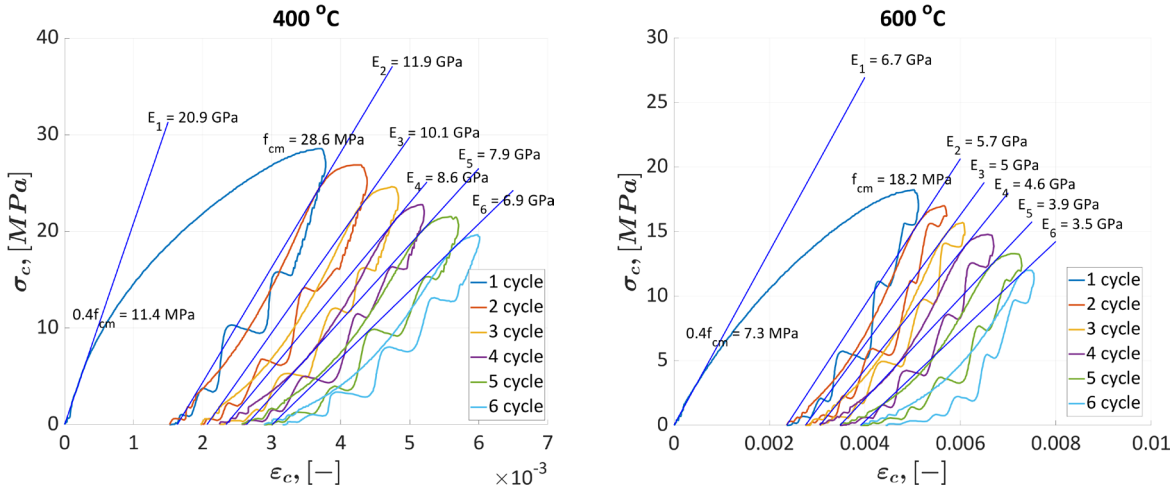

Figure 3. Cyclic loading diagrams for the given temperatures with designations of the ultimate strength f_{cm}, the conditional proportionality limit 0.4 f_{cm}, and the evolution of Young modulus.

Here σ_c is the compression normal stress, ε_c is the total axial strain, E_i is the Young modulus at the i-th cycle.

It is worth noting that the plotting of slope lines at each cycle characterizing the linear-elastic part can be carried out both along the unloading and loading path [26]. In this case, a variant of the slope of the line following from the end of unloading (the beginning of the next loading cycle) to the point where the dependence, having a negative second derivative, begins to acquire a non-linear character.

Based on the diagrams shown, it is easy to form the dependences of the scalar damage variable on inelastic strain. Inelastic strain can be recalculated through total ones according to the relation (1) [5, 6, 14, 26]:

$$\varepsilon_c^{in} = \varepsilon_c - \frac{\sigma_c}{E_c}, \tag{1}$$

where $E_c \equiv E_1$ is the initial Young modulus.

At the same time, the relationship between the actual Young modulus at the i-th cycle and the initial one is determined by dependence (2) [5, 6, 16]:

$$E_i = \left(1 - d_c\right) E_c, \tag{2}$$

where $d_c = d_c\left(\varepsilon_c^{in}\right)$ is the scalar damage (stiffness degradation) variable.

In addition to inelastic strain, the plastic component is separately identified. It is obviously less than inelastic one when taking into account damage, but in the absence of such, these values are the same. In this case, plastic strain cannot be negative and must increase with increasing load. Plastic component of strain is related to total and inelastic according to expression (3) [27]:

$$\varepsilon_c^{pl} = \varepsilon_c - \frac{\sigma_c}{\left(1 - d_c\right) E_c} = \varepsilon_c^{in} - \frac{1}{\left(1 - d_c\right)} \frac{\sigma_c}{E_c}. \tag{3}$$

Being a function of inelastic strain, the parameter d_c is calculated at each loading cycle using expression (2) for a given value of ε_c^{in}. By performing this procedure for each diagram, a family of dependencies is obtained for each temperature. Fig. 4 shows a family of dependencies of the scalar damage variable on inelastic strain for temperatures of 20, 100, 400, and 600 °C. It is clear that $d_c\left(0\right) = 0$.

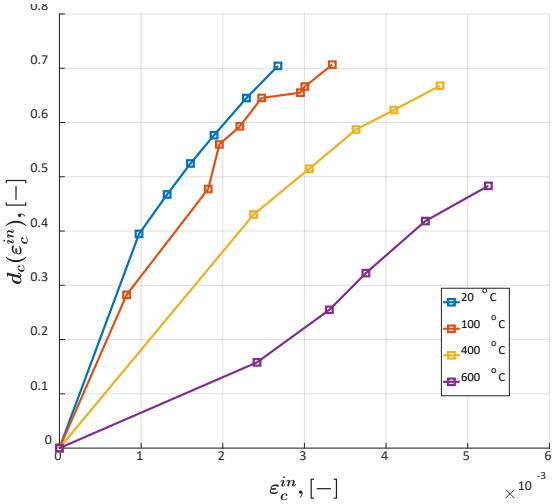

Figure 4. Family of dependencies of scalar damage variable on inelastic strain for temperatures of 20, 100, 400, and 600 °C.

The obtained characteristics fully correspond to the experiments, however, for the setting of numerical procedures, they require more detailed analysis. This is primarily due to the features of the CDP model. For the full-fledged operation of the model, at least it is necessary to specify the basic elastic characteristics, a stress-strain curve describing nonlinear (including plastic) strain, as well as information on the initial stiffness properties degradation for optional damage accounting. At the same time, the specified characteristics should not contradict the basic principles of mechanics of a deformable solid.

So, not every arbitrarily defined envelope of a cyclogram can correspond to an adequate relationship between the plastic and inelastic parts of strain, as well as to a given law of properties degradation (equation (3)). In this case, it is more reasonable to use analytical approximations, which, when implemented in constitutive equation, obviously eliminate these disadvantages.

2.2. Analytical Dependencies

Expressions (1)–(3) underlie the dependence of normal compression stress on relative axial strain, taking into account damage [25] in the form of expression (4):

$$\sigma_c = \left(1 - d_c\right) E_c \left(\varepsilon_c - \varepsilon_c^{pl}\right). \tag{4}$$

The difference between a model of a material with plasticity, a model of a material with damage, and a model of a material with damage and plasticity is best demonstrated in Fig. 5 [25].

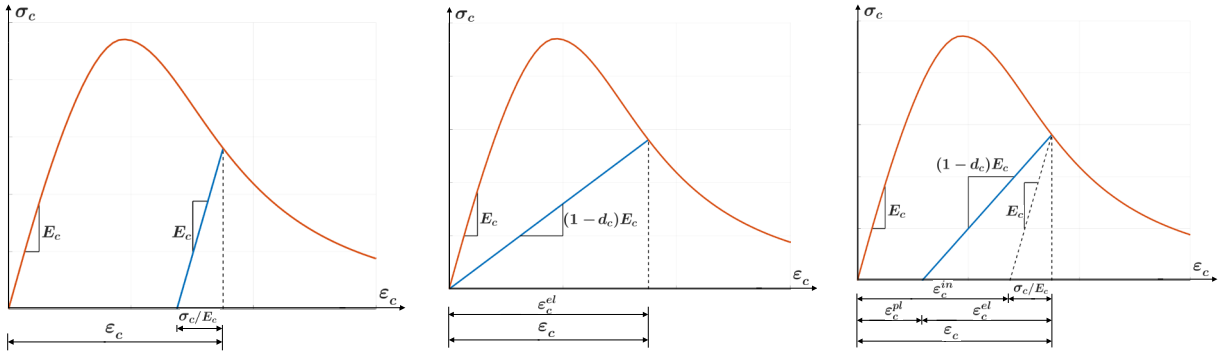

Figure 5. Comparison of model behavior: material model with plasticity (left), material model with damage (middle), and material model with damage and plasticity (right).

Here ε_c^{el} is the total elastic strain.

For the analytical description of stress-strain curves, piecewise analytical dependencies (5)–(7) are used [26]. The diagram is divided into three sections: the linear-elastic section, the ascending part up to the ultimate strength, and the descending part. A division into sections scheme can be seen in Fig. 6 [26].

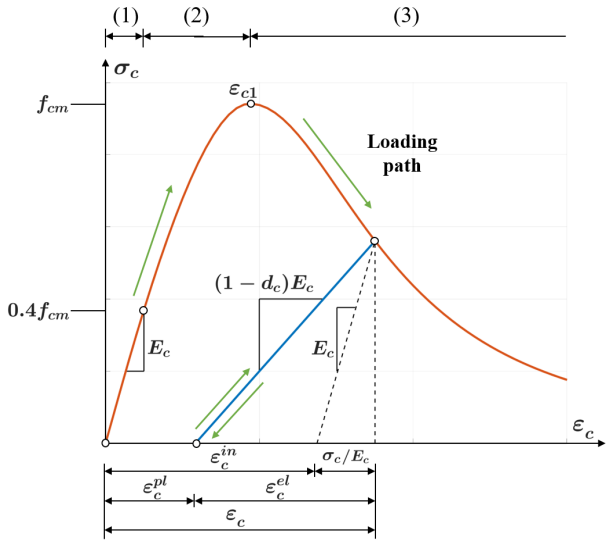

Figure 6. Piecewise analytical partition of a stress-strain curve.

Here ε_{c1} is the ultimate compression strain.

$$\sigma_{c(1)} = E_c \varepsilon_c; \tag{5}$$

$$\sigma_{c(2)} = \frac{E_{ci}\dfrac{\varepsilon_c}{f_{cm}} - \left(\dfrac{\varepsilon_c}{\varepsilon_{c1}}\right)^2}{1 + \left(E_{ci}\dfrac{\varepsilon_c}{f_{cm}} - 2\right)\dfrac{\varepsilon_c}{\varepsilon_{c1}}}; \tag{6}$$

$$\sigma_{c(3)} = \left(\frac{2 + \gamma_c f_{cm}\varepsilon_{c1}}{2 f_{cm}} - \gamma_c \varepsilon_c + \frac{\gamma_c \varepsilon_c^2}{2\varepsilon_{c1}}\right)^{-1}, \tag{7}$$

where E_{ci}, γ_c are the parameters of analytical approximations to be identified.

The relationship between the scalar damage variable and inelastic (or plastic) strain is obtained from the expression (3):

$$d_c = 1 - \frac{\sigma_c / E_c}{\left(\varepsilon_c^{in} + \varepsilon_c^{pl}\right) + \sigma_c / E_c}. \tag{8}$$

From expression (3) and Fig. 6, it can be seen that plastic strain, taking into account damage, is obviously less than inelastic one. This gives reason to believe that one can be expressed through the other using the proportionality coefficient. The proposed approach is outlined in [24–26] and shown in ratio (9):

$$\varepsilon_c^{pl} = b_c \varepsilon_c^{in}, \tag{9}$$

where $0 < b_c \le 1$ is the parameter of analytical approximations to be identified.

In this case, dependence (8) is transformed into the form:

$$d_c\left(\varepsilon_c^{in}\right) = 1 - \frac{\sigma_c / E_c}{\varepsilon_c^{in}\left(1 - b_c\right) + \sigma_c / E_c}. \tag{10}$$

Parameter identification is supposed to be carried out using the built-in procedures of the MATLAB computational environment.

2.3. Parameter Identification for Stress-strain Curves

To plot stress-strain diagrams, it is necessary to obtain cyclogram envelopes, the parts of which are described by expressions (5)–(8). The Curve Fitting Toolbox built into the MATLAB environment is well suited for this.

Fig. 7 shows the envelopes of the cyclograms for temperatures of 20, 100, 400, and 600 °C.

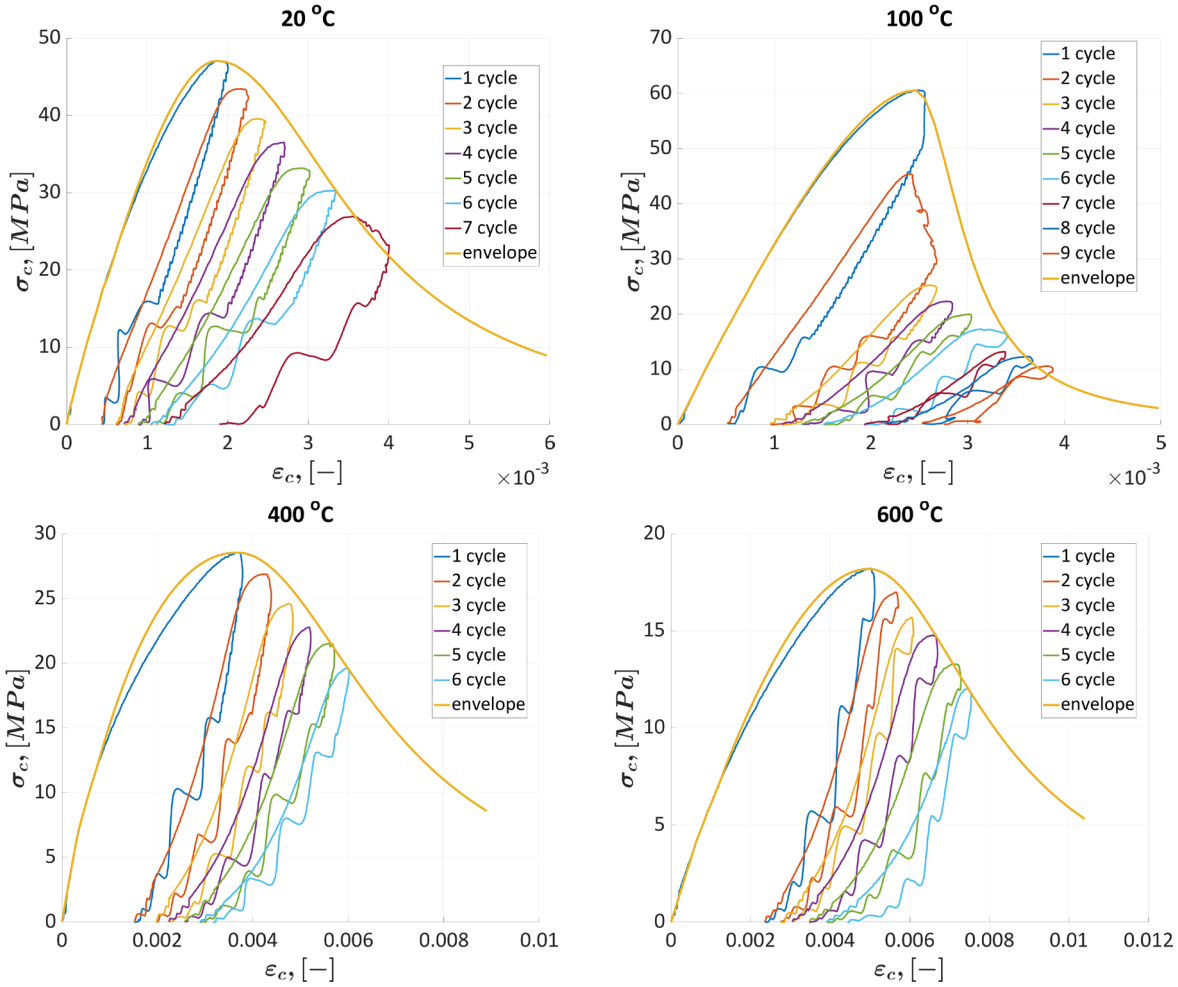

Figure 7. Cyclogram envelopes for temperatures of 20, 100, 400, and 600 °C.

The values of the selected parameters of analytical dependencies for all temperatures are presented in Table 1 of Section 2.5, as well as in Figs. 10 and 11.

2.4. Parameter Identification for Scalar Damage Variable

The identification of the b_c parameter that is present in dependence (10) is carried out based on the approach described in [28]. The *fmincon* tool implemented in the MATLAB environment, which is based on the gradient descent method, is used [29]. The algorithm block scheme is shown in Fig. 8.

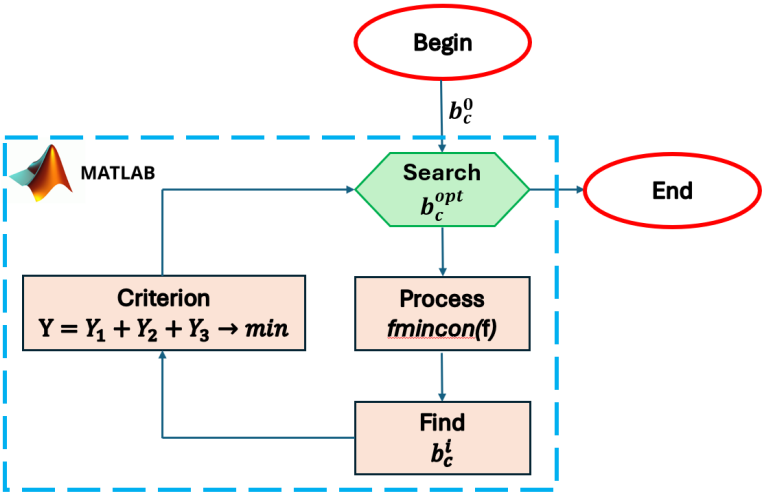

Figure 8. The b_c parameter search algorithm.

Here b_c^0 is the initial value of the parameter; b_c^i is the value of the parameter at the i-th iteration of the optimization procedure; b_c^{opt} is the optimal value of the parameter according to the criterion; Y is the minimized functional; Y_1, Y_2, Y_3 are the functionals that characterize the degree of closeness of the analytical dependence to its experimental etalon.

The functional Y_1 considers the standard deviation of two values [30]. The formulation of this functional is described by the expression (11):

$$Y_1 = \sum\left(d_c^{\exp}\left(\varepsilon_c^{in}\right) - d_c^{analyt}\left(\varepsilon_c^{in}\right)\right)^2. \tag{11}$$

The functional Y_2 considers the linear Pearson correlation coefficient between two values and its proximity to 1 [31]. The formulation of this functional is described by the expression (12):

$$Y_2 = \frac{\sum\left(d_c^{\exp}\left(\varepsilon_c^{in}\right) - \overline{d_c^{\exp}\left(\varepsilon_c^{in}\right)}\right)\sum\left(d_c^{analyt}\left(\varepsilon_c^{in}\right) - \overline{d_c^{analyt}\left(\varepsilon_c^{in}\right)}\right)}{\sum\left(d_c^{\exp}\left(\varepsilon_c^{in}\right) - \overline{d_c^{\exp}\left(\varepsilon_c^{in}\right)}\right)^2 \sum\left(d_c^{analyt}\left(\varepsilon_c^{in}\right) - \overline{d_c^{analyt}\left(\varepsilon_c^{in}\right)}\right)^2} - 1. \tag{12}$$

The functional Y_3 considers the difference in areas under dependencies. The formulation of this functional is described by the expression (13):

$$Y_3 = \int_0^{\varepsilon_{c,\max}^{in}} \left(d_c^{\exp}\left(\varepsilon_c^{in}\right) - d_c^{analyt}\left(\varepsilon_c^{in}\right)\right) d\varepsilon_c^{in}. \tag{13}$$

Fig. 9 shows a comparison of the analytical and experimental dependencies of scalar damage variables on the value of inelastic strain for temperatures of 20, 100, 400, and 600 °C. It is assumed that these dependencies will be extended to the final values of inelastic strain on corresponding stress-strain curves.

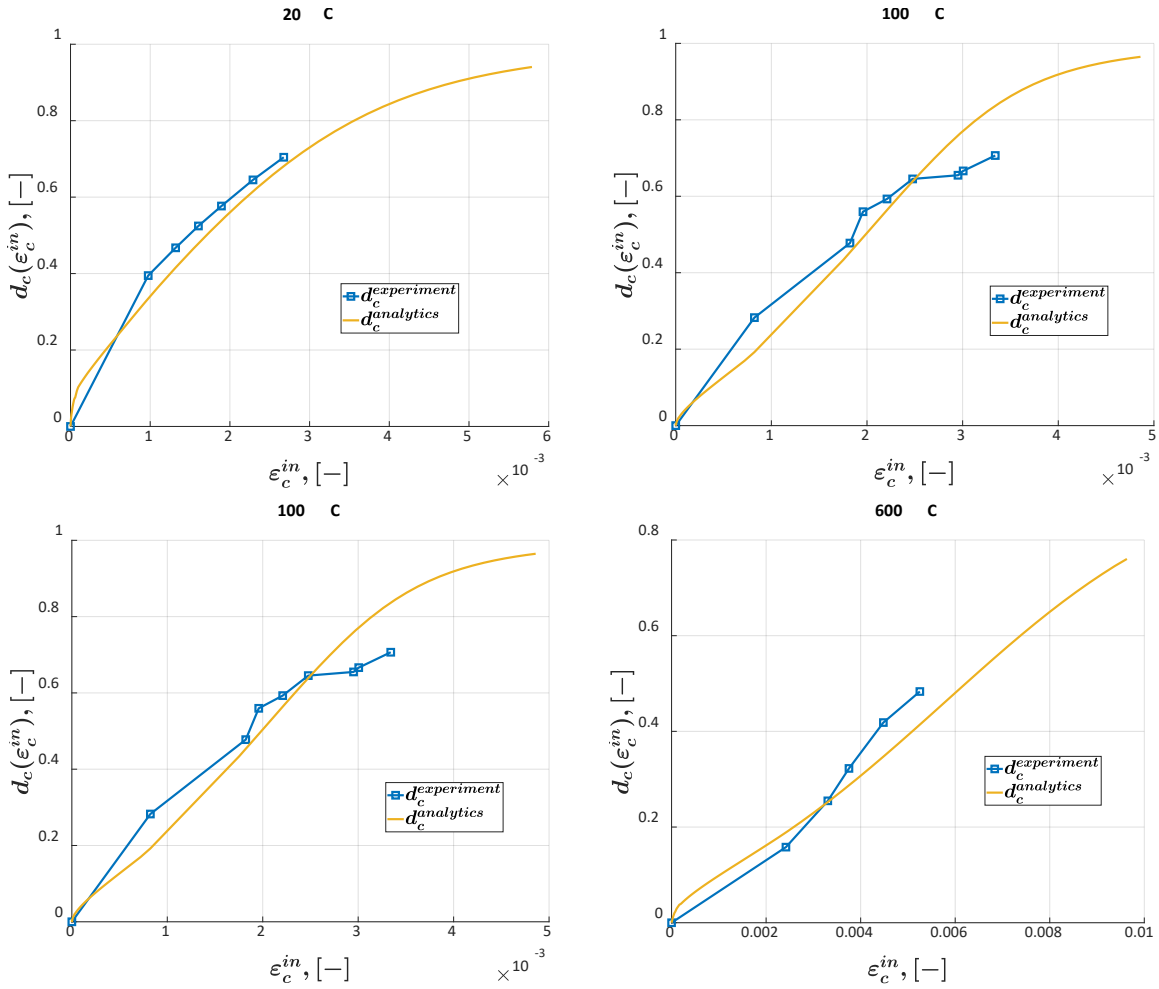

Figure 9. Comparison of analytical and experimental dependencies of scalar damage variable on the value of inelastic strain for temperatures of 20, 100, 400, and 600 °C.

The values of the b_c parameter for all temperatures are presented in Table 1 of Section 2.5, as well as in Figs. 10 and 11.

2.5. Temperature Dependencies

The obtained stress-strain and scalar damage variable curves were used in the verification of the CDP mathematical model based on the problem of uniaxial monotonic and cyclic loading of a prismatic concrete sample in the ABAQUS FEA. In problems with intense high-gradient temperature loading, due to a large gap in the temperature grid, interpolation errors can occur when determining the physical and mechanical characteristics of the material. In this regard, it is proposed to plot the obtained analytical dependencies for an extended family of temperatures. Figs. 10 and 11 show the dependence of the basic constants of the material on temperature. Using the linear interpolation method, the temperature grid is expanded from 20, 100, 400, and 600 °C to 20, 100, 150, 200, 300, 400, 500, and 600 °C.

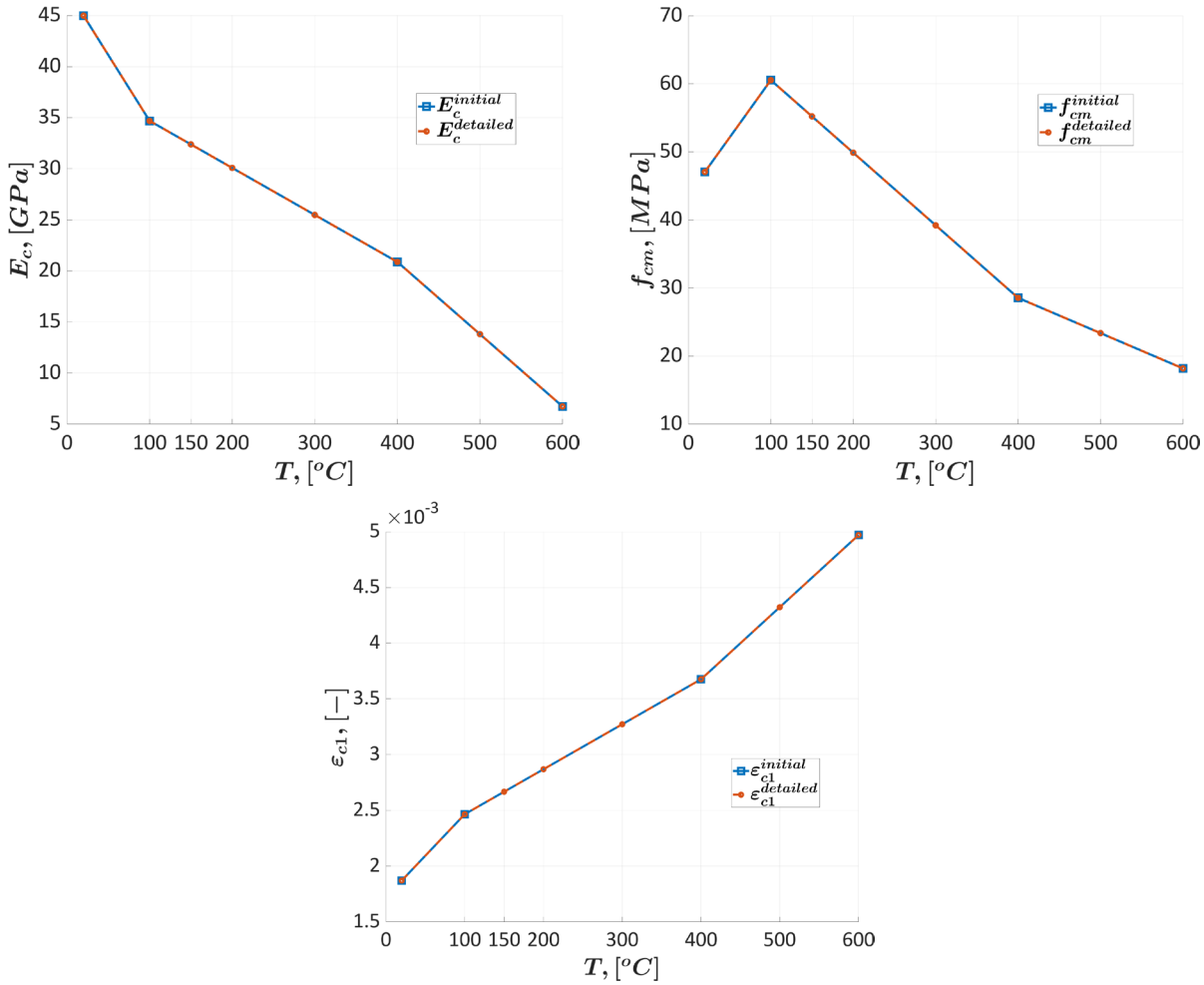

Figure 10. Interpolation of basic physical and mechanical characteristics on an extended temperature grid.

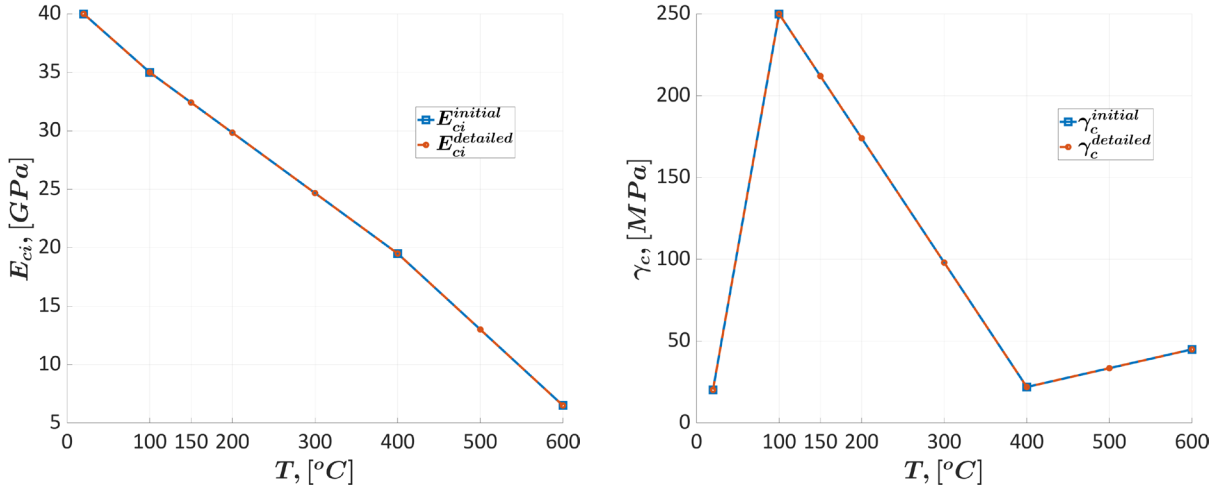

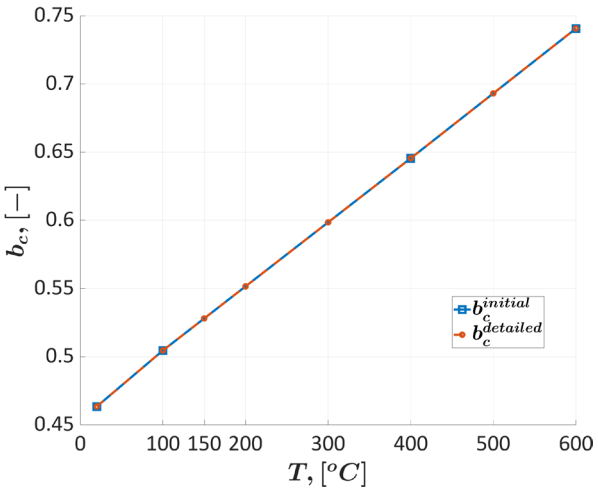

Figure 11. Interpolation of analytical function parameters to an extended temperature grid.

Here, the index "initial" indicates constants that have been identified based on experimental data for temperatures of 20, 100, 400, and 600 °C, and the index "detailed" indicates constants that have been interpolated to an extended value of temperatures of 20, 100, 150, 200, 300, 400, 500, and 600 °C.

In Table 1, the results of identifying for all parameters are shown.

Table 1. Summary table of identification results.

Temperature	20 °C	100 °C	150 °C	200 °C	300 °C	400 °C	500 °C	600 °C
E_c, [GPa]	44.9916	34.6872	32.3861	30.0849	25.4826	20.8802	13.8075	6.73477
f_{cm}, [MPa]	47.0642	60.5492	55.2167	49.8842	39.2192	28.5542	23.3732	18.1922
$\varepsilon_{c1}\cdot 10^3$, [–]	1.87101	2.46612	2.66787	2.86961	3.27309	3.67657	4.32343	4.97028
E_{ci}, [GPa]	40.0000	35.0000	32.4167	29.8333	24.6667	19.5000	13.0000	6.50000
γ_c, [MPa]	20.3100	250.000	212.000	174.000	98.0000	22.0000	33.5000	45.0000
b_c, [–]	0.46357	0.50465	0.52814	0.55163	0.59861	0.64559	0.693165	0.74074
Y_1	0.00792	0.10066	–	–	–	0.10495	–	0.05962
Y_2	0.00735	0.01174	–	–	–	0.01048	–	0.00954
Y_3	5.91e–5	3.27e–5	–	–	–	8.11e–5	–	3.64e–5
Y	0.00866	0.11244	–	–	–	0.11551	–	0.06920

The dependencies shown in Figs. 7 and 9 can be fully used to verify the numerical calculation method in the ABAQUS FEA. Figs. 12 and 13 show the extended compression strain values of the corresponding dependencies family.

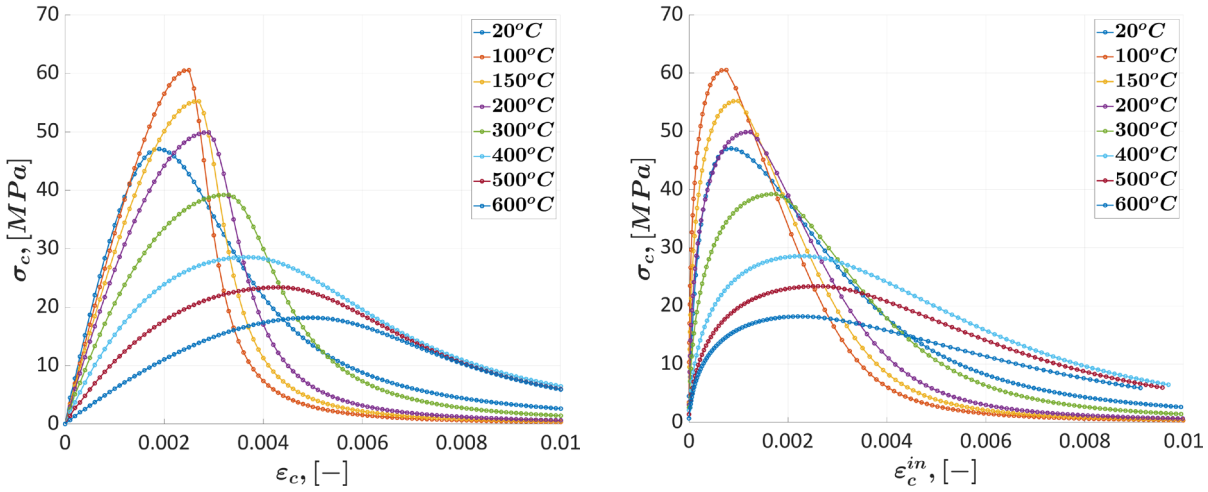

Figure 12. Stress-strain curves family: $\sigma_c(\varepsilon_c, T)$ (left), $\sigma_c(\varepsilon^{in}{}_c, T)$ (right).

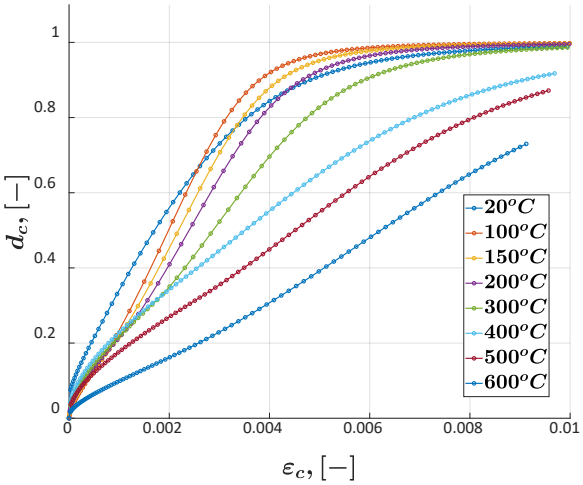

Figure 13. Scalar damage variable family curves $d_c(\varepsilon^{in}{}_c, T)$.

3. Results and Discussion

3.1. Verification of the CDP Model with Identified Parameters

Fig. 14 shows the formulation of the problem in the ABAQUS FEA for a prismatic concrete sample with dimensions of 70×70×280 mm. In addition to the concrete sample, the model contains steel plates with linear-elastic properties. Density of steel is ρ_{steel} = 7850 kg/m^3, Young modulus is E_{steel} = 200 GPa, Poisson's ratio is ν_{steel} = 0.3. To determine the mechanical properties, it is advisable to model a concrete specimen with a single finite element. In this case, the sample is perceived as a sample of the material, and not as a structure.

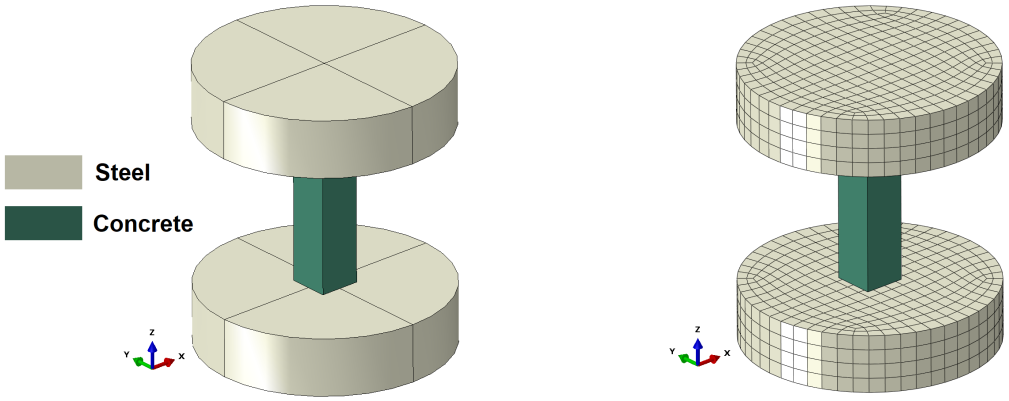

Figure 14. Geometric (left) and finite element (right) model.

In addition to the basic properties, in order to stabilize the applied explicit numerical integration scheme (ABAQUS/EXPLICIT solver), the concrete model also takes into account Rayleigh damping according to the relations (14).

$$\frac{\alpha}{2\omega_i}+\frac{\beta\omega_i}{2}=\xi_i, \tag{14}$$

where α is the coefficient of mass matrix; β is the coefficient of stiffness matrix; ω_i is the i-th natural frequency; ξ_i is the damping coefficient by i-th natural frequency and its value assumed to be equal 0.1.

In this formulation, only damping proportional to the mass is considered, based on the lowest and unique frequency of oscillations of the sample as a rod within the single-element model, so it can be assumed that β = 0. In turn, the first natural frequency of the concrete sample with the given dimensions and properties will be found according to expression (15).

$$\omega_1 = \frac{\pi}{2l}\sqrt{\frac{E_c}{\rho_{concrete}}}. \quad (15)$$

The temperature is set on the concrete element to detect differences in behavior due to properties change. For verification, it is proposed to compare the sample response obtained by calculation with the analytical stress-strain curves specified as material properties for temperature values of 20 and 100 °C.

Fig. 15 shows the boundary conditions in the model. The lower surface of the steel plate is rigidly fixed in space, and the upper surface is connected to the master node, which moves in proportion to the cube of time $u_z \sim t^3$ (kinematic loading) throughout the loading step. Cubic dependence is used for the smooth increase in the acceleration of the plate movement.

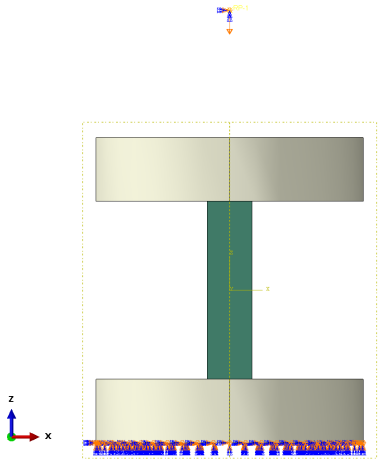

Figure 15. Boundary conditions.

The calculation is carried out in the "*Dynamic Explicit*" formulation. In the case of uniaxial loading, the displacement value (16) corresponding to the final total strain value for the respective temperature shall be applied to the master-node.

$$\varepsilon_c = \frac{u_z}{l}, \quad (16)$$

where u_z is the absolute vertical displacement of the master-node; l is the initial length of specimen.

For cyclic loading, the total calculation time is divided by the number of cycles, and the calculation of each cycle is done independently, but with the initial state of the previous cycle. This can be implemented using "*initial state*" technology in the ABAQUS FEA. Moreover, the resulting displacement value applied to the master-node is also distributed equally across the cycles. However, for this it is necessary not only to divide the total displacement by the number of cycles but also to take into account the accumulated strain.

An important point in the calculation for a sign-constant cyclic load is force control, since it is necessary to stop the calculation at the desired value, without entering the tension region. To do this, it is suggested to modify the ABAQUS keyword file. Moreover, using the "*initial state*" technology, it is possible to set different values of stop force at each load cycle. A description of the commands that should be added to the keyword-file is shown in Table 2.

Table 2. ABAQUS keyword-file modification.

***EXTREME VALUE, HALT=YES**	The "YES" parameter meets the requirement to stop calculation when the critical value is reached.
***EXTREME NODE VALUE, NSET=RP2, MAX**	The calculation stops when the maximum value "MAX" of the monitored value is reached in a set of nodes named "RP2".
RF3, 0.0	The calculation stops when the vertical force reaction "RF3" reaches a value of "0.0" in a set of nodes named "RP2".

At the end of the calculation, information about the reaction, as well as about the displacement, is taken from the master-node, which is converted by scaling into stress and strain according to the ratios (16) and (17).

$$\sigma_c = \frac{R_z}{A}, \tag{17}$$

where R_z is the vertical force reaction in the master-node, A is the cross-sectional area of the specimen.

Then the stress-strain curves are compared – specified as a material properties and obtained from the calculations one.

3.2. Results of Calculations for Uniaxial Compression

Fig. 16 shows a comparison of the uniaxial compression response of a concrete specimen in ABAQUS with the initial, analytically determined, stress-strain curve for temperatures of 20 and 100 °C.

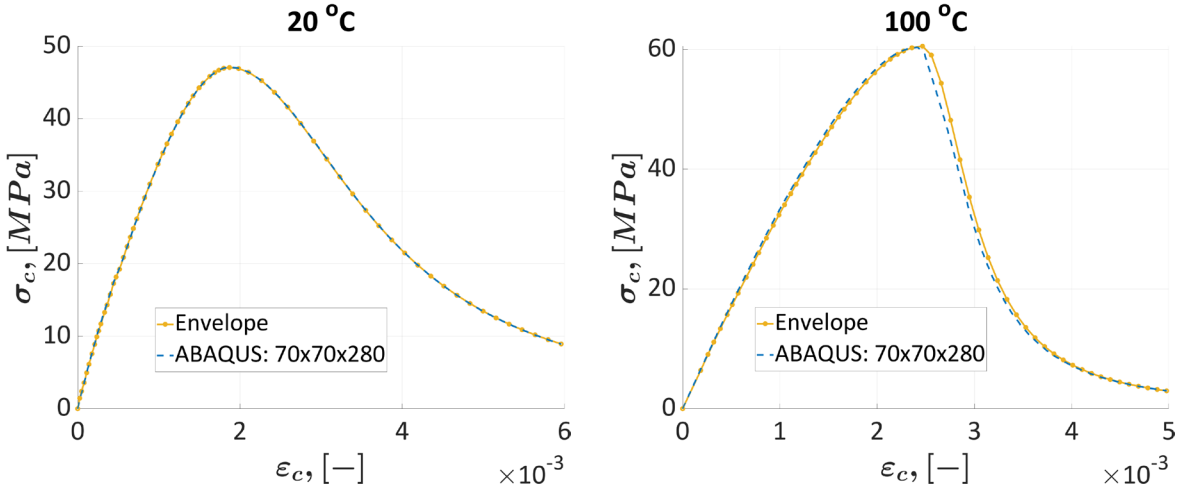

Figure 16. Comparison of calculations: 20 °C (left), 100 °C (right).

There is a complete correspondence of the obtained result with the analytically specified stress-strain curve.

3.3. Results of Calculations for Cyclic Loading

Figs. 17 and 18 show the results of the calculation for cyclic loading. The number of cycles for assessing the degradation of initial elastic properties varied, and options for different values of the reaction in the master-node at which the calculation stops were considered.

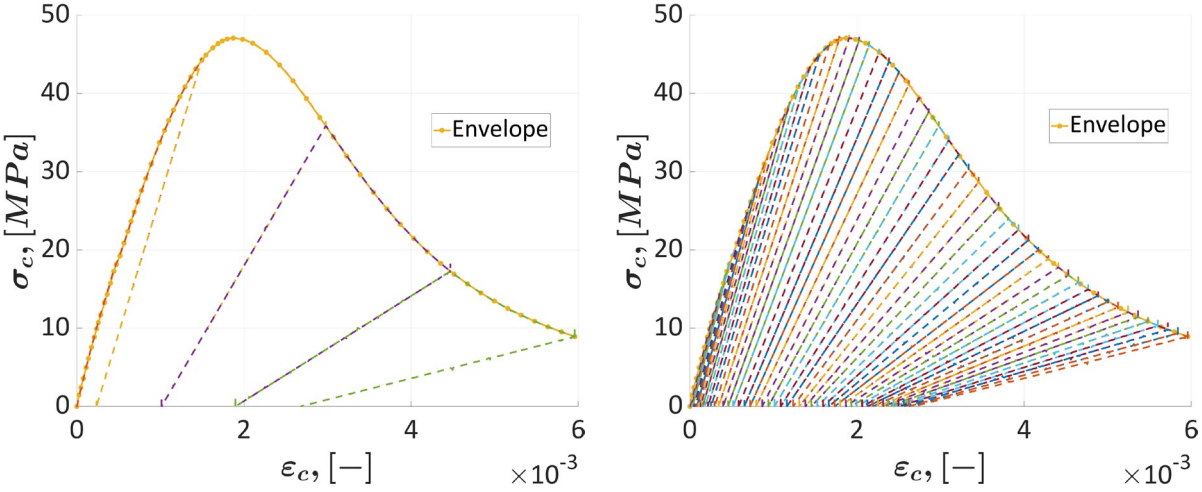

Figure 17. Cyclic load calculation results: 4 cycles with discharge up to 0 kN (left), 50 cycles with unloading up to 0 kN (right)

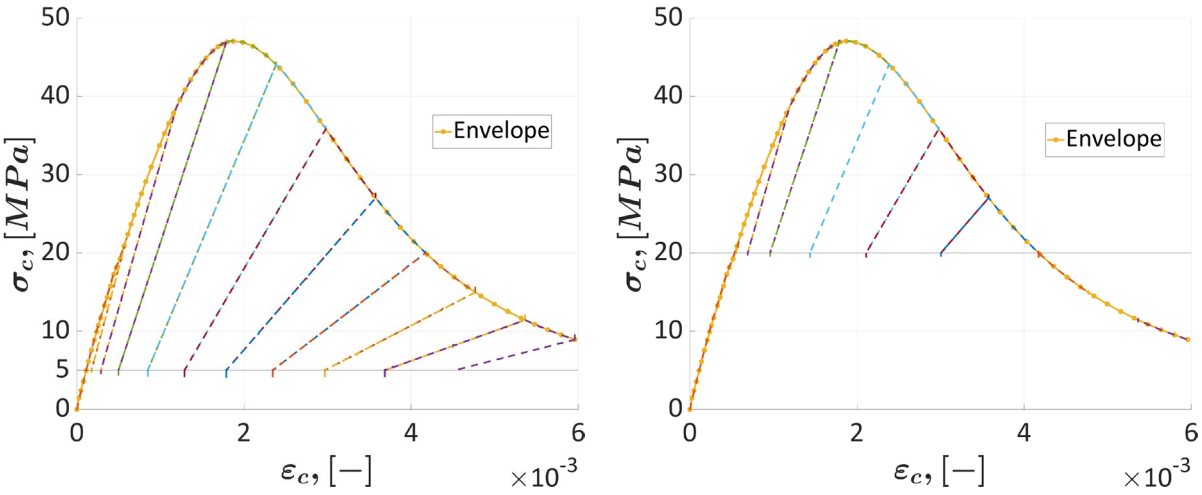

Figure 18. Cyclic load calculation results: 10 cycles with unloading up to 24.5 kN (left), 10 cycles with unloading up to 98 kN (right)

As can be seen from the presented results, under cyclic loading, the general contour of the stress-strain coincides with the initial one, analytically approximated based on experiments [26]. It should be noted that the procedure for stopping the calculation at a given value of vertical force reaction demonstrates its viability. When unloading to force values less than any value on the envelope, the calculation continues two branches of the calculation in the cycle – both for loading and unloading. In turn, when unloading to force values greater than the value on the envelope, the unloading branch is not included, and the calculation follows further along the loading path.

It can also be noted that the results obtained reflect the global practice of modeling inelastic deformation of concrete [4–6, 15–21]. The main aspects of nonlinear behavior under uniaxial and cyclic loading are observed, the temperature dependence of mechanical properties is taken into account, and the behavior of materials with a granular structure in terms of degradation of primary properties (fracture) is taken into account.

4. Conclusions

The paper demonstrates the validation of the CDP mathematical model of nonlinear deformation and strength using the ABAQUS FEA. Using hardware and software complex and test equipment developed separately for this task, the general mechanical properties of heat-resistant concrete were determined, obtained during experiments on cyclic sign-constant loading after exposure to high temperatures. With the help of analytical approximations, the appearance of stress-strain curves, as well as curves of scalar damage (stiffness degradation) variable for different temperatures, was restored.

The proposed methods for identifying parameters make it possible to fully construct a ready-made mathematical model in the MATLAB environment, the input to which is sufficient to provide the initial experimental data. The process of identifying parameters is accompanied by well-known statistical indicators. At the same time, the analytical forms of approximation eliminate the shortcomings associated with the physical nature of the values.

An important aspect of solving the problems of mechanics of a deformable solid is the presence of inhomogeneous, including high-gradient, temperature fields, which significantly affect the physical and mechanical properties of materials and the behavior of structures. Often, when operating under limited data, it is necessary to obtain dependencies for intermediate temperature values. Using the linear interpolation method based on the proposed analytical dependencies, a family of curves for an extended temperature grid was obtained.

In conclusion, the verification problem for uniaxial cyclic sign-constant loading was implemented. The problem was solved for a concrete sample with fixed dimensions. Finite-element formulation implied single-element mesh subdivision. The validity of this solution lies in the fact that in the case of multi-element subdivision, the tested object ceases to be interpreted as a sample, but is a construction of a non-trivial form. This approach also has the right to exist, but often the increase in the number of elements is associated with side effects and, as a result, this can lead to distorted results.

The results obtained on the verification task showed full compliance of the material model with its initial characteristics based on experimental data.

References

1. Rabotnov, Yu.N. O mekhanizme dlitelnogo razrusheniia [On the mechanism of long-term destruction]. Voprosy prochnosti materialov i konstrukciy [Issues of Strength of Materials and Structures]. M.: Ak. Nauk SSSR. 1959. Pp. 5–7.
2. Kachanov, L.M. Osnovy mekhaniki razrusheniia [Foundations of Fracture Mechanics]. M: Nauka. 1974. 312 p.
3. Karpenko, N.I. Obschie modeli mekhaniki zhelezobetona [General models of reinforced concrete mechanics]. M: Stoijizdat. 1996. 416 p.
4. Watanabe, K., Niwa, J., Yokota, H., Iwanami, M. Experimental Study on Stress-Strain Curve of Concrete Considering Localized Failure in Compression. Journal of Advanced Concrete Technology. 2004. 2(3). Pp. 395–407. DOI: 10.3151/jact.2.395
5. Benin, A., Semenov, S., Semenov, A, Bogdanova, G. Parameter identification for coupled elasto-plasto-damage model for overheated concrete. MATEC Web of Conferences. 2017. 107. Article no. 00042. DOI: 10.1051/matecconf/201710700042
6. Benin, A.V., Semenov, A.S., Semenov, S.G., Beliaev, M.O., Modestov, V.S. Methods of identification of concreteelastic-plastic-damage models. Magazine of Civil Engineering. 2017. 8(76). Pp. 279–297. DOI: 10.18720/MCE.76.24
7. Karpenko, N.I., Eryshev, V.A., Latysheva, E.V. Stress-strain Diagrams of Concrete Under Repeated Loads with Compressive Stresses. 2015. 111. Pp. 371–377. DOI: 10.1016/j.proeng.2015.07.103
8. Wang, H., Li, L., Du, X. A thermo-mechanical coupling model for concrete including damage evolution. International Journal of Mechanical Sciences. 2024. 263. Article no. 108761. DOI: 10.1016/j.ijmecsci.2023.108761
9. Lubliner, J., Oliver, J., Oller, S., Onate, E. A plastic-damage model for concrete. International Journal of Solids and Structures. 1989. 25(3). Pp. 299–326. DOI: 10.1016/0020-7683(89)90050-4
10. Lee, J.H., Fenves, G.L. Plastic-Damage Model for Cyclic Loading of Concrete Structures. Journal of Engineering Mechanics. 1998. 124. Pp. 892–900.
11. Lei, B., Qi, T., Li, Y., Jin, Zh., Qian, W. An enhanced damaged plasticity model for concrete under cyclic and monotonic triaxial compression. European Journal of Mechanics – A/Solids. 2023. 100. Article no. 104999. DOI: 10.1016/j.euromechsol.2023.104999
12. Kakavand, M.R.A., Taciroglu, E. An enhanced damage plasticity model for predicting the cyclic behavior of plain concrete under multiaxial loading conditions. Frontiers of Structural and Civil Engineering. 2020. 14(6). Pp. 1531–1544. DOI: 10.1007/s11709-020-0675-7
13. Budarin, A.M., Rempel, G.I., Kamzolkin, A.A., Alekhin, V.N. Concrete damage–plasticity model with double independent hardening. Vestnik MGSU [Monthly Journal on Construction and Architecture]. 2024. 19(4). Pp. 527–543. DOI: 10.22227/1997-0935.2024.4.527-543
14. Abaqus [Online]. URL: https://docs.software.vt.edu/abaqusv2025/English/?show=SIMULIA_Established_FrontmatterMap/sim-r-DSDocAbaqus.htm (reference date:19.10.2025).
15. Fakeh, M., Jawdhari A., Fam A. Recommended concrete damage plasticity parameters and constitutive models for UHPC in ABAQUS. Engineering Structures. 2025. 333. Article no. 120154. DOI: 10.1016/j.engstruct.2025.120154
16. Rainone, L.S., Tateo, V., Casolo, S., Uva, G. About the Use of Concrete Damage Plasticity for Modeling Masonry Post-Elastic Behavior. Buildings. 2023. 13. Article no. 1915. DOI: 10.3390/buildings13081915
17. Bayat, H., Chalecki, M., Lesniewska, A., Maj, M., Rybak, J., Ubysz, A. The cyclic load effect on the elasticity and plasticity deformation of high-strength reinforced concrete elements. Archives of Civil and Mechanical Engineering. 2024. 24. Article no. 135. DOI: 10.1007/s43452-023-00855-9
18. Lovlev, G., Zileev, A.G. Concrete Damage Plasticity model testing in numerical modeling of cemented rock fill. Gornyi Zhurnal. 2025. 9. Pp. 77–97. DOI: DOI: 10.17580/gzh.2025.09.10
19. Dewi, P.A.P, Sudarsana, I.K., Susila, I.G.A. Validation control in finite element analysis of wide beam-column connections using concrete damage plasticity under cyclic loading. Journal of Infrastructure Planning and Engineering. 2025. 4(1). Pp. 1–3. DOI: 10.22225/jipe.4.1.2025.1-9
20. Hu, A., Chen, X., Du, X., Wang, F. Dynamic Compressive Damage Constitutive Correction of Concrete Under Freeze-Thaw Cycle. Materials. 2025. 18(6). Article no. 1238. DOI: 10.3390/ma18061238
21. Feng, W., Hussin, T.A.R., Yang, X. A temperature-indexed concrete damage plasticity framework for thermomechanical analysis of concrete structures. Journal of Engineering and Applied Science. 2025. 72. Article no. 177. DOI: 10.1186/s44147-025-00753-2
22. Jankowiak, T., Lodygowski, T. Identification of parameters of concrete damage plasticity constitutive model. Foundations of civil and environmental engineering. 2005. 6. Pp. 53–69.
23. Hafezolghorani, M., Hejazi, F., Vaghei, R., Jaafar, M.S.B., Karimzade, R. Simplified Damage Plasticity Model for Concrete. Structural Engineering International. 2017. 27(1). Pp. 68–78. DOI: 10.2749/101686616X1081
24. Rakić, D.M., Bodić, A.S., Milivojević, N.J., Dunić, V.L., Živković, M.M. Concrete damage plasticity material model parameters identification. Journal of the Serbian Society for Computational Mechanics. 2021. 15(2). Pp. 111–122. DOI: 10.24874/jsscm.2021.15.02.11
25. Alfarah, B., López-Almansa, F., Oller, S. New methodology for calculating damage variables evolution in Plastic Damage Model for RC structures. Engineering Structures. 2017. 132. Pp. 70–86. DOI: 10.1016/j.engstruct.2016.11.022
26. Birtel, V., Mark, P. Parameterised Finite Element Modelling of RC Beam Shear Failure. Proceedings of the ABAQUS Users' Conference. 2006. 14. Pp. 95–108.
27. Niu, Y., Wang, W., Su, Y., Jia, F., Long, X. Plastic damage prediction of concrete under compression based on deep learning. Acta Mechanica. 2024. 235. Pp. 255–266. DOI: 10.1007/s00707-023-03743-8
28. Murtazin, I.R., Melnikov, B.E., Semenov, A.S. Simulation of Inelastic Response of Polycrystalline Nickel Based on Micromechanical Model Homogenization. Advanced Problem in Mechanics III. Springer. Cham, 2023. Pp. 427–444. DOI: 10.1007/978-3-031-37246-9_32
29. Yurchenko, V.V., Peleshko, I.D. Improved gradient projection method for parametric optimisation of bar structures. Magazine of Civil Engineering. 2020. 6(98). Article no. 9812. DOI: 10.18720/MCE.98.12
30. Tiraturyan, A.N., Uglova, E.V., Simchuk, E.N., Kadyrov, G.F., Gorskiy, M.Yu. Prediction of temperature distribution in asphalt concrete layers. Magazine of Civil Engineering. 2024. 17(7). Article no. 13101. DOI: 10.34910/MCE.131.1

31. Lukash, K.A., Shurshilin, E.A., Olekhnovich, Y.A., Radaev, A.E. Correlation model for cost and technical characteristics of thermal insulation material used in enclosing structure. Magazine of Civil Engineering. 2025. 18(1). Article no. 13306. DOI: 10.34910/MCE.133.6

Information about the authors:

Ilnar Murtazin,
ORCID: https://orcid.org/0000-0002-7580-5669
E-mail: murtazin_ir@spbstu.ru

Roman Fedorenko,
ORCID: https://orcid.org/0000-0002-2115-1751
E-mail: fedorenko_rv@spbstu.ru

Aleksei Lukin, *PhD in Physics and Mathematics*
ORCID: https://orcid.org/0000-0003-2016-8612
E-mail: lukin_av@spbstu.ru

Victor Modestov, *PhD in Technical Sciences*
ORCID: https://orcid.org/0000-0003-0845-638X
E-mail: vmodestov@spbstu.ru

Andrey Malinkin, *PhD in Technical Sciences*
E-mail: mas193cm@mail.ru

Mikhail Fedotov,
E-mail: domzagorodom@mail.ru

Sergey Panarin, *PhD in Technical Sciences*
E-mail: tekhnoarm@mail.ru

Received 19.06.2025. Approved after reviewing 12.09.2025. Accepted 12.09.2025.

Magazine of Civil Engineering

ISSN 2712-8172

journal homepage: http://engstroy.spbstu.ru/

Research article

UDC 624

DOI: 10.34910/MCE.138.9

The expansion deformation characteristics of expansive soil under acid pollution

H. Lu[1] , ***S. Song***[2] , ***G. Xiang***[2] ✉ , ***X. Wang***[2] , ***M. Luan***[1]

[1] *School of Civil Engineering, Wanjiang University of Technology, Maanshan, China;*

[2] *School of Civil Engineering and Architecture, Anhui University of Technology, Maanshan, China*

✉ *Xianggsh2011@163.com*

Keywords: expansive soil, acid rain, swelling, deforming, fractals, acid pollution

Abstract. Soil pollution incidents occur frequently in China. After contamination by acid, the expansion performance of expansive soil is further intensified, posing a significant threat to infrastructure. Using sulfuric acid as the contaminant source, expansion deformation tests of expansive soil under sulfuric acid immersion were conducted, followed by scanning electron microscopy and X-ray diffraction analyses to investigate the evolution of the microstructure and mineral composition of the samples under acidic conditions. The results demonstrated that the acidic environment increased the expansion rate of the samples, with higher sulfuric acid concentrations correlating to greater expansion rates. Under acidic conditions, cementing materials (e.g., free oxides) in expansive soil underwent varying degrees of dissolution and leaching, thereby weakening the connections between overlapping structures. This process resulted in a more dispersed arrangement of the surface-overlapping structures, accompanied by a continuous increase in both the volume and number of micropores. The post-acid-rain expansion deformation of expansive soil can be quantified using the e–p_e fractal relationship. Furthermore, the e–p_e fitting analysis of the experimental data revealed that the enhancement of expansion performance by acid rain primarily stems from the reduction in cementing content, leading to an increase in the expansion coefficient (κ).

Funding: This article is funded by the National Natural Science Foundation of the People's Republic of China (Grant Number: 42577533) and Scientific Research Project of Colleges and Universities in Anhui Province of China (No. 2024AH051868).

Citation: Lu, H., Song, S., Xiang, G., Wang, X., Luan, M. The expansion deformation characteristics of expansive soil under acid pollution. Magazine of Civil Engineering. 2025. 18(6). Article no. 13809. DOI: 10.34910/MCE.138.9

1. Introduction

Soil pollution incidents occur frequently in China. According to statistical data from relevant studies, 209 soil pollution incidents were recorded between 2005 and 2022, 51 of which involved acidic contaminants. Researchers have consistently observed that acidic contamination generally degrades the mechanical properties of soil. Under acidification, the dissolution of cementing materials and the dissociation of cations ($Ca^{2+}$and Mg^{2+}) in silicate minerals weaken interparticle bonding forces, promote pore development, and ultimately lead to reduced soil strength, increased deformation, and severe deterioration of mechanical performance. Empirical data indicate that a 1-unit decrease in the pH of the acid-etching solution corresponds to a 20–25 % [1] reduction in soil cohesion and an 18–26 % [2] increase in the compression index, triggering geotechnical hazards such as soil loosening, foundation subsidence, and slope instability [3–6]. Expansive soils, widely distributed in China with a coverage exceeding

100,000 km^2, affect regions inhabited by over 300 million people. Intensive human activities in these areas have heightened the frequency of acidic contamination incidents. These soils are primarily composed of hydrophilic clay minerals (montmorillonite and illite), whose unique crystal layer structures exhibit strong cation exchange capacity and hydration properties. Their characteristic “swell-shrink” behavior – expansion upon water absorption and contraction upon dehydration – represents a critical engineering challenge. Acidic solutions react chemically with components of expansive soils, significantly altering their swelling-shrinkage characteristics and jeopardizing the safety of regional infrastructure. Therefore, elucidating the effects of acid solutions on the swelling deformation behavior and microstructure of expansive soils, along with developing a scientifically robust model for predicting expansion deformation, is imperative for the safety assessment of acid-contaminated expansive soils.

For expansive soil, Chang et al. [7] found that a lower pH environment markedly increased the unloading expansion rate, expansion force, and shrinkage rate of Beise expansive soil. Microscopic analysis revealed that this was due to the dissolution of cementing agents, the development of porosity, and a consequent reduction in interparticle bonding strength. Li et al. [8] have consistently observed that acidic solutions lead to accelerated swelling rate, prolonged stabilization time, and noticeable chemical swelling phenomena in the expansive soils of the Mengzi region, China. Sivapullaiah et al. [9] also found that the expansion performance of black cotton expansive soil was significantly enhanced after being treated with sulfuric acid. By analyzing the microstructure, the researchers found that the specific surface area of expansive clay, after being corroded by acid solution, would increase significantly, even by 3 to 5 times [10]. When not acidified, expansive clay basically shows a flocculent structure of multiple layers of clay combined together, with strong agglomeration among them; while after acidification, the agglomeration of the original aggregate weakens, evolving from the surface-overlapping structure to the edge-edge structure, presenting a dispersed structure, and the volume and number of micropores also increase continuously, resulting in enhanced expansion performance [11]. Further analysis reveals that the main cause of the loose structure of acidified expansive soil is the acid leaching of cementing materials such as free oxides in the expansive soil. Unbound oxides residing in disordered configurations within the interparticle voids of soil matrices function as cohesive binders for clay mineral colloids, with their accumulation significantly reinforcing the intergranular adhesion forces in swelling clay soils [12, 13]. As the pH value of the acidic solution decreases, the free cements such as SiO_2, Al_2O_3, K_2O, MgO, Fe_2O_3, and CaO in the expansive soil will be eroded and leached to varying degrees, resulting in an increase [14–16] in expansive properties and a gradual weakening of the structural bonding between expansive aggregates [17], which is one of the main reasons why acidic solutions lead to an increase in expansive properties such as the expansion of expansive soil.

In addition, researchers have generally found that the reaction of acidic solutions with expansive soil can also cause changes in mineral composition, especially the changes in the content of hydrophilic minerals such as montmorillonite and illite have an important impact on expansive properties. However, the evolution of hydrophilic minerals under acidified conditions remains unclear. Some scholars believe that acids have an erosive effect on aluminum in montmorillonite crystals, which can destroy the crystal structure and cause a decrease in the content of hydrophilic minerals. Gratchev and Towhata [18] studied the consolidation and compression properties of three types of clay around the coast of Japan and found that sulfuric acid erosion had different effects on the consolidation and compression properties of different types of clay because different clays had different mineral compositions and had different initial microstructures of the soil. Liu et al. [19] found that acidic conditions led to the dissolution of montmorillonite, resulting in a significant reduction in its content. Gratchev and Towhata [11] also found the dissolution effect of sulfuric acid on montmorillonite in Kawasaki clay. However, some scholars have found that in acidic conditions, illite or illite-montmorillonite mixed layers are more likely to undergo potassium removal and transform into montmorillonite, resulting in an increase in montmorillonite content. Zhao et al. [20] experimental studies revealed that acidic precipitation accelerates the mineralogical transformation of illite and illite-smectite interstratified minerals in swelling clays through hydrolysis-driven alteration processes, and believed that this was one of the main causes of landslides in the Three Gorges Reservoir Area. Chang et al. [21] employed bulk mineralogical characterization combined with thermodynamic geochemical modeling to systematically decipher the hydro-chemo interaction dynamics of acidic leaching solutions with swelling clay strata, and concluded that some illite depotassium was transformed into montmorillonite clay minerals, resulting in a decrease in illite content and an increase in montmorillonite content.

In addition, acidic solutions can also trigger ion exchange in expansive soil. Prasad et al. [15] pointed out that cation exchange and changes in mineral composition in acidic conditions led to an increase in expansive properties of expansive soil. Chavali et al. [22] suggest that the enhanced expansion performance of expansive soil under the action of acid solution is closely related to the substitution of exchangeable cations by hydrated hydrogen ions, which can promote the dissociation of cations such as Ca^{2+} and Mg^{2+} in silicate minerals and reduce the electrostatic attraction effect of exchangeable cations on the clay surface.

The acidic environment profoundly compromises the engineering performance of expansive soils by dissolving cementing agents, altering the microstructure, and influencing clay mineral transformation. To mitigate these effects, future research and practice should prioritize the development of economical countermeasures, primarily through three avenues: material modification (e.g., incorporating lime or fly ash to neutralize acidity), the construction of impermeable barriers (e.g., using geosynthetics or clay liners to prevent acid infiltration), and enhancing chemical stability (e.g., via ion exchange and cementation). In line with the principles of a circular economy, there is a growing research focus on sustainable remediation using industrial and urban waste. For instance, Randhawa et al. [23] demonstrated that a blend of 60 % lime-stabilized soil, 20 % municipal solid waste incineration bottom ash (MSWI BA), and 20 % calcium carbide residue (CCR) could increase the unconfined compressive strength (UCS) and splitting tensile strength (STS) of expansive clay by up to 526.03 and 463.41 %, respectively, after 28 days of curing. Furthermore, Shen et al. [24, 25] showed that embedding MSWI BA columns into soft kaolinite clay – with a column penetration ratio (CPR) of 0.8 – increased shear strength by 58.66 %, attributable to the column's drainage and skeleton effects. A synergistic enhancement was achieved by mixing bottom ash with silica fume to form a composite column (BASF), which increased the shear strength by up to 88.59 % due to pozzolanic reactions and improved stiffness. Additionally, Ghalandarzadeh et al. [26] confirmed that encasing these columns with geotextiles further optimizes load transfer, confines lateral bulging, and enhances the overall stability of the composite foundation.

Some progress has been made in the study of the expansion properties of expansive soil under acidic solutions. Due to the differences in mineral composition and microstructure of expansive soil in different regions, the reactions with acidic solutions are somewhat different, resulting in different mechanisms of changes in expansive properties. Therefore, further research is needed on the mechanism of the change in expansive properties of expansive soil under acidic solution contamination. This paper takes expansive soil from areas with severe soil pollution in China as the research object, with sulfuric acid as the pollution source, and conducts an expansion test on the expansive soil soaked in sulfuric acid to test the variation of expansive properties with the concentration of sulfuric acid, By means of X-ray diffraction (XRD), scanning electron microscopy (SEM), and other testing methods, physical and chemical indicators such as mineral composition, cementation composition, and microscopic pore structure of expansive soil under sulfuric acid pollution are analyzed to reveal the mechanism of the effect of acid rain on expansive properties. At the same time, combined with the fractal theory of porous media surface, an expansion fractal model of expansive soil under the action of acidic solution is constructed for the scientific prediction of expansion performance, which can provide scientific guidance for the prevention and control of geological disasters in acid-contaminated expansive land areas.

2. Methods

2.1. Materials

Sulfuric acid is widely used in industry, agriculture, medicine, chemical engineering, and other fields. China produces about 100 million tons of sulfuric acid annually. Leakage is inevitable during the production and transportation of sulfuric acid, causing pollution to the soil. Therefore, in this study, sulfuric acid with concentrations of 1, 10, and 20 % (corresponding to molar concentrations of 0.102, 1.087, and 2.324 mol/L) was used as the acidic contaminant. Distilled water was also used as the control group. The 20 % maximum sulfuric acid concentration used in this study was dictated by the following considerations: (1) Environmental Relevance: The acidity of soil pore water in real-world contamination incidents is generally lower than this level; (2) Chemical Saturation: Preliminary tests indicated that concentrations above 20 % caused the expansion rate trend to flatten, implying that the dissolution of key cementing agents was nearing completion; (3) Operational Safety: Higher concentrations exhibit strong corrosivity, introducing substantial risks to laboratory personnel and procedures.

Kunming, Yunnan is the largest sulfuric acid production base in China, the sampling site was selected within the historical leakage area downwind of a sulfuric acid plant, ensuring it is representative of industrially impacted acidic environments. This region features widely distributed expansive soils, primarily composed of montmorillonite and illite, which exhibit strong swell-shrink potential and are representative of southwestern China. The mineral composition of the studied soil is similar to that of well-known expansive soils such as Baise clay and Indian black cotton soil as it is also rich in hydrophilic minerals like montmorillonite and illite. Therefore, it is representative in terms of its engineering geological characteristics. Preliminary analysis identified a high content of free oxides (e.g., Fe_2O_3, Al_2O_3, CaO), which are key cementing agents for structural stability. Their susceptibility to acid dissolution makes this soil highly sensitive to acidic environments, providing an ideal medium for investigating the relationship between cement dissolution and macroscopic swelling. Soil samples were collected from a 2-meter depth, avoiding zones of active root penetration and significant human disturbance to ensure the obtained samples were pristine and representative. Laboratory tests determined the soil's physical properties and mineral

composition. Following the methods of Shen and Britto [27, 28], the permeability coefficient, maximum dry density, and optimum moisture content of the Kunming expansive soil were calculated as summarized in Table 1.

Table 1. Physical properties and mineral composition of expansive soil.

Optimal moisture content w (%)	Maximum dry density ρ (g/cm^3)	permeability coefficient k(m/s)	Plastic limit w_P (%)	Liquid limit w_L (%)	Free expansion rate δ_{ef} (%)	Mineral composition and content (%)				
						Montmorillonite	Illite	Kaolinite	Chlorite	Quartz
23.5	2.32	4.26×10^{-10}	31.4	76.1	81.9	37.4	31.3	15.6	13.3	2.2

2.2. Expansion Test

Cut the original Kunming soil retrieved from the site into a sample in the shape of a circular knife section and place it in a stainless steel plate with polyethylene film at the bottom. Place a piece of filter paper and a permeable stone on each of the upper and lower sides of the sample in sequence. Install a dial indicator, record the initial reading, and apply the required load. Five loads of 6.25, 12.5, 25, 50, and 100 kPa were selected to simulate the force state of the soil at different depths. The load was applied at one time, that is, it remained constant during the test. Then pour sulfuric acid into the consolidation instrument to submerge the sample by about 1 cm. After that, record the changes in the dial indicator reading over time. When the dial indicator pointer changes less than 0.01 within 12 hours, it is considered that the expansion deformation has stabilized.

2.3. Characterization Tests

After the expansion test is completed, remove the sample saturated with acid solution and cut the sample in half. Transfer half of the sample to an aluminum container filled with liquid nitrogen for rapid freezing. Subsequently, the aluminum boxes containing expansive soil were placed in a freeze dryer (–50 °C) and vacuum-dried for 24 hours to remove moisture. Finally, the samples were taken out for SEM tests. At the same time, the other half of the sample was placed in a 50 °C oven to dry. The dried soil particles and precipitated minerals were ground and sifted through a 2 mm sieve, and the minerals and their chemical composition in the sample were measured using an X-ray diffractometer.

2.4. Test of Cementing Content

The cementing materials in expansive soil are mainly free oxides, but some free oxides are encapsulated in the surface of other silicate minerals or fill the pores and are difficult to separate. When testing free oxides, a suitable solution should be chosen to avoid affecting silicate minerals and to dissolve all types of free oxides. Existing studies have shown that sodium citrate-sodium dithionite ($C_6H_5Na_3O_7$–$Na_2S_2O_4$) performs well in selectively dissolving free oxides. Therefore, this method is used to test the cementing materials content, and the specific test process is as follows:

First, weigh about 2.0 g of the pre-treated soil sample and place it in a 100 mL centrifuge tube. Then, add 40 mL of 0.3 mol/L sodium citrate ($C_6H_5Na_3O_7$) solution and 6 mL of 1.0 mol/L $NaHCO_3$ solution. Heat the tubes in a water bath to 80 °C. Then, add 1.0 g of solid sodium dithionite ($Na_2S_2O_4$) to the centrifuge tube and stir constantly until the soil sample is completely grayish-white. Add 10 mL of saturated NaCl solution to facilitate the flocculation of the clay particles. After cooling, solid-liquid separation is carried out using a centrifuge, and the soil residue in the centrifuge tube is washed twice with 1.0 mol/L NaCl solution. It is then washed three times with distilled water, filtered, and weighed. The cementing content c_c can be calculated by the following formula:

$$c_c = \frac{m_1 - m_2}{m_1} \times 100\%. \quad (1)$$

In the formula: c_c represents the content of cementing in acidified expansive soil, m_1 represents the mass of expansive soil without $C_6H_5Na_3O_7$-$Na_2S_2O_4$ treatment, and m_2 represents the mass of the residue in the treated soil.

3. Results and Discussion

3.1. Expansion Deformation Test

Fig. 1 shows the relationship curves of the expansion rate of expansive soil in different sulfuric acid solutions under a load of 6.25 kPa over time. Experimental observations reveal that swelling clay specimens subjected to varying sodium sulfate concentrations exhibit analogous deformation trajectories, characterized by three consecutive phases: initial gradual expansion, subsequent accelerated growth, and ultimate stabilization [29, 30]: slow increase at first, then rapid increase, and finally stabilization. Fig. 1 shows that the expansion rate is the smallest in distilled water at 20.3 %, while the expansion rates are 23.1 and 24.6 % under 1 and 10 % sulfuric acid solutions, respectively, indicating that the expansion performance of the expansive soil is somewhat enhanced by sulfuric acid solutions.

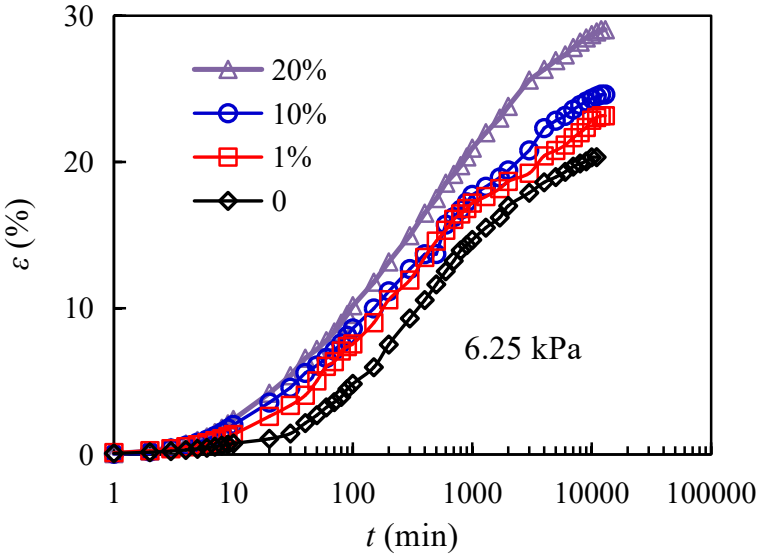

Figure 1. The relationship between the expansion rate of bentonite and time at 6.25 kPa.

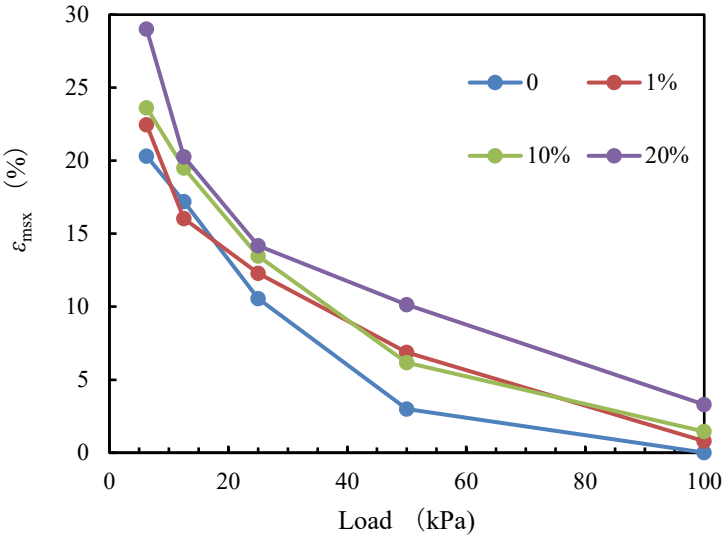

Figure 2. Relationship between maximum expansion deformation and load.

Fig. 2 illustrates the correlation between peak swelling strain in expansive soils and applied compressive stress. The figure shows that when the solution remains constant, the expansion rate gradually decreases as the load increases. When the load increased from 6.25 to 100 kPa, the maximum expansion rate decreased from 29.1, 24.6, 23.1, and 20.3 % to 3.4, 1.57, 0.768, and 0.127 %, respectively, indicating that the increase in load significantly affected the expansion of expansive soil. When the load was constant, the expansion rate curve of the expansive soil shifted upward with increasing sulfuric acid solution concentration, indicating that higher sulfuric acid concentrations enhanced the expansive properties of the soil. For example, under a load of 50 kPa, the maximum expansion rates of expansive soil in 0, 1, 10, and 20 % sulfuric acid were 2.98, 6.88, 6.17, and 10.14 %, respectively. The mechanism, by which sulfuric acid

enhances the expansive properties of expansive soil, will be explained through composition analysis and microstructure tests.

3.2. Chemical Composition Changes

Fig. 3 shows the XRD comparison patterns of expansive soil under neutral and acidic conditions, where M denotes montmorillonite, I – illite, K – kaolinite, and Q – quartz. When the solution environment changed from neutral to acidic, the intensity of characteristic peaks at specific diffraction angles decayed, with this decay becoming more pronounced as environmental acidity increased. After soaking in 10 and 20 % sulfuric acid, the characteristic peak intensity of montmorillonite near 5.7 ° decreased from 485 (original soil) to 405.25 and 352.5, respectively. Similarly, the characteristic peak intensity of illite at 9.0° decreased from 317.5 to 292.5 and 270, while that of kaolinite at 20.9° decreased from 327.5 to 301.5 and 271.35. The underlying mechanism involves the attack of H^+ ions from the acidic solution on the mineral framework of expansive soils, particularly the octahedral sheets (e.g., Al-O-OH in montmorillonite and kaolinite). These ions react with cations such as Al^{3+}, Mg^{2+}, and Fe^{3+}, leading to their selective dissolution and a consequent “de-octahedralization.” Simultaneously, the Si-O-Si or Si-O-Al bonds in the tetrahedral sheets may undergo protonation and breakage in a strongly acidic environment. This localized dissolution and degradation of the crystal framework reduce the overall crystallinity and diminish the proportion of well-ordered mineral structures. Macroscopically, this is evidenced by the universal attenuation of characteristic XRD peak intensities. Mineral composition, quantified using X'Pert HighScore Plus software (Table 2), shows subtle but indicative changes after acid soaking: the illite content decreased from 31.3 to 26.4 %, while the montmorillonite content increased from 37.4 to 40.8 %. This shift is attributed to the acid-driven enhancement of ion exchange. K^+ in the illite interlayer was likely replaced by solution cations like Ca^{2+} and subsequently leached out. This potassium release destabilizes the illite structure, thereby promoting its transformation into metastable montmorillonite, a pattern consistent with findings by Chang et al. [21]. Overall, however, the minor changes in hydrophilicity had negligible effects on expansion performance.

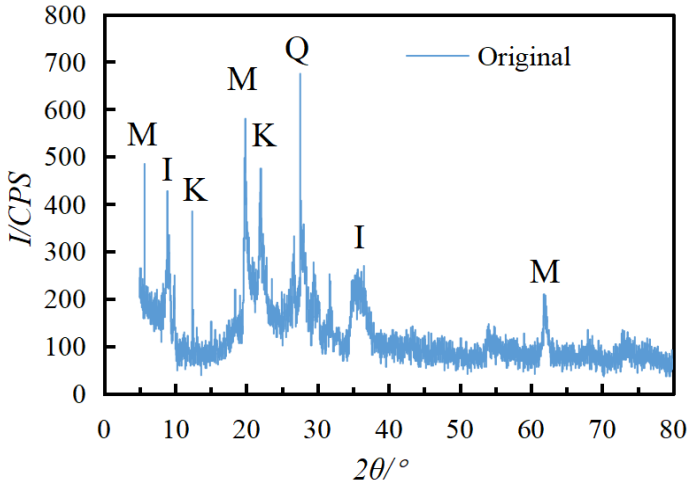

a – water

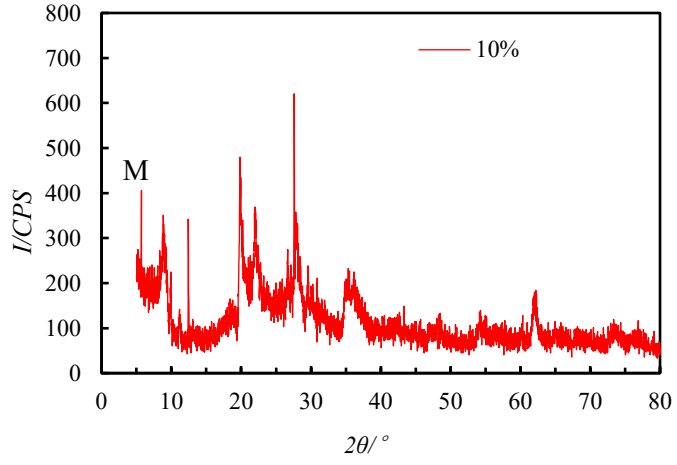

b – 10% H_2SO_4

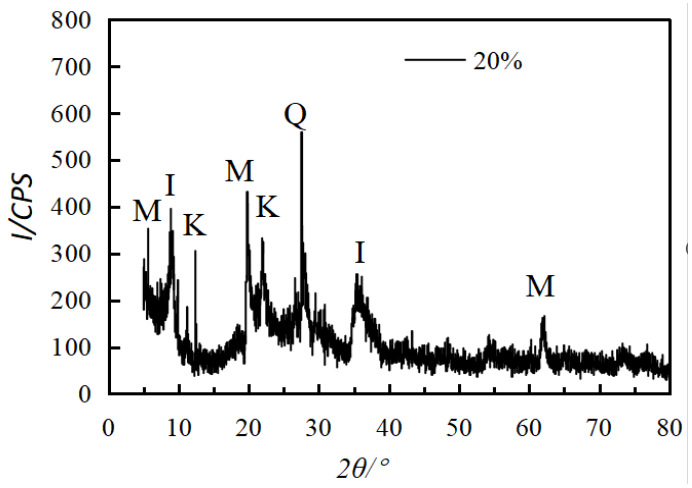

c – 20% H2SO4

Figure 3. XRD pattern of expansive soil samples: M – Montmorillonite, K – Kaolinite, I – Illite, Q – Quartz.

Table 2. Mineral composition of expansive soil soaked in sulfuric acid.

	Montmorillonite	Illite	Kaolinite	Chlorite	Quartz
Original soil	37.4	31.3	15.6	13.3	2.2
Soak in 10 % sulfuric acid	39.6	28.7	14.3	12.8	4.3
Soak in 20 % sulfuric acid	40.8	26.4	13.5	12.1	6.6

Natural expansive soil contains a certain amount of cementing materials, primarily free oxides, which mostly exist in amorphous forms and act as binding agents between clay particles. During water absorption, the interparticle distance remains stable, thereby limiting expansion. Thus, the presence of free oxides significantly influences the expansive properties of the soil. However, these oxides cannot be directly quantified from XRD images, and XRD-based mineral composition calculations do not account for their mass fraction. To address this, the $C_6H_5Na_3O_7$-$Na_2S_2O_4$ method was employed. The free oxide content measured 7.5 % in undisturbed soil, whereas values for expansive soil soaked in 1, 10, and 20 % sulfuric acid solutions decreased to 6.1, 4.5, and 3.8, respectively. These results demonstrate sulfuric acid's strong dissolving effect on free oxides. The reduced cementing content weakens interparticle bonding strength, allowing soil pores to respond more readily to moisture variations, which ultimately enhances the soil's expansion performance. Chemical reaction formula:

$$RO + H^+ = Fe^{3+} + AI^{3+} + Ca^{2+}. \quad (2)$$

3.3. Microstructure

The effect of cementing content changes on the expansion properties of expansive soil is further evidenced by SEM images. As shown in Fig. 4a, the original soil sample (soaked in distilled water) displays a dense, face-to-face stacked microstructure. Well-organized plate-like clay aggregates form larger clusters with limited, small-sized pores. This dense fabric is attributed to cementation by free oxides (e.g., Fe_2O_3, Al_2O_3, CaO), which suppresses soil expansion upon water uptake. In contrast, samples soaked in sulfuric acid solution (Figs. 4b–d) exhibit significant structural loosening and dispersion. With increasing acid concentration (from 1 to 20 %), the high H^+ concentration dissolves the natural oxide cements (e.g., $Fe_2O_3 + 6H^+ \rightarrow 2Fe^{3+} + 3H_2O$), severely weakening or even destroying interparticle bonds. This causes the aggregated structures to disintegrate. As cementation diminishes, the stability of the face-to-face stacking decreases, allowing plate-like particles to separate at the edges and reassemble into more unstable edge-edge and edge-face configurations. Consequently, the overall structure becomes disordered and open, accompanied by a notable increase in the volume and number of micropores. These newly formed micropores provide additional channels and space for water intrusion, directly accounting for the increased macroscopic expansion rate. In summary, the SEM results are consistent with the binder content tests and XRD analysis. The dissolution of key cementing agents in acidic environments compromises the microstructural integrity of the expansive soil, transforming it from a dense aggregated state to a loose dispersed one with developed pore networks, thereby enhancing its macroscopic expansion.

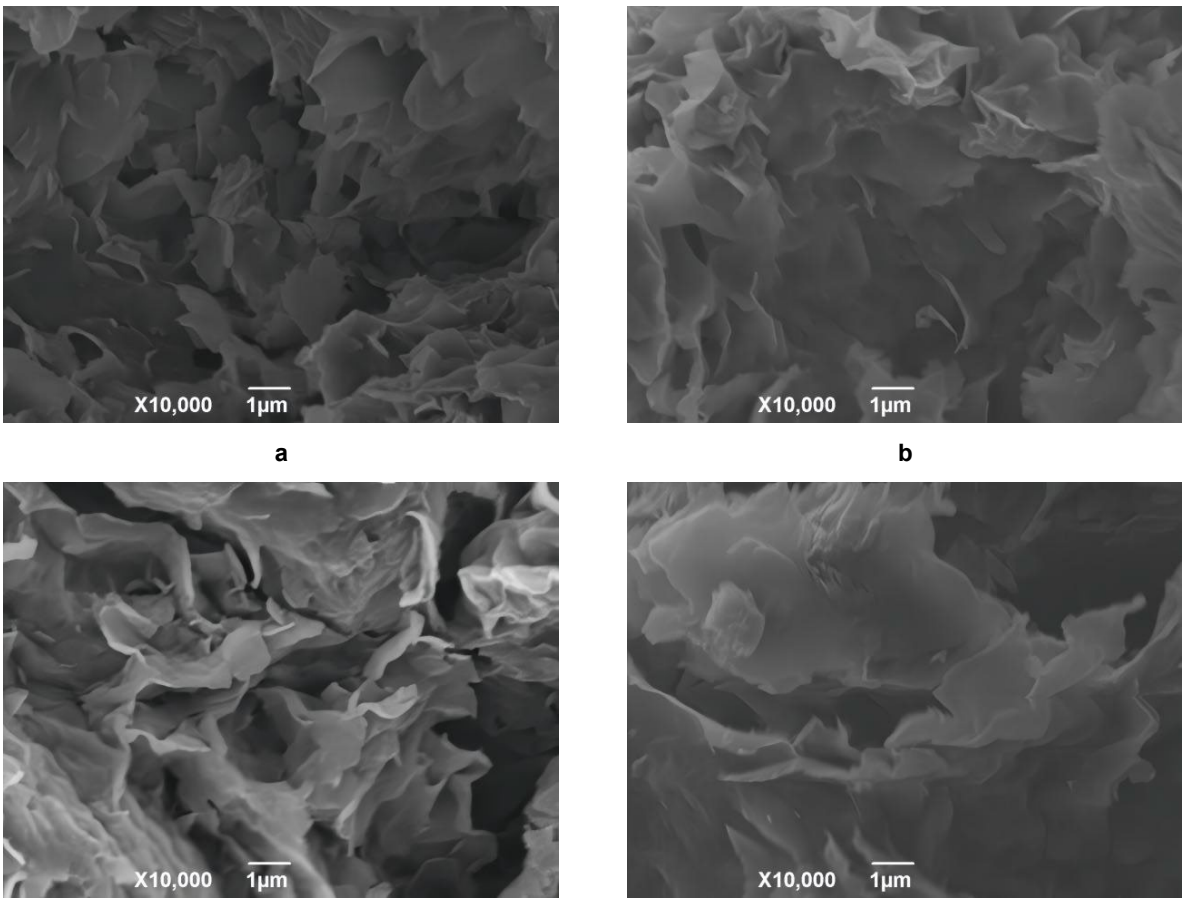

Figure 4. SEM images of expansive soil under each solution: a – water; b – 1 % H_2SO_4; c – 1 % H_2SO_4; d – 20 % H_2SO_4.

3.4. Measurement of Fractal Dimension by Nitrogen Adsorption Method

The surface dimension of expansive soil can be measured by the nitrogen adsorption test. Fig. 5 shows the N_2 adsorption-desorption isotherm of the expansive soil sample, presenting an upward convex curve in the low P/P_0 region; in the higher P/P_0 region, the adsorbate undergoes capillary coagulation, and the isotherms rise rapidly. Due to capillary coagulation, a hysteresis phenomenon can be observed in this region: that is, the isotherms obtained during desorption do not coincide with those obtained during adsorption, and the desorption isotherms are above the adsorption isotherms, forming a hysteresis loop. By using the FHH [35] equation, double logarithmic curves of adsorption capacity versus relative air pressure were plotted based on the N_2 isothermal adsorption lines of each powder sample in double logarithmic coordinates. And Fig. 6 shows the $\ln V_{ads}$–$\ln[\ln(p_0/p)]$ fitting curve. The surface fractal dimension results were calculated as shown in Table 3. It can be seen from the table that the surface dimension decreases with the increase in sulfuric acid concentration. The SEM image can fully explain this phenomenon. When the concentration of sulfuric acid solution is low, the hydration reaction of expansive soil is less intense and the surface is rougher (Fig. 4a), with the surface fractal dimension being larger. However, as the concentration of sulfuric acid solution increases, the hydration reaction becomes more intense and the surface of expansive soil tends to be smoother (Fig. 4d), resulting in a decrease in the surface fractal dimension.

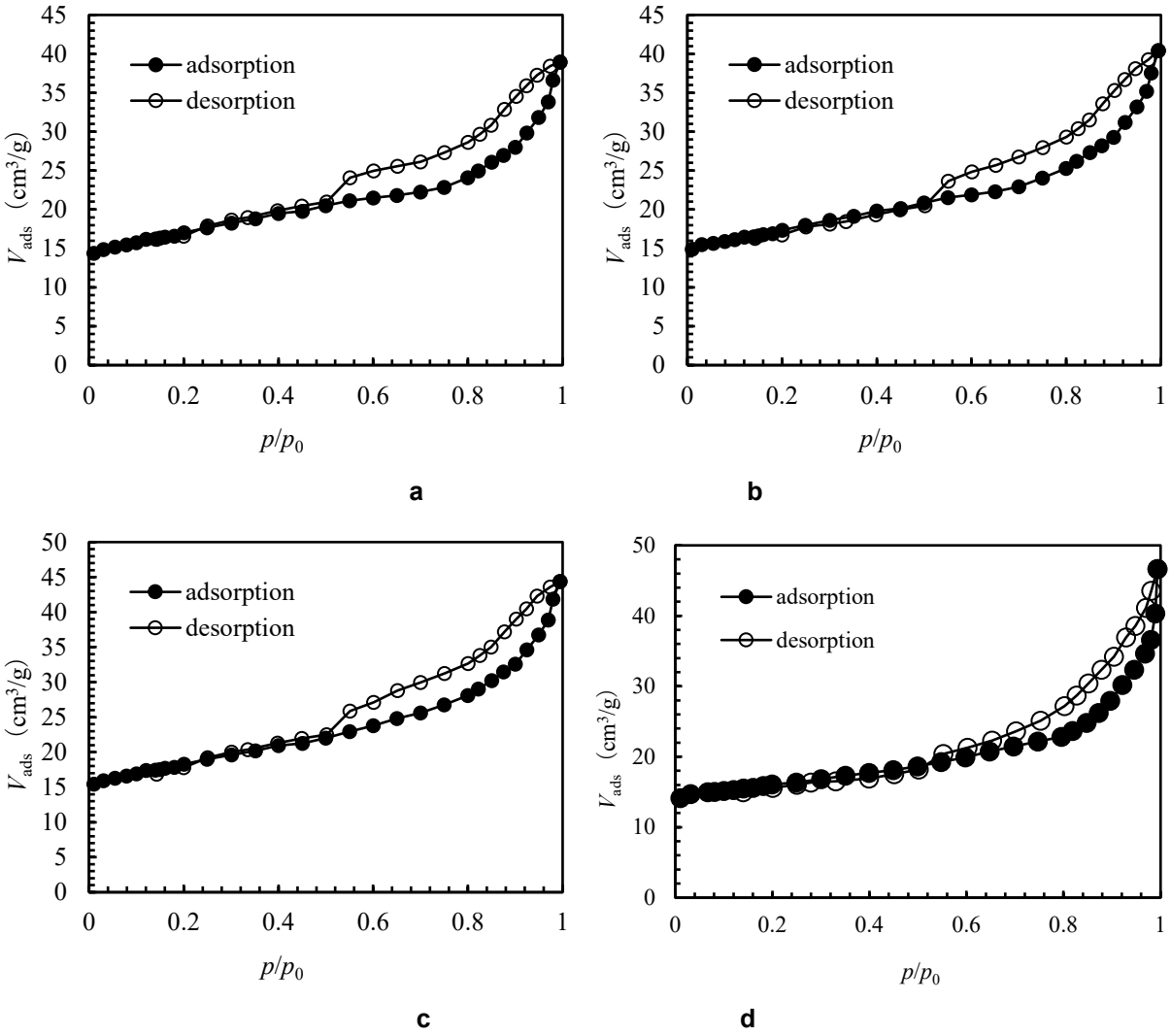

Figure 5. N_2 adsorption-desorption isotherms of the expansive soil samples: a – 0 %; b – 1 %; c – 10 %; d – 20 %.

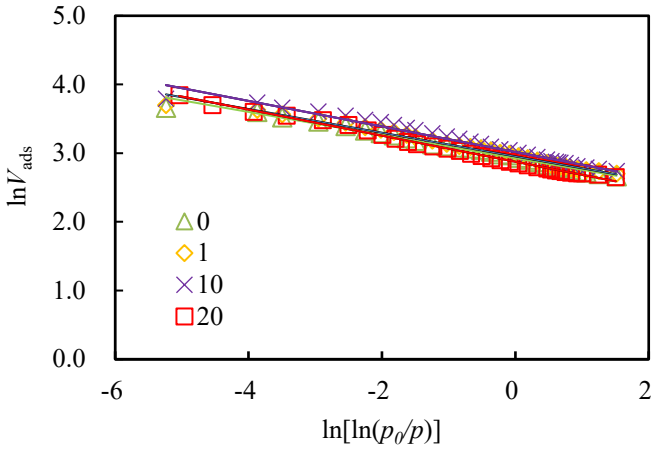

Figure 6. Equation curves of expansive soil samples after soaking in sulfuric acid solutions of different concentrations.

Table 3. Surface dimension division of expansive soil under nitrogen adsorption.

Sulfuric acid concentration	Fit the relationship	R^2	*D*
0	$\ln V_{ads}$ = 0.1684 ln [ln (p_0/p)] + 2.9265	0.9842	2.8316
1 %	$\ln V_{ads}$ = 0.1722 ln [ln (p_0/p)] + 2.9531	0.9831	2.8278
10 %	$\ln V_{ads}$ = 0.186 ln [ln (p_0/p)] + 3.0165	0.9767	2.814
20 %	$\ln V_{ads}$ = 0.1897 ln [ln (p_0/p)] + 2.8757	0.994	2.8103

3.5. Calculation Model

The swelling deformation of bentonite decreases as the effective stress p_e increases. Within the framework of fractal theory, the Debye–Hückel formula can be introduced to obtain the osmotic suction coefficient and calculate osmotic suction, thereby establishing a theoretical relationship between effective stress and swelling deformation. Analysis of the $e - p_e$ fitting curve was conducted to further explore the erosion mechanism of sulfuric acid solution on expansive soil.

Xu et al. [31] derived the relationship between the expansion deformation of bentonite and the corrected effective stress based on; the fractal theory:

$$e = \kappa p_e^{D_s - 3}, \tag{3}$$

where e is the pore ratio of the sample and D_s is the fractal dimension of the bentonite surface; p_e is the corrected effective stress; κ is the coefficient of expansion. According to the fractal theory, the modified effective stress can be derived from the overlying pressure and the infiltration stress, and the calculation formula is as follows [32–34]:

$$P_e = \sigma + \pi \left(\frac{\sigma}{\pi} \right)^{D_s - 2}, \tag{4}$$

where σ is the overlying pressure and π is the osmotic suction, $\pi = \varepsilon RTc\Phi$. ε is the number of ions decomposed by the solute (H_2SO_4: $\varepsilon = 3$); R is the generalized gas constant (8.314 J/mol/k); T is absolute temperature; c is the mass molar concentration of the solute; Φ is the osmotic suction coefficient. For solutions containing monovalent ionic electrolytes, the formula proposed by Li et al. [34] was used to calculate the osmotic suction coefficient Φ for 1, 10, and 20 % sulfuric acid, which were 0.791, 0.641, and 0.624, respectively, and the corresponding osmotic suction π was 599.69, 5178.87, and 10778.75, respectively.

The $e - p_e$ relationship of expansive soil in different sulfuric acid solutions can be obtained by fitting the test data using Equation (3) as shown in Fig. 7. It can be seen that the expansion deformation of expansive soil after soaking and erosion in the acid solution still conforms to the fractal relationship in Equation (3), and the corresponding $e - p_e$ relationship is listed in Table 4. It can be found that the fractal dimension after fitting the experimental data is basically consistent with the results of the nitrogen adsorption test.

As can be seen from Table 4, an increase in the concentration of sulfuric acid solution will, on the one hand, increase the effective stress of saturated expansive soil, which leads to a decrease in expansive deformation; on the other hand, the coefficient of expansion κ increases significantly with the increase in the degree of acid erosion. As can be seen from Fig. 7, the increase in sulfuric acid concentration leads to an increase in the effective stress p_e, but the porosity *e* also increases accordingly, thus increasing the expansion deformation. A good linear relationship between the expansion coefficient κ and the cementation was found in Fig. 8. As the expansion coefficient increases, the cementing content decreases. However, the decrease in cementing content weakens the bonding strength between the particles, making the soil pores more prone to change with moisture, thereby increasing the expansion deformation. To sum up, an increase in the concentration of sulfuric acid solution leads to an increase in the expansion performance of expansive soil.

By comparison, we found that the measured values obtained by previous researchers [36–38] were in excellent agreement with the theoretical values calculated by the $e-p_e$ fractal model in this paper. The results are shown in Fig. 9. This verifies the scientificity and accuracy of the model.

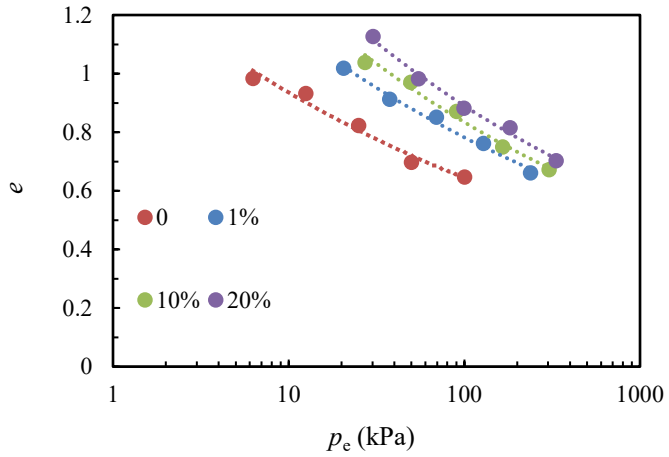

Figure 7. e–p_e relationship of expansive soil in different sulfuric acid solutions.

Table 4. e–p_e relationship under different concentrations of sulfuric acid solutions.

Sulfuric acid concentration	e–p_e relationship	κ	D
0	$e = 1.36p_e^{-0.162}$	1.36	2.838
1 %	$e = 1.72p_e^{-0.171}$	1.71	2.829
10 %	$e = 1.97p_e^{-0.187}$	1.97	2.813
20 %	$e = 2.12p_e^{-0.188}$	2.12	2.812

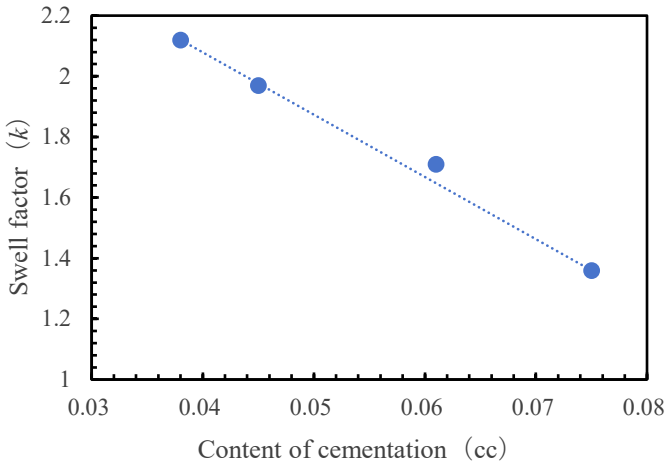

Figure 8. Relationship between expansion coefficient and cementing content.

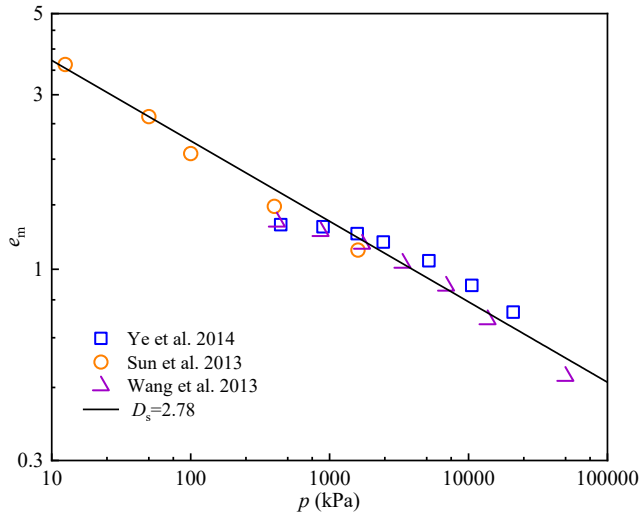

Figure 9. Model validation.

4. Conclusions

1. The initial expansion rate of expansive soil increases after being eroded by sulfuric acid and increases with the concentration. After being treated with 1, 10, and 20 % sulfuric acid, the expansion rate of expansive soil at 6.25 kPa increased from 20.32 % (distilled water) to 22.45, 23.63, and 29.02 %, respectively. When the load increased, the expansion rate decreased in all samples, especially in the samples treated with a high concentration of sulfuric acid.
2. By XRD and SEM analysis, it was found that the content of mineral components other than montmorillonite in the expansive soil after sulfuric acid treatment decreased. The montmorillonite content increased slightly, possibly due to the formation of montmorillonite resulting from the depletion of K^+ in illite. As the concentration of sulfuric acid increases, the free oxides in the expansive soil react with H^+, resulting in a decrease in the cementation content in the sample, weakening the bonding strength between the particles, increasing the porosity of the soil and the seepage channels available for the solution to penetrate the soil, thereby increasing the expansion deformation.
3. The expansion deformation of expansive soil treated with sulfuric acid can be calculated by the $e - p_e$ fractal model. The experimental data after erosion with the acid solution still conform to the $e - p_e$ fractal model. At the same time, with the increase in sulfuric acid concentration, on the one hand, the increase in effective stress p_e inhibits the expansion deformation of expansive soil, but on the other hand, the expansion coefficient κ shows a significant linear increase with the decrease in cementing content, further indicating that the mechanism by which sulfuric acid enhances the expansion performance of expansive soil is mainly due to the dissolution of free oxides and the decrease in cementing content.
4. While the developed $e - p_e$ fractal model effectively describes the swelling behavior of acid-etched expansive soils, some limitations exist. Firstly, its applicability to other soils, especially kaolinite-dominated expansive soils, remains unverified and may yield less accurate predictions. Secondly, the model cannot self-optimize with new data due to the absence of a feedback mechanism. Thirdly, the model has only been validated at the laboratory scale and requires field testing to identify potential deviations in practical applications.

Addressing the significant engineering risks posed by widely distributed acidic contaminated soils, this paper has focused on the fundamental theory for predicting swelling deformation. Future efforts should aim at developing sustainable remediation strategies and enhancing model robustness. Key directions include: leveraging industrial wastes (e.g., calcined lime slag, steel slag) for chemical stabilization; implementing a data-driven feedback mechanism, where long-term field data are used to dynamically calibrate the model parameters to maintain accuracy; and conducting multi-factor coupling studies (e.g., acid-heat-stress interactions) to decipher complex soil behavior and improve the model's performance in intricate field conditions.

References

1. Hassanlourad, M., Khatami, M.H., Ahmadi, M.M. Effects of sulphuric acid pollutant on the shear behaviour and strength of sandy soil and sand mixed with bentonite clay. International Journal of Geotechnical Engineering. 2017. 11(2). Pp. 114–119. DOI: 10.1080/19386362.2016.1193662
2. Tang, H. Liu, Ch., Wang, N., Li, H., Wu, G., Luo, J., Zeng, M. Influence of Acidic Substances on Compression Deformation Characteristics of Loess. Advances in Civil Engineering. 2021. 2021. Article no 6614391. DOI: 10.1155/2021/6614391
3. Sun, S. et al., The physical-mechanical properties degradation mechanism and microstructure response of acid–alkali-contaminated Xiashu loess. Natural Hazards. 2021. 106(3). Pp. 2845–2861. DOI: 10.1007/s11069-021-04570-7
4. Lei, H., Bo, Y., Zhang, W., Wang, L., Toma, A. Effects of acidity and magnesium ions on the self-weight consolidation settlement of Tianjin dredged fill. Bulletin of Engineering Geology and the Environment. 2021. 80(5). Pp. 4035–4047. DOI: 10.1007/s10064-021-02177-7
5. Li, K., Zhao, X., Xiao, D. Acid rain: an unsuspected factor predisposing Panzhihua airport landslide, China. Environmental Science and Pollution Research. 2021. 28(27). Pp. 36753–36764. DOI: 10.1007/s11356-021-13308-8
6. Xiao, D. et al., Influence of acid rain on slope instability mechanism – a case study in Sichuan provincial highway, China. Bulletin of Engineering Geology and the Environment. 2021. 80(5). Pp. 3659–3673. DOI: 10.1007/s10064-021-02170-0
7. Chang, J., Yang, H.P., Xiao, J., Liu, X., Chen, G.Y., Mao, R. Effect of acid environment on swelling-shrinkage properties of Baise expansive soil and its microscopic interpretation. Journal of Traffic and Transportation Engineering. 2019. 19(1). Pp. 24–32. DOI: 10.19818/j.cnki.1671-1637.2019.01.004
8. Li, Z., Tang, C., Hu, R., Zhou, Y. Experimental research on expansion characteristics of Mengzi expansive soil with water, salt and acid immersion. Environmental Earth Sciences. 2014. 72(2). Pp. 363–371. DOI: 10.1007/s12665-013-2957-z
9. Sivapullaiah, P.V., Prasad, B.G., Allam, M.M. Effect of Sulfuric Acid on Swelling Behavior of an Expansive Soil. Soil and Sediment Contamination. 2009. 18(2). DOI: 10.1080/15320380802660289
10. Zhou, B.C., Kong, L.W., Liang, W.Y., Ma, Q.G., Zhang, B. Hydro-mechanical coupling effects on volume change and water retention behaviour of unsaturated expansive soils during compression. Chinese Journal of Geotechnical Engineering. 2015. 37(4). Pp. 629–640. DOI: 10.11779/CJGE201504008
11. Gratchev, I., Towhata, I. Stress-strain characteristics of two natural soils subjected to long-term acidic contamination. Soils and Foundations. 2013. 53(3). Pp. 469–476. DOI: 10.1016/j.sandf.2013.04.008
12. Li, K.P., Zhao, X.Y., Xiao, D., Li, J. Mechanism of silty mudstone slaking aggravated by acid rain-induced chemical damage. Rock and Soil Mechanics. 2020. 41(8). Pp. 2693–2702. DOI: 10.16285/j.rsm.2019.1590
13. Wheeler, S.J., Sharma, R.S., Buisson, M.S.R. Coupling of hydraulic hysteresis and stress-strain behaviour in unsaturated soils. Geotechnique. 2003. 53(1). Pp. 41–54. DOI: 10.1680/geot.2003.53.1.41
14. Gowthaman, S., Nakashima, K., Kawasaki, S. Durability analysis of bio-cemented slope soil under the exposure of acid rain. J Soils Sediments. 2021. 21(8). Pp. 2831–2844. DOI: 10.1007/s11368-021-02997-w
15. Rama Vara Prasad, C., Hari Prasad Reddy, P., Ramana Murthy, V., Sivapullaiah, P.V. Swelling characteristics of soils subjected to acid contamination. Soils and Foundations. 2018. 58(1). Pp. 110–121. DOI: 10.1016/j.sandf.2017.11.005
16. Reddy, P.H.P., Prasad, C.R.V., Pillai, R.J. Swelling of Natural Soil Subjected to Acidic and Alkaline Contamination. Periodica Polytechnica Civil Engineering. 2017. 61(3). Pp. 611–620. DOI: 10.3311/PPci.8185
17. Sun, D.A., Sun, W.J., Li, J. Elastoplastic modelling of hydraulic and mechanical behaviour of unsaturated expansive soils. Proceedings of sessions of Geoshanghai. American Society of Civil Engineers (ASCE). Reston, VA, 2010. Pp. 119–127. Ref. 5. DOI: 10.1061/41103(376)15
18. Gratchev, I., Towhata, I. Compressibility of soils containing kaolinite in acidic environments. KSCE Journal of Civil Engineering. 2016. 20(2). Pp. 623–630. DOI: 10.1007/s12205-015-0141-6
19. Liu, J., Cui, P. Influence of water-soil chemical interaction on cohesive force: A case study of montmorillonite-quartz remolded soil. Rock and Soil Mechanics. 2017. 38(2). Pp. 419–427 and 434. DOI: 10.16285/j.rsm.2017.02.015
20. Zhao, Y., Cui, P., Hu, L. Relation between evolution of clay shear strength and landslide induced by acid rain: Taking landslides in Three Gorges reservoir area for example. Chinese Journal of Rock Mechanics and Engineering. 2009. 28(3). Pp. 576–582. DOI: 10.3321/j.issn:1000-6915.2009.03.017
21. Chang, J., Yang, H.P., Xiao, J., Xu, Y.F. Soil-water chemical tests and action mechanism of acid rain infiltration into expansive soil. Chinese Journal of Geotechnical Engineering. 2022. 44(8). Pp. 1483–1492. DOI: 10.11779/CJGE202208013
22. Chavali, R.V.P., Ponnapureddy, H.P.R. Swelling and compressibility characteristics of bentonite and kaolin clay subjected to inorganic acid contamination. International Journal of Geotechnical Engineering. 2018. 12(5). Pp. 500–506. DOI: 10.1080/19386362.2017.1299418
23. Randhawa, K.S., Kumar, R., Alkaabi, H., Alkahtani, M.Q., Islam, S., Prakash, Ch., Kumar, R., Ammarullah, M.I. Bioengineering solutions for expansive soil stabilization using waste materials: An experimental evaluation. AIP Advances. 2025. 14(5). Article no. 055308. DOI: 10.1063/5.0210939
24. Shen, N.J., Hasan, M., Yee, T.K. Stabilization of Soft Clay Soil by the Reinforcement of Single Bottom Ash Silica Fume (BASF) Column. Rehabilitation in Civil Engineering. 2024. 12(3). Pp. 117–131. DOI: 10.22075/jrce.2024.32181.1925
25. Shen, N.J., Hasan, M., Fakeh, N.M.M. Effect of the waste bottom ash strengthened the problematic clay soil: The use of by-product material. Engineering and Applied Science Research. 2025. 52(2). Pp. 229–239. DOI: 10.14456/easr.2025.20
26. Ghalandarzadeh, S., Maghoul, P., Ghalandarzadeh, A., Courcelles, B. Effect of nanoparticle-enhanced biocementation in kaolinite clay by microbially induced calcium carbonate precipitation. Construction and Building Materials. 2024. 414. Article no. 134939. DOI: 10.1016/j.conbuildmat.2024.134939
27. Shen, N.J., Hasan, M. Installation of polyethylene terephthalate (PET) columns to promote the soil-bearing capacity of soft kaolin clay. Journal of King Saud University – Engineering Sciences. 2025. 37(14). Article no. 14. DOI: 10.1007/s44444-025-00011-z
28. Britto, T.S.S., Silva Costa, W.G., Muñoz, Y.O., Patzsch, J.C., da Silva, C.S., dos Santos Izzom, R.L. Influence of Suction on Mass Loss of Compacted Clayey Soil from the Guabirotuba Formation in Southern Brazil. Geotechnical and Geological Engineering. 2024. 42. Pp. 6339–6361. DOI: 10.1007/s10706-024-02894-2
29. Chen, Y.G., Zhu, C.M., Ye, W.M., Cui, Yu-J., Chen, B. Effects of solution concentration and vertical stress on the swelling behavior of compacted GMZ01 bentonite. Applied Clay Science. 2016. 124–125. Pp. 11–20. DOI: 10.1016/j.clay.2016.01.050

30. Rao, S.M., Thyagaraj, T. Role of direction of salt migration on the swelling behaviour of compated clays. Applied Clay Science. 2007. 38(1–2). Pp. 113–129. DOI: 10.1016/j.clay.2007.02.005
31. Xu, Y.F., Matsuoka, H., Sun, D.A. Swelling Characteristics of Fractal-Textured Bentonite and Its Mixtures. Applied Clay Science. 2003. 22(4). Pp. 197–209. DOI: 10.1016/S0169-1317(02)00159-X
32. Xiang, G., Ye, W., Hu, Z., Fu, W. Effects of alkaline solution on shear strength of GMZ bentonite as a buffer/backfill material in China. Acta Geotechnica. 2024. 19. Pp. 2013–2021. DOI: 10.1007/s11440-023-01990-6
33. Xiang, G., Ye, W., Hu, Z., Ge, L., Zhou, Y. Swelling Characteristics of Fractal-Textured Bentonite Eroded by Alkaline Solution. Advances in Civil Engineering. 2022. 2022. Article no. 9100822. DOI: 10.1155/2022/9100822
34. Li, X., Li, C., Xu, Y. Representation of Volume Change for Bentonite in Saline Solution based on Modified Effective Stress. KSCE Journal of Civil Engineering. 2019. 23(5). Pp. 2065–2073. DOI: 10.1007/s12205-019-0789-4
35. Pfeifer, P., Obert, M., Cole, M.W. Fractal BET and FHH theories of adsorption: A comparative study. Proceeding of the Royal Society of London. Series A: Mathematical and Physical Science. 1989. 423(1864). Pp. 169–188. DOI: 10.1098/rspa.1989.0049
36. Ye, W.M., Zhang, F., Chen, B., Chen, Y.G., Wang, Q., Cui, Y.J. Effects of salt solutions on the hydro-mechanical behavior of compacted GMZ01 Bentonite. Environmental Earth Sciences. 2014. 72(7). Pp. 2621–2630. DOI: 10.1007/s12665-014-3169-x
37. Sun, D., Zhang, J., Zhang, J., Zhang, L. Swelling characteristics of GMZ bentonite and its mixtures with sand. Applied Clay Science. 2013. 83–84. Pp. 224–230. DOI: 10.1016/j.clay.2013.08.042
38. Wang, Q., Tang, A.M., Cui, Y.J., Barnichon, J.D., Ye, W.M. Investigation of the hydro-mechanical behaviour of compacted bentonite/sand mixture based on the BExM model. Computers and Geotechnics. 2013. 54. Pp. 46–52. DOI: 10.1016/j.compgeo.2013.05.011

Information of the authors:

Hongbin Lu,
ORCID: https://orcid.org/0009-0002-4300-5277
E-mail: 176855347@qq.com

Shaohui Song,
ORCID: https://orcid.org/0009-0007-7030-7269
E-mail: Songsh1999@163.com

Guosheng Xiang,
ORCID: https://orcid.org/0000-0002-3522-3074
E-mail: xianggsh2011@163.com

Xinxin Wang,
ORCID: https://orcid.org/0009-0005-2597-2214
E-mail: x15686201208@163.com

Mengyuan Luan,
ORCID: https://orcid.org/0009-0004-0690-7313
E-mail: 2647426899@qq.com

Received 04.06.2025. Approved after reviewing 17.091.2025. Accepted 19.09.2025.

Magazine of Civil Engineering

ISSN 2712-8172

journal homepage: http://engstroy.spbstu.ru/

Research article

UDC 691.3

DOI: 10.34910/MCE.138.10

Ternary blended concrete synergy of mineral admixtures

A. Kumar[1]***, V. Kumar***[1]***, S. Kumar***[1]***, A.K. Orlov***[2]***, S. Dixit***[3] ✉

[1] *National Institute of Technology, Jamshedpur, India*

[2] *National Research University "Moscow State University of Civil Engineering", Moscow, Russian Federation*

[3] *Centre of Research Impact and Outcome, Chitkara University, Rajpura, Punjab, India*

✉ *sauravarambol@gmail.com*

Keywords: ternary blended concrete, workability, compressive strength, synergy, efficiency factor

Abstract. Concrete that uses supplementary mineral admixtures offers a route to reduce clinker use while maintaining performance, yet the combined action of multiple admixtures in one binder remains uncertain. The potential for synergy among metakaolin (MK), fly ash (FA), and rice husk ash (RHA) has been emphasized in prior work as a means to enhance packing and pozzolanic reaction. The gap addressed here is the absence of a practical way to quantify the combined efficiency of MK–FA–RHA and to predict strength across a broad range of ternary blends. The objective is to evaluate ternary MK–FA–RHA concretes and to derive synergy/efficiency-based equations to predict compressive strength and to correlate it with split tensile and flexural strength. An M25 mixture with water/binder 0.45 and 39 combinations (MK 6–8 %, FA 5–15 %, RHA 5–20 %) was produced; slump, compressive strength (7, 28, 56 days), split tensile and flexural strength were measured using IS:516 specimens (150 mm cubes, 75×150 mm cylinders, 100×100×500 mm beams). Workability decreased with increasing fines: at MK 7 %, the slump fell from 188 mm to ≤100 mm as FA and RHA rose, and reached 35 mm at MK 8 %, FA 10 %, and RHA 20 %. Strength responses showed that 8 % MK alone raised 28- and 56-day compressive strength to 37.24 and 41.76 MPa (vs 34.87 and 38.87 MPa for the control), while RHA ≥15 % produced 15–30 % lower 28-day strength; the best ternary blend across all mixes was 8 % MK + 10 % FA + 10 % RHA. Regression-based equations that incorporated a synergy factor accurately reproduced compressive strength, with most errors within 0–10 %, and yielded R^2 values of 0.73–0.82. Companion correlations predicted split tensile and flexural strengths from compressive strength. These findings suggest that MK 8 % with FA and RHA at 10 % each balances clinker reduction and strength, although high RHA contents require rheology control to avoid consolidation-limited results. Future work is recommended on durability mechanisms and admixture optimization to extend the predictive framework.

Citation: Kumar, A., Kumar, V., Kumar, S., Orlov, A.K., Dixit, S. Ternary blended concrete synergy of mineral admixtures. Magazine of Civil Engineering. 2025. 18(6). Article no. 13810. DOI: 10.34910/MCE.138.10

1. Introduction

Concrete production had relied heavily on ordinary Portland cement (OPC), which carried both environmental and performance costs when mixtures were pushed to meet durability targets in aggressive exposures. Supplementary mineral admixtures had offered a practical path to reduce clinker content while sustaining mechanical and transport properties, and construction practice had increasingly combined more than one admixture in the same binder. The combined use of metakaolin (MK), fly ash (FA), and rice husk ash (RHA) was expected to densify the paste through particle packing and extend hydration through pozzolanic reactions that continued beyond the early ages [1]. The concept of synergy among mineral

admixtures had been central to this promise, because the interaction of several fine powders had produced effects greater than the arithmetic sum of their individual actions. The literature had captured this idea and had described how very fine MK particles and even finer FA and RHA particles had filled voids and refined the matrix, thereby enhancing strength and durability metrics when the mixture had been proportioned appropriately. The efficiency factor framework for pozzolans had also been advanced, with prior work defining k-values to express the cement-equivalent contribution of a single additive, and several authors adopting or extending Bolomey's strength relation to estimate the binder response as replacement levels changed [2]. Despite this foundation, applied mixture design still lacked a clear way to express the combined efficiency of several admixtures acting simultaneously in concrete, and designers often treated the separate k-values independently, even when the paste contained more than one additive.

The gap that motivated the present work lay in the absence of a practical, data-supported framework that quantified the joint efficiency of MK, FA, and RHA and predicted compressive strength for a wide range of ternary blends using a single set of equations. Prior research had typically addressed one admixture at a time or reported ternary results without developing those observations into a predictive tool that mixture designers could use directly [3]. The literature had indicated the importance of this step because efficiency-based accounting had allowed for cement reductions by crediting the equivalent cement content of each additive; yet, a ternary binder had demanded a means to capture the synergy that arose from concurrent physical filling and pozzolanic reactions. The novelty of this work lay in the explicit derivation of strength equations for MK–FA–RHA concrete using Bolomey's relation as the backbone, augmented with an efficiency construct that had represented the combined action of the three powders rather than treating them as isolated substitutions. It also lay in the development of companion correlations that linked compressive strength to split tensile and flexural strength, so that the dataset supported multiple performance predictions from a single measured variable [4].

This work was executed on a broad experimental matrix that covered realistic dosing ranges for practical concretes. The mixture set had included concretes, in which MK had been held at 6, 7, or 8 %, and where FA and RHA had been varied from low to relatively high contents, producing a family of mixes that spanned 39 combinations. Evidence within the dataset showed MK at 6 % with FA and RHA stepped at 5, 10, 15, and 20 %, as well as MK at 8 % paired with the same FA and RHA increments. The ranges captured both moderate and fine-rich pastes [5]. Fresh properties had been recorded through slump, and mechanical properties had been measured at 7, 28, and 56 days so that early and later age behavior had been represented. This design allowed for a direct examination of how additional fines and pozzolanic silica influenced workability, consolidation tendencies, and strength development. Slump observations had shown that the fines content had mattered greatly: mixtures with high RHA and elevated FA at constant MK had exhibited steep reductions in slump, with severe combinations yielding very low values indicative of high yield stress, admixture adsorption, and limited free water for lubrication. Guidance on keeping RHA at or below 10 % when FA had been 5 % or higher had emerged from the data to avoid consolidation defects during strength testing [6].

Responses within this matrix highlighted two patterns essential to the motivation for a predictive framework. First, MK, by itself, had elevated 28- and 56-day strength when dosed at 8 %, confirming the beneficial filler-pozzolanic role of this highly reactive aluminosilicate. Second, the ternary combinations exhibited a clear optimum in the vicinity of 10 % FA and 10 % RHA when MK was 8 %, with that mixture delivering the strongest performance among all 39 combinations. Where RHA exceeded 10 %, the dataset showed persistent reductions in strength that aligned with the mechanistic expectation of increased specific surface, dilution of clinker and greater admixture demand [7]. Yet at about 10 % RHA, gains between 28 and 56 days had been marked, consistent with sustained pozzolanic consumption of portlandite and secondary C–S–H formation that had densified the matrix as curing had progressed. These observations had reinforced the need for a model that had combined physical packing and chemical reaction effects into a single efficiency term applicable to ternary systems [8].

The research gap therefore lay not just in missing data but in the lack of a design-level tool that had transformed such data into equations ready for proportioning work. While single-admixture k-values had existed, they had not accounted for the mutual influence that three powders had exerted on water demand, dispersion, and reaction kinetics when they had been blended in one binder [9]. The novelty statement for the present work captured two contributions. First, the work proposed an efficiency representation that was calibrated directly from the ternary dataset, allowing designers to estimate compressive strength from a chosen set of replacement levels using Bolomey's equation, augmented to include the combined effect of MK, FA, and RHA. Second, the work had produced empirical links between tensile and flexural strength, allowing one model to serve multiple mechanical performance needs without requiring additional calibration data. This pairing of a ternary efficiency construct with cross-property correlations had not been presented for MK–FA–RHA concretes in prior works. The scope of the 39-mix matrix allowed the model to be grounded in a wide range of replacement combinations [10].

The purpose of the investigation was stated accordingly. The work had aimed to evaluate the performance of ternary concretes made with MK, FA, and RHA across practical replacement levels, to document the fresh and hardened responses at relevant curing ages, and to derive a synergy-aware efficiency formulation integrated with Bolomey's strength relation that had predicted compressive strength across the matrix [11]. A second aim was to establish regression-based correlations that connected compressive strength to split tensile and flexural strength, thereby supporting their use in practice when only one property had been readily measured. The introduction had grounded the research questions in the need for clinker reduction through intelligent use of waste-derived mineral admixtures while preserving structural performance, had framed the missing predictive capability for ternary systems as a barrier to adoption and had justified the program design by showing how the experimental matrix had captured both the beneficial and the adverse regimes identified by slump and strength outcomes in the research. The objective of the work was therefore to generate and calibrate an efficiency-based predictive framework for MK–FA–RHA ternary concrete, using a comprehensive set of mixtures and tests to quantify workability and strength at three ages, and to provide correlations to additional strength measures so that the resulting equations had served as practical design aids grounded in the data presented in the research [12].

2. Materials and Methods

2.1. Materials Used

Cement as a binding material

The cement employed was OPC 43 grade, conforming to the Indian standard IS 8112 (1989). The binder material's physical properties are as follows:

- the fineness modulus is 2.74;
- the normal consistency is 29 %;
- the specific gravity is 3.15;
- the initial setting time is 90 minutes;
- the ultimate setting time is 220 minutes.

The strength measurements at 3, 28, and 56 days were recorded as 32.5, 42.5, and 56.5 MPa, respectively.

The chemical parameters of OPC are as follows:

- lime saturation factor: 0.85;
- alumina to iron oxide ratio: 1.13 %;
- insoluble residue: 1.69 %;
- magnesium oxide: 3.02 %;
- loss on ignition: 2.43 %;
- total chloride: 0.018 %.

2.2. Aggregate

The fine aggregate utilized in this study was sourced locally and conformed to the IS 383 (1970) Zone II grading specifications. A sieve analysis was conducted to assess the fineness modulus, specific gravity and water absorption of the fine aggregate. The results were as follows:

- the fineness modulus was 2.75;
- the specific gravity was 2.62;
- the water absorption was 1.3 %.

Alternatively, crushed stone measuring 20 and 12.5 mm was utilized. The fineness modulus, specific gravity and water absorption of 20 mm coarse aggregate was 8.22, 2.63, and 0.42 %, respectively. Identical values to 12.5 mm coarse aggregate: 7.7, 2.73, and 0.54 %.

Water reducing agent

The experiment utilized Auramix 400, a high-range water-reducing admixture produced by the FOSROC brand. This product adheres to the requirements stated in IS 9103 (1999) (2007). To improve the workability of the concrete, a consistent addition of 0.8% (by weight of cement) was incorporated as an enhancement. Nonetheless, potable water was employed for the casting and curing of all concrete specimens. A water-to-binder (w/b) ratio of 0.45 has been used for the concrete mixture design.

Supplementary cementitious materials

This experimental study employed three distinct supplementary cementitious materials: MK, FA, and RHA. This article presents a summary of the physical and chemical characteristics of various admixtures, as detailed in Tables 1 and 2.

Table 1. Physical property of mineral admixtures.

Physical Properties	Metakaolin	Fly Ash	Rice Husk Ash
Physical State	Micronized Powder	Powder Form	Powder
Odor	Odorless	Odorless	Odorless
Appearance	White Color Powder	Grey White Powder	Grey/off White Powder
Color	White	Grey	Off White
Pack Density	0.5 gm/cc	0.9 gm/cc	9.94 gm/cc
Bulk Density (Loose)	–	–	0.37 gm/cc
PH of 5 % Solution	–	–	7.3
Specific Gravity	2.64	2.10	2.26
Water Absorption	66.80 ml/100 gm	58.60 ml/100 gm	0.12 %
Oil Absorption	64 ml/100 gm	–	97.70 %

Table 2. Chemical properties of mineral admixtures.

Chemical Properties	Metakaolin	Fly Ash	Rice Husk Ash
Silica (SiO_2)	52.86 %	58.72 %	88.90 %
Alumina (Al_2O_3)	44.10 %	42.25 %	2.60 %
Ferric Oxide (Fe_2O_3)	0.45 %	4.6 %	2.23 %
Titanium Oxide (TiO_2)	0.36 %	0.56 %	–
Calcium Oxide (CaO)	0.28 %	0.38 %	0.21 %
Magnesium Oxide (MgO)	0.21 %	0.20 %	–
Pottasium Oxide (K_2O)	0.20 %	0.45 %	0.33
Sodium Oxide (Na_2O)	0.25 %	0.35 %	0.36
Loss on Ignition	0.85 %	3.2 %	4.03 %

2.3. Methods Adopted

In compliance with IS 10262 (2009), the concrete mixtures were combined using the absolute volume method for the M25 grade of concrete. The components were proportioned according to their relative weights. Each concrete mixture was formulated using cementitious materials with a density of 350 kg/m^3, a water-to-cementitious materials ratio of 0.45 and a coarse aggregate-to-total aggregate ratio of 0.60 during manufacture. The application of a specific quantity of superplasticizer aimed to achieve the desired workability by facilitating a slump value adjustment within the range of 100±25 mm. M0 refers to the control mix composed solely of OPC. The classification system categorizes the total combinations of ternary blended concrete mixtures into three distinct categories:

1. Group I: The specimens in this category were formulated by substituting 6–41 % of the cement with 6 % MK, 5–15 % FA, and 5–20 % RHA. The specimens are designated as M1 through M13.
2. Group II: The specimens in this category were formulated by substituting 7–42 % of the cement with 7 % MK, 5–15 % FA, and 5–20 % RHA. The specimens are designated as M14 through M26.
3. Group III: The specimens in this category were formulated by substituting 8–43 % of the cement with 8 % MK, 5–15 % FA, and 5–20 % RHA. The specimens are designated as M27 through M39.

The volume of one batch was determined to be 0.045 m^3, factoring in a 20 % wastage. Table 3 presents the substitution thresholds for various waste products, while Table 4 outlines the quantities of distinct components used in different mixes. Fig. 1 illustrates a series of concrete examples submerged in a water tank for curing purposes [13].

Table 3. Details of replacement levels for ternary cement concrete.

Mix [M]	Materials			
	OPC (%)	MK (%)	FA (%)	RHA (%)
M0	100	0	0	0
M1	94	6	0	0
M2	84	6	5	5
M3	79	6	5	10
M4	74	6	5	15
M5	69	6	5	20
M6	79	6	10	5
M7	74	6	10	10
M8	69	6	10	15
M9	64	6	10	20
M10	74	6	15	5
M11	69	6	15	10
M12	64	6	15	15
M13	59	6	15	20
M14	93	7	0	0
M15	83	7	5	5
M16	78	7	5	10
M17	73	7	5	15
M18	68	7	5	20
M19	78	7	10	5
M20	73	7	10	10
M21	68	7	10	15
M22	63	7	10	20
M23	73	7	15	5
M24	68	7	15	10
M25	63	7	15	15
M26	58	7	15	20
M27	92	8	0	0
M28	82	8	5	5
M29	77	8	5	10
M30	72	8	5	15
M31	67	8	5	20
M32	77	8	10	5
M33	72	8	10	10
M34	67	8	10	15
M35	62	8	10	20
M36	72	8	15	5
M37	67	8	15	10
M38	62	8	15	15
M39	57	8	15	20

Table 4. Quantities of several ingredients for different mixes per unit volume (kg/m³).

Mix [M]	Materials (kg)				FA (kg)	CA (kg)	
	OPC	MK	FA	RHA		12.5 mm	20 mm
M0	350	0	0	0	771.31	481.81	687.33
M1	329	21	0	0	769.94	480.95	686.11
M2	294	21	17.5	17.5	764.68	477.67	681.43
M3	276.5	21	17.5	35	762.35	476.21	679.35
M4	259	21	17.5	52.5	760.02	474.76	677.27
M5	241.5	21	17.5	70	757.68	473.30	675.19
M6	276.5	21	35	17.5	761.76	475.85	678.82
M7	259	21	35	35	759.43	474.39	676.74
M8	241.5	21	35	52.5	757.09	472.93	674.66
M9	224	21	35	70	754.76	471.47	672.59
M10	259	21	52.5	17.5	758.84	474.02	676.22
M11	241.5	21	52.5	35	756.51	472.56	674.14
M12	224	21	52.5	52.5	754.17	471.11	672.06
M13	206.5	21	52.5	70	751.84	469.65	669.98
M14	325.5	24.5	0	0	769.71	480.81	685.91
M15	290.5	24.5	17.5	17.5	764.46	477.53	681.22
M16	273	24.5	17.5	35	762.12	476.07	679.14
M17	255.5	24.5	17.5	52.5	759.79	474.61	677.06
M18	238	24.5	17.5	70	757.45	473.15	674.99
M19	273	24.5	35	17.5	761.53	475.70	678.62
M20	255.5	24.5	35	35	759.20	474.25	676.54
M21	238	24.5	35	52.5	756.87	472.79	674.46
M22	220.5	24.5	35	70	754.53	471.33	672.38
M23	255.5	24.5	52.5	17.5	758.61	473.88	676.02
M24	238	24.5	52.5	35	756.28	472.42	673.94
M25	220.5	24.5	52.5	52.5	753.94	470.96	671.86
M26	203	24.5	52.5	70	751.61	469.50	669.78
M27	322	28	0	0	769.48	480.67	685.70
M28	287	28	17.5	17.5	764.23	477.39	681.02
M29	269.5	28	17.5	35	761.89	475.93	678.94
M30	252	28	17.5	52.5	759.56	474.47	676.86
M31	234.5	28	17.5	70	757.23	473.01	674.78
M32	269.5	28	35	17.5	761.30	475.56	678.42
M33	252	28	35	35	758.97	474.10	676.34
M34	234.5	28	35	52.5	756.64	472.64	674.26
M35	217	28	35	70	754.30	471.19	672.18
M36	252	28	52.5	17.5	758.38	437.37	675.81
M37	234.5	28	52.5	35	756.05	472.28	673.73
M38	217	28	52.5	52.5	753.72	470.82	671.65
M39	199.5	28	52.5	70	751.38	469.36	669.57

Note: Quantity of super plasticizer was calculated as 2.8 kg/m^3 for all mixes.

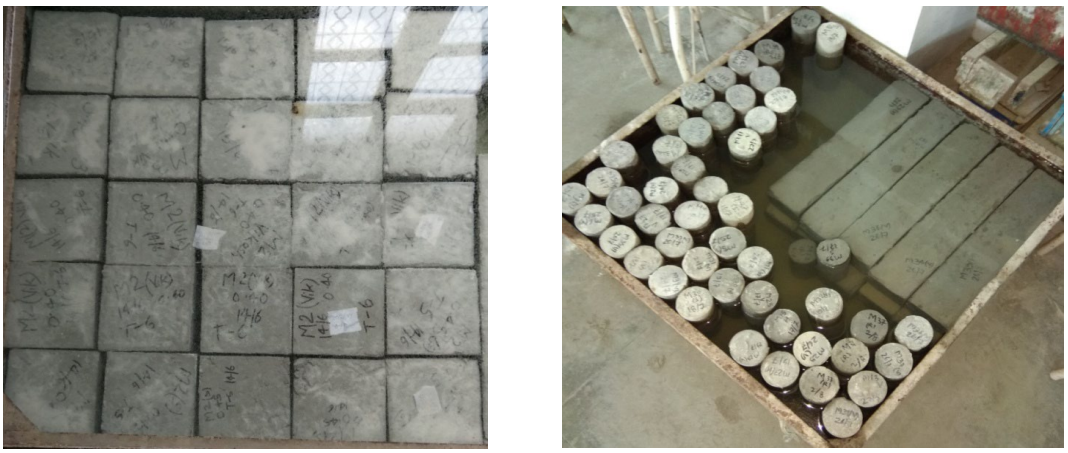

Figure 1. A set of concrete specimens prepared for each mix.

2.4. Testing of Concrete Specimens

The workability of concrete refers to its ability to undergo efficient mixing, placement, consolidation, and finishing. The quality of freshly mixed concrete significantly influences its ease and homogeneity during these operations. The workability of concrete was evaluated utilizing a slump cone measuring 100×200×300 mm, in compliance with the IS 1199 (1959) standard. The slump test is performed between batches to evaluate the uniform quality of concrete throughout the construction process.

The compressive strength of a material denotes the greatest force it can endure prior to complete failure. The compressive strength was calculated by dividing the failure force by the cross-sectional area that bore the load. The compressive strength of 150 mm cube specimens was assessed in accordance with IS 516 (1959) using a digital compression testing machine after 7, 28, and 56 days of curing.

The split tensile strength of 75×150 mm cylinder specimens was measured in accordance with IS 516 (1959). The split tensile strength was determined by applying the formula $T = 2 \times P \big/ \left(\text{ПП} \times D \times L \right)$. However, the flexural strength was assessed using beam specimens of 100×100×500 mm, in accordance with IS 516 (1959), which is commonly referred to as four-point loading. The flexure strength was determined by applying the formula

$$F_b = PL \big/ bd^2 ,$$

where F_b is the flexure strength; P is the applied load; L is the length; b is the width; d is the thickness of the material.

This calculation was used because the shear span is less than 110 mm.

3. Results and Discussions

3.1. Characteristics of Freshly Mixed Concrete

The workability of concrete is typically employed to assess its fresh qualities. Four categories have been established based on the workability findings of the concrete.

1. Group I: Ternary blended concrete produced by replacing 6–8 % of the cement with MK;
2. Group II: Ternary blended concrete produced by replacing 6 % MK, 5–15 % FA, and 5–20 % RHA for the cement in M1, M14, and M27. M2–M13;
3. Group III: Ternary blended concrete produced by replacing 7 % MK, 5–15 % FA, and 5–20 % RHA for the cement, which constitutes 17–42 % of the mixture. M15–M26;
4. Group IV: Ternary blended concrete produced by replacing 8 % MK, 5–15 % FA, and 5–20 % RHA for 18–43 % of cement, specifically M28–M39 [14].

The optimal depiction of these configurations, illustrating diverse category outcomes, can be located in Figs. 2–5.

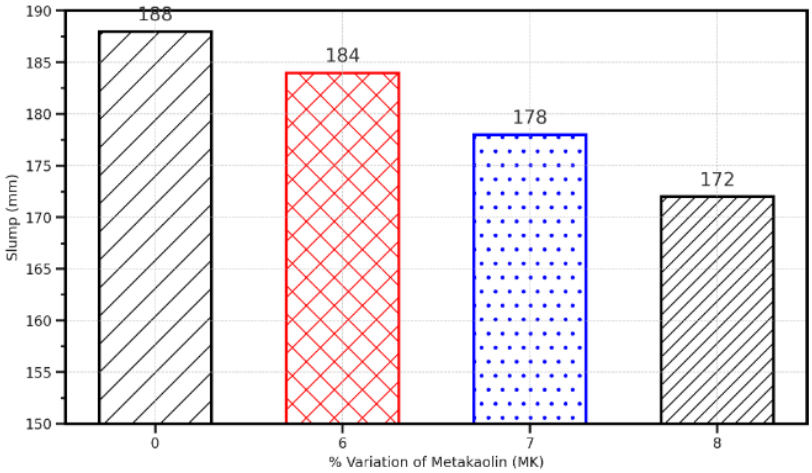

Figure 2. Workability of Group I ternary blended concrete specimens using 6–8 % MK.

Fig. 2 shows the slump response as MK replaces cement from 0 to 8 %. Workability declines steadily: from 188 mm at 0 % MK to 184 mm at 6 % (−4 mm; **−2.1 %**), then to 178 mm at 7 % (**−5.3 %** vs control) and to 172 mm at 8 % (**−8.5 %** vs control). Stepwise losses are modest up to 6 % MK but become more pronounced between 6→7 % (**−3.3 %**) and 7→8 % (**−3.4 %**), indicating a threshold where MK's rheological effects outweigh any dispersion from the superplasticizer. This trend aligns with MK's very high fineness and angular morphology, which increase the specific surface area and water demand; the additional surfaces promote flocculation and inter-particle friction, thereby thickening the paste. MK's early pozzolanic reactivity also scavenges $Ca(OH)_2$ and releases C–S–H nuclei, which stiffen the suspension and reduce the amount of free water available for lubrication. Practically, mixes at 7–8 % MK may require either a higher superplasticizer dose or a slightly lower aggregate packing density to maintain the target slump without increasing the w/b ratio [15]. This matters for strength and durability experiments: inadequate slump compromises compaction, elevating entrapped air, and biasing compressive strength downward, while also increasing sorptivity in permeability tests. To isolate MK's chemical benefits in later tests (e.g., strength, chloride penetration), keep slump constant across mixes by adjusting admixture dosage at fixed w/b; otherwise, differences in mechanical or transport results could be partly rheology-driven rather than true binder chemistry effects. The small −2.1 % slump drop at 6 % MK suggests a workable upper bound for field placement without admixture retuning, whereas ≥7 % MK should be paired with mix-control steps to preserve placement quality [16].

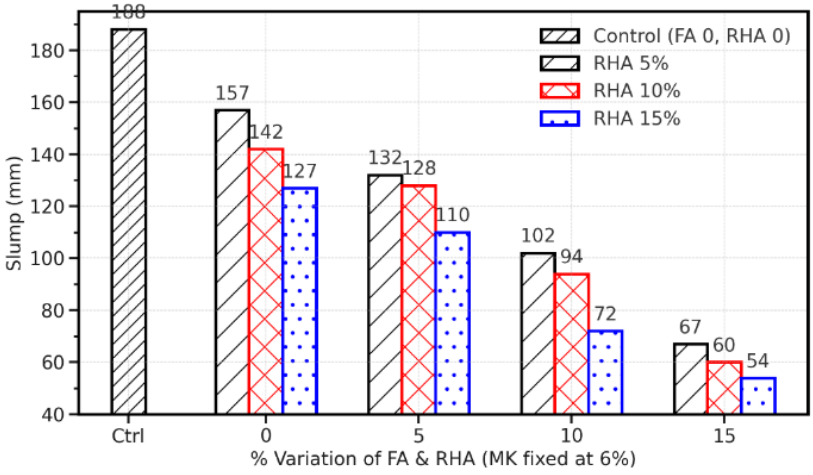

Figure 3. Workability of Group II ternary blended concrete specimens.

Fig. 3 shows the slump response when FA and RHA are varied, while MK is held at 6 %. Relative to the control (188 mm; FA = 0 %, RHA = 0 %), any addition of RHA at FA = 0 % reduces slump: 157 mm at 5 % RHA (−16.5 %), 142 mm at 10 % RHA (−24.5 %), and 127 mm at 15 % RHA (−32.4 %). At fixed RHA, increasing FA sharply lowers workability by roughly the same proportion across all RHA levels: from FA 0→15 %, slump drops 57–58 % (e.g., at RHA 5 %: 157→67 mm, −57.3 %; at RHA 15 %: 127→54 mm, −57.5 %). Raising RHA at fixed FA compounds the loss: at FA = 10 %, going from RHA 5 to 15 % cuts the slump from 102 to 72 mm (−29.4 %), while at FA = 15 %, the step is from 67 to 54 mm (−19.4 %). The most severe combination, FA 15 % + RHA 15 %, yields 54 mm, with a yield stress of 71.3 % versus the control, indicating a paste with high yield stress and poor flow under standard compaction energy. Mechanistically,

the strong slump reductions arise from the very high specific surface of RHA and the fine, reactive MK already present; both increase water demand and adsorb superplasticizer, leaving less free water for lubrication [17]. FA can act as a “ball-bearing”, but at these dosages within a ternary fines-rich system, its benefit is outweighed by increased surface area and potential admixture adsorption (especially for low-lime, high-LOI FA). For subsequent strength or transport tests, these rheology shifts are significant: inadequate slump can raise entrapped air and depress compressive strength while increasing sorptivity. To isolate chemistry-driven performance, keep slump constant across mixes – e.g., cap FA at ≤5 % when RHA ≥ 10 % or increase superplasticizer dosage at fixed w/b – so later durability and strength results are not confounded by compaction differences [18].

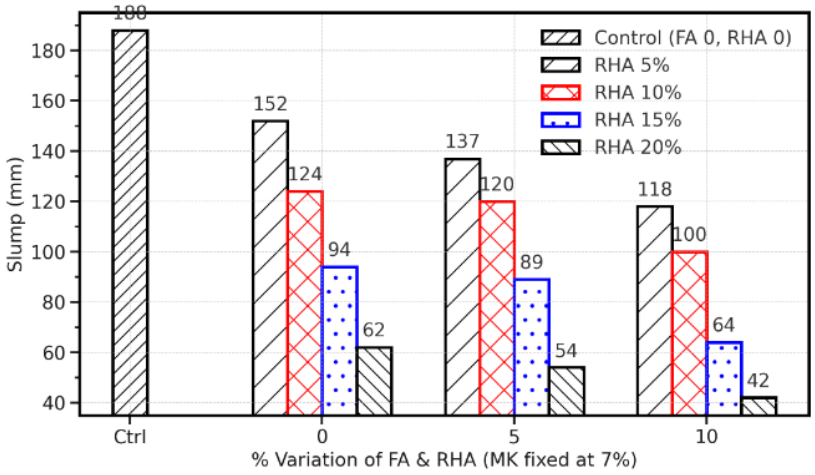

Figure 4. Slump variation of Group III ternary blended concrete mixes.

Fig. 4 illustrates the slump response when FA and RHA are varied, while MK is maintained at a constant 7 % level. Relative to the control (188 mm; FA = 0 %, RHA = 0 %), any RHA addition reduces workability at FA = 0 %: 152 mm at 5 % RHA (−19.1 %), 124 mm at 10 % (−34.0 %), 94 mm at 15 % (−50.0 %), and 62 mm at 20 % (−67.0 %). At FA = 5 %, slump falls to 137, 120, 89, and 54 mm for RHA 5–20 % (−27.1, −36.2, −52.7, and −71.3 % vs. control). At FA = 10 %, the decline is strongest: 118, 100, 64, and 42 mm (−37.2, −46.8, −66.0, and −77.7 %) [19]. The data indicate two compounding effects: (i) increasing RHA sharply increases specific surface area, raising water demand and adsorbing superplasticizer; and (ii) a higher FA level, when combined with reactive MK at 7 %, further elevates fines content and admixture adsorption, leaving less free water to lubricate the paste. Practically, mixes with RHA ≥15 % slip below 100 mm slump, even at FA ≤ 5 %, signaling a risk of poor consolidation unless the admixture is retuned. For FA = 10 % and RHA ≥ 10 %, the slump is 100 mm or lower, which can elevate entrapped air and depress compressive strength, while increasing capillary porosity – factors that will bias results in strength and permeability experiments. To maintain consistent placement while studying MK–FA–RHA chemistry, keep RHA ≤ 10 % when FA ≥ 5 % (slump ≥ 120 mm at FA 5 %, RHA 10 %), or raise superplasticizer dosage/adjust paste volume at fixed w/b. These thresholds help prevent compaction differences from masquerading as binder-performance differences in subsequent mechanical and durability testing [20].

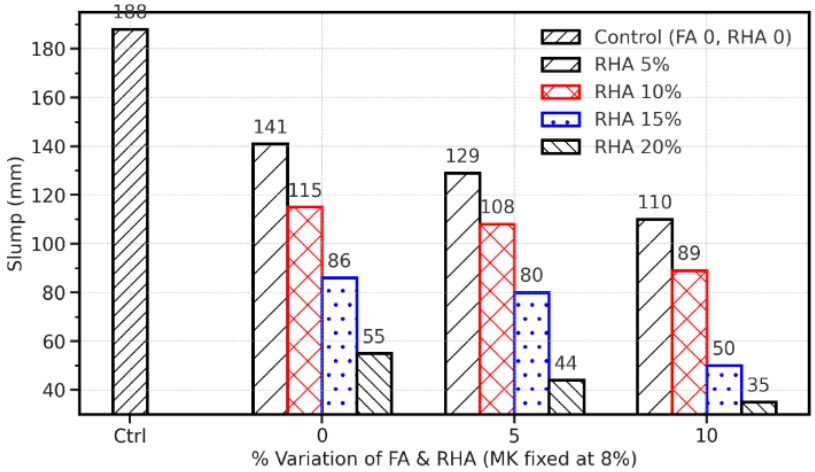

Figure 5. Slump variation of Group IV ternary blended concrete mixes.

Fig. 5 shows the slump response when FA and RHA are varied at a higher MK level (8 %). Relative to the control (188 mm), the FA = 0 % series already exhibits steep losses as RHA increases: 141 mm at 5 % (−25.0 %), 115 mm at 10 % (−38.8 %), 86 mm at 15 % (−54.3 %), and 55 mm at 20 % (−70.7 %). Adding FA further suppresses slump across each RHA level. At RHA=5 %, raising FA from 0→10 % drops slump from 141→110 mm (−22.0 %); at RHA = 10 %, the drop is 115→89 mm (−22.6 %) [21]. The fines-rich combinations are most severe: at RHA = 15 %, FA 0→10 % reduces slump 86→50 mm (−41.9 %), and at RHA = 20 %, 55→35 mm (−36.4 %), culminating in the lowest value (35 mm; −81.4 % vs. control) for FA 10 % + RHA 20 %. Mechanistically, MK at 8 % provides an abundance of reactive, angular particles. Adding porous, ultra-fine RHA increases the specific surface area and admixture adsorption, thereby reducing the water film thickness and elevating the paste yield stress. FA's spherical grains can improve packing, but at these MK–RHA loadings, the net effect is higher surface area and stronger superplasticizer demand, so the "ball-bearing" benefit is overwhelmed. For subsequent mechanical or durability experiments, this rheology shift can confound outcomes, as poor slump risks inadequate consolidation, entrapped air and artificially low compressive strength, with higher sorptivity. To maintain comparable placement, keep RHA ≤ 10 % when FA ≥ 5 % (slump ≥ ~108–115 mm), or re-tune the admixture dosage/paste volume at a fixed w/b ratio. Avoid FA 10 % with RHA ≥ 15 % unless a higher superplasticizer dose is used, as these mixes fall well below 100 mm and are prone to compaction-related scatter [22].

3.2. Hardened Properties of Concrete

Characteristic compressive strength

The specimens were analyzed following 7, 28, and 56 days of water cure. The results have been categorized into three primary groups:

1. Group I consists of ternary blended concrete specimens, wherein 6 % MK, 5–15 % FA, and 5–20 % RHA replace 6–41 % of the cement. The specimens have been assigned the designations M1–M13.
2. Group II consists of ternary blended concrete specimens, in which 7–42 % of the cement is replaced with 7 % MK, 5–15 % FA, and 5–20 % RHA.
3. Group III consists of ternary blended concrete specimens, wherein 8–43 % of the cement is replaced with 8 % MK, 5–15 % FA, and 5–20 % RHA. The specimens are labelled M27–M39.

To elucidate the trend behavior of RHA, each category has been subdivided into multiple forms. This has been accomplished while preserving the equivalent content level for MK and FA. Fig. 6 presents the most precise depiction of the typical values for compressive strength [23].

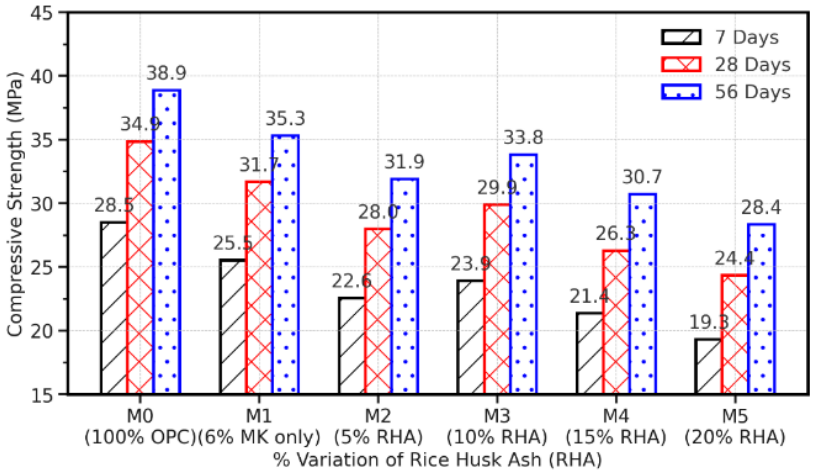

Figure 6. Typical results for compressive strength of Group I ternary blended concrete mixes.

Fig. 6 shows the strength response as RHA rises while MK is fixed at 6 % and FA at 5 %. Against the control M0 (100 % OPC), strengths decrease at every age when RHA is added. At 28 days, M0 reaches 34.9 MPa. With RHA = 5 % (M2) and 10 % (M3), strengths are −19.8 % (27.99 MPa) and −14.2 % (29.91 MPa) relative to M0; higher RHA of 15 and 20 % drop further to −24.6 % (26.28 MPa) and −30.1 % (24.36 MPa). A local optimum appears at RHA = 10 %, which is +6.9 % higher than RHA=5 % and +13.8 % above RHA = 20 % at 28 days. The same pattern holds at 56 days: M0 = 38.9 MPa; M3 = 33.8 MPa (−13.0 % vs M0) yet +6.0 % vs RHA = 5 % and +19.3 % vs RHA = 20 %. Age gains are strong across mixes, highlighting the delayed pozzolanic action of RHA: from 7 to 28 days, strength rises by ~24–26 % (e.g., M3: 23.91 to 29.91 MPa, +25.1 %); from 28 to 56 days, gains are ~13–17 % (M4: 26.28 to 30.73 MPa, +16.9 %). Physically, finely porous RHA consumes $Ca(OH)_2$ to form secondary C–S–H, which explains the

sustained gains from 28 to 56 days; however, excess RHA (>10 %) elevates the specific surface and dilutes the clinker, raising water and superplasticizer demand, which reduces early packing and limits later strength [24]. For downstream durability or modulus tests, the RHA = 10 % condition offers the best balance within this MK–FA matrix, providing higher late-age strength than RHA at 5 % or 15–20 %. Mixes with ≥15 % RHA result in lower compaction quality and higher capillary porosity, without requiring admixture retuning.

Table 3. Compressive strength of Group I ternary blended concrete mixes.

Mix[M]	Blending				Mean Compressive Strength (7 Days)	Mean Compressive Strength (28 Days)	Mean Compressive Strength (56 Days)
	OPC	MK	FA	RHA			
M0	100	0	0	0	28.50	34.87	38.87
M1	94	6	0	0	25.54	31.69	35.32
M2	84	6	5	5	22.58	27.99	31.91
M3	79	6	5	10	23.91	29.91	33.84
M4	74	6	5	15	21.39	26.28	30.73
M5	69	6	5	20	19.32	24.36	28.36
M6	79	6	10	5	25.32	31.17	35.02
M7	74	6	10	10	26.73	32.65	36.58
M8	69	6	10	15	24.65	30.13	34.58
M9	64	6	10	20	22.87	28.50	31.99
M10	74	6	15	5	24.80	30.87	34.73
M11	69	6	15	10	23.76	28.87	33.69
M12	64	6	15	15	21.84	26.87	31.61
M13	59	6	15	20	20.06	25.47	29.69

Nonetheless, the results of the enhancement of compressive strength in Group II ternary blended concrete mixtures, which incorporate the replacement of a designated percentage of cement with 7 % MK, 5 % FA, and 5–20 % RHA, in addition to one control mixture, are illustrated in Fig. 7. The compressive strength values were measured at 27.76, 33.84, and 38.43 MPa after 7, 28, and 56 days of curing, respectively, when ordinary concrete was combined with 7 % MK completely. The readings were recorded following the concrete's curing period of 7, 28, and 56 days. Moreover, the incorporation of 7 % MK, in conjunction with 5 % FA and 5–10 % RHA, results in a reduction in concrete strength relative to the control mix. This phenomenon is noted in several mixtures, notably M15–M18. When concrete is produced by amalgamating varying proportions of RHA with a constant content of 7 % MK and 5 % FA, a significant enhancement in compressive strength has been seen for the concrete containing 10 % RHA (M16) after 7, 28, and 56 days of curing. This pattern resembles that observed in the concrete mixed with merely 7 % MK, as per the M14 formula. Table 4 presents the compressive strength values for Group II ternary blended concrete compositions. The optimal replacement percentage for Group II concrete specimens is 7 % MK, 10 % FA, and 10 % RHA, corresponding to an M20 mix [25].

Table 4. Compressive strength of Group-II ternary blended concrete mixes.

Mix[M]	Blending				Mean Compressive Strength (7 Days)	Mean Compressive Strength (28 Days)	Mean Compressive Strength (56 Days)
	OPC	MK	FA	RHA			
M0	100	0	0	0	28.50	34.87	38.87
M14	93	7	0	0	27.76	33.84	38.43
M15	83	7	5	5	23.61	30.13	34.58
M16	78	7	5	10	25.17	32.21	35.91
M17	73	7	5	15	22.50	29.39	33.24
M18	68	7	5	20	20.06	27.32	31.91
M19	78	7	10	5	26.87	33.54	37.84
M20	73	7	10	10	28.73	36.50	39.47
M21	68	7	10	15	25.69	31.91	35.61
M22	63	7	10	20	23.91	29.84	33.84
M23	73	7	15	5	26.58	33.54	37.76
M24	68	7	15	10	23.91	30.87	34.87
M25	63	7	15	15	23.76	29.99	34.43
M26	58	7	15	20	21.10	28.65	33.10

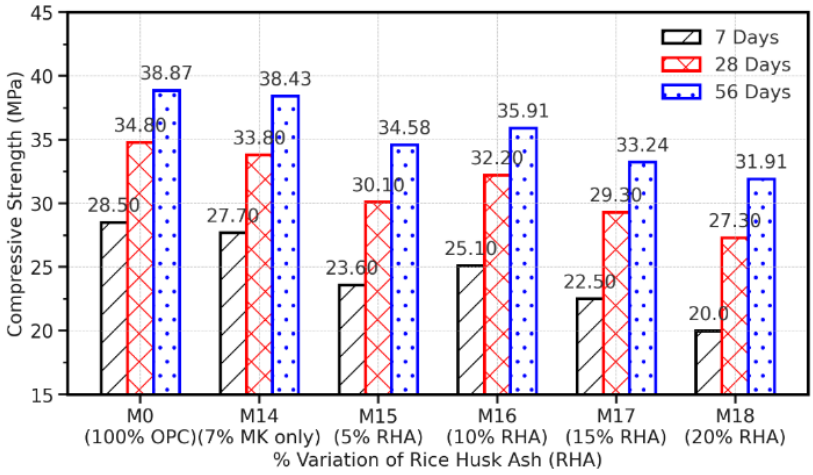

Figure 7. Typical results for compressive strength of Group II ternary blended concrete mixes.

Fig. 7 shows the strength evolution as RHA increases with MK held at 7 % and FA at 5 %. Compared with the 100 % OPC control (M0: 34.8 MPa at 28 days, 38.87 MPa at 56 days), mixes with RHA are lower at both ages, yet 10 % RHA (M16) is consistently the best among the RHA series: 32.2 MPa at 28 days and 35.91 MPa at 56 days −7.5 % (28 d) and −7.6 % (56 d) vs the control, but +7.0 % (28 d) and +3.8 % (56 d) higher than 5 % RHA (M15). At higher RHA, the penalty grows: 15 % RHA (M17) is −15.8 % (28 d) and −14.5 % (56 d) vs control; 20 % RHA (M18) is −21.6 % (28 d) and −17.9 %(56 d). Age gains reveal delayed pozzolanic activity of RHA, which strengthens later, from 28 to 56 days, with strengths rising by ~11–17 % (e.g., M18: +16.9 %, M15: +14.9 %, M16: +11.5 %). Early (7→28 days) gains are larger as RHA increases, reaching +36.5 % for M18, indicating slow early reactivity and progressive secondary C–S–H formation. Mechanistically, modest RHA (~10 %) provides reactive silica and fine filler to densify a paste already enriched with MK, whereas excessive RHA (>10 %) dilutes the clinker, increases surface area, and increases admixture demand, thereby curbing early packing and limiting late strength. For follow-on durability or transport tests, these maturity effects are significant: higher-RHA mixes may appear inferior at 28 days but close the gap by 56 days as pores refine [26]. If the goal is to reduce clinker content while maintaining acceptable strength, 10 % RHA within this MK–FA matrix is a practical upper bound without retuning the admixture or paste volume. A RHA content of ≥15 % should be paired with workability control to avoid compaction-induced scatter in strength and permeability results.

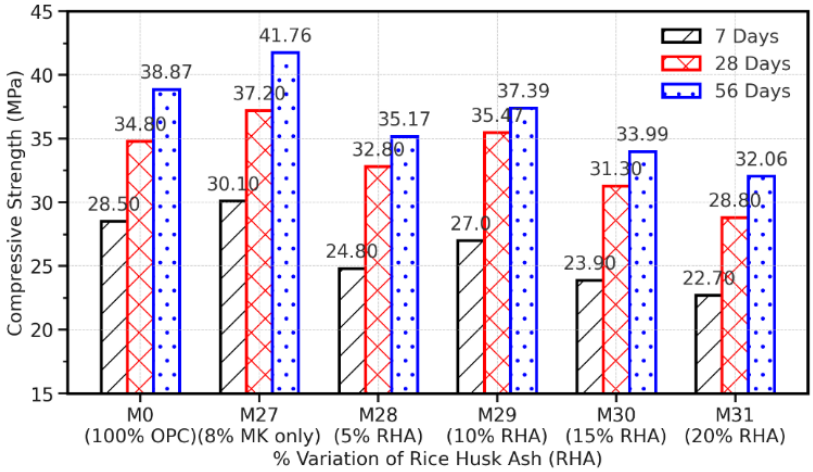

Figure 8. Typical results for compressive strength of Group III ternary blended concrete mixes.

The increase in compressive strength of Group III ternary mixed concrete specimens is illustrated in Fig. 8. This scenario involves substituting 8 % of the cement with MK, 5 % with FA, and 5–20 % with RHA, alongside a control mix. Based on the findings presented in Fig. 8, it can be concluded that incorporating MK into conventional cement concrete enhances the compressive strength of the concrete. For instance, when the concrete is combined with 8 % MK exclusively, the compressive strength values are 30.18, 37.24, and 41.76 MPa after curing for 7, 28, and 56 days, respectively. When the MK concentration reaches 8 %, a noticeable enhancement in compressive strength occurs. Furthermore, when the concrete incorporates 8 % MK alongside 5 % FA and 5–10 % RHA, a decline in strength is observed in other mixtures (namely M28–M31). The reduction in strength is analogous to the decline observed in the control mix. Concrete composed of varying proportions of RHA, combined with a constant 8 % MK and 5 % FA, exhibits a

significant enhancement in compressive strength at 10 % RHA blending (M29) after 7, 28, and 56 days of curing. This observation was made after the concrete had cured for 7, 28, and 56 days. Initially, the compressive strength of the Group III ternary blended concrete specimens was quite low; however, after 56 days of curing, a significant enhancement in strength was noted. Table 5 delineates the specific compressive strength values for ternary mixed concrete mixtures classified under Group III. The optimal replacement proportion for Group III concrete specimens, as well as for all 39 combinations, was established as 8 % MK + 10% FA + 10 % RHA, corresponding to the M33 mix [27].

Table 5. Compressive strength of Group III ternary blended concrete mixes.

Mix[M]	Blending				Mean Compressive Strength (7 Days)	Mean Compressive Strength (28 Days)	Mean Compressive Strength (56 Days)
	OPC	MK	FA	RHA			
M0	100	0	0	0	28.50	34.87	38.87
M27	92	8	0	0	30.18	37.24	41.76
M28	82	8	5	5	24.80	32.80	35.17
M29	77	8	5	10	27.02	35.47	37.39
M30	72	8	5	15	23.91	31.32	33.99
M31	67	8	5	20	22.73	28.80	32.06
M32	77	8	10	5	29.69	37.10	40.80
M33	72	8	10	10	30.87	38.87	42.58
M34	67	8	10	15	27.91	33.99	38.13
M35	62	8	10	20	25.99	30.87	36.36
M36	72	8	15	5	28.80	36.50	39.32
M37	67	8	15	10	26.87	34.43	35.91
M38	62	8	15	15	25.39	31.76	34.87
M39	57	8	15	20	24.21	30.73	34.43

3.3. Flexural Strength

The mean flexural strength of concrete specimens is reported following a 28-day water curing period.

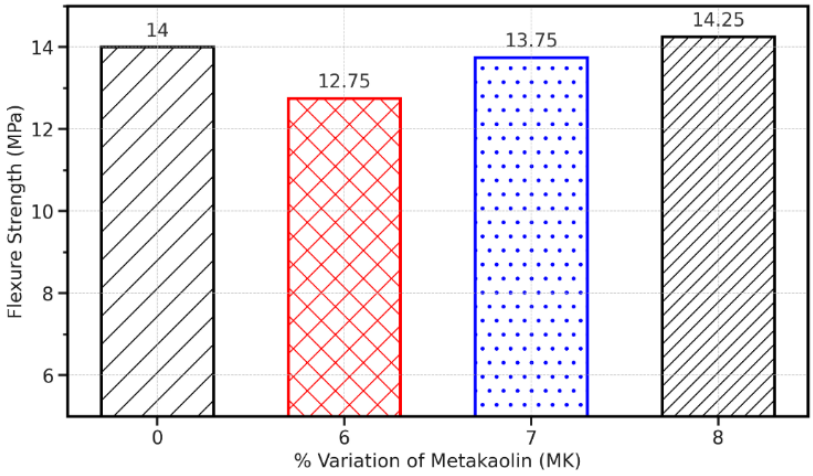

Figure 9. Flexure strength of ternary blended concrete mixes using 6–8 % MK only.

Fig. 9 shows the flexural response as MK replaces cement from 0 to 8 % with no other SCMs. The control (0 % MK) reaches 14.00 MPa. Introducing 6 % MK lowers flexural strength to 12.75 MPa (−8.9 % vs control), likely due to higher water demand and tighter rheology, which reduces fiber bridging at the paste–aggregate interface when the admixture dosage isn't retuned. Raising MK to 7 % recovers strength to 13.75 MPa (+7.8 % vs 6 % MK; −1.8 % vs control), indicating better packing and budding pozzolanic gel that densifies the interfacial transition zone (ITZ). At 8 % MK, flexure improves to 14.25 MPa (+3.6 % over 7 % MK, +11.8 % over 6 % MK, and +1.8 % above the control) showing that once workability is adequate, MK's ultrafine filler effect and rapid aluminosilicate reaction strengthen tensile load paths and crack-arresting bridges. For downstream fracture or fatigue tests, this matters: MK near 8 % should widen the stable microcrack regime and delay first-crack formation, yielding higher modulus of rupture scatter resistance. Conversely, the 6 % MK data warn that under-dosed superplasticizer or suboptimal paste

volume can mask MK's chemical benefits by weakening compaction and the ITZ [28]. If you plan to compare toughness or flexural fatigue across binders, keep slump consistent and use MK 7–8 % as the reference region; it maximizes ITZ refinement without excessive dilution of clinker. These trends suggest that modest MK additions primarily enhance matrix continuity rather than just compressive capacity, which is crucial when bending governs performance (e.g., slabs, pavements, thin precast elements).

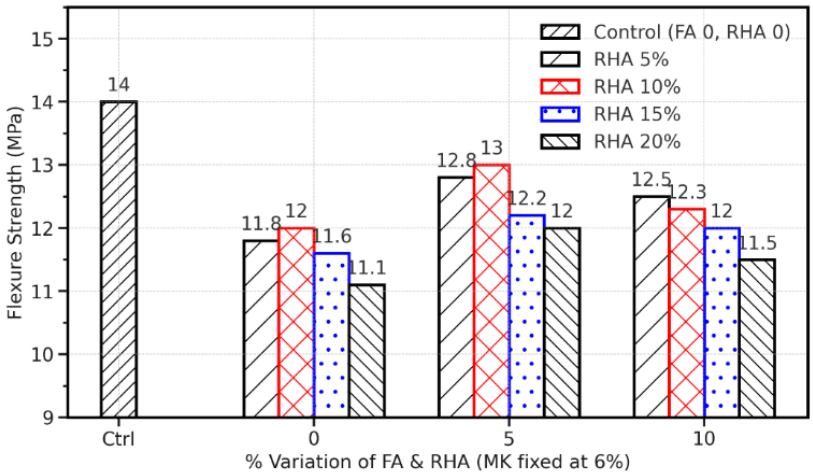

Figure 10. Typical results for flexure strength of ternary blended concrete mixes at 28 days curing.

Fig. 10 depicts the advancement of flexural strength in concrete mixtures incorporating various cement replacement ingredients, specifically 6 % MK, 5–15 % FA, and 5–20 % RHA. An experiment was conducted to investigate the effect of varying RHA percentages on the flexural strength of concrete. The concrete mixture comprised a constant composition of 6 % MK and 5 % FA. The results indicated a significant enhancement in flexural strength after 28 days of curing with the addition of 10 % RHA (M3). This rise parallels the trend noted when combining alone with 6 % MK. Further investigation indicates similar variations for 10 and 15 % FA, alongside a range of 5–20 % RHA and 6 % MK. Following a 28-day curing period, it was observed that the formulation designated as M7, comprising 74 % OPC, 6 % MK, 10 % FA, and 10% RHA, exhibited marginally inferior flexural strength relative to the control mixture (M0). The conclusion reached is illustrated in Fig. 10. The predominance of FA's behavior is evident in the M6–M9 mix, especially in contrast to the M2–M5 mix, particularly with the addition of 10 % FA. The ideal blending combination that produces the highest flexural Strength for all mixes is identified as 8 % MK + 10 % FA + 10 % RHA (designated M33) for ternary blending, and 8 % MK (designated M27) for single blending [29].

Split tensile strength

The mean split tensile strength of concrete specimens, assessed after 28 days of water curing, is recorded. Fig. 11 shows the split tensile strength response as MK replaces cement from 0 to 8 %. The control (0 % MK) records 2.44 MPa. Introducing 6 % MK reduces the strength to 2.27 MPa, a 7.0 % drop, consistent with the higher specific surface area of MK, which raises water and superplasticizer demand. If the admixture dosage is not adjusted, compaction efficacy and ITZ quality suffer, which depresses the tensile capacity. Increasing MK to 7 % lifts strength to 2.41 MPa (+6.2 % vs 6 % MK; −1.2 % vs control), suggesting improved particle packing and early pozzolanic refinement that stabilizes microcrack initiation. At 8 % MK, strength reaches 2.47 MPa (+8.8 % relative to 6 % MK and +1.2 % above the control) indicating that once slump is managed, MK's ultrafine filler and reactive aluminosilicate gels densify the ITZ and enhance crack-bridging paths under diametral loading. Practically, the 6 % MK dip signals sensitivity to rheology; maintaining constant workability across mixes is critical so tensile results reflect binder chemistry rather than casting artifacts. For fracture energy, permeability, or chloride tests that are strongly influenced by microcrack networks, an MK near 7–8 % is a useful setting: it slightly increases tensile strength while also promoting a tighter pore structure, which should reduce connected capillaries. If your study explores synergy with FA/RHA, use MK 8 % as the tensile-strength benchmark and adjust superplasticizer to match control slump; this will help prevent porosity differences from skewing strength, transport, or durability outcomes [30].

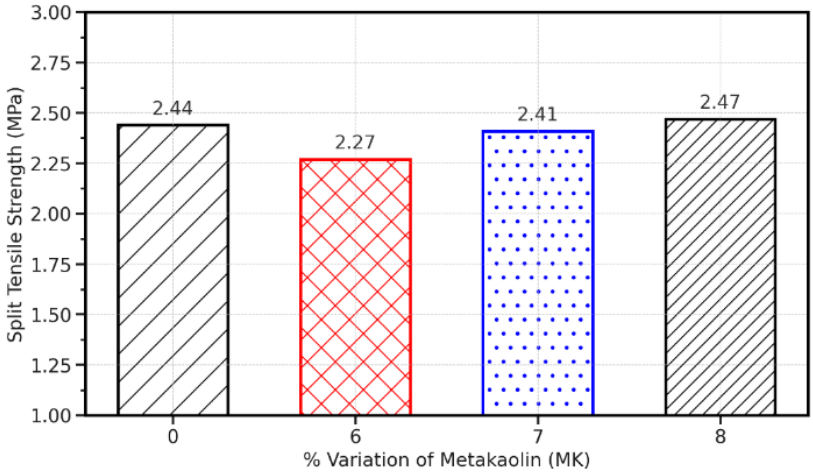

Figure 11. Split tensile strength of ternary blended concrete mixes using 6–8 % MK only.

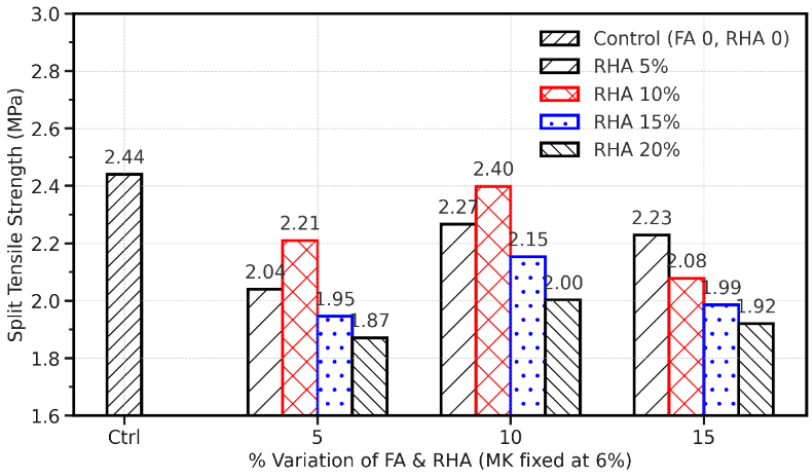

Figure 12. Typical results for split tensile strength of ternary blended concrete mixes at 28 days curing.

Fig. 12 illustrates the standard outcomes of split tensile strength progression in ternary blended concrete mixtures. These combinations consist of substituting a designated quantity of cement with 6 % MK, 5–15 % FA, and 5–20 % RHA, along with one control mixture. The results depicted in Fig. 12 indicate a significant increase in the split tensile strength of concrete with the addition of varying quantities of RHA to a constant mixture comprising 6 % MK and 5 % FA. A notable enhancement in split tensile strength is observed when 10 % RHA (designated as M3) is incorporated into the concrete, with a 28-day curing duration. Subsequent analysis reveals analogous fluctuations for 10 and 15 % FA in relation to the range of 5–20 % RHA and 6 % MK. Furthermore, the influence of FA is more pronounced in combinations M6–M9 than in mixtures M2–M5, particularly when FA is integrated at a 10 % level [31].

According to the results illustrated in Fig. 12, the M10 mixes demonstrate superior values compared to the M11–M13 mixes. Nonetheless, they remain inferior to both the control mixture and the other combinations employed for M6–M9. Fig. 12 illustrates that the strength values improve when the FA concentration rises from 5 to 10 %. Nonetheless, a shift in tendency occurs from M10–M13 as the FA percentage increases from 10 to 15 %. The findings clearly indicate that the ideal proportion of FA for these mixtures is 10 %. According to Fig. 12, the optimal outcome is achieved by employing a combination of all chemicals, particularly 6 % MK, 10 % FA, and 10 % RHA. The incorporation of MK in plain cement concrete resulted in a minor reduction in split tensile strength, however the decrease was not substantial. Consequently, thorough study reveals that the optimal formulation for attaining maximum split tensile strength across all mixtures is a combination of 8 % MK, 10 % FA, and 10 % RHA (designated as M33) for ternary blending, and 8 % MK (designated as M27) for single blending.

3.4. Proposed Approach for the Combined Effect (Synergy) of Mineral Admixtures

The term “synergistic impact” denotes the interaction of two or more substances that results in a combined effect beyond the cumulative effects of the individual substances. Prior research has shown that

the synergistic effect and efficiency factor of MK are superior in binary cement concrete compared to analogous single blended cement concrete. This applies when contrasting the two compounds. These data suggest that the efficiency factor of MK is superior in a ternary blending system of concrete mixes compared to the efficiency factor observed in binary or single blending cement concrete.

A formula has been presented to ascertain the efficiency factor of MK, FA, and RHA in ternary cement concrete. This formula, as elucidated by researchers, is derived from Bolomey's equation, which is used to estimate the strength of concrete incorporating mineral admixtures. The water-to-cement ratio has been maintained at a constant value of 0.45 during the entire experimental research. Bolomey's equation can be utilized to forecast the compressive strength of the control mix:

$$f_c\left(days\right) = A_1\left(C/W\right) + A_2, \tag{1}$$

where f_c is the anticipated compressive strength; A_1 and A_2 are the constants that take into consideration the varying ages of concrete; C is the amount of cement, kg/m^3; W is the amount of water present per unit volume, kg/m^3.

In (1), the constants A_1 and A_2 have been included to account for various factors, such as the age of the concrete and exposure conditions, that may influence the development of the concrete's strength. These parameters can be determined by regression analysis. The concrete's strength was previously determined in research by examining the precise effects of admixtures on its chemical composition. This was achieved by altering Bolomey's equation, as seen in (2) [32]:

$$f_c\left(days\right) = A_1\left\{\left(C + k_{MA}P_{MA}\right)/W\right\} + A_2. \tag{2}$$

In the context of concrete mixes, k_{MA} refers to the efficiency factor of the mineral addition that is utilized, while P_{MA} reflects the amount of mineral admixture, kg/m^3. In addition, the efficiency factor k_{MA} has been calculated using (3), as provided by the researchers:

$$k_{MA} = \left(1/P_{MA}\right)\left\{-C + W\left(f_c - A_2\right)/A_1\right\}. \tag{3}$$

After calculating the individual effect $\left(k_{MA}\right)$, it is important to determine the combined effect, known as the synergy, of this mineral admixture. This synergy or combined effect of two or more additives are used, which is represented as k_{TB}, which is a factor that represents the combined effect of the mineral admixture in binary, ternary, or quaternary cement concrete. The value of k_{TB} is predicted using the following equation:

$$k_{TB} = \left\{W\left(f_c - A_2\right)/A_1 - C\right\}/\left(k_{MA}P_{MA}\right). \tag{4}$$

As a result, the overall efficiency factor for mineral admixture $\left(k'_{MA}\right)$ is calculated by taking into consideration the combined effect of all of the admixtures that are utilized in the concrete mixes. The value was determined by applying (5) to the data:

$$k'_{MA} = k_{TB} \times k_{MA}. \tag{5}$$

The symbol *k* denotes the final efficiency factor of mineral admixture in binary cement concrete. With the use of the following connection, a formula has been developed to estimate the compressive strength of binary cement concrete. The formula is as follows:

$$f_c\left(days\right) = A_1\left\{C/W + k_{TB}\left(k_{MA}P_{MA}\right)/W\right\} + A_2, \tag{6}$$

where f_c is the predicted compressive strength; A_1 and A_2 are the constants that take into account the varying ages of the concrete; C is the cement content, kg/m^3; W is the water content, kg/m^3, k_{TB} is the synergic impact factor of mineral admixture; k_{MA} is the efficiency factor of mineral admixture; P_{MA} is the mineral admixture content, kg/m^3.

It is important to note that the equation presented above only displays compressive strength values for cement blends that contain only two components. Consequently, the equation that was presented earlier

can also be extended to include ternary or quaternary cement concrete conditions. The equation for ternary concrete (7) can be produced by carrying out the aforementioned steps. In a similar manner, it is possible to develop an equation for quaternary concrete, which is represented by (8):

$$f_c\left(days\right) = A_1\left\{C/W + k_{TB}\left(k_{MA_1}P_{MA_1} + k_{MA_2}P_{MA_2}\right)/W\right\} + A_2; \tag{7}$$

$$f_c\left(days\right) = A_1\left\{C/W + k_{TB}\left(k_{MA_1}P_{MA_1} + k_{MA_2}P_{MA_2} + k_{MA_3}P_{MA_3}\right)/W\right\} + A_2. \tag{8}$$

The variables k_{MA_1}, k_{MA_2}, and k_{MA_3} represent the efficiency factors for mineral admixture types 1, 2, and 3, respectively. The variables P_{MA_1}, P_{MA_2}, and P_{MA_3} represent the content of mineral admixture types 1, 2, and 3, respectively.

However, in this particular investigation, the identical equation form for f_c (8) has been utilized for predictive purposes. However, new coefficient terms have been substituted for k_{TB} and k_{MA_1}, k_{MA_2} and k_{MA_3}. There were three different types of admixtures used in the research: MK, FA, and RHA. According to the equation, the coefficients that are allocated to each admixture are denoted by the symbols α_{MK}, α_{FA}, and α_{RHA}. These coefficients can be considered analogous to the efficiency factors of MK, FA, and RHA, denoted as k_{MK}, k_{FA}, and k_{RHA}, respectively. It is also worth noting that k_{TB} is considered equivalent to α_{TB}.

$$f_c\left(days\right) = A_1\left\{C/W + \alpha_{TB}\left(\alpha_{MK}P_{MK} + \alpha_{FA}P_{FA} + \alpha_{RHA}P_{RHA}\right)/W\right\} + A_2. \tag{9}$$

The terms α_{MK}, α_{FA}, and α_{RHA} correspond to the efficiency factors of MK, FA, and RHA, respectively. Additionally, α_{TB} is the factor that corresponds to the factor that shows how all of the admixtures in ternary blended concrete mixes work together synergistically. As a result, the final proposed equation (9) is used in the same way as described earlier and serves as an analogy for (8).

The overall efficiency factor for each admixture, represented as k'_{MA}, is calculated by assessing the collective impact of all the admixtures employed in the concrete mixes, as outlined in (5). In this study, the component is represented as α'_{MK}, which can be seen as comparable to k'_{MK}. The value has been calculated using the equation $\alpha'_{MK} = \alpha_{TB} \times \alpha_{MK}$, where α'_{MK} represents a comparable parameter to the final efficiency factor of MK (i.e., k'_{MK}). Therefore, (5) may also be used to generate analogous derivations for FA and RHA.

Equation (9) can be used in nonlinear regression analysis to predict the efficiency factor for numerous mineral admixtures simultaneously. The subsequent procedures have been executed to predict the collective influence and the related coefficients of MK, FA, and RHA for ternary blended concrete mixes:

Step 1: A_1 and A_2 are constants that represent the varying ages of concrete. These constants were determined by regression analysis using (9), as displayed in Table 6.

Table 6. A_1 and A_2 at different ages of concrete.

Age of Concrete (days)	A_1	A_2
7	9.79	1.41
28	10.88	24.29
56	11.43	30.55

Step 2: The coefficients α_{MK}, α_{FA}, and α_{RHA}, which represent the equivalent properties of MK, FA, and RHA in ternary blended concrete mixes at various ages, were computed using (9). The calculated coefficients are presented in Table 7.

Table 7. Analogous coefficient of MK, FA and RHA in ternary blended concrete.

Age of Concrete (days)	α_{MK}	α_{FA}	α_{RHA}
7	1.06	0.63	–0.20
28	1.71	1.09	–3.93
56	1.84	1.11	–4.62

Step 3: The synergistic impact factor of additives (α_{TB}) was determined using (9) for various combinations of ternary blended concrete, as presented in Table 8.

Table 8. Synergic effect factor of all admixtures in ternary blended concrete.

Age of Concrete (days)	α_{TB}
7	1.97
28	2.14
56	2.88

Step 4: Table 9 contains the comparable parameter to the final efficiency factor of all additions in ternary blended concrete mixes.

Table 9. Analogous parameter to the final efficiency factor of all admixtures in ternary blended concrete.

Age of Concrete (days)	$\alpha'_{MK} = \alpha_{TB} \times \alpha_{MK}$	$\alpha'_{FA} = \alpha_{TB} \times \alpha_{FA}$	$\alpha'_{RHA} = \alpha_{TB} \times \alpha_{RHA}$
7	2.08	1.24	–0.39
28	3.65	2.33	–8.41
56	5.29	3.19	–13.30

The rate of increase in the final efficiency factor of all admixtures is continually rising for concrete of all ages. Nevertheless, the deviation in parameters for concrete at 28 and 56 days is negligible in comparison to the fluctuation in parameters for admixtures at 7 and 28 days.

3.5. Estimating the Compressive Strength of Concrete Using Ternary Blending

The compressive strength of various ternary blending concrete mixes in this investigation can be determined using the following formulae:

$$f_c\left(7\ days\right) = 9.79\left\{C/W + 1.97\left(\left(1.06\right)P_{MK} + \left(0.63\right)P_{FA} + \left(-0.20\right)P_{RHA}\right)/W\right\} + 1.41; \quad (10)$$

$$f_c\left(28\ days\right) = 10.88\left\{C/W + 2.14\left(\left(1.71\right)P_{MK} + \left(1.09\right)P_{FA} + \left(-3.93\right)P_{RHA}\right)/W\right\} + 24.29; \quad (11)$$

$$f_c\left(56\ days\right) = 2.55\left\{C/W + 2.88\left(\left(1.84\right)P_{MK} + \left(1.11\right)P_{FA} + \left(-4.62\right)P_{RHA}\right)/W\right\} + 34.62. \quad (12)$$

Figs. 13–15 display the comparison between the experimental and projected values of compressive strength at 7, 28, and 56 days, respectively.

Fig. 13 illustrates the regression equation obtained with the MS Excel application utilizing the Solver function. This equation is utilized to create a graph that juxtaposes the experimental results with the expected values of compressive strength at 7 days. Of the 40 data sets, 10 sets, including 25 % of the total, have forecast errors exceeding 10 %. The remaining 30 sets, including 75 % of the total, exhibit an enhancement in inaccuracy within the range of 0–10 %.

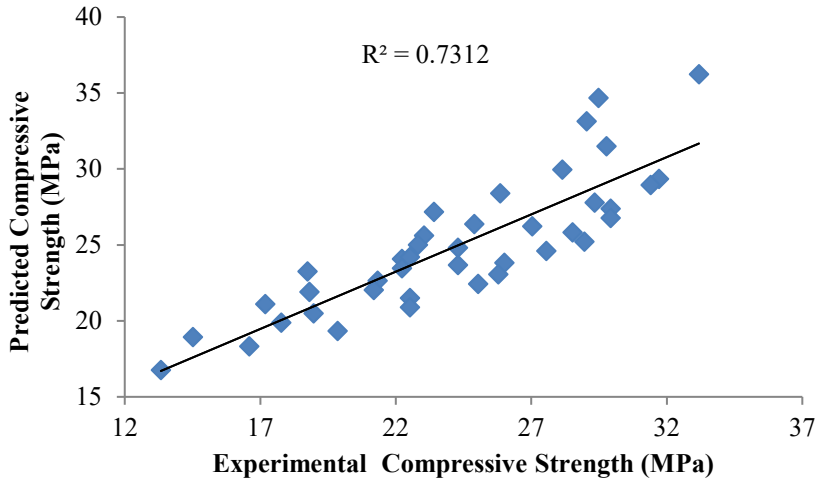

Figure 13. Comparison between experimental vs. predicted values at 7 days.

Fig. 14 illustrates the regression equation produced by the MS Excel application with the solver function. This equation is used to create a graph that compares the measured and projected values of compressive strength after 28 days. Out of 40 data sets, 30 % (12 sets) exhibit an error exceeding 10 %, whilst the remaining 70 % (28 sets) demonstrate a decrease in error, ranging from 0 to 10 %.

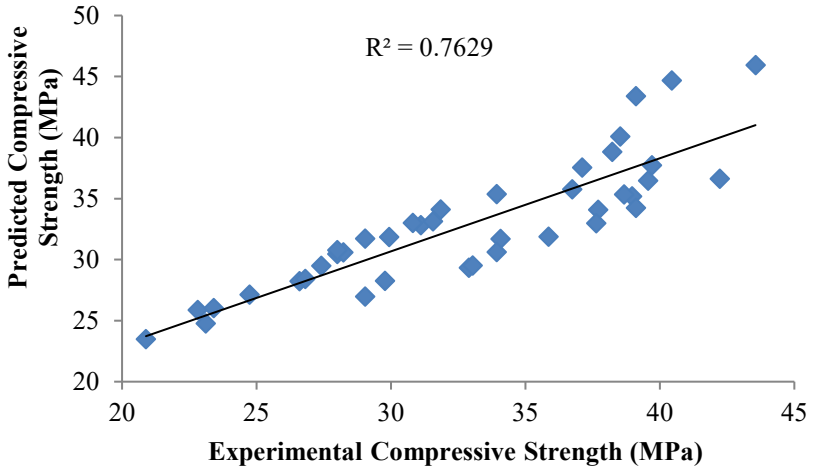

Figure 14. Comparison between experimental vs. predicted values at 28 days.

Fig. 15 illustrates the regression equation generated by the MS Excel application using the Solver function. This equation is employed to illustrate a graphical comparison between the actual experimental data and the anticipated values of compressive strength after 56 days. Of the 40 data sets, 20 % (8 sets) exhibit forecast errors exceeding 10 %, whilst the remaining 80 % (32 sets) demonstrate error reductions within the 0–10 % range.

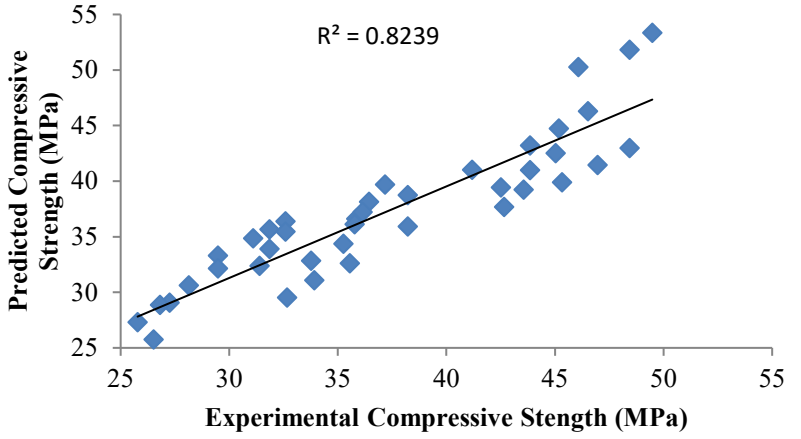

Figure 15. Comparison between experimental vs. predicted values at 56 days.

The observed disparity indicates a substantial correlation between the actual results and the expected data. The error variation appears to be within an acceptable range, since over 80 % of the data exhibits substantial concordance with the testing results. The R^2 values for maturity periods of 7, 28, and 56 days are 0.73, 0.76, and 0.82, respectively, as illustrated in Figs. 13–15. Despite the low results, the link may still be established by examining the variation in errors. The comparatively low value of R^2 can be attributed to the principle of analogy.

3.6. Correlation between Compressive Strength and Split Tensile Strength

Regression analysis was employed to establish the link between split tensile strength and compressive strength. The compressive strength of the specimens was determined by measuring the resistance to compression using cubic samples with dimensions of 150×150×150 mm. The split tensile strength was determined by measuring the resistance to splitting using cylindrical samples with dimensions of 75×150 mm after a 28-day period. By utilizing regression analysis with the provided equations, we may examine the present strength data of all concrete mixes and ascertain the most suitable curve that fits the data.

Following expression has been adopted with a confidence level of good predictions.

$$f_t = \left[x_1 \times \left(f_c \right)^{x_2} \right] - x_3.$$

In this context, the constants x_1, x_2, and x_3 are determined through the utilization of Non-Linear Regression analytical techniques. The values of the constants obtained are: x_1 = 5.31, x_2 = 0.14, x_3 = 6.51. In light of this, the empirical equation can be written as:

$$f_t = \left[5.31 \times f_c^{\,0.14} \right] - 6.51, \tag{13}$$

where f_t is equal to the split tensile strength, MPa; f_c equals the compressive strength, MPa.

Due to concrete's greater levels of uncertainty compared to other materials, the equation yields an underestimated result, which is practically logical. Consequently, it is preferable to formulate an equation that yields a result inferior to the anticipated one. Out of the forty data sets, eight sets (20 %) demonstrate forecast errors above 10 %, whereas the remaining thirty-one sets (80 %) indicate error reductions ranging from 0 to 10 %. However, discrepancies in the expected outcomes may arise from the unpredictability and dispersion of the experimental data set. The correlation may be validated by examining the error variability in the projected data, which clearly demonstrates a high level of confidence in the predicted values and facilitates the alignment of results with the experimental data. Fig. 16, which illustrates a dataset with an error margin of ±10 %, has been included for clarity.

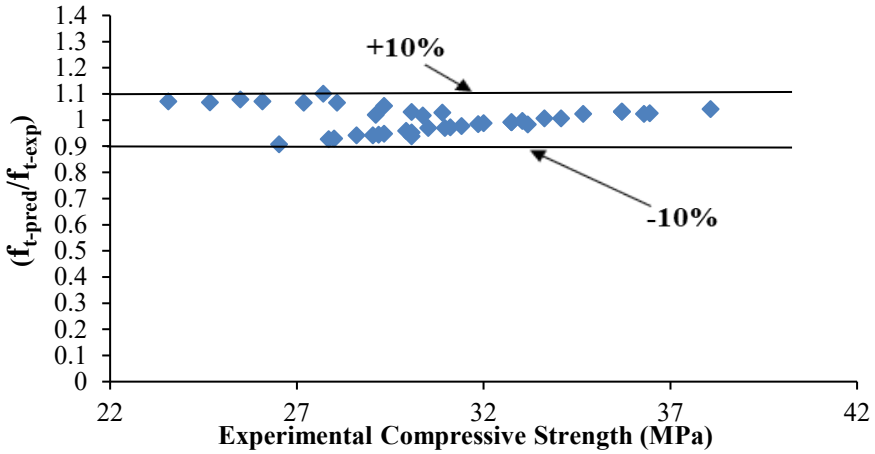

Figure 16. Error variation of predicted vs experimental values of split tensile strength.

3.7. Correlation between Compressive Strength and Flexure Strength

A regression analysis was performed to establish the degree of correlation between flexural strength and compressive strength. As part of the research, cubes measuring 150×150×150 mm were utilized to evaluate the compressive strength of the material. Additionally, beams measuring 100×100×500 mm were utilized to measure the flexural strength after a period of 28 days:

Following expression has been adopted with a confidence level of good predictions.

$$f_b = \left[x_1 \times \left(f_c \right)^{x_2} \right] / x_3 .$$

The values of constants x_1, x_2, and x_3 are determined by the use of nonlinear regression analysis. The values acquired for the aforementioned constants are: x_1 = 0.85, x_2 = 0.68, x_3 = 0.77. Hence the final expression is formed as:

$$f_b = \left[\left[0.85 \times \left(f_c \right)^{0.68} \right] / 0.77 \right], \quad (14)$$

where f_b represents the flexure strength, MPa; f_c represents the compressive strength of a material, MPa.

Out of the 40 data sets, 6 sets (15 %) exhibit forecast errors over 10 %, whereas the remaining 34 sets (85 %) have errors below 10 %, specifically within the range of 0 to 10 %. However, discrepancies in the expected outcomes may arise from the unpredictability and dispersion of the experimental data set. The correlation can be validated by examining the error variability in the projected data, which clearly demonstrates the reliability of the predicted values and facilitates the alignment of results with the experimental data. Nonetheless, Fig. 17, which depicts a dataset with a ±10 % margin of error, has been included here to enhance comprehension.

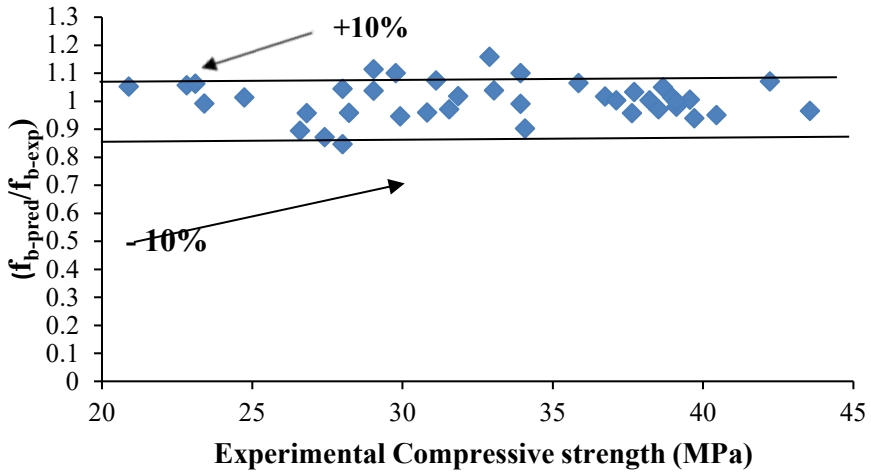

Figure 17. Error variation of predicted vs experimental values of flexure strength.

4. Conclusion

This work has shown that ternary mineral admixtures can reduce clinker while preserving structural performance when proportioned with attention to rheology and late-age reactions. Slump had decreased as fines increased: raising MK from 0 to 8 % reduced slump from 188 to 172 mm (−8.5 %), and at MK 6 % the combinations FA 0/RHA 20 %, FA 10 %/RHA 20 %, and FA 15 %/RHA 20 % had yielded 67, 44, and 35 mm, respectively, which had indicated strong water and superplasticizer demand. Strength responses had mapped a clear hierarchy. MK alone at 8 % produced 30.10 MPa at 7 days, 37.20 MPa at 28 days, and 41.76 MPa at 56 days, surpassing the 100 % OPC control at both 28 and 56 days. The most effective ternary blend across the 39 mixtures was MK 8 % + FA 10 % + RHA 10 %, reaching approximately 30.9 MPa at 7 days, 38.9 MPa at 28 days, and 42.6 MPa at 56 days. At the same MK level, pushing RHA beyond 10 % had depressed 28-day strength to 31.3 MPa at 15 % RHA and 28.8 MPa at 20 % RHA, with 56-day values of 33.99 and 32.06 MPa, respectively. This confirms that excessive porous silica had diluted the clinker and increased admixture adsorption. Tensile responses were sensitive but recoverable: with MK 6 %, the mix FA 10 %/RHA 10 % had reached 2.40 MPa in splitting, compared with 2.44 MPa for the control. Meanwhile, MK 8 % alone had increased flexural strength to 14.25 MPa, compared with 14.00 MPa for the control. The synergy-based equations had predicted compressive strength across the matrix and had supported conversion to split-tensile and flexural values, providing a design-ready pathway for clinker reduction. The findings supported an MK near 8 % with FA and RHA at about 10 % each, coupled with admixture retuning to maintain the target slump, as a practical recipe for strength retention. Future work is encouraged to quantify permeability, chloride ingress and freeze-thaw resistance for the recommended

blends, to couple rheology measurements with admixture chemistry for reliable placement at low w/b ratios, and to validate the predictive framework using multi-source materials and field-cast elements.

References

1. Das, M., Adhikary, S.K., Rudžionis, Ž. Effectiveness of fly ash, zeolite, and unburnt rice husk as a substitute of cement in concrete. Materials Today: Proceedings. 2022. 61(2). Pp. 237–242. DOI: 10.1016/j.matpr.2021.09.005
2. Bui, P.-T., Huynh, T.-P. Performance and microstructural evaluation of rice husk ash-ground granulated blast furnace slag-CFBC fly ash mixtures produced as an eco-cement. Journal of Materials in Civil Engineering. 2022. 34(3). Article no. 04021485. DOI: 10.1061/(ASCE)MT.1943-5533.0004119
3. Chindaprasirt, P., Rukzon, S. Pore structure changes of blended cement pastes containing fly ash, rice husk ash, and palm oil fuel ash caused by carbonation. Journal of Materials in Civil Engineering. 2009. 21(11). Pp. 666–671. DOI: 10.1061/(ASCE)0899-1561(2009)21:11(666)
4. Alrowaili, Z.A., Alnairi, M.M., Olarinoye, O.I., Alhamazani, A., Alshammari, G.S., Al-Buriahi, M.S. Radiation attenuation of fly ash and rice husk ash-based geopolymers as cement replacement in concrete for shielding applications. Radiation Physics and Chemistry. 2024. 217. Article no. 111489. DOI: 10.1016/j.radphyschem.2023.111489
5. Kuffner, B.H.B., Tambara Jr., L.U.D., Marangon, E, Lübeck, A. Development of self-compacting concretes using rice husk or fly ashes and different cement types. REM – International Engineering Journal. 2023. 76(1). Pp. 9–19. DOI: 10.1590/0370-44672021760007
6. Kathirvel, P., Saraswathy, V., Karthik, S.P., Sekar, A.S.S. Strength and durability properties of quaternary cement concrete made with fly ash, rice husk ash and limestone powder. Arabian Journal for Science and Engineering, 2013. 38. Pp. 589–598. DOI: 10.1007/s13369-012-0331-1
7. Öztürk, M., Karaaslan, M., Akgöl, O., Sevim, U.K. Mechanical and electromagnetic performance of cement based composites containing different replacement levels of ground granulated blast furnace slag, fly ash, silica fume and rice husk ash. Cement and Concrete Research. 2020. 136. Article no. 106177. DOI: 10.1016/j.cemconres.2020.106177
8. Vijaya, S.K., Jagadeeswari, K., Karri, S. Behaviour of M60 grade concrete by partial replacement of cement with fly ash, rice husk ash and silica fume. Materials Today: Proceedings, 2021. 37(2). Pp. 2104–2108. DOI: 10.1016/j.matpr.2020.07.523
9. Subramaniam, D.N., Sathiparan, N. Comparative study of fly ash and rice husk ash as cement replacement in pervious concrete: mechanical characteristics and sustainability analysis. International Journal of Pavement Engineering. 2023. 24(2). Article no. 2075867. DOI: 10.1080/10298436.2022.2075867
10. Darsanasiri, A.G.N.D., Matalkah, F., Ramli, S., Al-Jalode, K., Balachandra, A., Soroushian, P. Ternary alkali aluminosilicate cement based on rice husk ash, slag and coal fly ash. Journal of Building Engineering. 2018. 19. Pp. 36–41. DOI: 10.1016/j.jobe.2018.04.020
11. Ouypornprasert, W., Traitruengtatsana, N., Kamollertvara, K. Optimum Partial Replacement of Cement by Rice Husk Ash and Fly Ash Based on Complete Consumption of Calcium Hydroxide. Materials for Sustainable Infrastructure. GeoMEast 2017. Sustainable Civil Infrastructures. Springer. Cham, 2018. Pp. 145–184. DOI: 10.1007/978-3-319-61633-9_10
12. Chindaprasirt, P., Kanchanda, P., Sathonsaowaphak, A., Cao, H.T. Sulfate resistance of blended cements containing fly ash and rice husk ash. Construction and Building Materials. 2007. 21(6). Pp. 1356–1361. DOI: 10.1016/j.conbuildmat.2005.10.005
13. Payá, J., Monzó, J., Borrachero, M.V., Amahjour, F., Girbés, I., Velazquez, S., Ordóñez, L.M. Advantages in the use of fly ashes in cements containing pozzolanic combustion residues: silica fume, sewage sludge ash, spent fluidized bed catalyst and rice husk ash. Journal of Chemical Technology and Biotechnology. 2002. 77(3). Pp. 331–335. DOI: 10.1002/jctb.583
14. Chindaprasirt, P., Rukzon, S. Strength, porosity and corrosion resistance of ternary blend Portland cement, rice husk ash and fly ash mortar. Construction and Building Materials. 2008. 22(8). Pp. 1601–1606. DOI: 10.1016/j.conbuildmat.2007.06.010
15. Fernando, S., Gunasekara, C., Law, D.W., Nasvi, M.C.M., Setunge, S. Development of Blended Fly Ash-Rice Husk Ash–Based Alkali-Activated Bricks: A Sustainable Alternative to Portland Cement Brick. Lecture Notes in Civil Engineering. 2023. 266: 12th International Conference on Structural Engineering and Construction Management. Pp. 643–653. DOI: 10.1007/978-981-19-2886-4_45
16. Chindaprasirt, P., Rukzon, S., Sirivivatnanon, V. Resistance to chloride penetration of blended Portland cement mortar containing palm oil fuel ash, rice husk ash and fly ash. Construction and Building Materials. 2008. 22(5). Pp. 932–938. DOI: 10.1016/j.conbuildmat.2006.12.001
17. Muthanand, P., Nagarajan, M., Sarathbabu, M. Experimental study on rice husk ash and fly ash as partial replacement of cement in concrete. International Journal of Civil Engineering and Technology. 2018. 9(11). Pp. 1170–1177.
18. Karim, M.R., Zain, M.F.M., Jamil, M., Lai, F.C. Development of a zero-cement binder using slag, fly ash, and rice husk ash with chemical activator. Advances in Materials Science and Engineering. 2015. 2015. Article no. 247065. DOI: 10.1155/2015/247065
19. Bhanumathidas, N., Mehta, P.K. Concrete mixtures made with ternary blended cements containing fly ash and rice-husk ash. Seventh CANMET/ACI International Conference on Fly Ash, Silica Fume, Slag and Natural Pozzolans in Concrete. American Concrete Institute. Farmington Hills, MI, 2001. Pp. 379–391.
20. Behnood, A., Modiri Gharehveran, M., Gozali Asl, F., Ameri, M. Effects of copper slag and recycled concrete aggregate on the properties of CIR mixes with bitumen emulsion, rice husk ash, Portland cement and fly ash. Construction and Building Materials. 2015. 96. Pp. 172–180. DOI: 10.1016/j.conbuildmat.2015.08.021
21. Medina, C., Sáez del Bosque, I.F., Frías, M., Sánchez de Rojas, M.I. Design and characterisation of ternary cements containing rice husk ash and fly ash. Construction and Building Materials. 2018. 187. Pp. 65–76. DOI: 10.1016/j.conbuildmat.2018.07.174
22. Kanthe, V.N., Deo, S.V., Murmu, M. Effect of fly ash and rice husk ash on strength and durability of binary and ternary blend cement mortar. Asian Journal of Civil Engineering. 2018. 19. Pp. 963–970. DOI: 10.1007/s42107-018-0076-6
23. Kanthe, V.N., Deo, S.V., Murmu, M. Effect of fly ash and rice husk ash as partial replacement of cement on packing density and properties of cement. International Journal of Innovative Technology and Exploring Engineering (IJITEE). 2019. 8(7). Pp. 1940–1945.
24. Hou, Y., Yin, S., Wang, L., Zheng, K., Yang, K., Wang, Y. Mechanical properties, microstructure and parameter optimization of fly ash-rice husk ash cement backfill. China Mining Magazine. 2025. 34(8). Pp. 178–189. DOI: 10.12075/j.issn.1004-4051.20241972

25. Sathawane, S.H., Vairagade, V.S., Kene, K.S. Combine Effect of Rice Husk Ash and Fly Ash on Concrete by 30% Cement Replacement. Procedia Engineering. 2013. 51. Pp. 35–44. DOI: 10.1016/j.proeng.2013.01.009
26. Fernando, S., Gunasekara, C., Law, D.W., Nasvi, M.C.M., Setunge, S., Dissanayake, R. Engineering properties of waste-based alkali activated concrete brick containing low calcium fly ash and rice husk ash: A comparison with traditional Portland cement concrete brick. Journal of Building Engineering. 2022. 46. Article no. 103810. DOI: 10.1016/j.jobe.2021.103810
27. Khalil, N.M., Hassan, E.M., Shakdofa, M.M.E., Farahat, M. Beneficiation of the huge waste quantities of barley and rice husks as well as coal fly ashes as additives for Portland cement. Journal of Industrial and Engineering Chemistry. 2014. 20(5). Pp. 2998–3008. DOI: 10.1016/j.jiec.2013.11.034
28. Sukkarak, R., Thangjaroensuk, B., Kongkitkul, W., Jongpradist, P. Strength and Equivalent Modulus of Cement Stabilized Lateritic with Partial Replacement by Fly Ash and Rice Husk Ash. Engineering Journal. 2021. 25(10). Pp. 13–25. DOI: 10.4186/ej.2021.25.10.13
29. Krishna, P.U.S., Reddy, K.R., Devi, L.I., RadhaKrishna, V., Kumar, D.P. Experimental Investigation on the Strengths of Cement Bricks Using Fly Ash and Rice Husk Wastes: Recycling Waste Materials. Innovations in Energy Efficient Construction Through Sustainable Materials. IGI Global Scientific Publishing, 2025. Pp. 83–106. DOI: 10.4018/979-8-3693-3398-3.ch004
30. Subramaniam, D.N., Sathiparan, N. Correction (Comparative study of fly ash and rice husk ash as cement replacement in pervious concrete: mechanical characteristics and sustainability analysis). International Journal of Pavement Engineering. 2023. 24(2). Article no. 2148067. DOI: 10.1080/10298436.2022.2148067
31. Rukzon, S., Chindaprasirt, P. Mathematical model of strength and porosity of ternary blend Portland rice husk ash and fly ash cement mortar. Computers and Concrete. 2008. 5(1). Pp. 75–88. DOI: 10.12989/cac.2008.5.1.075
32. Sukkarak, R., Thangjaroensuk, B., Jongpradist, P. Evaluation of fly ash and rice husk ash on the unconfined compressive strength of the compacted cement treated lateritic soil. Suranaree Journal of Science and Technology. 2022. 29(5). Article no. 010169.

Information about the authors:

Ashok Kumar,
E-mail: ashokkumar.civil@nitjsr.ac.in

Virendra Kumar,
E-mail: virendrakumar.ce@nitjsr.ac.in

Sanjay Kumar,
E-mail: sanjaykumar.civil@nitjsr.ac.in

Alexandr Orlov,
E-mail: orlovak@mgsu.ru

Saurav Dixit, *PhD*
E-mail: sauravarambol@gmail.com

Received: 06.01.2025. Approved: 10.09.2025. Accepted: 11.09.2025.